Structural, mechanical and transport characterization of organosulphur nanoscaled molecular films.

Memoria presentada para optar al grado de Doctora en Ciencias Físicas por

Carmen Munuera López

Directora: Carmen Ocal García
Tutor: Jose María Sanz Martínez

Departamento de Física Aplicada
Facultad de Ciencias
Universidad Autónoma de Madrid

Instituto de Ciencia de Materiales de Madrid

Julio 2007

CONTENTS

RESUMEN.

En estos últimos años se está dedicando un considerable esfuerzo al estudio de las películas orgánicas autoensambladas (self-assembled monolayers; SAMs). El interés en estas películas proviene de su posible aplicación en diferentes campos tecnológicas que incluyen desde el control de las propiedades lubricantes de las superficies al estudio de procesos biológicos (por ejemplo, el anclaje de enzimas) e incluso estudios de transferencia electrónica. Pero realmente lo que ha renovado el interés en estas películas, conocidas desde mediados del siglo XIX, ha sido la continua miniaturización de dispositivos tecnológicos que en última instancia está demandando materiales que sean capaces de modificar las propiedades de las superficies a escala nanométrica.

Las SAMs de películas orgánicas ofrecen esta posibilidad ya que su tamaño vertical es de unos pocos nanómetros y se han convertido en componentes ideales de dispositivos nano-electro-mecánicos y nanoelectrónicos (nano-electro-mechanical systems (NEMs), field effect transistors (FETs), organic light emiting devices (OLEDs)…).

Sin embargo, para que la aplicación tecnológica de estas películas tenga éxito, es imprescindible el estudio y comprensión de sus propiedades tanto estructurales como mecánicas y electrónicas. Y aquí es donde juega un papel destacado la investigación a nivel fundamental.

Las propiedades de las películas dependen en última instancia tanto de la estructura interna de las moléculas que la forman como de la calidad y orden cristalino de las mismas. Por ello, el diseño de sistemas de características definidas y/o sintonizables, requiere una caracterización estructural a escala molecular, así como establecer y aprovechar las diferentes relaciones estructura-propiedad para crear películas con propiedades "a la carta".

Este ha sido el punto de partida de esta tesis cuyo objetivo principal es contribuir a alcanzar un mayor conocimiento acerca de las relaciones estructura-propiedad en el campo de la tribología y de la electrónica molecular. Para ello se han realizado medidas tanto de propiedades estructurales como de fricción, mecánicas y de conductividad. Las moléculas estudiadas son las denominadas alcanotioles ($C_nH2_{n+1}SH$), que están formadas por una cadena alcano ($C_{n-1}H_{2n-2}$), un grupo tiol (SH) en uno de sus extremos y un grupo funcional en el otro. El grupo funcional puede elegirse según las características que se deseen, en nuestro caso, interesados en una terminación hidrofóbica se utilizan terminaciones metilo (CH_3). El substrato utilizado es la superficie de Au(111). Los espesores de la película se han controlado mediante el uso de diferentes longitudes (n=10,12,16,18,22). También se han preparado SAMs de alcano-disulfuros. Estas moléculas estan formadas por dos cadenas alcanos unidas por un enlace S-S. Se usaran tanto disulfuros simétricos (con ambas cadenas idénticas) como disulfuros asimétricos (con cadenas de diferente longitud). Estos últimos son especialmente atractivos para la preparación de películas mixtas formadas, en nuestro caso, por moléculas de diferente longitud.

Una de las novedades de este trabajo es el uso de recubrimientos parciales frente a las monocapas completas. Esta forma de abordar el estudio de las SAMs se ha venido utilizando en nuestro laboratorio desde 1998, y permite la obtención de configuraciones moleculares nuevas, diferentes a la de la película completa y, además, proporciona una referencia in-situ (el substrato sin cubrir) tanto para la determinación estructural como para las medidas tribológicas y de conductividad.

La técnica que se ha utilizado es el microscopio de fuerzas atómicas (SFM). Está técnica, es una herramienta básica en la caracterización, manipulación e investigación de problemas básicos a escala nanométrica y permite estudiar de manera precisa y a escala molecular tanto la estructura como las propiedades tribológicas (estabilidad mecánica, fricción…) y de transporte de las SAMs. Además, mediante la adquisición de *películas* de SFM, hemos sido capaces de visualizar el proceso de autoensamblado en tiempo real. Este estudio nos ha permitido obtener nuevos conocimientos acerca de los procesos de reorganización molecular.

Para una mejor comprensión tanto de los resultados experimentales como de las discusiones de los mismos, en el capítulo 2 se han resumido las características generales de las SAMs, principalmente de alcanotioles y disulfuros (que son las moléculas utilizadas en este trabajo) así como los puntos más conflictivos que actualmente existen en la literatura. A pesar de la simplicidad de la molécula constituyente, se puede observar que la caracterización tanto del crecimiento como de la estructura final de las configuraciones moleculares es una tarea compleja. De hecho, para recubrimientos por debajo de la monocapa (que son los utilizados en este trabajo) existe bastante confusión en la determinación de la configuración molecular para las diferentes fases que se observan. Como se muestra en el capítulo 4, el SFM es una técnica muy adecuada para abordar el estudio de estas fases. Dado que en el marco de esta tesis se recurre continuamente al balance entre las diferentes interacciones implicadas en el proceso de autoensamblado, en este capítulo se incluye una descripción detallada de las mismas.

La caracterización estructural se ha enfocado en el estudio de las diferentes configuraciones moleculares que se obtienen para recubrimientos parciales y en condiciones ambientales. Para todas las moléculas estudiadas (excepto los disulfuros asimétricos) se han obtenido resultados similares que muestran que, a estos recubrimientos, hay una coexistencia de fases. Mediante la obtención de imágenes de resolución molecular y la medida de alturas, se ha determinado cual es la configuración molecular en cada una de las fases que se corresponden con: una configuración denominada *striped phase* con las moléculas situadas con sus ejes paralelos al plano del substrato, una configuración rectangular, (2×√3)rect conmensurada con el substrato y con un ángulo de inclinación de 50° y la configuración que se observa en la monocapa, una red hexagonal, (√3×√3)R30°, conmensurada con el substrato y con las moléculas inclinadas 30° respecto de la normal a la superficie. Mediante la adquisición de películas de SFM en muestras recién preparadas, ha sido posible observar que la fase

tumbada o *striped phase* se transforma irreversiblemente en una de las otras dos configuraciones, lo que indica que, bajo nuestras condiciones de trabajo, es una configuración metaestable.

La caracterización tribológica se ha dividido en dos partes, una primera parte sobre el estudio de la estabilidad mecánica y una segunda donde se aborda el estudio de la fricción. Los estudios de estabilidad mecánica están enfocados principalmente hacia la configuración rectangular, ya que esta no se ha sido observada con anterioridad y es conveniente saber si se trata de una estructura metaestable que se forma a recubrimientos parciales. Los resultados muestran un comportamiento diferente de las moléculas denominadas cortas (n=10, 12) frente a las largas (n=16, 18, 22). En el primer caso, la configuración rectangular resulta ser una configuración al menos energéticamente equivalente a la hexagonal. Para cadenas cortas, esta configuración es energéticamente menos estable que la correspondiente hexagonal. La discusión de estos resultados se ha realizado en base a las diferentes interacciones que participan en la estabilidad de estas películas y se han realizado cálculos que explican este comportamiento observado en función de la cadena. Para el estudio de las medidas de fricción se han obtenido curvas de fricción frente a fuerza aplicada para diferentes longitudes y para las diferentes configuraciones. El análisis comparativo de estas curvas nos ha permitido identificar los diferentes mecanismos de disipación de energía que contribuyen a la señal de fricción. Entre ellos se encuentran la creación de defectos *gauche*, y la inclinación colectiva de las moléculas. Estos resultados también han sido analizados en función de las interacciones implicadas en el proceso de autoensamblado.

En el último capítulo de esta tesis se ha abordado el estudio de las propiedades de transporte en estas películas. Este estudio es de gran actualidad ya que estas moléculas se están utilizando como componentes de dispositivos electrónicos en el campo denominado "electrónica molécular". El objetivo principal de este capítulo es estudiar los diferentes mecanismos de conducción a lo largo de estas moléculas. En principio, las SAMs de alcanotioles son aislantes y entre los mecanismos de conducción dominantes que se han propuesto está el efecto túnel a través de la barrera que supone la distancia entre electrodos, en cuyo caso la corriente dependería sólo del espesor de la película, y mecanismos dependientes de la estructura molecular interna y de la película: i) el mecanismo a lo largo de los orbitales solapados de la molécula (through bond tunnelling TB) en que la corriente dependerá del número de enlaces dentro de la molécula, o dicho de otra manera, de la longitud de la molécula y ii) un segundo tipo de túnel entre moléculas adyacentes (through-space tunnelling, TS) que se espera relevante en configuraciones donde las moléculas estén inclinadas. Estudiar los diferentes mecanismos individualmente es complicado, ya que normalmente para variar el espesor se varía la longitud de la cadena (y por tanto el número de enlaces). En este trabajo se presenta una alternativa que implica el uso de moléculas de distintas longitudes y de películas de distinto espesor formadas por la misma moléculas (estas últimas las conseguimos variando el ángulo

de inclinación de la molécula). Esto permitirá analizar la importancia relativa de cada uno de los mecanismos.

Con los estudios presentados en este trabajo, dedicados a la caracterización estructural de las películas orgánicas, a la compresión del proceso de autoensamblado y la importancia relativa de las interacciones que incluye dicho proceso, así como la comprensión de las relaciones "propiedades tribológicas-estructura" y "propiedades de transporte-estructura", se pretende contribuir (al margen de su interés para la física fundamental) al desarrollo y optimización de la películas autoensambladas para su aplicación en los diferentes campos de la nanotecnología.

1.1 MOTIVATION AND OBJECTIVES

Designing surfaces with specific physical and/or chemical properties is of enormous importance from a scientific point of view since these properties influence phenomena such as catalysis, corrosion, lubrication, adhesion, wettability, electrochemistry, biocompatibility, etc… among many others [Love05]. If this design is not a costly process and can be performed in a micro and even at the nanometre scale, the idea is, in addition, attractive from technological point of view. These are basically the main reasons why, during the last two decades, the interest in self-assembled monolayers (SAMs) of organic molecules has spectacularly grown.

The most appealing feature of these SAMs is their ability to organize spontaneously into well ordered structures on a wide variety of surfaces, under different environmental conditions and without external manipulation. Moreover, owing to their small size (in the nanometre range) and their versatility to provide functional surface properties, different from that of the underlying substrate, these layers constitute promising components on the near future technology. In fact, one of the fundamental approaches of Nanotechnology for device fabrication, the so-called bottom-up strategy, relies in self-assembly processes that considerably reduce the need for complex metodologies to manipulate objects with nanometre resolution.

Besides constituting one of the hopes to solve practical issues in Nanotechnology, self-assembled monolayers are also intrinsically interesting from the point of view of basic science since they are model systems for studying different fundamental process occurring at the surfaces. They are leading protagonists in the Nanoscience scenario, eventually linking molecular-level structures to macroscopic interfacial phenomena.

It is then understandable and justified the enormous attention that the self-assembled monolayers have caught, and still are receiving, within the scientific community. This attention has been mainly focused to shed some light on the growth mechanism and structural properties of the systems, which include complex molecular behaviour and the subtle interplay of different interactions.

Firstly, these studies are essential for potential applications of these films, since understanding the correlation between structure and physical/chemical properties facilitates indeed the fabrication and high performance of a particular device. Secondly, they have provided valuable information on fundamental aspects of surface science.

Few SAMs have received as much attention as alkanethiols on Au(111). The enormous interest originates from the system's two-dimensional crystalline order which has made of it an archetypical system for a large variety of studies. To date, an impressively detailed knowledge,

provided by both experimental and theoretical investigations, has been gained on their growth, molecular structure and self-assembly mechanism. However, some aspects still remain unravelled and the relevance of their consequences deserves further specific and directed studies.

In the present theses we have addressed some new aspects of this subject to give insight in lacking details about the structural, mechanical and transport characterization of organosulphur nanoscaled molecular films.

Why? Because, on one hand, in the development of nanomechanical and nanoelectromechanical devices, it is crucial to count on nanometre sized lubricant layers with good nanotribological properties under working conditions. The severity of most practical environments in many applications questions about the molecular order under load and at ambient conditions. And, on the other hand, for the development of organic based molecular devices, it is essential to understand, predict, and control mechanical behaviour and electrical conduction through molecules and their aggregates, in order to tune the materials properties at the molecular scale by tailoring molecules and their interactions. SAMs constitute the most appealing molecular junction for practical molecular electronic devices.

For the studies presented in this theses, we have used high-resolution scanning force microscopy using different strategies to unravel the room-temperature adsorption structures of different organosulphur molecules (at submonolayer coverages and obtained from solution) and their tribological and transport properties. The manuscript is organized as to first introduce the state of the art of the self-assembled monolayer subject including the applications under interest (Chapter2) and introduce the experimental technique and the different proposed strategies and approaches used throughout the theses (Chapter 3). With this background, the complete structural characterization and surface dynamics at submonolayer coverages is presented (Chapter 4) before envisaging the mechanical stability and friction response under applied pressure (Chapter 5). Finally, making use of the experience accumulated from the methodology employed, very recent conductivity experiments and their results are described (Chapter 6) with the aim of contributing a further step in clarify about the charge transport mechanisms in these organic films.

The aim of this work has been offering new strategies for both, sample preparation and data acquisition, with the ability of providing valuable and reliable information obtained from controlled methodologies. This has opened a way of elucidating existing controversies but overall, has opened the possibility to solve some new issues and we hope will be useful to face future challenges. In

particular, as a consequence of the present theses results, foreseen interesting properties of hetereogeneous functionalized samples obtained by soft-methods are on the focus of our near future investigation, to be used as "chemical contrast" and "transport contrast" templates for ulterior growth and molecular anchoring.

CHAPTER 2.- SELF-ASSEMBLED MONOLAYERS.

Although the beginning of the study of self-assembled monolayers (SAMs) properties dates back to the mid part of the last century, the structure and growth mechanisms of these organic layers are far from being completely understood. Moreover, due to the capabilities to synthesize new organic compounds, this research area is continuously growing, and the variety of possible SAMs systems seems to be only limited by our imagination.

When getting into this field, there are several general and widely accepted issues regarding the self-assembling process and the monolayer structure that provide a really valuable background. In this chapter we review some of these useful concepts as well as part of the, on the other hand, extensive literature existing on SAMs, to provide an adequate scenario for the results and discussions presented within the following chapters. Though many issues are common to SAMs in general, we mainly focus on those formed by alkanethiol and dialkyl disulphide molecules on gold which, in fact, are the systems investigated in this work. Before proceeding reviewing what is known about their structure and growth, we give a short introduction to the concept of self-assembly.

2.1 THE CONCEPT OF SELF-ASSEMBLY.

The term self-assembly is nowadays extensively used, which occasionally causes confusion. In a general sense, it can be defined as the spontaneous formation of complex hierarchical structures from pre-designed building blocks, typically involving multiple energy scales and multiple degrees of freedom. Rather than being an unusual process, the self-assembly concept is present in our daily life and is a very general principle in Nature as seen, for example, in the formation of micelles by surfactants, membranes by lipid molecules or biological cells by living organisms.

More specifically related with this work, self-assembly is the phenomenon in which a number of independent organic molecules suspended in an isotropic state come together to form an ordered aggregate. Self-assembled films are thus formed when molecules organize themselves in a 2D arrangement on the surface of a substrate as shown schematically in figure 2.1.

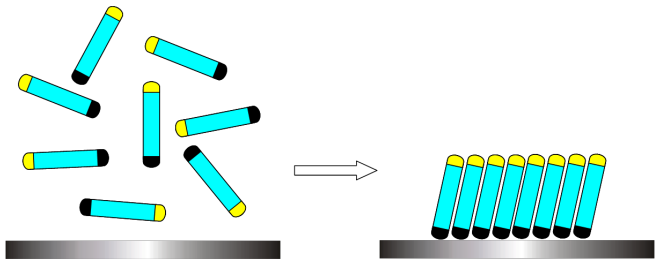

Figure 2.1 Self-assembly of molecular adsorbates onto a solid surface.

An early description of self-assembled films was reported by Benjamin Franklin in the 18th century, when he observed that a spoonful of oil spontaneously spread to cover the surface of a pond. In the 19th century, Agnes Pockles and Lord Rayleigh performed the first fundamental experiments on oil-water interfaces, which established methods for reproducibly generating these films and provided evidence of a layered structure that was only one molecule thick. Despite these studies, oil-on-water films are now named after the scientist Irving Langmuir (20th century), because he was the first to

provide a modern understanding of their structure at the molecular level (e.g. orientation of the molecules). Later, Katherine Blodgett and Langmuir showed that the adsorbates in a Langmuir monolayer could be transferred to a solid support to generate a physisorbed monolayer. The development of these Langmuir-Blodgett (LB) films was of great significance, because it demonstrated that the interfacial properties of solid surfaces could be influenced by adsorbing a thin organic film.

However, the concept of self-assembled monolayer (SAM) was not used to describe these films. W. A. Zisman has been often credited with originating this concept in 1946 [Bigelow46]. These films were generated by dipping a metal or metal oxide surface into a solution of polar organic molecules, and the different feature between these "self-assembled" and the LB films was the adsorbate-substrate interaction. In the latter case these interactions were primarily of a physical nature whereas the SAM concept implicitly entails chemical interactions and bond formation between the molecule and the substrate.

In the early 1980s, the self-assembled monolayer concept was brought into the popular scientific consciousness with the study of Nuzzo and Allara (thiols on gold) [Nuzzo83] and Maoz and Sagiv (trichlorosilanes on silicon oxide) [Maoz84]. These studies introduced what were to become the two most popular SAMs systems to date.

Figure 2.2 shows a more detailed picture of a self-assembled monolayer. When describing the formation and organization of SAMs, it is useful to divide the structure of the molecule into three parts:

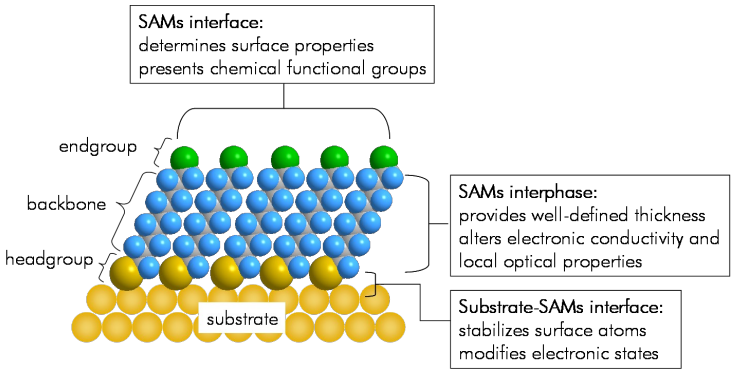

Figure 2.2 Schematic representation of a SAM: the different parts of the molecules and their influence on the monolayer properties have been highlighted.

- headgroup: it is the part of the molecule that interacts with the substrate and its chemisorption to the substrate is essential in monolayer formation. A typical headgroup-substrate pair is S-Au, formed in the adsorption of organosulphur compounds, such as thiols (R-SH), sulphides (RSR′) or disulphides (RSSR′) [1] on gold.

[1] R and R′ denote the rest of the compound attached to the headgroup.

- spacer or backbone: this part of the molecule act as a physical barrier between the substrate and the external environment. For the simplest SAMs studied, the backbone is formed by an alkyl chain (CH_2 groups) whose length normally varies between 1 and 3 nm, depending on the number of methylene groups.
- terminal group or endgroup: it is the part of the molecule in direct contact with the external environment and the one that determines the SAMs´ surface properties.

The wide range of applicability of these SAMs stems mainly from the flexibility to modify one or several of these parts and thus change the final film's properties. Variation in the chemical contact between the molecule and the substrate controls the strength of the interaction and thereby, the stability of the assembly, but also properties such as the electron transmission from the molecule to the surface under an applied potential [Selzer02]; changes in the inner structure and nature of the film affects its innate ability to order [Lee00]; and the terminal functional group of a SAM exerts the most direct influence on the surface properties of the film: hydrophobic/hydrophilic character, adhesive and frictional characteristics, reactivity, etc… For this reason, chemical modification of the endgroup is an active field of research [Laibinis98][Witt04].

2.2 SAMs OF ORGANOSULPHUR COMPOUNDS.

SAMs formed from sulphur-containing compounds on gold, and in particular the alkanethiol/Au(111) system, have attracted most of the research interest on the field since the first work by Nuzzo and Allara [Nuzzo83]. The main reasons that have made this system so interesting are twofold: these SAMs are easy to generate from either solution or the gas phase and they form densely packed and precisely oriented films, whose thickness and surface properties can be adjusted using standard organic synthetic methods.

Moreover, the use of gold substrates provide additional advantages; firstly it binds thiols with high affinity, which promotes the displacement of adsorbed solvent from the gold surface readily. Secondly, it is a reasonably inert metal. When compared with other metals, gold has the lowest tendency to react with air to form oxides; it does not react with atmospheric O_2; it does not react with most chemicals. This allows working for relatively long periods of time under ambient conditions which for example in experiments with biological samples is somehow preferred than UHV conditions. Although expensive and not essential to many purposes, single crystals are available commercially. More conveniently, gold can be acquired both, as a thin film and as a colloid, and in particular, thin films can be prepared by physical vapour deposition, sputtering, or electrodeposition and are commonly used as substrates for a number of experimental investigations involving spectroscopies or other analytical techniques, including surface plasmon resonance (SPR) spectroscopy, quartz crystal microbalances (QCM), reflection adsorption infrared spectroscopy (RAIRS), and ellipsometry. Tough

this is only a brief summary on the attributes of the alkanethiol/Au system, it helps to understand why it has become one of the most popular systems in the SAMs field.

2.2.1 The Alkanethiol And Dialkyl Disulphide Molecules.

In organic chemistry, a thiol is a compound that contains an -SH functional group which is referred to either as a thiol group or a sulfhydryl group. The number of thiol-based systems is immense differing in the characteristics of the rest of the compound attached to the thiol group (RSH).

As a point of interest, many thiols are colourless liquids and have a strong and repulsive odour, particularly those of low molecular weight. This is the reason why natural gas distributors began adding various forms of thiols, usually ethanethiol, to natural gas, which is naturally odourless, to be able to "smell" possible leakages within the pipes.

Back to the molecular description, an alkanethiol molecule, therefore, consists of a thiol group attached to a chain of methylene groups (CH_2). When the other end of the molecule is a methyl group (CH_3), as depicted in figure 2.3(a), it is referred as unsubstituted alkanethiol. Regarding the molecular description made in the previous section, in this case the SH is the headgroup, and the CH_3 the endgroup of the molecule. The CH_2 chain constitutes the molecular backbone. The general formula is $CH_3(CH_2)_{n-1}SH$ but are often denoted as Cn. From now on we will use this short notation.

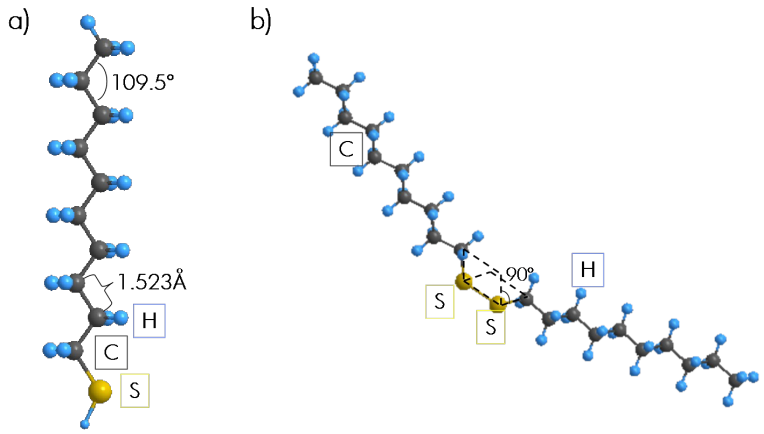

Figure 2.3 Depiction of (a) a decanethiol (C10) and (b) a didecyl disulphide (C10C10) molecule. In both cases the alkane chains are in the extended *trans* configuration. The planes that define the CSSC diehedral angle of the disulphide molecule have been indicated.

Depending on the number of carbon atoms in the chain (n), the length of the molecule varies between 1 and 3nm. For instance, the molecular length for n=10, in the extended configuration, is ~1.65 nm, considering the bond lengths given table 2.1 and including an additional 1.92 Å for the terminal CH_3 group [Wasserman89].

This extended or *trans* conformation is the lowest energy configuration for an alkanethiol molecule. The alkyl chain is completely extended with the carbon atoms located in a zig-zag arrangement (backbone structure) within the same plane. The cross section or area per molecule

perpendicular to the chain axis in this configuration is ~18.4 Å^2. This results in a minimum packing distance between two alkanethiol molecules of ~4.3 Å, that can only be achieved if both molecules present the *trans* configuration and the C-C backbone of one of the chains fits into the other (see following sections). The intermolecular interaction between molecules (of van der Waals type for unsubstituted alkanethiols) reaches its maximum at this distance, which also is referred as the van der Waals diameter of the molecule [Kitaigorodskii61].

Table 2.1 Bond distances and angles for the alkane-based molecules of figure 2.3 [Kitaigorodskii61].

	Bond length (Å)					Angle (°)		
	S-H	S-C	C-C	C-H	S-S	C-C-C	S-S-C	C-S-S-C[2]
alkanethiol	1.345	1.815	1.523	1.113		109.5		
dialkyl disulphide		1.815	1.523	1.113	2.024	109.5	120	90

Figure 2.3(b) shows the structure of a dialkyl disulphide molecule. These molecules have an S-S bond and two alkane chains attached to each sulphur atom. If both chains are identical, in length and with the same endgroup (as in figure 2.3(b)), the molecule is called a symmetrical disulphide. Conversely, molecules obtained either varying the length or the endgroup of one of the chains with respect to the other are referred as asymmetrical disulphides. The symmetrical and asymmetrical disulphides that have been studied in the frame of this thesis all have the same endgroup, CH_3. Consequently, the asymmetry of the latter arises from a difference in length between both alkyl chains.

The general formula for these dialkyl disulphides is $CH_3(CH_2)_{n-1}S\text{-}S(CH_2)_{m-1}CH_3$, and in short notation we will refer to them as CnCm.

Since this thesis concerns the study of the self-assembled monolayers formed by the molecules above described on A(111), table 2.2 collects some physical properties of particular interest of the respective surfaces.

Table 2.2 Magnitudes listed for the Au surface and CH_3-terminated SAM: total surface energy (γ), Young modulus (E) and Hamaker constant (A).

	Au	CH_3-SAM
γ (mJ/m^2)	50 [Ahn03]	~20 [Ahn03]
E (GPa)	80 (bulk value)	~10 [Weihs91]
A (J)	~40·10^{-20} [Israelachvili92]	5-7·10^{-20} [Israelachvili92][Salmeron93] [Aveyard99][Ederth01]

In the following sections we summarize some of the general growth and structural properties reported for these systems.

2.2.2 Alkanethiols on Gold: Structure Of The Complete Monolayer.

[2] This is the dihedral angle defined as the angle formed by the two unit vectors orthogonal to the two planes formed by atoms (C1,S,S) and (S,S,C2) respectively. In solution, the preferred disulfide conformation yields a value of 90° for this angle [Bain89b][Biebuyck94]. See figure 2.3.

SAMs of organosulfur-based compounds on gold (particularly on the lowest energy (111) surface), are usually prepared by two different methods: from solution or from the gas phase. Several works have reviewed the growth and evolution of the SAMs as function of coverage and, though differences in the kinetics of monolayer formation and the configurations found at submonolayer coverages have been reported (see section 2.2.3), the molecular structure of the complete monolayer is essentially identical regardless the preparation method used [Schreiber00] [Schwartz01][Love05].

To study the structural characteristics, different and complementary surface techniques have been employed (some of them are summarized in table 2.3. For a more complete description see [Vericat06]). When the results obtained from each analysis are put together, an almost complete picture of the structure of the full coverage phase of alkanethiols on Au(111) is achieved.

Table 2.3 Surface science techniques used to study alkanethiolate SAMs on Au(111). From [Vericat04]

Technique	Main information provided	Reference
GIXRD/XRD	2D SAM structures (periodic) Adsorbate-substrate distances	[Fenter93][Schreiber98] [Schreiber00][Torrelles04]
IR spectroscopy	Molecular orientation SAM crystallinity SAM vibrational properties/functional groups	[Porter87][Nuzzo90][Laibinis91]
LEAD	2D SAM structures (periodic)	[Chidsey89][Camillone93]
LEED	2D SAM structures (periodic)	[Schreiber98]
SFG	Molecular orientation SAM crystallinity SAM vibrational properties	[Yeganeh95]
SFM	2D SAM structure (also non-periodic features)	[Alves92][Delamarche96][Xu98] [Barrena99]
STM	2D SAM structure (also non-periodic features) SAM defects Electronic structure	[Poirier94][Delamarche94] [Delamarche96][Poirier97] [Terán Arce98] [Schreiber00][Zeng02]
TPD	Composition SAM adsorption/desorption energies	[Nuzzo87][Schreiber00]
XPS	Elemental composition and chemical state SAM coverage SAM thickness	[Nuzzo90][Schreiber00] [Vericat01]
XSW	Adsorbate-substrate distances	[Roper04][Fenter98]

Two useful perspectives are commonly used in the description of this structure: the top view, which presents the 2D structure of the adsorbates projected onto the surface of the substrate (figure 2.4) and the side view, which presents the structure of the adsorbates extending above the surface (figure 2.5).

2.2.2.a Top view.

This view describes the 2D symmetry of the packing structure and the commensurability of molecular and substrate lattices. As shown in figure 2.4(a), the alkanethiol molecules form a (√3×√3)R30° hexagonal lattice, commensurate with the underlying Au(111) surface.

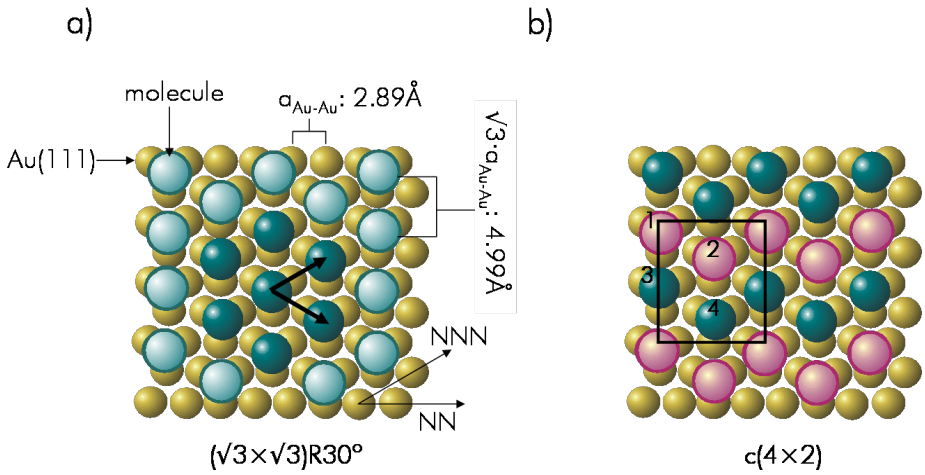

Figure 2.4 Top view of the full coverage structure of alkanethiols on Au(111). The small and large circles represent the gold atoms and the molecule endgroups, respectively. (a) (√3×√3)R30° arrangement of the alkanethiol molecules with respect to the substrate. The darker circles highlight the hexagonal cell. The nearest-neighbor (NN) and next-nearest-neighbour (NNN) direction of the Au(111) have been marked. (b) Scheme for the c(4×2) superstructure with the rectangular (3×2√3)rect unit mesh.

Given that surface lattice parameter is a_{Au-Au}=2.89 Å (the nearest-neighbour (NN) distance in the Au(111) plane), the 2D lattice parameter of the monolayer is √3·a ~5 Å, coinciding with the next-nearest-neighbor (NNN) distance in the substrate surface. The unit cell contains one molecule and the area per molecule is 21.65 $Å^2$. This is the highest density phase obtained for alkanethiols on A(111) and yields a surface coverage of 0.33. This structure has been reported for chains with n=2, 4-18 and 22 carbon atoms.

A conflicting point regarding the full coverage structure arises when trying to determine the sulphur binding site. The picture in figure 2.4(a) is the projection of the molecules onto the substrate surface but not necessarily represents the sulphur positions. Attempts to clarify this issue by theoretical and experimental methods have given irreconcilable results and thus, no conclusive picture has emerged yet on the adsorption site of the sulphur atom.

The literature also confirms that the (√3×√3)R30° structure can be modulated by a c(4×2) superlattice whose symmetry is shown in figure 2.4(b) [Camillone93][Bucher94][Delamarche94] [Poirier94][Fenter98]. In fact, taking into account the registry with the substrate, the correct form to denominate this superstructure is (3×2√3)rect, but we will keep the widely used notation of c(4×2) which refers to the symmetry with respect to the hexagonal alkanethiol lattice.

The area per molecule is identical to the hexagonal model of figure 2.4(a), but there are two pairs of non-equivalent molecules per unit cell, highlighted and labelled as 1(3) and 2(4) in figure 2.4(b). This results in unit cell dimensions of 9.99 × 8.65 $Å^2$, four times larger than that of the (√3×√3)R30° lattice.

This superlattice is usually observed in defect-free, very dense monolayers, but its origin is still a controversial subject. It has been attributed, for instance, to the existence of different orientations of the hydrocarbon chain planes of the molecule within the unit cell, to the existence of non-equivalent binding sites for the sulphur headgroups that deviate from the (√3×√3)R30° arrangement or even to a sulphur dimerization on the surface. A detailed description and comparison of the different proposed models can be found in [Ulmanbook][Schreiber00] [Vericat05] and references therein.

2.2.2.b Side view.

This view describes the conformation, tilt and twist angle of the alkyl chain with respect to the surface normal. The molecules on the substrate surface are described by three angles (figure 2.5(a)): the molecular tilt (θ), the angle of rotation of the hydrocarbon chain plane about the molecular axis (β) and the angle of precession or azimuth (φ), which defines the tilt direction and is obtained from the projection of the molecule on the substrate plane.

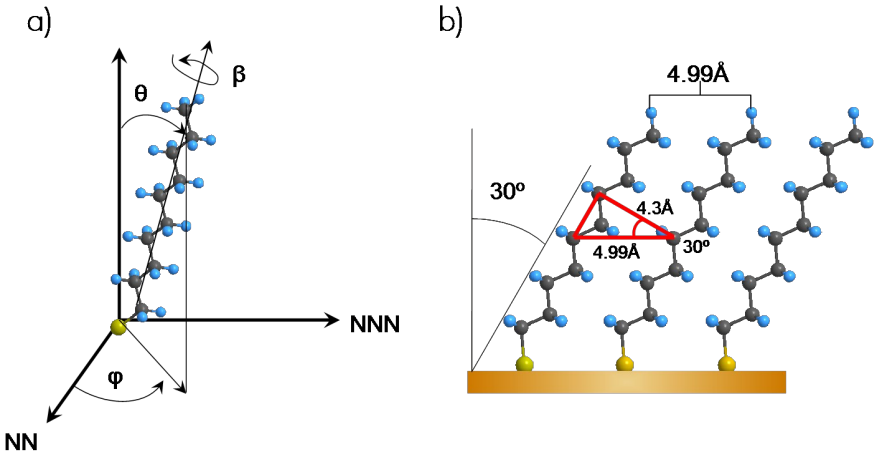

Figure 2.5 (a) Scheme of an alkanethiol molecule and the angles used to describe its configuration. The NN and NNN directions of the Au(111) lattice are indicated. (b) Side view of the full monolayer configuration of alkanethiols on Au(111): the molecules packed in an all-*trans* configuration with their alkyl chains tilted θ=30° from the surface normal towards the NN direction of the gold substrate (φ=14°) [Fenter93]. The average value of β is 55° [Nuzzo90]

Studies on the molecular orientation of alkanethiols monolayers on Au(111) have shown that the molecules are in a *trans* configuration, tilted about 30° from the surface normal (figure 2.5(b)) [Nuzzo90][Hähner92][Fenter93].

This organization of the alkyl chains results from optimizing the molecular lateral interactions within the geometric constrains imposed by the sulphur-gold bonding. Optimizing the van der Waals interaction between chains (obtained for a chain-chain distance of 4.3 Å) while maintaining the 2D lattice distance of the hexagonal (√3×√3)R30° structure (~5 Å), can only be achieved if the molecules are tilted respect to the surface normal. In particular, as shown in figure 2.5(b), a 30° tilt results in a chain-chain distance equal to that of the optimal packing.

Regarding the tilt direction, i.e. the azimuth angle, it is commonly accepted as an average value the 14° away from the NN direction of the Au (111) (i.e. almost along the NNN molecular direction) reported in [Fenter93]. However, in a systematic investigation as a function of chain length, this tilt direction exhibited a trend of shifting away from the NNN direction towards the NN direction of the (√3×√3)R30° structure, for shorter chain lengths (N≤14). The explanation to this behaviour was based in the competition between the intermolecular and the molecule-substrate interactions: whereas the former dominates in long-chain SAMs and promotes a structure similar to that found in n-alkane molecules in the bulk, both interactions become comparable in short-chain SAMs and the final configuration is somehow modified by the substrate [Fenter97]. As we show in the frame of this thesis, this relative balance between interactions is essential in determining the properties (structure, stability, frictional characteristics….) of these organic layers.

This section is just a summary of what has been reported for alkanethiols on gold, regarding the structure of the complete monolayer. Though conflicting points still remain, it is a well determined configuration and there is a general consensus on its structural characteristics. This is not the case for the configurations formed at submonolayer coverages, where different structures have been reported by different groups and their formation seems to depend on the particular experimental conditions. Though there is not a unique picture, since the results presented in this work have been mainly obtained at coverages below monolayer completion, the following section collects the most relevant results reported at low coverages for the Cn/Au(111) system.

2.2.3 Alkanethiols on Gold: Structure At Submonolayer Coverages.

One of the most appealing characteristics of the self-assembled monolayers is the self assembly process itself: the different regimes and configurations found prior to the completion of the monolayer, the kinetics and thermodynamics aspects of the assembly…The first study on the kinetics of the adsorption of thiols on gold was performed in 1989 and the results indicated the existence of two distinct regimes: the first regime taking place within the range of seconds to a few minutes and which

almost covers the formation of the 80%-90% of the film; the second regime taking place within the range of minutes to several hours during which, film properties such as the contact angle and thickness reached limiting values [Bain89].

Subsequent studies performed with different techniques (including IRRAS, QCM, STM, XPS, SHG, NEXAFS, SPR, SFM and TPD) supported the aforementioned two-regimes model although the exact details of the process (e.g. regime duration) varied among them [Ulmanbook][Schreiber00] [Schwartz01][Love05]. These variations plausibly arise from differences in the experimental conditions used: the nature of the adsorption medium (i.e. gas-phase versus solution-phase or polar solvents versus non polar solvents), the purity, concentration and/or chain length of the adsorbates, the cleanliness and quality of the gold substrate and the temporal sensitivity of the analysis. Despite these differences, a general picture of the self-assembly of alkanethiol molecules on gold can be sketched (figure 2.6): the initial fast regime is proposed to involve adsorption of the headgroup to the gold surface, formation of a low-density configuration of lying-down molecules (with their molecular axis aligned parallel to the gold surface) and transition from this lying-down phase to the standing-up configuration during which, intermediate configurations are formed. During the second regime, structural healing of the alkyl chains has been proposed to occur, to adopt the all-*trans* extended configuration that optimizes the chain packing.

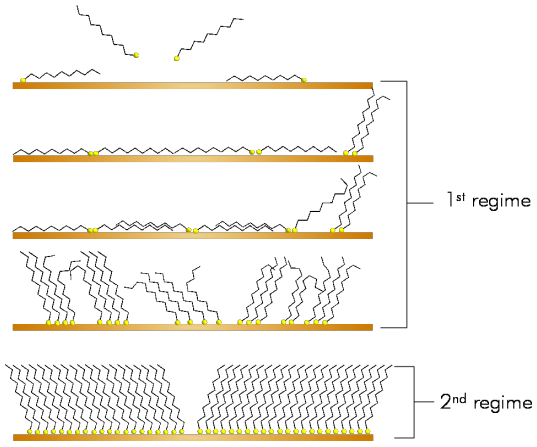

Figure 2.6 General representation of the evolution of structures during self-assembling of alkanethiols on Au(111). For simplicity, only the zigzag structure of the molecule backbone has been drawn. The two regimes mentioned in the reported studies are identified (see text).

The discrepancies arise when trying to determine how many different intermediate structures exist, their stability and/or dependence on the experimental conditions.

2.2.3.a Striped configuration.

Intuitively, it can be already expected that, at sufficient low coverage, the molecular backbone is lying down flat on the surface, which is in fact the defining feature of the lowest-density phase reported for alkanethiols on Au(111): the lying-down or striped phase. This configuration is generally

characterize by a p×√3 unit cell, where p is the stripe separation and √3 the spacing within the stripes, both in units of the Au(111) lattice parameter. In the first study reporting this configuration, values of p=11 and p=13 were measured for C10 and C12 molecules, respectively [Camillone94]. Subsequent studies confirmed that this periodicity perpendicular to the stripes was length-dependent and equal to twice the chain length of the corresponding molecule [Camillone96][Poirier96] [Balzer97][Yamada97][Yamada98][Staub98][Poirier99][Kondoh99][Toerker00][Poirier01].

The real space model proposed based in the experiments, is shown in figure 2.7 for decanethiol (C10). For theses molecules, the measured separation between stripes is 11×2.89 Å ≈32 Å. Each stripe contains two rows of sulphur atoms running along the NNN direction of the gold substrate, and the molecules lie fully stretched in a head-to-head arrangement along the long axis of the unit cell (the NN direction of the Au(111) surface). Once again, the exact position of the sulphur atoms is not known, although an STM study at submolecular resolution indicated the possibility of hollow hcp sites and atop sites for sulphur binding within the two rows forming a stripe [Staub98]. This possibility is the one depicted in figure 2.7.

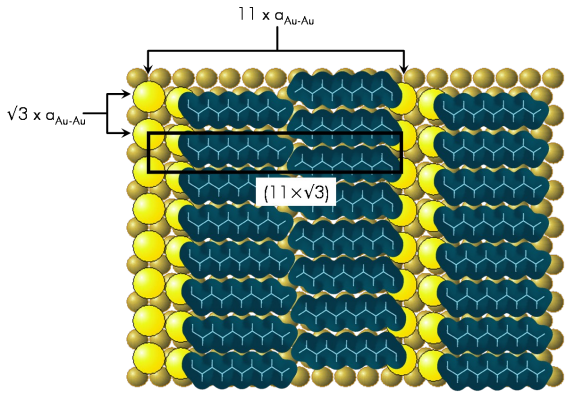

Figure 2.7 Real space model of the (11×√3) striped phase observed for C10 on Au(111). The structure consists of pairs of molecular rows with the sulphur atoms aligned along the NNN direction of the gold surface and the molecular axis fully stretched along the NN direction, in a head-to-head arrangement. The (11×√3) cell has been marked.

In some cases, instead of the primitive unit cell of figure 2.7, a centred one with approximate twice the lattice parameter p, was found. For hexanethiol (C6) these structures were labelled p(8×√3) and c(15×√3); for decanethiol (C10), p(11×√3) and c(23×√3). A closer inspection showed that to switch from the primitive to the centred structure, only a small displacement of every second row of stripes is needed. In fact, the two different phases were found within one set of experiments for slightly different preparation conditions and are very similar in terms of area per molecule (in the case of C10, 79 $Å^2$/molecule and 82 $Å^2$/molecule for the primitive and the centred cell respectively) [Kondoh99].

The striped configuration has been observed for molecules of different length (n=6-12) and the model of figure 2.7, that fulfils the experimental periodicity and its dependence on the molecular length, is the widely accepted real space picture. This is the configuration with the lowest reported surface density and, in the example of figure 2.7, the coverage is 27% of the complete monolayer.

2.2.3.b Intermediate configurations.

Intermediate configurations have been observed for different molecular length (n=10-18) during gas-phase deposition [Schreiber98][Schwartz99][Poirier99][Camillone96], immersion in dilute solutions (≤10μM) [Yamada97][Yamada98][Noh01], after thermal annealing of densely packed SAMs under UHV [Staub98][Toerker00], ambient conditions [Xiao01], during SAMs patterning [Larsen97] or dip pen nanolithography [Sheehan02]. Some of these configurations also present a striped structure and, by analogy with the lowest density phase, are described with a unit cell in the p×√3 form. But their defining feature is that the periodicity perpendicular to the stripes is, in all cases, lower than twice the respective molecular length.

For the extensively studied C10/Au(111) system, intermediate striped configurations with p=9.5, 9 and 7.5 have been reported, coexisting with other *mesh* structures [Camillone94] [Yamada98][Poirier99][Toerker00][Qian03].

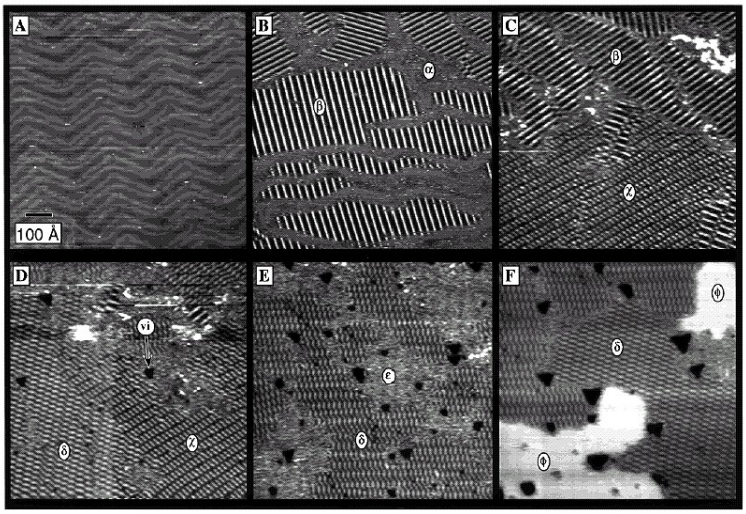

Figure 2.8 STM images of the vapour-growth of C10 molecules on Au(111) in UHV, showing the coexistence of different configurations as a function of coverage. (A) clean Au(111) surface measured prior to alkanethiol evaporation, showing the herringbone reconstruction. (B)-(F) configurations observed when the coverage increases. From [Poirier01].

The complexity of this regime arises from the fact that, at intermediate coverage, there is a broad spectrum of different non equilibrium structures. As an example, we have taken figure 2.8 from [Poirier01], where the evolution of the C10/Au(111) system has been monitored as a function of coverage. Image A shows the herringbone reconstruction typical of the clean Au(111) surface, and from B to F, the C10 coverage is gradually increased. The configurations denoted as β and ϕ

correspond to the striped and hexagonal configurations described in sections 2.2.3.a and 2.2.2, respectively. The other four (α, ε, δ and χ) are intermediate configurations. In that work it was proved that their stability depended on experimental parameters, such as the temperature during growth [Poirier01].

This dependence on the particular experimental conditions makes it difficult to present a unifying picture of the intermediate-coverage regime. Moreover, since many structural studies do not provide direct information about the molecular density nor about film height, it is also difficult to determine, within a particular configuration, the number of molecules per unit cell and the true molecular arrangement (flat, tilted or upright molecules).

Specially revealing of these difficulties is the case of the (7.5×√3) striped phase[3] observed in different studies (STM, LEED and LEAD) and for various preparation conditions. Models based either on lying down or standing up molecules have been found in the literature to be responsible for the same surface periodicity [Dubois93][Schoenenberger95][Camillone96][Porier99][Toerker00][Qian03]. Figure 2.9 shows two of the models proposed to account for the stripe periodicity of 21.6 Å (p=7.5) observed in the C10/Au(111) system.

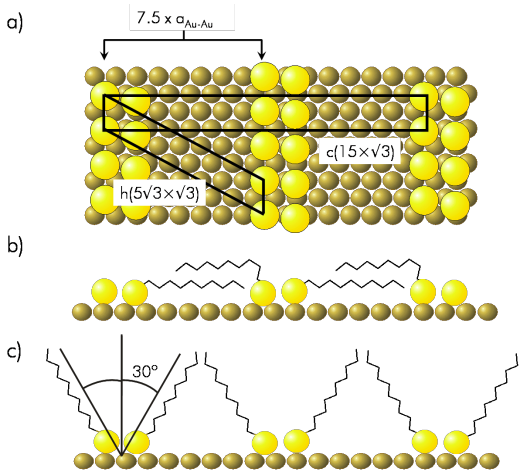

Figure 2.9 (a) Schematic top view representation of the sulphur arrangement in the (7.5×√3) striped phase of C10. The two unit cells (centred and hexagonal) used to label the same structure have been highlighted. (b) Interdigitation model [Poirier99] (side view) (c) Model proposed in [Quian03] (side view).

In both cases the sulphur atoms are arranged in double rows, with a √3 periodicity along the row, as in the model proposed for the lowest density (11×√3) phase, but with smaller distance between stripes to match the smaller periodicity of the (7.5×√3) phase.

In the first model, figure 2.9(b), half of the molecules are lying flat on the substrate, and the other half are tilted out of the surface plane, lying atop the counter oriented molecules. The difference between twice the chain length (~33 Å) and the measured periodicity is thus overcome with the overlapping of the alkyl chains. This is called the interdigitation model and was first proposed in

[3] This phase has also been described as an hexagonal (5√3×√3)R30° and a centred (15×√3) unit cell.

[Poirier99] to explain the transition, as the coverage increased, between the lying down and standing up configurations. Note that this model implies a distortion of the *trans* configuration of the molecules lifted out the surface.

Figure 2.9(c) shows an alternative model proposed in [Qian03], where the molecules present the tilt angle of the full coverage phase, approximately 30° from the surface normal.

Both models meet the experimental periodicity but yield completely different molecular configuration. However, the lack of experimental data makes it difficult to rule out one of the models in favour of the other.[4]

An effective way to circumvent the above ambiguity in molecular orientation is shown in [BarrenaThesis][Barrena01]. In those studies, the low coverages achieved (which led to the coexistence of molecular islands and bare gold areas) and the use of a scanning force microscopy, allowed to in-situ measure the thickness and lattice periodicity of the configurations obtained for C18 molecules. Apart from the already described hexagonal (√3×√3)R30° configuration, islands exhibiting a (2×√3)rect structure were found. But what is really interesting is that, from the in situ measurement of the corresponding island's thickness, the molecular orientation in this new configuration could be precisely determined: the molecules were tilt 50° with respect to the surface normal. Figure 2.10 shows the top and side view of possible schemes for this rectangular configuration.

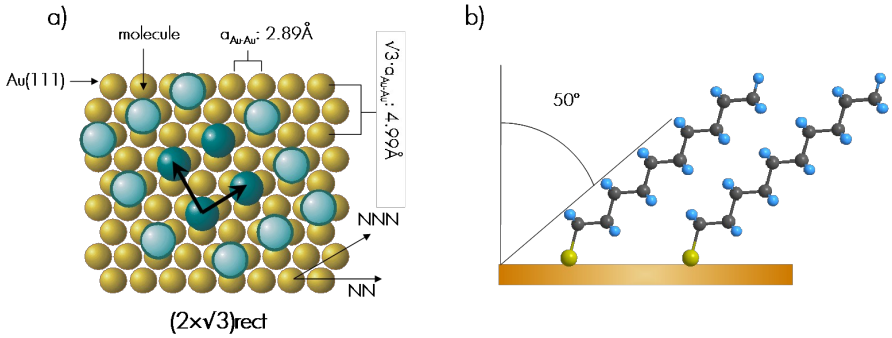

Figure 2.10 (a) 2D molecular arrangement proposed for the (2×√3)rect configuration. The darker circles highlight the rectangular lattice. The nearest-neighbor (NN) and next-nearest-neighbour (NNN) direction of the Au(111) have been marked. (b) side view showing the 50° molecular tilt.

The spontaneous formation of this 50°-tilted configuration for C18 molecules has been explained based on a 3D interlocking model. Since throughout this thesis this model is mentioned several times, we will briefly describe it in this section. For a more extended explanation, see [Barrena00].

[4] It might be possible that both models are correct and that the particular molecular arrangement depends on the experimental conditions. However in [Poirier99] and [Quian03] these conditions are quite similar (growth from the gas phase in UHV, STM at room temperature…).

The model is based on the fact that the optimum chain-chain distance can be achieved at different specific tilt angles (those yielding the interlocking of the molecular backbones). For molecules with their C-C axis oriented parallel, backbone interlocking is achieved when sliding adjacent molecules by integer multiples of the distance between alternate carbon atoms along the chain, a=2.5Å. Whereas for adjacent molecules with perpendicularly oriented axis, interlocking occurs when sliding them by half integer multiples of a. As a consequence of interlocking by sliding, different tilt angles are obtained (figure 2.11(a)). Mathematically this is expressed by:

$$tg\theta_n = \frac{n \cdot a}{d} \qquad n=0,\ 0.5,\ 1,\ 1.5,\ 2... \qquad (2.1)$$

where d is the distance between chains.

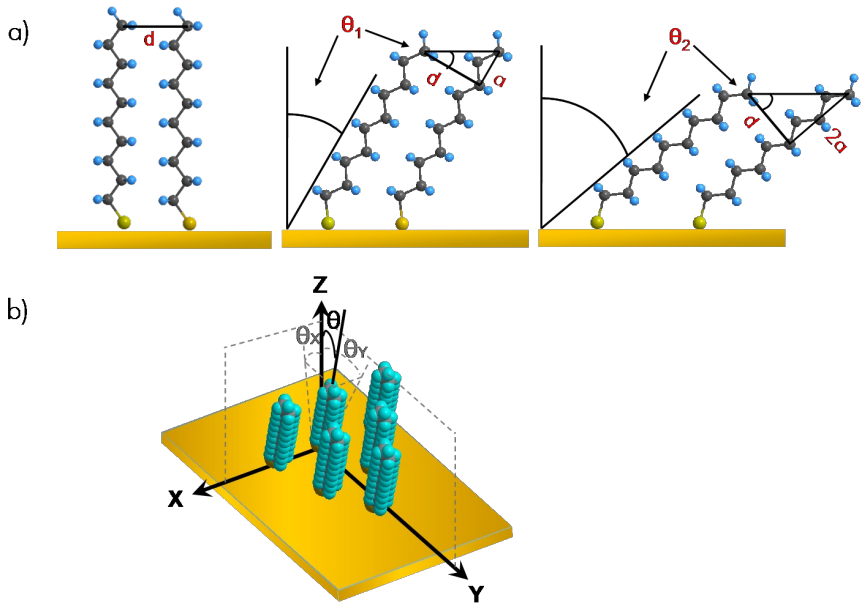

Figure 2.11 (a) Schematic two-dimensional model of all-trans alkyl chains. Only at specific angles do the methylene units of one chain interlock into the depression of the neighbour chain. At these angles the optimum intermolecular distance is preserved. (b) Three-dimensional model of the packing of all-trans alkyl molecules. The tilt angle is decomposed in a tilt along the X and Y directions (the NN and NNN directions of the molecular structure, respectively).

Due to the two-dimensional nature of the packing of alkanethiols on Au, the above condition has to be applied along two orthogonal directions of the molecular structure to obtain the angles of favourable packing. In the 3D model, as shown in figure 2.11(b), the tilt from the surface normal is thus described by two angles in two perpendicular directions, the next neighbour (NN) direction of the molecular structure in the X axis and the next nearest neighbour (NNN) direction, in the Y axis. Within each direction, following equation 2.1, the interlocking of the C-C backbone is imposed:

$$tg\theta_X = \frac{n \cdot a}{d_X} \qquad n=0,\ 0.5,\ 1,\ 1.5\ldots \tag{2.2}$$

$$tg\theta_Y = \frac{m \cdot a}{d_Y} \qquad m/2=0,\ 0.5,\ 1,\ 1.5\ldots \tag{2.3}$$

where d_X and d_Y corresponds to the chain-chain separation in the NN and NNN directions, respectively. Figure 2.11(b) shows that, due to the symmetry of the system, d_x matches the distance between molecules in the NN direction whereas d_y is twice the distance between molecular planes in the NNN direction. m values are divided by 2 in order to obtain the interlock order between nearest-neighbour chains along the other two NN directions [Barrena00].

With this model, the (√3×√3)R30° structure of the complete monolayer is obtained for n=0 and m/2=1, which yields a total tilt angle of θ=35° along the molecular NNN direction. The (2×√3)rect structure spontaneously formed in C18 molecules, is ascribed to a configuration with θ_X=41° and θ_Y=30° (n=1,m/2=1.5) which leads to the total tilt angle of 50° experimentally measured [Barrena01].

This 3D model was firstly proposed motivated by the behaviour of the SAMs' height under increasing applied pressure: the film height exhibited plateaus which indeed corresponded to configurations with the favourable angles predicted by the model [Barrena00]. However, in those experiments, once the pressure was released the molecules recovered the original height corresponding to the 30°-tilt, i.e. the configurations were not stable enough in the absence of applied pressure. The fact that the 50°-tilted configuration is spontaneously formed points to the important role played by the balance between interactions in the stability of the molecular configurations: this configuration is, among those predicted by the interlocking model, one of the few commensurate with the underlying substrate. Therefore the S-Au interaction favours its spontaneous formation. In chapter 5 we show that, besides the chain-chain and sulphur-Au interaction, the chain-substrate interaction also play a crucial role concerning the configurations formed at submonolayer coverages.

The general believe is that, at partial coverages, the formation of different configurations is largely influenced by the experimental conditions. The picture of molecules fully stretched and lying flat on the surface for the lowest-density phase is somehow widely accepted. Conversely, as coverage increases, the agreement on the molecular configurations formed is not so general. This could be due either to differences in experimental conditions or to the lack of experimental data to unambiguously determine the structure.

Apart from the spectrum of lying down configurations, other structures different from the hexagonal (√3×√3)R30° but with the molecular axis out of the surface plane have been reported. Of

special interest in the frame of this thesis is the spontaneous formation of a 50°-tilted, (2×√3)rect structure for C18 molecules at fixed coverage under monolayer completion.

2.2.4 Dialkyl Disulphides On Gold.

Although the nature of the S-Au bond and the quality of the films generated from alkanethiols and dialkyl disulphides are generally regarded as indistinguishable [Biebuyck94][Castner96] [Jung98], recent studies have suggested distinct properties and final coverages of SAMs.

Regarding the chemisorption of the molecules, different studies have shown that both type of molecules yielded the same species on the surface: a gold-thiolate ($RS^-Au(I)$) [Nuzzo87][Nuzzo87b][Bain89b][Li92][Tarlov92][Hagenhoff93]. These results are in accordance with a model in which the disulphide molecules dissociate at the gold surface.

Studies of the kinetics of monolayer formation and/or molecular exchange in solution have found that normal alkanethiols are kinetically more labile than their corresponding dialkyl disulphides [Bain89b][Hähner93][Biebuyck94][Jung98]. The difference in rates has been attributed to (1) the large value of the CSSC angle of the disulphide (see figure 2.3) that sterically hinders the adsorption of the sulphur [Bain89b][Biebuyck94], (2) preferential displacement of adsorbed solvent by the thiols [Hähner93][Jung98], and/or (3) preferential chemical interactions between the thiols and the surface of gold [Bain89b][Jung98]

With respect to the structural order of the complete monolayer, wettability measurements showed subtle differences between pure alkanethiol and disulphide SAMs. The former showed a higher degree of order, probably reflecting the difficulty of inserting the last few percent of the disulphide molecules into the well packed SAM [Bain89b]. Yet, the molecular structure in the full coverage phase is the same for both molecules (section 2.2.2)

Most studies show that both constituents of a disulphide are found in a 1:1 proportion in the resulting SAM on Au. This is obvious for symmetrical ones and interesting for asymmetrical disulphide, since it provides a direct way to generate two-component SAMs [Takami95][Schönherr96][Ishida97]. Phase segregation in these mixed monolayers has only been found at low concentration of the disulphide solution (10 μM) [Azehara99].

From high resolution SFM imaging, the existence of the hexagonal (√3×√3)R30° configuration in SAMs of symmetrical and asymmetrical disulphides has also been proved [Nelles98]. However, although lattice symmetry could be imaged, obtaining a good contrast was more difficult for increasing chain length asymmetry [Nelles98][Chen01]. This is probably caused by the easier formation of defects at the end of the longer disulphide chain due to the free space left by the short chains. This latter result support the absence of phase separation in SAMs of asymmetrical disulphides when adsorbed on gold [Chen01].

2.2.5 Interactions Involved In The Self-Assembly Process.

From what has been said up to now, it is fairly clear that the process leading to the formation of self-assembled monolayers involves subtle interplay of the energetics of metal-sulphur bonds and intermolecular interactions. These two interactions determine both the degree of order within the film and its lattice relationship with the substrate. In this section we describe and give the order of magnitude of these and other important interactions involved in the monolayer formation.

molecule-substrate interaction: we have to distinguish between the chemisorption and the physisorption of the molecule. The former refers to the headgroup-substrate interaction, i.e. the formation of the S-Au bond, whereas the latter refers to the van der Waals interaction between molecule and substrate.

Evidences from XPS, vibrational spectroscopy, mass spectrometry and electrochemical studies suggest that both, alkanethiol and disulphide molecules, prior to adsorption and S-Au bonding, form a thiolate (RS^-). In alkanethiol, this implies thiol reduction [Ulman96] whereas in disulphide molecules, S-S bond cleavage [Nuzzo87][Bain89b]. Although the exact fate of the hydrogen atoms upon adsorption of the alkanethiol molecule remains still unresolved, (formation of H_2, reaction with the gold surface to form metal hydrides or formation of water or hydrogen peroxide, are among the reported possibilities), to estimate the energy of adsorption, the following reactions are generally considered for alkanethiols and disulphides:

$$RSH + Au \rightarrow RSAu + \tfrac{1}{2} H_2$$

$$RSSR + 2Au \rightarrow 2RSAu$$

The reported value for the bonding of the thiolate group to the gold is ~1.3 eV regardless the length of the molecular chain [Scheribler00].

In the physisorbed state, the molecule is adhered to the surface only through van der Waals forces. The steep decrease of this interaction with distance (it varies as $1/r^6$) explains to a great extent the lying flat configuration generally preferred by the physisorbed molecules. In [Wetterer98] it was established that the contribution to the physisorption energy of hydrocarbons on Au(111) could be broken down into additive contributions of atoms or group of atoms. In particular, for a lying down molecule, a CH_2 group contributes ~0.065 eV, while a CH_3 group contributes ~0.16 eV. The SH contribution is 0.35 eV. These are small values when compared with the S-Au bond, but due to the additive property of the van der Waals interaction, an interesting effect shows up: for molecules with $n \geq 10$ carbon atoms, physisorption becomes comparable to the chemical S-Au bond (e.g. for C10 the physisorption energy is ~1.08 eV).

chain-to-chain interaction: in the case of alkanethiols (and in general, for non polar molecules), intermolecular interactions are also dominated by van der Waals forces. To obtain a numerical value of this interaction within a close-packed film, the cohesive energy per molecule can be approximately computed by summing A/r^6 pair potentials between the CH_2 units of the chain and the rest of the film.

For C18, the cohesive energy reported is ~0.07 eV per CH_2 group which results in a total molecular cohesive energy of ~1.3 eV [Israelachvili92]. Experimental results support the validity of this calculation [Dubois92][Lavrich98][Wetterer98].

A more detailed study carried out by Salmeron shows the dependence of the van der Waals interaction on the position of the CH_2 group within the chain [Salmeron01]. The upper graph of figure 2.12 indicates that in fact, for the calculation of the cohesive energy per CH_2 (inside a long alkyl chain within a self-assembled monolayer), only the 8 nearest CH_2 planes are significant to reach the saturation value of ~0.075 eV per CH_2. And within each plane, only the nearest 100 neighbours play a significant role in the sum. Moreover, the energy per CH_2 group depends on the position of the group inside the chain: the energy is lower near the chain edges but saturates after moving about 8 carbon distances down along the chain (bottom graph in figure 2.12). All these results are consequences of the steep decrease of this interaction with distance.

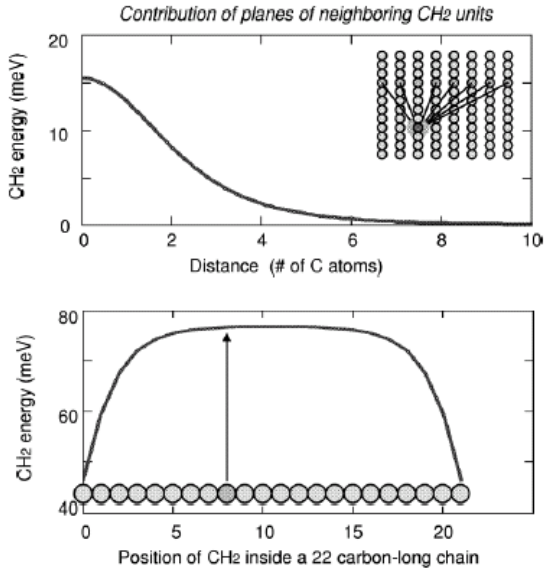

Figure 2.12 Calculated cohesive energy per CH_2 group. Top graph shows the van der Waals stabilization energy contributed by successive planes of CH_2 units. Bottom graph shows the cohesive energy per CH_2 as a function of its position in the chain, for a C22 alkane. From [Salmeron01]

Due again to the additive property of the van der Waals interaction, for chain lengths greater than 14 carbon atoms, the intermolecular energy might dominate over the headgroup-substrate interaction.

We would like to remark that the values above calculated for the intermolecular interaction have been obtained considering a hexagonal close-packing of perpendicular molecules with 0° tilt angle (like the one depicted in the inset of figure 2.12), separated the optimum van der Waals distance. In chapter 5 we show that the tilt of the molecular axis imposed by the interaction with the Au(111) considerably reduces this cohesive energy (e.g. for a C18 molecule in the 30°-tilted

hexagonal configuration the computed cohesive energy is ~0.6 eV, half of that obtained in the perpendicular configuration)

conformational energy: to maximize the intermolecular interaction and achieve the highest packing efficiency, each molecule should present the *trans* configuration with all the carbon atoms located in the same plane exhibiting a zig-zag structure (figure 2.3). However, the chains might present conformational defects that alter this optimal configuration. The most common are the so-called gauche defects which are due to a ±120° rotation of a part of the alkanethiol molecule around a C-C bond. The energy difference between the *trans* (t) and *gauche* (g) conformations has been reported to be small (0.02-0.04 eV) [Smith96]. However, the magnitudes of the energy barriers between both configurations are considerably higher. For a free alkane chain, Smith and Jaffe calculated that the activation energy for the *trans-gauche* rotation is 0.14 eV [Smith96].

In the monolayer, *gauche* defects are energetically less costly when produced at the free endgroup due to the lower cohesive energy of this group located at the edge of the chain (see previous figure). Internal *gauche* defects are more difficult to produce since, due to the increase in cohesive energy of the internal groups, the energy required to alter the internal packing is much higher. The energetic cost reported for these internal *gauche* defects is ~0.5 eV [Schertel96].

2.3 APPLICATIONS OF SAMS.

Self-assembled monolayers in general, and in particular alkanethiol SAMs, have proved to be extremely useful systems for studying a variety of surface phenomena and reactions. Originally confined to basic research, SAMs are rapidly finding industrial applications and nowadays, the technologies of several companies rely on them (e.g. Biacore [SPR], SurfaceLogix [cellular assays], Platypus Technologies [DNA chips], Bioscale [sensors])

Arguably, the earlier application of these SAMs was based on their lubricant character (which considerably reduced the friction and increased the wear resistance between sliding surfaces) and their ability to prevent the corrosion of the underlying metal surface. Therefore, they have long been used as protective/lubricant coatings in micro- and nanofabrication. Nowadays, the applications range has considerably widened from electronics and spintronics, to biosensors, bio-recognition devices and drug delivery, just to name a few. Moreover, their use in soft lithography, to generate micropatterned SAMs, renders these systems ideal for bottom-up nanostructured growth.

Due to the endless list of applications, it is not possible to give further details for each particular case. Yet, since this work is concerned with frictional and transport properties of SAMs, we find it useful to conclude this chapter with the role of SAMs on those specific fields. More information on these and other applications can be found in the recently reviews [Witt04][Love05].

2.3.1 SAMs In Boundary Lubrication.

The term boundary lubrication was firstly used by W. B. Hardy in 1922 to describe the regime in which very thin films, of molecular proportions, are effective in reducing the friction between solids in relative sliding motion. However, it was the recent development of high-density storage technologies and micro- and nanomechanical systems what certainly revitalised the use of ultrathin organic layers as protective/lubricant coatings. When this trend towards miniaturization in device fabrication started, new materials were required to modify surface properties under severe space constraints.

All of the tribological phenomena (friction, adhesion, wear), have their ultimate origin at the atomic and molecular levels at which the formation and breaking of chemical bonds, electronic excitations or molecular rearrangements contribute to the energy dissipation. On this scale, molecular properties such as local conformation, packing arrangement and chemical composition can directly influence the performance of the lubricant system.

The aim of most of the fundamental studies in systems such as LB and SAMs films is therefore to correlate their tribological characteristics with the atomic structure of the surface and identify the different dissipation mechanisms during friction. Moreover, since the performance of lubricated mechanical systems often requires bearing high loads, understanding the tribological response under applied pressure is also a fundamental question.

In self-assembled monolayers, adjustable frictional properties have been obtained varying the chain length [McDermott97], packing density [Lee00] or molecular order [Perry01]. The results point to a direct relationship between the lubricant efficiency and the monolayer packing density, i.e. loosely films facilitate the presence of numerous kinks, gauche defects, ect…that provide many deformation or excitation modes (rotation, bending…) to efficiently dissipate energy and thus enhance friction response [Salmeron01]. The influence of the chemical identity of the endgroup on friction and adhesion has also been investigated [Kim99][Leggett05].

Among the different dissipation channels observed when these films are subjected to an external pressure, three types of viscoelastic defects are considered of special interest, because their lifetime is of the order of the sliding time in friction experiments. The first type involves the creation of gauche distortion at the free endgroup. As shown in section 2.2.5, the energy associated with a gauche defect is comparable to the thermal energy at room temperature (~0.03 eV) so that little energy has to be provided to overcome this barrier. The production of gauche distortion within the film (internal gauche defects) belongs to the second type of defects. It requires the displacement of the neighboring molecules and, in principle, does not operate for highly ordered and very dense films. The third type consists in the collective tilting of the molecules under applied pressure. In [Barrena99b][Barrena00] the contribution of these collective molecular tilts to friction response was addressed. The estimated activation barrier for such tilts is 0.2 eV for C12 molecules [Salmeron01].

In this work we have made considerable effort to design experiments in which one of these processes dominates, to be able to single out and study its contribution to the lubricant response of the film.

2.3.2 SAMs In Molecular Electronics.

Miniaturization of electronic devices has also reached molecular dimensions and the idea of wiring individual molecules into an electronic circuit has been pursued by many groups. The possible technological application of these devices has given rise to an actively research area so-called molecular electronics, in which the fabrication, measurement and understanding of the current-voltage response of a metal-molecule-metal junction are the major goals.

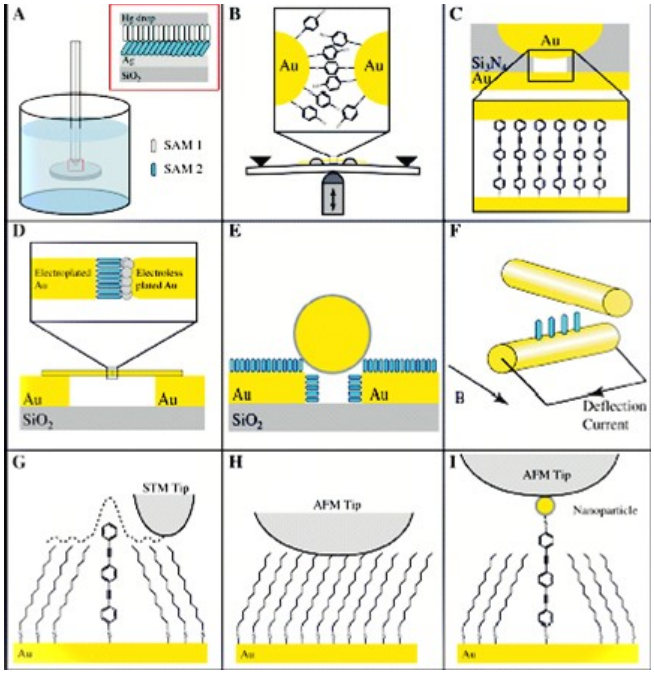

Figure 2.13 Various techniques used to measure electronic properties of molecules. Note that images are not to scale. (A) Hg drop junction. (B) mechanically controlled break junctions. (C) nanopore. (D) nanowire. (E) nanoparticle bridge. (F) crossed wires. (G) STM. (H) contact CP-SFM. (I) nanoparticle coupled CP-SFM. From [Mantooth03]

.

Alkanethiol molecules on gold are good candidates for such studies because of the inherent chemical and physical properties of these molecules to form controlled local geometries and for the excellent electrical contact derived from the strong Au–S covalent bond at the interface. As shown in figure 2.13 different type of junctions have been used to sandwich molecules (several, a few, or individual molecules) between two metal surfaces, and to measure their electrical properties [Datta97] [Slowinski97][Bumm99][Cui01][Holmlin01][Wold01][Labonte02][Rampi02][Selzer02][York03]

Based on the existing results, reviewed in [Mantooth03][Salomon03][McCreery04] [Wang05], conduction through the alkanethiol film has been found to be consistent with coherent, non-resonant electron tunnelling. At low voltages, the tunnelling rate decreases exponentially with the thickness of the barrier (d) and the simplest form for the electron current density (J) is given by the Simmons relation which, in the low bias regime, can be written as:

$$J \propto Be^{-\beta d} \qquad (2.4)$$

where β is the tunnelling decay factor in units of $(\text{length})^{-1}$ (see chapter 6 for a more detailed description)

However, the identification of the specific electron transport mechanisms is still controversial, and factors such as lack of good film quality (molecular order, conformational changes, domain boundaries, pinholes, contact failure…), unknown applied pressure or inherent peculiarities of the different techniques used might be at the origin of some non-reconcilable results [Salomon03].

The design of experiments in which solely one possible factor is changed (molecular length, headgroup-substrate bond, molecular order….) while keeping the rest unchanged would help to shed some light on the electrical characteristics of these molecular junctions.

2.4 REFERENCES.

[Ahn03] H.-S. Ahn, P. D. Cuong, S. Park, Y.-W. Kim, J.-C. Lim. "Effect of molecular structure of self-assembled monolayers on their tribological behaviors in nano- and microscales" 2003 Wear 255; 819.

[Alves92] C. A. Alves, E. L. Smith, M. D. Porter "Atomic Scale Imaging of Alkanethiolate Monolayers at Gold Surfaces with Atomic Force Microscopy" 1992 J . Am. Chem. Soc. 114; 1222.

[Aveyard99] R. Aveyard, B. D. Beake, J. H. Clint "Alkane adsorption from vapour onto hydrophobic solid/vapour and hydrophobic solid/water interfaces" 1999 Phys.Chem.Chem.Phys. 1; 2513.

[Azehara99] H. Azehara, S. Yoshimoto, H. Hokari, U. Akiba, I. Taniguchi, M. Fujihira. "Investigation of the structure of self-assembled monolayers of asymmetrical disulfides on Au(111) electrodes by electrochemical desorption" 1999 J. Electroanal. Chem. 473; 68.

[Bigelow46] W.C. Bigelow, D. L. Pickett, W. A. Zisman. "Oleophobic Monolayers I. Films Adsorbed From Solution In Non-Polar Liquids" 1946 J. Colloid Interface Sci. 1; 513.

[Bain89] C. D. Bain, E. B. Troughton, Y-T. Tao, J. Evall, G. M. Whitesides, R. G. Nuzzo "Formation of monolayer films by the spontaneous assembly of organic thiols from solution onto gold." 1989 J. Am. Chem. Soc. 111; 321.

[Bain89b] C. D. Bain, H. A. Biebuyck, G. M. Whitesides "Comparison of Self -Assembled Monolayers on Gold: Coadsorption of Thiols and Disulfides" 1989 Langmuir. 5; 723.

[Balzer97] F. Balzer, R. Gerlach, G. Polanski, H-G. Rubahn "Chain length dependence of the structure of alkane thiol films on Au(111)" 1997 Chem. Phys. Lett. 274; 145.

[BarrenaThesis] E. Barrena ""Fricción y estructura molecular de películas de alcanosilanos y alcanotioles por debajo de la monocapa" 2001 Ph.D. Thesis.

[Barrena99] E. Barrena, C. Ocal, M. Salmeron "Evolution of the structure and mechanical stability of self-assembled alkanethiol islands on Au(111) due to diffusion and ripening" 1999 J. Chem. Phys. 111; 9797

[Barrena99b] E. Barrena, S. Kopta, D. F. Ogletree, D. H. Charych, M. Salmeron. "Relationship between Friction and Molecular Structure: Alkylsilane Lubricant Films under Pressure" 1999 Phys. Rev. Lett. 82; 2880.

[Barrena00] E. Barrena, C. Ocal, M. Salmeron "Molecular packing changes of alkanethiols monolayers on Au(111) under applied pressure" 2000 J. Chem. Phys. 113; 2413.

[Barrena01] E. Barrena, C. Ocal, M. Salmeron "Structure and stability of tilted-chain phases of alkanethiols on Au(111)" 2001 J. Chem. Phys. 114; 4210.

[Biebuyck94] H. A. Biebuyck, C. D. Bain, G. M. Whitesides "Comparison of Organic Monolayers on Polycrystalline Gold Spontaneously Assembled from Solutions Containing Dialkyl Disulfides or Alkanethiols'" 1994 Langmuir. 10; 1825.

[Bucher94] J. P. Bucher, L. Santesson, K. Kern "Selective imaging of self-assembled monolayers by tunneling microscopy"1994 Appl. Phys. A. 59;135.

[Bumm99] L. A. Bumm, J. I. Arnold, M. T. Cygan, T. D. Dunbar, T. P. Burgin, L. Jones, D. L. Allara, J. M. Tour, P. S. Weiss "Electron Transfer through Organic Molecules" 1999 J. Phys.Chem. B. 103; 8122.

[Camillone93] N. Camillone, C.E.D. Chidsey, G.-Y. Liu, G. Scoles, "Superlattice structure at the surface of a monolayer of octadecanethiol self-assembled on Au(111)" 1993 J. Chem. Phys. 98; 3503.

[Camillone94] N. III Camillone, P. Eisenberger, T. Y. B. Leung, P. Schwartz, G. Scoles, G. E. Poirier, M. J. Tarlov " New monolayer phases of n-alkane thiols self-assembled on Au(ll1): Preparation, surface characterization, and imaging " 1994 J. Chem. Phys. 101;11031.

[Camillone96] N. III Camillone, T. Y. B. Leung, P. Schwartz, P. Eisenberger, G. Scoles "Chain Length Dependence of the Striped Phases of Alkanethiol Monolayers Self-Assembled on Au(111): An Atomic Beam Diffraction Study "1996 Langmuir. 12; 2737.

[Castner96] D. G. Castner, K. Hinds, D. W. Grainger "X-ray Photoelectron Spectroscopy Sulphur 2p Study of Organic Thiol and Disulfide Binding Interactions with Gold Surfaces" 1996 Langmuir 12;5083.

[Chen01] S. Chen, L. Li, C. L. Boozer, S. Jiang "Controlled Chemical and Structural Properties of Mixed Self-Assembled Monolayers by Coadsorption of Symmetric and Asymmetric Disulfides on Au(111)" 2001 J. Phys. Chem. B. 105; 2975.

[Chidsey89] C. E. D. Chidsey, G-Y. Liu, P. Rowntree, G. Scoles "Molecular order at the surface of an organic monolayer studied by low energy helium diffraction" 1989 J. Chem. Phys. 91; 4421.

[Cui01] X. D. Cui, A. Primak, X. Zarate, J. Tomfohr, O. F. Sankey, A. L. Moore, T. A. Moore, D. Gust, G. Harris, S. M. Lindsay. "Reproducible Measurement of Single-Molecule Conductivity" 2001 Science 294; 571.

[Datta97] S. Datta, W. Tian, S. Hong, R. Reifenberger, J. I. Henderson, C. P. Kubiak "Current-Voltage Characteristics of Self-Assembled Monolayers by Scanning Tunnelling Microscopy" 1997 Phys. Rev. Lett. 79; 2530

[Delamarche94] E. Delamarche, B. Michel, Ch. Gerber, D. Anselmetti, H.-J. Güntherodt, H. Wolf, H. Ringsdorf "Real-Space Observation of Nanoscale Molecular Domains in Self-Assembled Monolayers" 1994 Langmuir 10; 2869.

[Delamarche96] E. Delamarche, B. Michel, H. A. Biebuyck and C. Gerber "Golden Interfaces: The Surface of Self- Assembled Monolayers"1996 Adv. Mater. 8; 719.

[Dubois92] L. H. Dubois, R. G. Nuzzo "Synthesis, Structure, and Properties of Model Organic Surfaces" 1992 Annu. Rev. Phys. Chem. 43; 437.

[Dubois93] L. H. Dubois, B. R. Zegarski, R. G. Nuzzo "Molecular ordering of organosulfur compounds on Au(111) and Au(100):Adsorption from solution and in ultrahigh vacuum" 1993 J. Chem. Phys. 98; 678.

[Ederth01] T. Ederth. "Computation of Lifshitz-van der Waals Forces between Alkylthiol Monolayers on Gold Films" 2001 Langmuir. 17; 3329.

[Fenter93] P. Fenter, P. Eisenberger, K.S. Liang "Chain-Length Dependence of the Structures and Phases of $CH_3(CH_2)_{n-1}SH$ Self-assembled on Au(111)" 1993 Phys. Rev. Lett. 70; 2447.

[Fenter97] P. Fenter, A. Eberhardt, K.S. Liang, P. Eisenberger "Epitaxy and chainlength dependent strain in self-assembled monolayers" 1997 J. Chem. Phys. 106; 1600.

[Fenter98] P. Fenter, F. Schreiber, L. Berman, G. Scoles, P. Eisenberger, M.J. Bedzyk "On the structure and evolution of the buried S/Au interface in self-assembled monolayers: X-ray standing wave results"1998 Surf. Sci. 412–413; 213.

[Hagenhoff93] B. Hagenhoff, A. Benninghoven, J. Spinke, M. Liley, W. Knoll "Time-of-flight secondary ion mass spectrometry investigations of self-assembled monolayers of organic thiols, sulfides, and disulfides on gold surfaces" 1993 Langmuir. 9; 1622.

[Hähner92] G. Hähner, M. Kinzler, C. Thrümler, Ch. Wöll, M. Grunze "Structure of self-organizing organic films: A near edge x-ray absorption fine structure investigation of thiol layers adsorbed on gold" J. Vac. Sci. Technol. A. 1992 10; 2758.

[Hähner93] G. Haehner, C. Wöll, M. Buck, M. Grunze "Investigation of intermediate steps in the self-assembly of n-alkanethiols on gold surfaces by soft x-ray spectroscopy" 1993 Langmuir 9;1955.

[Holmlin01] R. E. Holmlin, R. Haag, M. L. Chabinyc, R. F. Ismagilov, A. E. Cohen, A. Terfort, M. A. Rampi, G. M. Whitesides "Electron transport through thin organic films in metal-insulator-metal junctions based on self-assembled monolayers" 2001 J. Am. Chem. Soc. 123; 5075.

[Israelachvili92] J. Israelachvili "Intermolecular and surface forces" 1992, Academic Press, London, England.

[Ishida97] T. Ishida, S. Yamamoto, W. Mizutani, M. Motomatsu, H. Tokumoto, H. Hokari, H. Azehara, M. Fujihira "Evidence for Cleavage of Disulfides in the Self-Assembled Monolayer on Au(111)" 1997 Langmuir 13; 3261.

[Jung98] Ch. Jung, O. Dannenberger, Y. Xu, M. Buck, M. Grunze "Self-Assembled Monolayers from Organosulfur Compounds: A Comparison between Sulfides, Disulfides, and Thiols" 1998 Langmuir 14; 1103.

[Kim99] H. I. Kim, M. Graupe, O. Oloba, T. Koini, S. Imaduddin, T. R. Lee, S. S. Perry. "Molecularly Specific Studies of the Frictional Properties of Monolayer Films: A Systematic Comparison of CF_3-, $(CH_3)_2CH$-, and CH_3-Terminated Films" 1999 Langmuir 15; 3179.

[Kitaigorodskii61] A. Kitaigorodskii "Organic Chemical Crystallographic" 1961 Consultant bureau, New York

[Kondoh99] H. Kondoh, C. Kodama, H. Sumida, H. Nozoye "Molecular processes of adsorption and desorption of alkanethiol monolayers on Au(111)" 1999 J. Chem. Phys. 111; 1175.

[Labonte02] A. P. Labonte, S. L. Tripp, R. Reifenberger, A. Wei "Scanning Tunnelling Spectroscopy of Insulating Self-Assembled Monolayers on Au(111)" 2002 J. Phys. Chem. B. 106; 8721.

[Laibinis91] P. E. Laibinis, G. M. Whitesides, D. L. Allara, Y. T. Tao, A. N. Parikh, R. G. Nuzzo "Comparison of the Structures and Wetting Properties of Self-Assembled Monolayers of n- Alkanethiols on the Coinage Metal Surfaces, Cu, Ag, Au" 1991 J. Am. Chem. Soc. 113; 7152.

[Laibinis98] P. E. Laibinis, B. J. Palmer, S-W. Lee, G. K. Jennings "The synthesis of organothiols and their assembly into monolayers on gold" In: Ulman A (ed.) Self-Assembled Monolayers of Thiols, 1998 Thin Films. Vol. 24. Academic Press, San Diego,CA.

[Larsen97] N. B. Larsen, H. Biebuyck, E. Delamarche, B. Michel "Order in Microcontact Printed Self-Assembled Monolayers" 1997 J. Am. Chem. Soc. 119; 3017.

[Lavrich98] D. J. Lavrich, S. M. Wetterer, S. L. Bernasek, G. Scoles "Physisorption and Chemisorption of Alkanethiols and Alkyl Sulfides on Au(111)" 1998 J. Phys. Chem. B. 102; 3456.

[Lee00] S. Lee, Y.-S. Shon, R. Colorado Jr., R. L. Guenard, T. R. Lee, S. S. Perry. "The Influence of Packing Densities and Surface Order on the Frictional Properties of Alkanethiol Self-Assembled Monolayers (SAMs) on Gold: A Comparison of SAMs Derived from Normal and Spiroalkanedithiols" 2000 Langmuir 16; 2220.

[Leggett05] G. J. Leggett, N. J. Brewer, K. S. L. Chong "Friction force microscopy: towards quantitative analysis of molecular organisation with nanometre spatial resolution" 2005 Phys . Chem. Chem. Phys . 7; 1107.

[Li92] Y. Li, J. Huang, R. T. McIver, Jr. J. C. Hemminger "Characterization of thiol self-assembled films by laser desorption Fourier transform mass spectrometry" 1992 J. Am. Chem. Soc. 114; 2428.

[Love05] J. C. Love, L A. Estroff, J. K. Kriebel, R. G. Nuzzo, G. M. Whitesides "Self-Assembled Monolayers of Thiolates on Metals as a Form of Nanotechnology." 2005 Chem. Rev. 105; 1103.

[Mantooth03] B. A. Mantooth, P. S. Weiss "Fabrication, Assembly, and Characterization of Molecular Electronic Components" 2003 Proc. IEEE. 91; 1785.

[Maoz84] R. Maoz, J. Sagiv "On the Formation and Structure of Self-Assembling Monolayers" 1984. J. Colloid Interface Sci. 100;465.

[McCreery04] R. L. McCreery. "Molecular Electronic Junctions" 2004 Chem. Mater. 16; 4477.

[McDermott97] M. T. McDermott, J.-B. D. Green, M. D. Porter. "Scanning Force Microscopic Exploration of the Lubrication Capabilities of n-Alkanethiolate Monolayers Chemisorbed at Gold: Structural Basis of Microscopic Friction and Wear "1997 Langmuir13; 2504.

[Nelles98] G. Nelles, H. Schönherr, G. J. Vancso, H.-J. Butt "Monolayers of asymmetrical diethylalkanoat disulfides on gold(111):the influence of chain length difference on atomic force microscope images"1998 Appl. Phys. A 66; S1261

[Noh01] J. Noh, M. Hara "Molecular-scale growth processes of alkanethiol self-assembled monolayers on Au(111)" 2001 RIKEN review 38; 49.

[Nuzzo83] R. G. Nuzzo, D. L. Allara. "Adsorption of Bifunctional Organic Disulfides on Gold Surfaces" 1983 J. Am. Chem. Soc. 105; 4481.

[Nuzzo87] R. G. Nuzzo, B. R. Zegarski, L. H. Dubois "Fundamental Studies of the Chemisorption of Organosulfur Compounds on Au(11 1). Implications for Molecular Self-Assembly on Gold Surfaces" 1987 J. Am. Chem. Soc. 109; 733.

[Nuzzo87b] R. G. Nuzzo, F. A. Fusco, D. L.. Allara "Spontaneously organized molecular assemblies. 3. Preparation and properties of solution adsorbed monolayers of organic disulfides on gold surfaces" 1987 J. Am. Chem. Soc.109; 2358.

[Nuzzo90] R.G. Nuzzo, L.H. Dubois, D.L. Allara "Fundamental Studies of Microscopic Wetting on Organic Surfaces.1. Formation and Structural Characterization of a Self-Consistent Series of Polyfunctional Organic Monolayers" 1990 J. Am. Chem. Soc. 112; 558.

[Perry01] S. S. Perry, S. Lee, Y.-S. Shon, R. Colorado Jr., T. R. Lee. "The relationships between interfacial friction and the conformational order of organic thin films" 2001 Trib. Lett. 10; 81.

[Poirier94] G. E. Poirier, M. J. Tarlov "The c(4X2) Superlattice of n-Alkanethiol Monolayers Self-Assembled on Au(111)" 1994 Langmuir. 10; 2853.

[Poirier96] G. E. Poirier, E. D. Pylant "The self-assembly method of Alkanethiols on Au(111)" 1996 Science 272;1145.

[Poirier97] G. E. Poirier "Characterization of Organosulfur Molecular Monolayers on Au(111) using Scanning Tunneling Microscopy" 1997 Chem. Rev. 97; 1117.

[Poirier99] G. E. Poirier "Coverage-dependent phases and phase stability of decanethiol on Au(111)" 1999 Langmuir. 15; 1167.

[Poirier01] G. E. Poirier, W. P. Fitts, J. M. White "Two-Dimensional Phase Diagram of Decanethiol on Au(111)" 2001 Langmuir 17; 1176.

[Porter87] M. D. Porter, T. B. Bright, D. L. Allara, C. E. D. Chidsey "Spontaneously Organized Molecular Assemblies. 4. Structural Characterization of n-Alkyl Thiol Monolayers on Gold by Optical Ellipsometry, Infrared Spectroscopy, and Electrochemistry" 1987 J. Am. Chem. Soc. 109; 3559.

[Qian03] Y. Qian, G. Yang, J. Yu, T. A. Jung, G-Y. Liu "Structures of Annealed Decanethiol Self-Assembled Monolayers on Au(111): an Ultrahigh Vacuum Scanning Tunneling Microscopy Study" 2003 Langmuir 19; 6056.

[Rampi02] M. A. Rampi, G. M. Whitesides. "A versatile experimental approach for understanding electron transport through organic materials" 2002 Chemical Physics 281; 373.

[Roper04] M. G. Roper, M. P. Skegg, C. J. Fisher, J. J. Lee, V. R. Dhanak, D. P. Woodruff, R. G. Jones "Atop adsorption site of sulphur head groups in gold-thiolate self-assembled monolayers" 2004 Chem. Phys. Lett. 389; 87.

[Salmeron93] M. Salieron, G. Neubauer A. Folch, M. Tomitori, D. F. Ogletree, P. Sautet. "Viscoelastic and Electrical Properties of Self-Assembled Monolayers on Au(111) Films" 1993 Langmuir. 9; 3600.

[Salmeron01] M. Salmeron "Generation of defects in model lubricant monolayers and their contribution to energy dissipation in friction" 2001 Trib. Lett. 10; 69.

[Salomon03] A. Salomon, D. Cahen, S. Lindsay, J. Tomfohr, V. B. Engelkes, C. D. Frisbie. "Comparison of electronic transport measurements on organic molecules" 2003 Adv. Mater. 15; 1881.

[Schertel96] A. Schertel, G. Hähner, M. Grunze, Ch. Wöll "Near edge x-ray absorption fine structure investigation of the orientation and thermally induced order–disorder transition in thin organic films containing long chain hydrocarbons" 1996 J. Vac.Sci. Techn. A. 14; 1801.

[Schoenenberger95] C. Schoenenberger, J. Jorritsma, J. A. M. Sondag-Huethorst, L. G. J. Fokkink "Domain Structure of Self-Assembled Alkanethiol Monolayers on Gold"1995 J. Phys. Chem. 99; 3259.

[Schönherr96] H. Schönherr, H. Ringsdorf "Self-Assembled Monolayers of Symmetrical and Mixed Alkyl Fluoroalkyl Disulfides on Gold. 1. Synthesis of Disulfides and Investigation of Monolayer Properties" 1996 Langmuir 12; 3891.

[Schreiber98] F. Schreiber, A. Eberhardt, P. Schwartz, S. M. Wetterer, D. J. Lavrich, L. Berman, P. Fenter, P. Eisenberger, G. Scoles "Adsorption mechanisms, structures, and growth regimes of an archetypal self-assembling system: Decanethiol on Au(111)" 1998 Phys.Rev. B. 57; 12476.

[Schreiber00] F. Schreiber "Structure and growth of self-assembling monolayers" Prog. Surf. Sci. 2000 65; 151.

[Schwartz01] D. K. Schwartz "Mechanisms and kinetics of self-assembled monolayer formation" 2001 Annu. Rev. Phys. Chem. 52; 107.

[Selzer02] Y. Selzer, A. Salomon, D. Cahen "The Importance of Chemical Bonding to the Contact for Tunneling through Alkyl Chains" 2002 J. Phys. Chem. B. 106; 10432

[Sheehan02] P. E. Sheehan, L. J. Withman "Thiol Diffusion and the Role of Humidity in "Dip Pen Nanolithography"" 2002 Phys. Rev. Lett. 88; 156104.

[Slowinski97] K. Slowinski, R. V. Chamberlain, C. J. Millar, M. Majda. "Through-Bond and Chain-to-Chain Coupling. Two Pathways in Electron Tunnelling through Liquid Alkanethiol Monolayers on Mercury Electrodes"1997 J. Am. Chem. Soc. 119; 11910.

[Smith96] G. D. Smith, R. L. Jaffe "Quantum Chemistry Study of Conformational Energies and Rotational Energy Barriers in n-Alkanes " 1996 J. Phys. Chem. 100; 18718.

[Staub98] R. Staub, M. Toerker, T. Fritz, T. Schmitz-Hübsch, F. Sellam, K. Leo "Flat Lying Pin-Stripe Phase of Decanethiol Self-Assembled Monolayers on Au(111)" 1998 Langmuir 14; 6693.

[Tarlov92] M. J. Tarlov, J. G. Newman "Static secondary ion mass spectrometry of self-assembled alkanethiol monolayers on gold" 1992 Langmuir. 8; 1398.

[Terán Arce98] F. Terán Arce, M. E. Vela, R. C. Salvarezza, A. J. Arvia "Complex Structural Dynamics at Adsorbed Alkanethiol Layers at Au(111) Single-Crystal Domains" 1998 Langmuir 14; 7203.

[Toerker00] M. Toerker, R. Staub, T. Fritz, T. Schmitz-Hübsch, F. Sellam, K. Leo "Annealed decanethiol monolayers on Au(111) – intermediate phases between structures with high and low molecular surface density" 2000 Surf. Sci. 445; 100.

[Torrelles04] X. Torrelles, E. Barrena, C. Munuera, J. Rius, S. Ferrer, C. Ocal, "New Insights in the c(4×2) Reconstruction of Hexadecanethiol on Au(111) Revealed by Grazing Incidence X-ray Diffraction" 2004 Langmuir. 20; 9396.

[Ulmanbook] A. Ulman (ed.) "Self-Assembled Monolayers of Thiols", 1998 Thin Films. Vol. 24. Academic Press, San Diego,CA.

[Ulman96] A. Ulman "Formation and Structure of Self-Assembled Monolayers" 1996 Chem. Rev. 96; 1533.

[Vericat01] C. Vericat, M. E. Vela, G. Andreasen, R. C. Salvarezza, L. Vázquez, J. A. Martín-Gago, "Sulfur-Substrate Interactions in Spontaneously Formed Sulfur Adlayers on Au(111)" 2001 Langmuir 17; 4919.

[Vericat05] C. Vericat, M. E. Vela, R. C. Salvarezza "Self-assembled monolayers of alkanethiols on Au(111): surface structures, defects and dynamics" 2005 Phys.Chem.Chem.Phys. 7; 3258.

[Vericat06] C. Vericat, M- E. Vela, G. A. Benitez, J. A. Martin Gago, X.. Torrelles, R. C. Salvarezza." Surface characterization of sulfur and alkanethiol self-assembled monolayers on Au(111)" 2006 J. Phys.: Condens. Matter 18; R867.

[Wang05] W. Wang, T. Lee, M. A. Reed. "Electron tunnelling in self-assembled monolayers" 2005 Rep. Prog. Phys. 68; 523.

[Wasserman89] S. R. Wasserman, Y.-T Tao, G. M. Whitesides "Structure and Reactivity of Alkylsiloxane Monolayers Formed by Reaction of Alkyltrichlorosilanes on Silicon Substrates" 1989 Langmuir 5;1074.

[Weihs91] T. P. Weihs, Z. Nawaz, S. P. Jarvis, J. B. Pethica. "Limits of imaging resolution for atomic force microscopy of molecules" 1991 Appl. Phys. Lett. 59; 3536.

[Wetterer98] S. M. Wetterer, D. J. Lavrich, T. Cummings, S. L. Bernasek, G. Scoles. "Energetics and Kinetics of the Physisorption of Hydrocarbons on Au(111)" 1998 J. Phys. Chem. B. 102; 9266.

[Witt04] D. Witt, R. Klajn, P. Barski, B. A. Grzybowski "Applications, Properties and Synthesis of ω-Functionalized n-Alkanethiols and Disulfides–the Building Blocks of Self-Assembled Monolayers" 2004 Curr. Org. Chem. 8; 1763.

[Wold01] D. J. Wold, C. D. Frisbie "Fabrication and Characterization of Metal-Molecule-Metal Junctions by Conducting Probe Atomic Force Microscopy" 2001 J. Am. Chem. Soc.123; 5549.

[Xiao01] X. Xiao, B. Wang, C. Zhang, Z. Yang, M. M. T. Loy. "Thermal annealing e€ect of alkanethiol monolayers on Au(1 1 1) in air" 2001 Surf. Sci. 472; 41.

[Xu98] S. Xu, S. J. N. Cruchon-Dupeyrat, J. C. Garno, G.-Y. Liu, G. K. Jennings, T.-H. Yong, P. E. Laibinis 1998 J. Chem. Phys. 108; 5002.

[Yamada97] R. Yamada, K. Uosaki "In Situ, Real Time Monitoring of the Self-Assembly Process of Decanethiol on Au(111) in Liquid Phase. A Scanning Tunneling Microscopy Investigation" 1997 Langmuir 13; 5218.

[Yamada98] R. Yamada, K. Uosaki "In Situ Scanning Tunneling Microscopy Observation of the Self-Assembly Process of Alkanethiols on Gold(111) in Solution" 1998 Langmuir 14; 855.

[Yeganeh95] M. S. Yeganeh, S. M. Dougal, R. S. Polizzotti, P. Rabinowitz, "Interfacial Atomic Structure of a Self-Assembled Alkyl Thiol Monolayer/Au(111): A Sum-Frequency Generation Study" 1995 Phys. Rev. Lett. 74; 1811.

[York03] R. L. York, P. T. Nguyen, K. Slowinski. "Long-Range Electron Transfer through Monolayers and Bilayers of Alkanethiols in Electrochemically Controlled Hg-Hg Tunnelling Junctions" 2003 J. Am. Chem. Soc. 125; 5948.

[Zeng02] C. Zeng, B. Li, B. Wang, H. Wang, K. Wang, J. Yang, J. G. Hou, Q. Zhu "What can a scanning tunneling microscope image do for the insulating alkanethiol molecules on Au(111) substrates?" 2002 J. Chem. Phys. 117; 851.

CHAPTER 3.- INSTRUMENTATION AND SAMPLE PREPARATION.

3.1 THE SCANNING PROBE MICROSCOPY.

The dawn of the scanning probe microscopy (SPM) came in 1982 with the invention of the scanning tunnelling microscope (STM) by Heinrich Rohrer and Gerd Binnig [Binnig82]. As its name indicates, this technique is based on the quantum tunnelling effect, which formulates that a current can flow between two electrodes separated by a thin insulator or a vacuum gap. In this microscope, a sharp metallic tip is brought close to a conductive surface and, upon applying a voltage, a current flows between tip and surface provided their separation is small (in the nanometre range).

In a standard experiment the tip, attached to a piezoelectric actuator, is moved in three dimensions over the surface while an electronic controller keeps the tunnelling current constant by means of a feedback loop that varies the tip-sample distance. This distance is recorded as a function of the tip lateral position and displayed as a microscopic image[5]. Typical applied voltages and measured currents are in the range of mV to ~3V and pA to nA. These voltages result in large electric fields ($\simeq 10^{10}$ V/m) localized near the tip apex which implies that the tunnelling current flows from the very last atom of the tip apex to the single surface atom below, inherently providing atomic resolution. The exponential dependence of this current on the tip-sample distance is the key point in the success of STM, in terms of resolution, since for typical tip-sample systems, a change of only 0.1nm in the distance results in one order of magnitude difference in the measured current.

The invention of the STM immediately triggered the development of several other techniques that sense local properties of surfaces giving rise to the so-called SPM family. Generally speaking, in any scanning probe microscope, a short-range interaction is sensed by a local probe which is scanned over the surface under study. The magnitude of interest is measured, recorded and processed by a computer system.

The scanning force microscopy (SFM) was the first extension of the STM [Binnig86]. In this case, the metallic tip is replaced by a force sensor, so-called cantilever, to measure the interaction forces acting between probe and sample. These forces are usually in the range of nN to μN and, though atomic resolution can be achieved, typical lateral resolution ranges between 5nm and 20nm depending on the sharpness of the probe. Vertical distances can be measured with an accuracy of less than 1nm.

Besides surface topography, the probe-sample interactions also reveal information about lattice symmetry, adhesion, friction, elasticity, wear, etc… with unprecedented spatial resolution.

The success of the SFM technique mainly arises from the possibility to image surfaces independent of their conductivity properties, a severe limitation of the STM technique. But SPM in general and SFM in particular, offer much more than just imaging. Some alternative and outstanding applications of SPM in the field of material science have recently been collected in [Loos05].

[5]Generally, it is said that the movement of the tip at constant tunnelling current reveals the topography of the sample surface. Some caution is required when using the term topography. In STM, a map of constant density of states (DOS) at a given voltage is actually recorded, and this may differ from the atomic geometric topography.

3.2 COMPONENTS OF THE SFM: OUR EXPERIMENTAL SETUP.

Two different microscope systems have been employed to obtain the results presented in this work: the first one is a home-made SFM following the design by Kolbe et al. [Kolbe92] with an electronic control unit from Nanotec [Nanotec], and the second one is a commercial SPM from Nanotec [Nanotec]. The following descriptions are common to most of the SFM setups, and in particular, to both of them.

3.2.1 The Force Sensor.

Strictly speaking, the SFM does not measure forces but the bending and torsion of a lever (also called cantilever), induced by the forces acting on a nanometer-sized tip attached to one of the lever ends. Therefore, this cantilever has to be as soft as possible to be able to detect forces down to the pN. Ideally, the stiffness should be below interatomic spring constants, which are typically in the range of 10–20 nN/nm. To achieve this and additionally prevent the transmission of external vibrations to the cantilever, its effective mass has to be as small as possible.

Today, such cantilevers with integrated tips are commercially produced by standard microfabrication techniques, mostly from silicon or silicon nitride. The later use of a coating layer allows producing tips with different surface properties (conductive, magnetic…). Figure 3.1 shows the two most used cantilever geometries: the rectangular (a) and the V-shaped cantilever (b). Typical dimensions are: length (L) of 100-300 μm, width (W) of 10-30 μm, thickness (t) of 0.3-5 μm, tip height (a) of 3-15 μm and tip radius (R) of 10-100 nm, which yield typical spring constants from 1nN/nm to 40 nN/nm.

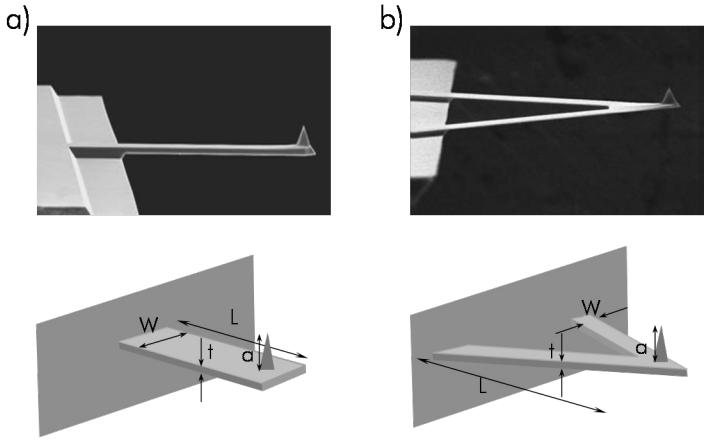

Figure 3.1 Top: SEM images of a silicon (a) rectangular and (b) triangular cantilever. From [μmash]. Bottom: schematic drawing showing the characteristic parameters for both geometries.

Rectangular cantilevers are generally preferred because they make theoretical calculations more tractable. However, they are prone to certain buckling behaviour that can be avoided with the triangular ones. Recent studies have also proved that, contrary to what was commonly accepted, V-

shaped cantilevers offer less resistance to lateral forces than rectangular cantilevers, and thus are more sensitive for frictional studies [Sader03][Sader03b].

The working principle is the same for both geometries and is schematically depicted in figure 3.2: normal forces acting on the tip (perpendicular to the cantilever plane) produce a vertical deflection of the cantilever (Δz), while lateral forces perpendicular to the long axis cause the torsion of the cantilever (Δx). Generally, the cantilever response is approximated by a spring in each direction, and the relation between the forces and the corresponding displacements is straightforward derived from the Hook's law:

$$F_n = k_Z \cdot \Delta z \tag{3.1}$$

$$F_l = k^T \cdot \Delta x \tag{3.2}$$

with k_Z and k^T the spring constants for normal deflection and lateral torsion, respectively. Throughout this thesis we sometimes refer to the cantilever deflection and others to the normal force since they are directly related as shown in equation 3.1.

It is clear that the determination of k_Z and k^T is the first step to obtain quantitative information of the SFM measurements. However, this is not a simple task. Comprehensive reviews of the different theoretical and experimental approaches proposed to obtain k_Z and k^T are given in [Butt05][Legget05][Clifford05][Cannara06]. Because of their inherent difficulties (some are lengthy and might damage the tip, other assume the knowledge of characteristics of the probe that can not be easily obtained), we have used the nominal force constant provided by the manufacturer for the vertical deflection (k_Z) to obtain the value of the normal forces acting on the tip. Nonetheless, to verify that this nominal value was representative, the resonance frequency of the cantilever was always measured and cantilevers presenting a value larger than 15%-20% of the nominal one have been discarded.[6]

In this work, different types of cantilevers, from Nanosensors™ and Veeco Probes, have been employed. V-shaped cantilevers with a nominal force constant k_Z=0.5nN/nm have been mainly used for the structural and frictional characterization, though in some experiments we have employed rectangular cantilevers, with k_Z=0.1nN/nm, for extremely soft samples. The electrical measurements have been performed with rectangular conductive diamond coated cantilevers (k_Z=2.8 nN/nm).

3.2.2 The Deflection Sensor.

Different techniques have been proposed to detect the small bending of the cantilever due to tip-sample forces [Sarid94]. Though in the first SFM setup, this deflection was measured with an STM

[6] The equation relating the resonance frequency of an object with its force constant (k) and effective mass (m) is $f_{res} = \frac{1}{2\pi}\sqrt{\frac{k}{m}}$

tip (the backside of the cantilever was metalized, and the tunnelling tip was brought close to it, to measure the normal deflection [Binnig86]), subsequent designs simplified the original by using optical (interferometer, beam reflection) or electrical methods (piezoresistive, piezoelectric).

Our systems employ the optical beam deflection method, proposed in [Alexander89] [Meyer90] and found nowadays in most of the microscopes. Within this method, a laser beam is focused on the rear metalized side of the cantilever and the reflected beam is collected by a segmented position-sensitive photodiode. Each sector of the photodiode generates a voltage proportional to the intensity received. If the photodiode is segmented in four quadrants (as in our systems), the normal bending and the torsion of the cantilever can be separated and quantified [Meyer90b]. A schematic drawing of our setup is shown in figure 3.2.

In the absence of forces the laser spot is centred, i.e. equal signals are measured in each of the four sectors. When a force acts on the tip, the lever is deflected and the reflected spot is displaced. As depicted in part (a), normal forces produce a vertical bending of the cantilever that is proportional to the signal difference between the upper and lower halves of the detector ($\Delta z \propto V_{A-B}$). Similarly, the main effect of lateral forces is the torsion of the cantilever (part (b)), which is proportional to the signal difference between the right and left halves of the photodiode ($\Delta x \propto V_{1-2}$).

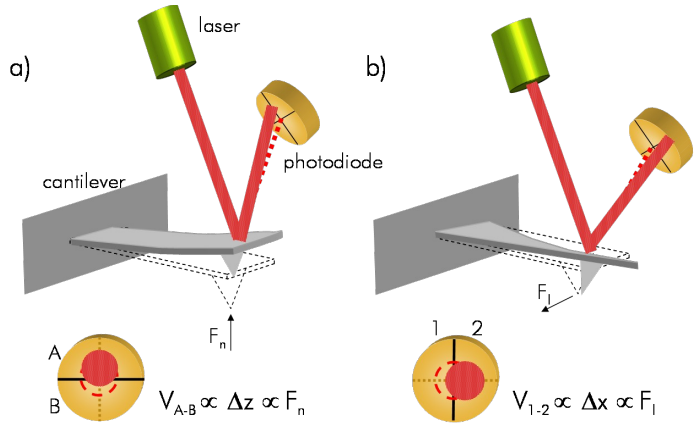

Figure 3.2 Schematic representations showing the optical detection method used to measure the cantilever displacement produced by (a) normal and (b) lateral forces. Dashed cantilever and laser path represent their respective position in the absence of forces. At this position V_{A-B} and V_{1-2} are adjusted to zero. Normal forces are proportional to the V_{A-B} signal whereas lateral forces, to the V_{1-2} signal.

For every cantilever used, a calibration of the photodiode response is required to obtain the conversion from the measured signals, V_{A-B} and V_{1-2}, to the cantilever displacements, Δz and Δx :

$$\Delta z = S_Z V_{A-B} \tag{3.3}$$

$$\Delta x = S_X V_{1-2} \tag{3.4}$$

where S_Z and S_X are the calibration factors for the bending in the vertical and lateral directions, respectively. As explained in section 3.3.1, S_Z is obtained from the force versus distance curves and, for our systems, it varies between 30nm/V and 45nm/V. The determination of S_X is further complicated and requires some assumptions that are not generally fulfilled [Bushanbook]. These difficulties in determining S_X together with the uncertainties in k^T pose a severe limitation when trying to obtain absolute values for the lateral force and, consequently, for the friction signal. To circumvent this problem, we have followed in chapter 5 a more reliable procedure that consists in the study of relative rather than absolute friction characteristics by using heterogeneous samples. Still, lateral forces are given in volt units (the photodiode output) throughout this thesis.

3.2.3 The Scanning System.

The scanning probe needs to be positioned with an accuracy of 1pm if atomic resolution is required. This is usually achieved by attaching either the tip or the sample (this latter is the configuration used in this work) to piezoelectric actuators. These generally consist of lead-zirconate-titanate (PZT) ceramic materials placed between two metal electrodes. When a potential difference is applied across the electrodes, the piezoelectric ceramic expand or contract in a direction that is perpendicular to the applied electric field. The motion of the ceramic is controlled by the polarity and magnitude of the applied voltage.

The tube shaped piezoelectric actuator of figure 3.3 is the most frequently used in SFM. It is a hollow cylinder that has one electrode on the inner surface and four equally spaced electrodes on the outer surface. Biasing the inner electrode controls the tube's motion in the ±z direction, part (a). This change will be referred to as the piezo displacement (Δz) from now on (though we use the same symbol, it can differ from the vertical cantilever displacement). Biasing two opposite outer electrodes moves the tube in the ±x and ±y directions, part (b). This provides the scan area (Δx, Δy) on the surface plane of a typical SPM image. The particular vertical and lateral displacements depend upon the geometrical and physical characteristics of the piezoelectric tube:

$$\Delta z = VL\frac{d_{31}}{t} \tag{3.5}$$

$$\Delta x(\Delta y) = 2\sqrt{2}Vd_{31}\frac{L^2}{\pi Dt} \tag{3.6}$$

where L is the length, t is the wall thickness, D is the outer diameter and d_{31} is the piezoelectric constant of the particular ceramics from which it is fabricated. We have used different scanners whose nm/V ratios vary between 10-30 nm/V for the vertical displacement and 40-250 nm/V for the lateral movement. This yield a maximum horizontal and vertical scan ranges of 10μm-70μm and 2μm-12μm

respectively, which allows measuring a wide variety of samples, from completely flat to extremely rough surfaces.

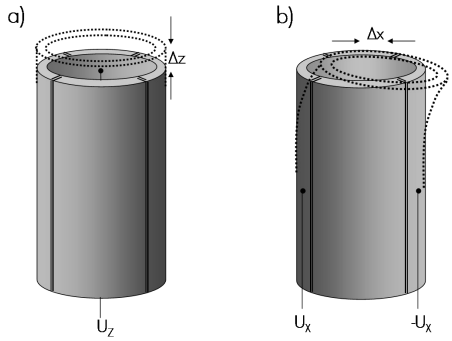

Figure 3.3 Schematic representation of the response of a tube-shaped piezo actuator to an applied voltage between the (a) internal and external electrodes and (b) two opposite external sectors.

The above equations serve as estimation but, in SPM, to avoid undesired uncertainties (intrinsic non-linearity, manufacturing differences, aging effects…) the piezos are usually in-situ calibrated to obtain an accurate conversion between the applied voltage and the displacement. Due to the non-linearity in the piezo movement, we have employed different calibration samples to obtain nm/V ratios for large and small scan areas.

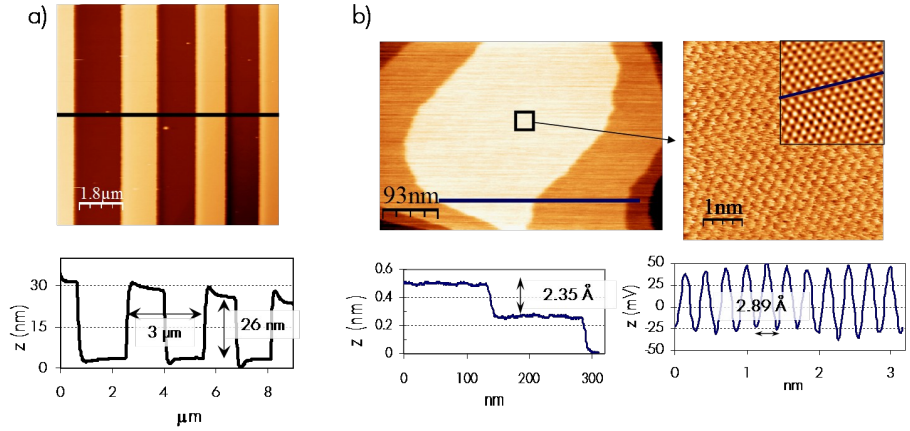

Figure 3.4 (a) SFM image (9x9 µm^2) of the grating used to calibrate the piezo scanner. The nominal step heights and periodicity are provided by the manufacturer. (b) Topographic (left) and lattice-resolved (right) images of the Au(111) surface. The monoatomic step height and lattice periodicity are used for vertical and lateral calibration on small scan areas. The latter is better obtained from profiles in corresponding 2D-Fast Fourier filtered image (inset).

In the first case, figure 3.4(a) shows the image of the commercial calibration grating used, which presents 1-D arrays of rectangular SiO_2 steps on a Si wafer [µmash]. The nominal height (26±1nm) and distance between steps (3 µm) are used for the vertical and lateral calibration, respectively. For small scan areas, the surface of the Au(111) has been employed. As shown in figure 3.4(b), the monoatomic terraces of known height (0.235 nm) are used to calibrate the vertical displacement whereas lattice-resolved images of the hexagonal periodicity ($a_{Au\text{-}Au}$=0.289nm) serve to calibrate the lateral movement.

3.2.4 The Control Unit.

A high voltage unit connected to a digital signal processor (DSP) inside a PC basically complete our experimental setups. The DSP board is mainly in charge of collecting the signal coming from the photodiode and controlling the movement of the piezo. Due to the limited voltage range of the DSP (±3 V) and the high voltages required by the piezo to work (up to 300 V), the signal is amplified and supplied to the microscope through a high voltage unit. The amplification gain is selected by the user depending on the vertical and lateral scales of the sample under study: lower gains imply smaller scanned area but increased resolution.

The DSP is also in charge of the so-called feedback loop, a way to control the vertical distance between tip and sample by maintaining a selected magnitude fixed to a preset value during the scanning. Throughout this work the magnitude used has been the normal deflection of the cantilever, i.e. the normal load. By means of the feedback loop, this deflection and the preset setpoint are continually compared at each point of the image. If they are not equal, a voltage is applied to the scanner in order to move the sample closer to or further from the probe, to maintain constant the normal load. This applied voltage is the signal used for generating the SFM image.

The software used for data acquisition and image processing is WSxM [Horcas07].

3.2.4 Vibration Isolation.

The construction of the tip holder, sample holder and piezo scanner should be as rigid as possible in order to increase the mechanical resonance frequency of the system. Moreover, to achieve sub-nanometre sensitivity, typical vibrations in buildings coming from elevators, stepping on the floor or motion of the entire building itself (frequency range between 0.1 and 2 Hz) and acoustic noise (frequency range of 10 to 20 Hz) must be eliminated. In this work, two different designs have been used to accomplish it. As shown in figure 3.5(a), one of the SFM is mounted on a rigid granite plate and the whole system is suspended with four bungee cords that act as springs. The resonance frequency of the system is ~1Hz and filters out higher mechanical vibrations. In the second design, figure 3.5(b), the SFM and the granite plate are supported by four damping legs that act as a low resonant frequency support. In both cases, a hood covers the scanning force microscope head (tip, sample, detection system and piezo actuator) which provides further acoustic isolation and allows controlling the relative humidity of the working atmosphere. The hygrometer used to measure the temperature and relative humidity inside and outside the hood has an accuracy of ±2% RH (in the 2-98% range) and ±0.2 °C (in the 0-70 °C range).

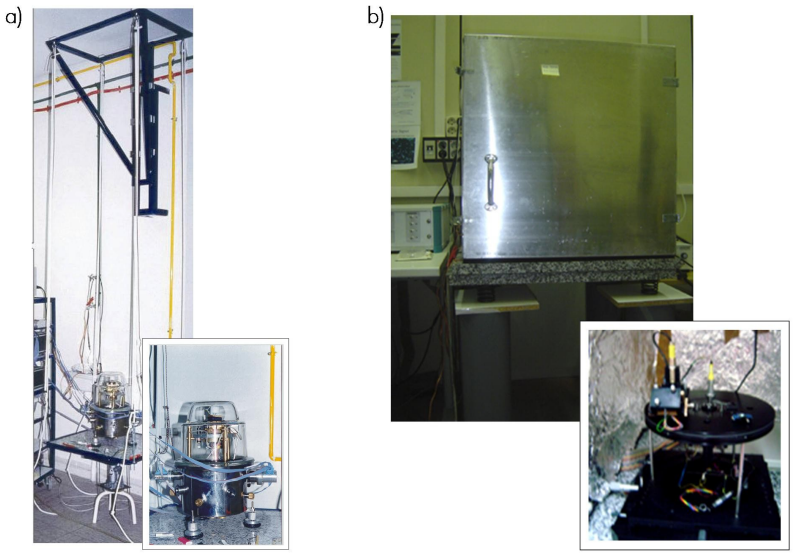

Figure 3.5 The SFM is mounted on a granite plate and (a) hanging from four bungee cords (b) suspended by a damping table, to eliminate building vibrations. In both systems the SFM head is covered to work under controlled relative humidity. Additionally, in (b) a metallic box is used to minimize electrical noise. The insets show the SFM head in more detail.

3.3 RELEVANT TIP-SAMPLE INTERACTIONS.

The operation principle of a scanning force microscope is the detection of the force acting between probe and sample. This force can have different origins and contributions and, depending on the tip-sample system under study, the predominant interaction mechanism might vary.

In this section we describe the most relevant forces for the work presented here. More detailed information on intermolecular and surface forces can be found in the book [Israelachvili92].

short range forces: these forces arise from the overlapping of electron wave functions and from the repulsion of the ion cores. Their range is comparable to the extension of the electron wave functions, i.e. less than one nanometre. They can be either attractive (as for example in bond formation) or repulsive (due to the Pauli exclusion principle).

As stated in the compilation work by Meyer and co-workers [Meyerbook], the magnitude of attractive short-range forces is around 0.5-1nN and the decay length around 0.2-0.3nm. Akin to the tunnelling current in STM, when these forces are predominant, true atomic resolution is possible in scanning force microscopy imaging [Moritabook].

When the short-range repulsive forces are predominant, the tip and the sample are considered to be in "contact" and, though lattice periodicity is possible for well ordered systems, true atomic resolution is however limited as we show in section 3.4.1.

van der Waals forces: we already mentioned this interaction when considering the intermolecular forces in self-assembled monolayers. In fact, these are dipole-dipole interactions always present between molecules and atoms. The most important are not those between permanent dipoles

but the so-called dispersion forces, which act between dipoles arising from fluctuations and dipoles induced in their electric field.

In order to model this interaction in SFM, macroscopic bodies rather than individual atoms or molecules are considered. The tip-sample geometry can be well approximated as a sphere approaching a plane and the van der Waals interaction for such configuration has the form:

$$F_{vdW} \approx -\frac{AR}{r^2} \qquad (3.7)$$

where R is the sphere radius, r is the sphere-plane distance and A is the Hamaker constant. The order of magnitude of this constant, which accounts for the materials involved, is $\sim 10^{-19}$ J [Israelachvili92].

In vacuum or air, this van der Waals interaction is always attractive. However, in other media the interaction can be attractive (A>0) or repulsive (A<0), depending on the dielectric constant (ε) and the refractive index (n) of the tip, the sample and the medium in-between. For example, a medium with ε and n close to the respective values of the tip and sample greatly reduce the van der Waals forces compared to the vacuum. For most solid materials, this is the case when immersing the tip and sample in water [Meyerbook].

This interaction acts between the surface and the mesoscopic tip end, i.e. not only the end atoms of the tip, and for typical tip-sample systems (e.g. Si_3N_4-Au in air) and tip radius R=30nm, the van der Waals force at a distance r=0.5nm is of the order of F_{vdW}=4nN.

friction and adhesion forces: during sliding, a macroscopic object has to overcome an opposing force which results in a loss of kinetic energy and, if no additional energy is supplied, the object finally stops. This force, that opposes the relative motion between objects in contact, is the friction force. In the SFM setup, friction causes the torsion of the cantilever when the tip is scanned over the sample as shown in figure 3.2(b). These lateral forces can be exploited to form an image or map of the dissipation energy, sometimes showing higher contrast than topographic images (see chapter 4). This contrast might arise from mechanical and/or chemical differences between regions.

Adhesion is the molecular attraction exerted between bodies in contact and can be defined as the free energy change to separate unit areas of two media from contact to infinity in vacuum or in a third medium [Israelachvili92]. Moreover, in SFM working under ambient conditions, there is another important contribution to the adhesion force coming from the water meniscus that forms between the tip and substrate due to adsorption of thin water films at surfaces, and subsequent capillary condensation [Colchero98]. The formation of this meniscus, schematically depicted in figure 3.6(a), produces an attractive adhesion force that depends on the relative humidity and the hydrophilicity of tip and sample. The final expression for this force between a sphere and a plane is:

$$F_{cap} = 2\pi R\gamma(\cos\theta_1 + \cos\theta_2) \qquad (3.8)$$

with R the sphere radius, θ_1 and θ_2 the contact angle of the respective surfaces and the liquid and γ the surface tension of the water.

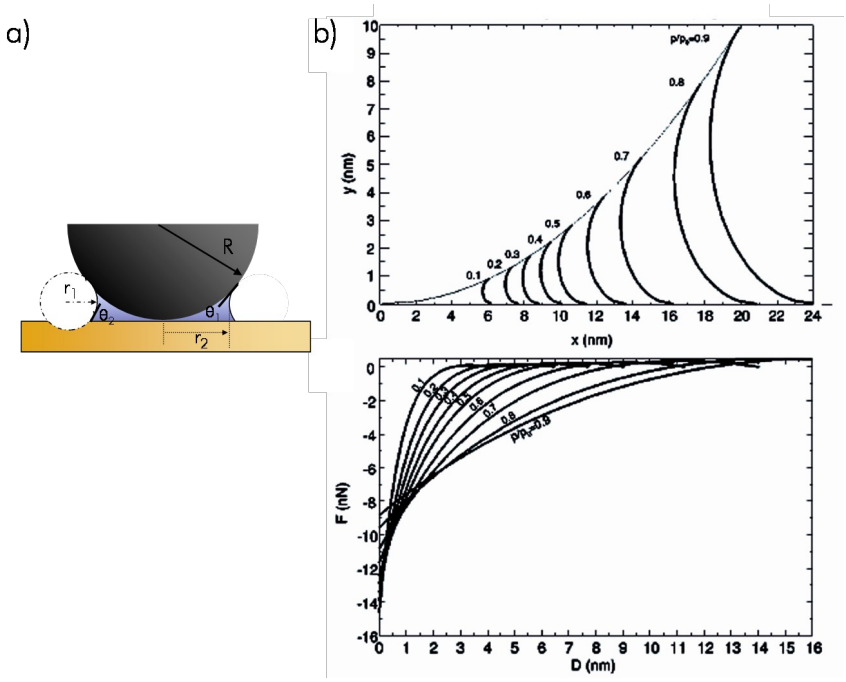

Figure 3.6 (a) Liquid meniscus formed between a sphere and a plane. Two radius, r_1 and r_2, generally define the shape of the meniscus. (b) Upper panel: calculated geometric shape of a water meniscus formed between an SFM tip (R=20nm) in contact with a surface, both hydrophilic, for various relative humidity values (p/p_0). Lower panel: calculated meniscus force as the SFM tip is retracted from the surface (i.e. as D is increased) as a function of the RH. From [Stifter00]

To better see the influence of this water layer on SFM measurements, figure 3.6(b) reproduces a theoretical calculation of the shape (upper panel) and meniscus force (lower panel) in scanning force microscopy, for different relative humidity values [Stifter00]. Even for low relative humidity, the order of magnitude of the adhesion force due to capillary condensation for typical silicon nitride tips, at a distance of 0.5nm, is ~10^{-8}N which is comparable to the forces used in SFM experiments. For high relative humidity, this force decreases but its range extends for longer distances when the tip is retracted (lower panel figure 3.6(b)).

Immersing the whole tip-sample area under liquids can completely remove capillary interaction.

electrostatic forces: these forces act between localized charges on insulating tip and samples. Their strength and distance dependence obey the Coulomb's law and are usually stronger than other long-range interactions such as the van der Waals or the magnetic interaction. Between conducting tip and sample, electrostatic forces appear when they are at a different potential. If one considers the tip-sample system as a capacitor, the force is given by

$$F_{el} = \frac{\partial C}{\partial z}\left(U_{bias} - U_{cpd}\right)^2 \qquad (3.9)$$

where U_{bias} is the bias voltage applied between tip and sample and U_{cpd} is the contact potential difference caused by their different work functions. The capacitance, C, depends on the tip-sample distance, the geometry of the system and the dielectric constant of the medium in-between. Therefore, the force also depends on these parameters, which are included in the derivative of the capacitance.

From equation (3.9) it is inferred that a zero bias voltage does not normally correspond to a minimal electrostatic force, since the contact potential difference is not compensated.

Due to the long-range character of these forces, electrostatic interactions act between the sample and the whole cantilever. Only for very small tip-sample distances (≤ 2nm), the electrostatic force contribution from the end of the tip dominates over the other terms [Gil03].

3.3.1 The Force Versus Distance Curve.

A typical measurement of the tip-sample interactions in SFM is to record the variation of the cantilever deflection as the sample is approached to and retracted from the tip. This is the so-called force spectroscopy mode based on the force versus distance curve analysis shown in figure 3.7. Upon tip-sample approach (red line), the cantilever deflection is approximately constant (i) until attractive interactions such as van der Waals, electrostatic or capillary forces cause a change in the cantilever deflection (ii). When these forces are stronger than the restoring force from the cantilever spring, the tip suddenly jumps into contact with the surface.

After the snap-in point, the cantilever deflects away from the surface approximately linearly with the scanner movement due to the repulsive short-range forces (iii)-(iv).

When full extension of the piezo is achieved, the scanner begins to retract and (in the absence of scanner hysteresis) the cantilever deflection retraces the same curve as the sample is moved away from the tip, until a snap-out instability is observed, indicating that the tip is no longer in contact with the sample (blue line).

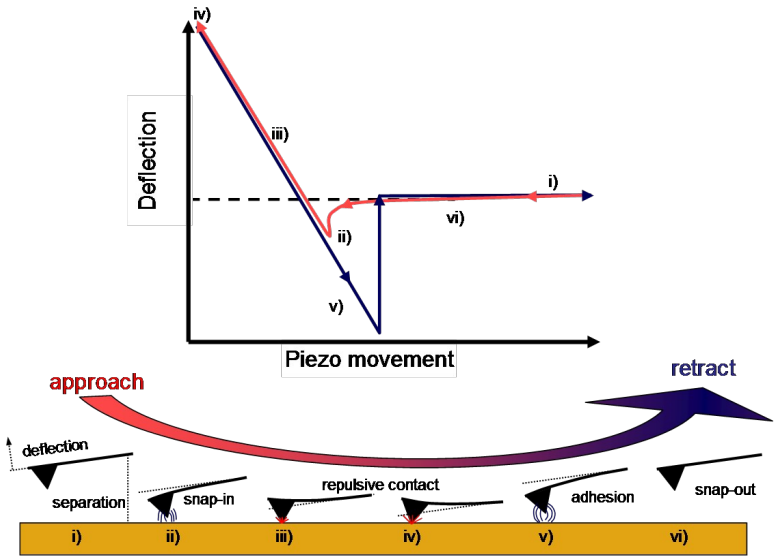

Figure 3.7 Force versus distance curve acquired during an approach-retract cycle of the sample towards the tip: the cantilever deflection is measured as a function of the piezo displacement. The different identified regions correspond to the different cantilever deflections schematically depicted in the bottom picture.

When measuring in air, the water meniscus holds the tip in contact with the sample (capillary adhesion) bending the cantilever strongly to the surface (v). This generates a hysteresis in the curve, and the snap-out point is not observed at the same piezo position as the snap-in instability, i.e extra piezo movement is needed to detach the tip from the surface. The value of the force at the snap-out point is generally denoted as the adhesion or pull-off force.

These curves are the direct result of the photodiode response ($V_{A\text{-}B}$) versus vertical movement of the piezo actuator (z). To obtain a true force versus distance curve, $V_{A\text{-}B}$ and z have to be converted into force and tip-sample distance respectively.

Regarding the conversion of the photodiode signal into force, we obtain the direct relation by combining equations (3.1) and (3.3):

$$F_n = k_Z \cdot S_Z \cdot V_{A-B} \qquad (3.10)$$

The cantilever force constant (k_Z) is provided by the manufacturer. The photodiode sensitivity (S_Z) is obtained from the curve itself, when the sample measured is hard enough to neglect surface deformation.[7]

The conversion of the piezo movement into tip-sample distance is more complicated, especially for deformable materials. Generally, the zero tip-sample distance is defined at the point where the sign of the force versus distance curve changes due to repulsive interactions, i.e point (ii) in

[7] In this case, after the jump to contact, the cantilever deflection is assumed to be equal to the piezo movement and therefore, the inverse slope of the repulsive part of the curve (from (ii) to (iv) in figure 3.7) yields the nm/V calibration ratio.

figure 3.7. At this point, the tip contacts the sample surface. If there is no sample deformation, beyond this point further piezo displacement does not change the tip-sample distance but only increases the applied force. When softer materials are under study, tip indentation and elastic/plastic deformation might play a significant role in the conversion of the piezo movement into tip-sample distance. In this case, after the contact with the surface, tip-sample distance can still be reduced due to tip indentation. This topic is extensively discussed in [Cappella99][Butt05] and will be taken into account in the analysis of the measurements performed on the SAMs islands.

The value of the adhesion force measured from the force versus distance curve is often used as a direct method to in situ check the tip condition. The dependence of this adhesion on the tip dimensions (see equation 3.8) allows correlating sudden changes on the adhesion value to changes in the tip contact area due to damage during the scanning. This verification has been done prior and after the friction analysis of chapter 5.

Finally, these force versus distance curves are also used to correct possible cross-talk between lateral and normal signals due to imperfect laser alignment which might cause a coupling of the topographic and friction data. Prior to the friction measurements presented in this work, both signals have been decoupled, so that the $V_{1\text{-}2}$ signal is constant during a force versus distance curve.

3.4 OPERATION MODES IN SFM.

The rich variety of interactions that can be detected in SFM has made possible a wide variety of operation modes.

The oldest one is the so-called contact mode where the tip and the sample are in direct mechanical contact. By measuring the change in the vertical deflection of the cantilever (due to repulsive forces) as the tip scans the sample surface, topographic images are obtained. Simultaneously to the surface topography, maps of friction or conductivity, which also imply direct contact, can be measured (see section 3.4.1). Another kind of operation modes are the so-called dynamic modes where the cantilever is oscillated near its resonance frequency at a given distance from the sample surface. Depending on the amplitude of oscillation, compared to the tip-sample distance, the tip may either not contact the sample (small amplitude) or intermittently contact the sample surface (large amplitude). By measuring changes in amplitude, phase or frequency of the oscillating cantilever in response to the existing tip-sample interactions, one can obtain not only topographic images of the surface but also dissipation, magnetic or electrostatic maps.

Though further details are given in next section on those modes employed throughout this work, a complete description of all of them can be found in general SFM books as [Meyerbook].

3.4.1 Contact Mode.

For our particular researching objectives, detailed throughout the manuscript, a methodology based in this mode has been used in most of our investigations. As commented above, it is based upon the static measurement of the deflection of the cantilever caused by repulsive forces when the tip contacts the sample surface. By means of a feedback loop, this deflection is kept constant to a setpoint value while scanning the tip over the sample surface. With the cantilever deflection held constant, the force applied to the sample during the scan is also constant.

At this point we have to distinguish between normal and total force between tip and sample. The former is directly obtained from the cantilever deflection and the force constant (equation 3.1) and, when the feedback is enabled, it is just the setpoint value multiplied by k_z. The latter is the sum of the normal load and the adhesion force obtained from the force versus distance curve. This implies that the minimum practicable setpoint to acquire an image in contact mode is close to the adhesion force in module, but with opposite sign. If the zero deflection is defined as the cantilever deflection in the absence of forces (dashed line in figure 3.7), this means a negative setpoint and a total applied load close to zero, which minimizes possible damage of delicate sample surfaces.

- Normal forces: topographic image.

The image is generated by plotting, at each point of the scanned area, the vertical piezo movement needed to keep the cantilever normal deflection constant. In contact mode, the variation of this deflection is mainly due to changes in surface topography (care has to be taken when measuring heterogeneous sample with areas of different elastic constant), and therefore a topographic image of the sample surface is generated.

The information collected during a scan of the surface is quantitative in three dimensions, two specifying the lateral position and the third specifying the height at that position. When presented as a topographic image, the elevation of each point in the picture is encoded according to a grey scale or a false colour scale. The general agreement is that higher (lower) features appear brighter (darker) in the top view image. Profiles or cross-sections through the surface can be plotted and quantitative horizontal and vertical distances measured.

To highlight topographic features such as steps or grain boundaries, error or derivative images are commonly presented. These images are generated by plotting the difference between the measured cantilever deflection and the setpoint value, at each point of the image.

- Lateral forces: friction and lattice-resolved images.

At each point of the scanned area our experimental setup allows to register, simultaneously with the normal cantilever deflection, the bending of the cantilever due to the lateral forces, generating a lateral force image. Care has to be taken when trying to get frictional characteristics from these images, since the contribution to the lateral signal is generally twofold: from topographic (steps, changes in surface slope…) and from friction characteristics [Meyerbook]. To obtain chemical or

material-specific contrast it is desirable to isolate the second contribution. This is usually dealt with by acquiring what is called a "friction loop". The lateral signal is recorded while the tip completes a trace-retrace loop along the same scan line as shown in figure 3.8. The forward and reverse components of the loop are subtracted and, because topographical forces do not depend on the scan direction while friction forces always oppose the motion of the tip, the friction force can be calculated as:

$$F(r) = \frac{1}{2}(F_l^f - F_l^b) \qquad (3.11)$$

where F_l^i is the lateral signal in the forward (i=f) and backward (i=b) scan direction. In this way, apart from cancelling the topographic contribution, any possible asymmetry in the friction loop arising from imperfect laser alignment (e.g. an offset in the 1-2 alignment) is also corrected.

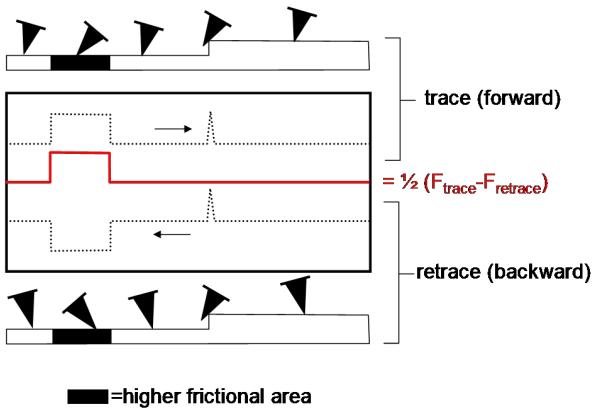

Figure 3.8 Friction loop formed by the trace and retrace lateral signals along the same scanned line. The upper and lower pictures represent the torsion movement of the tip as it encounters areas of different frictional properties or topographic changes. Dashed lines are the corresponding lateral force profiles. The solid line is the friction force obtained from equation (3.11).

Therefore, a friction image is, in fact, the subtraction between the forward and backward lateral force images.

Obtaining reduced error friction values as well as friction versus load plots implies further quantitative analysis. In this work we have followed the below described protocol for scan areas presenting an homogeneous friction:

1.- forward and backward lateral images are measured at a selected applied load.

2.- the friction force at each line of the image, $F_i(r)$, is calculated using equation (3.11), where F_l^f and F_l^b are now the averaged lateral signal on line j^{th}, in the forward and backward images, respectively.

3.- the friction force is calculated as the average over the total number of lines of the images (N):

$$F(r) = \sum_{i=1}^{N} F_i(r)/N \qquad (3.12)$$

4.- this procedure is repeated at different applied forces to obtain a friction versus load curve.

When the image covers regions of different frictional properties, the analysis procedure is analogous. Firstly, we make a zoom in the original image (within the same location and with the same number of lines on the forward and backward lateral force images) that includes only one of the regions. Afterwards, the procedure already described is applied to these zoomed images. This method has been employed to study the frictional properties of SAMs (chapter 5).

In addition, the lateral force measuring mode may provide atomic lattice resolution. This is shown in figure 3.9 for the Au(111) surface. These images have been used to study the molecular order of the islands of self-assembled alkanethiols (see chapter 4) as well as to calibrate the piezo for small scanned areas (see section 3.2.3). They do not correspond to true atomic resolution but atomic periodicity images.

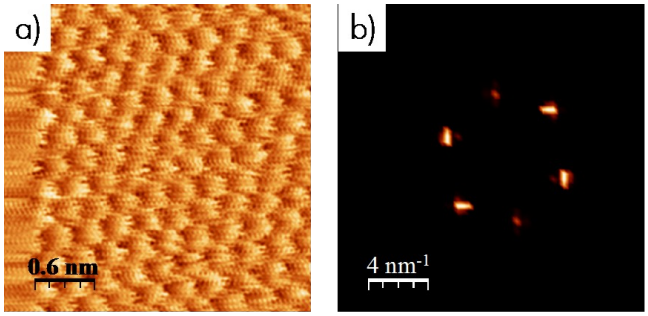

Figure 3.9 (a) High resolution lateral force image measured on a gold terrace. The hexagonal symmetry with the periodicity (2.89 Å) of the Au(111) is resolved. (b) corresponding 2D Fast-Fourier transformed (2D-FFT) image.

When a SFM tip is in mechanical contact with a surface, simple elastic contact mechanics show that, for typical tip radii, elastics constants and loads, the contact is not just a single atom. Contact-mode SFM therefore, can not possess single atom resolution akin to STM. But these so-called high resolution lateral force images often do display atomic scale stick-slip behaviour with the periodicity of the atomic lattice of the sample and result extremely useful for surface structural characterization. The explanation of this stick-slip behaviour has been discussed in numerous experimental and theoretical works (see for example [Carpick97]). It can be intuitively understood considering the combined action of the parabolic potential of the tip (modelled as a spring) and of the periodically varying potential of the surface (figure 3.10(a)). A potential presenting a series of local minima is created (blue profile in figure 3.10(a)) and, at a tip-sample relative lateral position, the tip resides in one of the minima. If the tip is pushed laterally, it will remain at that minimum ("sticking"),

until the restoring force of the cantilever is enough to overcome the energy barrier and effectively "un-stick" the cantilever, causing the tip to jump or slip to the nearest local equilibrium position, where it is locked again. The periodic dissipation of energy, when jumping from one minimum to the next one, can be measured in the lateral force image, yielding the lattice periodicity of the surface (figure 3.9(a)). This is not, however, true atomic resolution and, for example, isolated vacancies can not be visualized. Nonetheless, we still can detect their presence within the lattice since they affect the quality of the image. This is illustrated in the 1D simplified model in the cartoon of figure 3.10(b), where we assume that only three tip atoms interact with an atomically flat surface. To explain why vacancies are not individually resolved but affect the image quality, a vacancy has been generated. The total interaction, as the sum of the three contributions, shows a depression due to the presence of the vacancy at the surface. Note that neither the size not the position of the vacancy is well reproduced but, as a consequence of this effect, the recorded images of surfaces with vacancies, or lack of order quality, have the blurred aspect of a noisy signal.

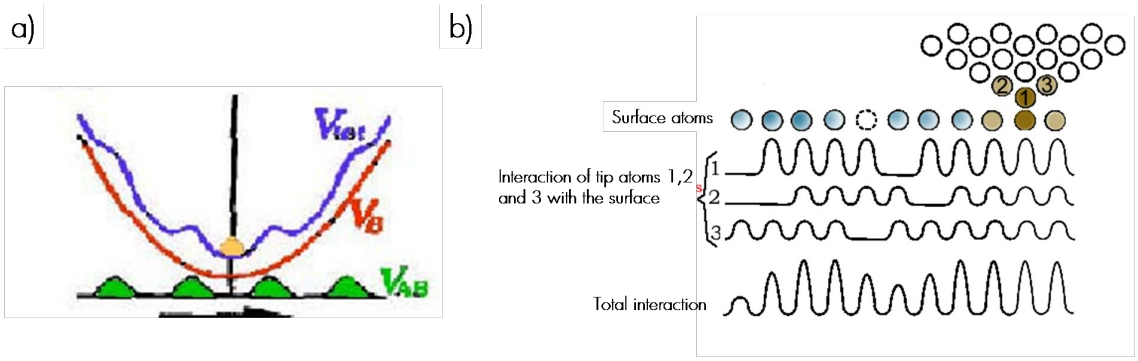

Figure 3.10 (a) Superposition of the parabolic potential of the tip (V_B) and the atomically periodic surface potential (V_{AB}) used to explain the lattice periodicity in the stick-slip process. (b) Schematic drawing of the interaction of a SFM tip with a vacancy considering that only the three outermost atoms of the tip interact with the surface.

- Current images:

Simultaneously to the topography and friction properties, our experimental setup allows obtaining maps of electronic conductivity, normally referred as current images. In those images the current flowing between a conductive tip and the sample is recorded at each tip location for a fixed applied bias voltage. A high sensitivity IV converter (10nA/V) allows measuring currents in the picoampere range. In our particular setup, the bias voltage is applied to the tip whereas the sample is grounded. This type of measurements and the methodology described in the next section have been used for the acquisition of the results presented in chapter 6.

3.4.2 Three-dimensional (3D) modes.

Strictly speaking, the 3D mode is not an operation mode but an alternative way of acquiring data [Nanotec][Colchero98]. As in any conventional SFM operation mode, it allows obtaining a

given magnitude as a function of two other, $f_i(x_1, x_2)$, but the novelty is that x_1 and x_2 do not necessarily correspond to scanned longitudinal dimensions. In the resulting image (generally denoted as 3D image) the colour scale represents the magnitude f_i and the horizontal and vertical axis, the two magnitudes chosen as variables (x_1 and x_2, respectively), whose influence on f_i is under study. Thus, horizontal profiles provide $f_i - x_1$ curves at the selected x_2 value and vertical profiles provide $f_i - x_2$ curves at the selected x_1 value. Since various images can be simultaneously recorded (this is only restricted by the number of acquisition channels available in the SFM employed) the dependence of more than one magnitude on the same two variables can be obtained. In the present work, the 3D modes have been applied to study the friction (chapter 5) and the transport (chapter 6) properties of self-assembled monolayers.

- 3D modes for friction measurements:

These measurements are performed over a *single line* (xy) along the sample surface. The tip movement along this line is the fast scan direction (x_1 = xy) and the z piezo movement is chosen as the slow scan direction (x_2 = z; positive values indicate the sample approaching the tip). This means that, at a given tip-sample distance, the tip scans the selected line, forward and backward. Afterwards, the piezo moves to increase/reduce the tip-sample distance, and the scan along the same line is repeated at this new distance. The magnitudes under study are the lateral and normal forces and figure 3.11 shows an example of the images obtained on a gold substrate.

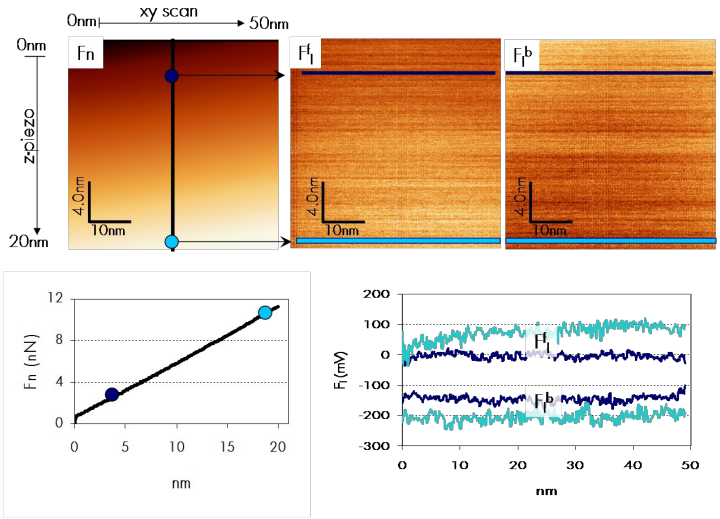

Figure 3.11 Top: simultaneous normal (Fn) and lateral (F_l^f and F_l^b) force images acquired on a gold substrate applying the 3D modes. The vertical piezo displacement and the scan length along the selected line are the same for the three images. Bottom left: force versus distance curve obtained from the vertical profile in the Fn image. Bottom right: friction loops extracted from the horizontal profiles in the F_l images.

Horizontal profiles in the F_l(xy,z) images (forward and backward) form a friction loop at the selected z distance. From F_n (xy,z) we can calculate the value of the applied load at each z value. Therefore, by combining the 3D images we can have a friction versus load plot. Though in chapter 5

we analyze in more detail the friction response as a function of the applied load, at a first sight the bottom graphs of figure 3.11 show that, in the gold surface, friction increases (= the area enclosed by the loop increases) when the applied load is increased. However, it is not a linear relation. This is due to the dependence of friction on the contact area, which leads to the relation $F_f \propto (F_n)^{2/3}$. The definition of the contact area and its relation with the friction force is more extensively explained in section 5.1.

- 3D modes for transport measurements:

These experiments are performed over a *single point* on the surface, i.e. the lateral scan of the tip is disabled. The fast scan direction is the bias voltage applied to the tip (x_1 = V) while the slow scan direction is again the piezo movement in the vertical direction (x_2 = z), i.e. the voltage is varied between two selected values at each tip-sample distance. The magnitudes under study are the current flowing between the conducting tip and sample (I) and the normal force (F_n). Typical images obtained are shown in figure 3.12, again for the gold surface.

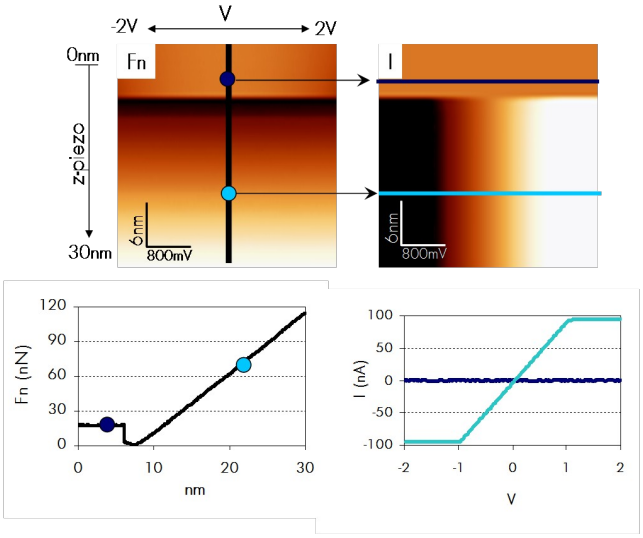

Figure 3.12 Top: normal force (Fn) and current (I) images simultaneously measured on a gold substrate applying the 3D modes. The vertical piezo displacement and the voltage range are the same for both images. Bottom left: force versus distance curve obtained from the vertical profile in the Fn image. Bottom right: current versus voltage curves extracted from the horizontal profiles in the current images.

The vertical profile in the F_n (V,z) image shows the force versus distance curve at an applied voltage of 0V. Before the snap-in point (dark circle), no current is measured between tip and sample (dark profile in the current image). Once the tip is in contact with the gold surface, at any given force, we observe a linear I-V curve typical of a metallic contact (light profile in the current image). Similar to the friction measurements, by combining the information of both images we can study the variation of the IV curves as the applied load cha

nges (see chapter 6).

3.5 SAMPLE PREPARATION.

3.5.1 Gold Substrate.

Polycrystalline gold substrates were purchased from Arrandee™. They consist of a gold film of 200-300nm in thickness on top of a chromium layer (1-4 nm thick) over a borosilicate glass surface. The chromium layer has the role of improving gold adhesion to the glass substrate, avoiding bubbles and undesired film pill off. Figure 3.13(a)-(b) shows the topography of the as-received sample surface. The surface roughness is 3-5 nm and consists of gold grains of a mean diameter of 60 nm, better seen in part (b). Prior to the formation of the self-assembled islands, these gold substrates are cleaned by immersion in a piranha solution (1:3; H_2O_2:H_2SO_4) for 10-15 minutes, in order to remove any possible contaminant, mainly of organic nature. Afterwards, the samples are thoroughly rinsed with deionised water (R≈18.2 MΩ) and dried under N_2 stream. The more hydrophilic the surface appears, the cleaner it is. Subsequent flame annealing in air with a small butane torch set for a conical blue (i.e. "reducing") flame is performed. Good annealing is normally achieved after ~1min, when samples are heated to the point where a dim reddish/orange glow is visible. A good flame annealing induces the formation of large grains as those shown in figure 3.13(c). The flame annealing process does not oxidize gold nor deposit soot on the surface. In fact, it has been reported that, apart from increasing the grain size and providing large terraces with the lowest energy (111) orientation, it can also contribute to eliminate contaminants [Dishner98].

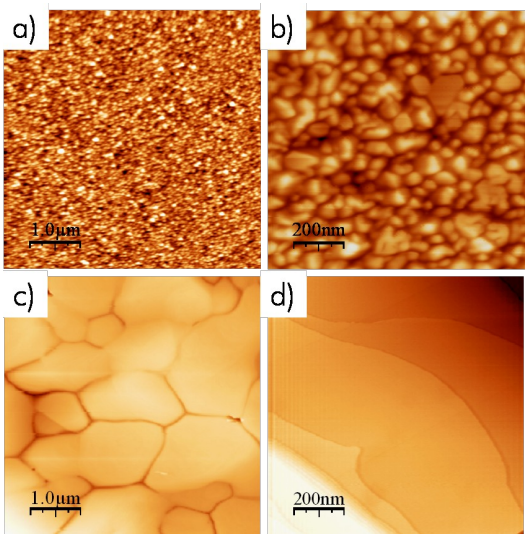

Figure 3.13 Topographic images of the gold surface, (a)-(b) before and (c)-(d) after the cleaning and annealing procedure described in the text. After this procedure, the average grain size is multiplied by ~20 and large terraces (hundreds of nm) separated by monoatomic steps (2.35 Å in height) are visible within the grains. Total z-scale: (a) 0-20nm; (b) 0-20nm; (c) 0-180nm; (d) 0-9nm.

The overall surface roughness considerably increases in these annealed samples due to the deep grain boundaries formed (hundreds of nanometre deep). However, the surface of the grains consists of extremely flat terraces separated by monatomic steps (part (d)). High resolution lateral force

images measured on these terraces, exhibit the hexagonal symmetry of the (111) orientation with the corresponding lattice parameter, $a_{Au\text{-}Au}$=2.89 Å, as shown in figure 3.9.

The flatness and quality of the final terraces depend considerably on:

(1) the immersion time on the piranha solution: long times (> 1/2h) have been observed to produce pits on the gold surface.

(2) the annealing time, the surface-flame distance and the flame shape and colour: long times (> 2min) and short distances (< 0.5cm from the flame end) roughen the surface and the presence of flat terraces is considerably reduced. Moreover, the flame should present a blue glow indicating that the temperature is similar to that of the gold melting point (1064°C). In orange flames, which appear when the gas is not being fully combusted, the temperature is not so high and there is risk of underheating the surface, which results in a reduced size of the terraces.

(3) the butane gas: high purity gas is essential to avoid possible contamination during annealing.

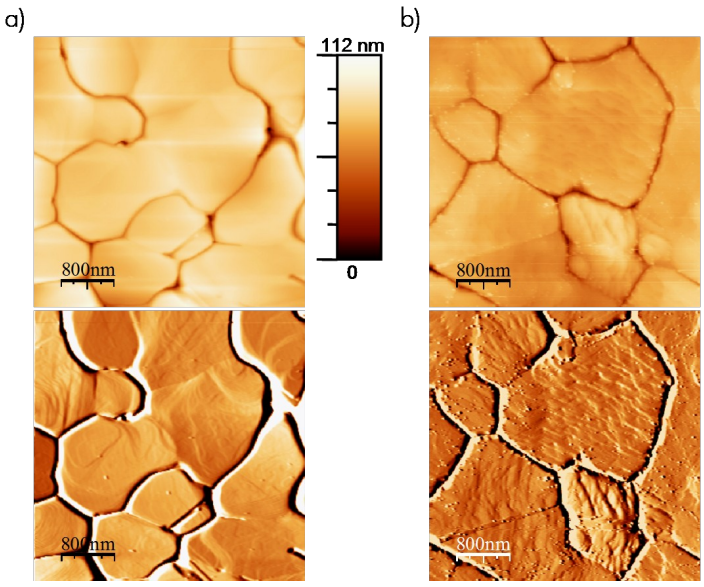

Figure 3.14 Topographic (top) and derivative (bottom) images of the gold surface after a (a) good and (b) failed cleaning and annealing procedure. The z-scale is the same for both topographic images (vertical bar).

Figure 3.14 compares the surface topography of a well annealed sample, part (a), with that of a sample in which the cleaning and annealing procedures were not properly done, part (b). In the corresponding derivative images, (c) and (d), it is clearly seen that the terraces are considerably smaller, and the surface roughness higher, for the second sample. The presence of contaminants is also observed in this sample, which might have contributed to reduce, by step pinning, the development of large flat terraces.

The results reported in next chapter highlight the importance of having large and flat gold terraces to obtain high quality samples.

3.5.2 Alkanethiol Solutions

Different alkanethiol (Cn) and disulfide (CnCm) molecules have been used. Decanethiol (C10, Aldrich 96%), dodecanethiol (C12, Aldrich 98%), hexadecanethiol (C16, Aldrich 92%) and octadecanethiol (C18, Aldrich 98%) are commercially available. Docosanethiol (C22), and diulfides (symmetrical, C12C12 and C16C16, and asymmetrical C12C16) were kindly provided by the groups of Dr. U. Jonas and Dr. A. Terfort at the Max-Planck-Institute for Polymer Research and Hamburg University, respectively.

All samples have been prepared by immersion in solution. Prior to solution preparation, the laboratory glassware (Petri dishes, flasks…) is cleaned with an alkaline concentrate (Hellmanex II), to remove any possible contamination, and rinsed with deionised water. Special care is taken to use a set of recipients for each type of molecule.

Solutions in the micromolar (μM) range are prepared in two or three consecutive dilution steps of the corresponding molecule in ethanol and, to obtain an homogeneous solution, we keep them in a magnetic stirrer (1/2 hour is enough is most cases). For long molecules (C18 and C22) and disulphides, additional heating (50°C) while stirring the solution is necessary.

3.5.3 Island's Formation.

One of the outstanding features of this work is the use of submonolayer coverages, i.e. we have focused on the study of islands instead of complete monolayers. To obtain alkanethiol islands, the clean gold substrates are immersed in the corresponding alkanethiol solution for very short time periods (10-50 seconds) and subsequently rinsed with absolute ethanol and dried under N_2 stream, to remove any weakly adsorbed molecule. The use of μM concentrations is essential to avoid complete substrate coverage.

As a practical hint, if the surface is not wetted when rinsed with ethanol, it is probably due to the formation of a complete monolayer instead of alkanethiol islands coexisting with bare gold areas. In this case, the cleaning procedure is repeated, and the immersion time shortened to obtain a partially covered surface.

Sample preparation is performed under ambient conditions and afterwards, the samples are stored in individual cases, also at ambient laboratory conditions.

3.6 References.

[Alexander89] S. Alexander, L. Hellemans, O. Marti, J. Schneir, V. Elings, P. K. Hansma, M. Longmire, J. Gurley. "An atomic-resolution atomic-force microscope implemented using an optical lever" 1989 J. Appl. Phys. 65; 164.

[Binnig82] G. Binnig, H. Rohrer. "Scanning tunneling microscopy" 1982 Helv. Phys. Acta. 55; 726.

[Binnig86] G. Binnig, C. F. Quate, C. H. Gerber. "Atomic force microscope" 1986 Phys. Rev. Lett. 56; 930.

[Bushanbook] B. Bushan "Handbook of nanotechnology" 2004 Springer.

[Butt05] H.-J. Butt, B. Cappella, M. Kappl. "Force measurements with the atomic force microscope: technique, interpretation and applications" 2005 Surf. Sci. Rep. 59; 1.

[Cannara06] R. J. Cannara, M. Eglin, R. W. Carpick. "Lateral force calibration in atomic force microscopy: A new lateral force calibration method and general guidelines for optimization" 2006 Rev. Sci.Instrum. 77; 053701.

[Cappella99] B. Cappella, G. Dietler. "Force-distance curves by atomic force microscopy" 1999 Surf. Sci. Rep. 34; 1.

[Carpick97] R. W. Carpick, M. Salmeron " Scratching the Surface: Fundamental Investigations of Tribology with Atomic Force Microscopy" 1997 Chem. Rev. 97; 1163.

[Clifford05] C. A. Clifford, M. P. Seah "The determination of atomic force microscope cantilever spring constants via dimensional methods for nanomechanical analysis" 2005 Nanotechnology. 16; 1666.

[Colchero98] J. Colchero, A. Storch, M. Luna, J. Gómez-Herrero, A. M. Baró. "Observation of Liquid Neck Formation with Scanning Force Microscopy Techniques" 1998 Langmuir, 14; 2230.

[Dishner98] M. H. Dishner, M. M. Ivey, S. Gorer, J. C. Hemminger, F. J. Feher. "Preparation of gold thin films by epitaxial growth on mica and the effect of flame annealing" 1998 J. Vac. Sci. Technol. A 16; 3295.

[Gil03] A. Gil, J. Colchero, J. Gómez-Herrero, A. M. Baró "Electrostatic force gradient signal: resolution enhancement in electrostatic force microscopy and improved Kelvin probe microscopy" 2003 Nanotechnology 14; 332.

[Horcas07] I. Horcas, R. Fernández, J. M. Gómez-Rodríguez, J. Colchero, J. Gómez-Herrero, A. M. Baro "WSXM: A software for scanning probe microscopy and a tool for nanotechnology" 2007 Rev. Sci. Instrum. 78; 013705.

[Israelachvili92] J. Israelachvili. "Intermolecular and surface forces" 1992, Academic Press, London, England.

[Kolbe92] W. F. Kolbe, D. F. Ogletree, M. Salmeron. "Atomic force microscopy imaging of T4 bacteriophages on silicon substrates" 1992 Ultramicroscopy. 42-44; 1113.

[Legget05] G. J. Leggett, N. J. Brewer, K. S. L. Chong "Friction force microscopy: towards quantitative analysis of molecular organisation with nanometre spatial resolution" 2005 , Phys . Chem. Chem. Phys. 7; 1107.

[Loos05] J. Loos. "The art of SPM: Scanning Probe Microscopy in Material Science" 2005 Adv. Mater. 17; 1821

[Meyerbook] E. Meyer, H. J. Hug, R. Bennewitz. "Scanning Probe Microscopy. The lab on a tip" 2004, Springe-Verlag, Berlin, Germany.

[Meyer90] G. Meyer, N. M. Amer. "Optical-beam-deflection atomic force microscopy: The NaCl (001) surface" 1990 Appl. Phys. Lett. 56; 2100.

[Meyer90b] G. Meyer, N. M. Amer. "Simultaneous measurement of lateral and normal forces with an optical-beam-deflection atomic force microscope" 1990 Appl. Phys. Lett. 57; 2089.

[Moritabook] S. Morita, R. Wiesendanger, E. Meyer. "Noncontact Atomic Force Microscopy" 2002, NanoScience and Technology, Springe-Verlag, Berlin, Germany.

[Nanotec] Nanotec TM Electrónica; www.nanotec.es

[Sader03] J. E. Sader. "Susceptibility of atomic force microscope cantilevers to lateral forces" 2003 Rev. Sci. Instrum. 74; 2438.

[Sader03b] J. E. Sader, R. C. Sader. "Susceptibility of atomic force microscope cantilevers to lateral forces: Experimental verification" 2003 Appl. Phys. Lett. 83; 3195.

[Sarid94] D. Sarid. "Scanning Force Microscopy" 1994 2nd ed. Oxford University Press, New York.

[Stifter00] T. Stifter, O. Mart, B. Bhushan. "Theoretical investigation of the distance dependence of capillary and van der Waals forces in scanning force microscopy" 2000 Phys. Rev. B. 62; 13667.

[µmash] MikroMash AFM; http://www.spmtips.com/

CHAPTER 4.- STRUCTURALCHARACTERIZATION AND GROWTH AT SUBMONOLAYER COVERAGES.

From the extensive literature existing on the alkanethiol/Au(111) system, partially reviewed in chapter 2, two main conclusions can be drawn. Firstly, once the self-assembly process has concluded, the system exhibits very high crystalline order. Secondly, during the self-assembly process, factors such as the surrounding environment, the growth method, the coverage or the presence of defects play an important role in the formation and coexistence of intermediate configurations.

The preparation procedure described in section 3.5 has been scarcely employed and, prior to the work developed in our laboratory since 1998, there was not much information on the growth behaviour under these conditions. Particular experimental factors such as a slow adsorption process induced by the use of very dilute solutions and short immersion times, kinetic effects and out of equilibrium growth explain to a great extent the observation of alkanethiol configurations no reported before [Barrenathesis][Barrena01].

On the basis of this experience, in this chapter we have extended the investigation of the SAM growth to alkanethiol molecules of different length (C10, C12, C16, C18 and C22) as well as to symmetrical and asymmetrical dialkyl disulphide molecules. Our motivation for undertaking this study is twofold: firstly, to present a more general picture on the growth and self-assembling process of these molecules on the Au(111) surface; secondly, to provide a comprehensive structural characterization to correlate with the frictional and transport measurements presented in chapter 5 and 6.

At this point, we remark that any comparison of the results reported herein with those obtained under conditions involving in situ studies or ultrahigh vacuum preparation and continued exposure to a molecular flux must be made with care, since our sample preparation procedure involves ambient conditions where kinetic effects, the presence of water and out of equilibrium growth play an important role. However, we would like to highlight the interest of these close-to-practical-environmental conditions to provide useful information for applications of these SAMs.

To circumvent the differences in z-range needed to image complete gold grains (up to hundreds of nanometres) and molecular layers (1-3 nm thick), we have combined SFM topography and friction measurements. This is illustrated in figure 4.1 for a scanned area of $9\mu m^2$. In the topographic image, part (a), only the gold grain boundaries are resolved whereas the lateral force image, part (b), exhibits different contrast regions within each grain. Following the colour code (brighter = higher values for both, topography and friction), and being aware of the lubricant character of the alkanethiol molecules (see 2.3.1), a direct identification of the brighter areas with the bare gold terraces can be made in figure 4.1(b). Therefore, we use the lateral force imaging to easily distinguish the molecule-covered regions on large scale areas while height measurements are carried out on small-size topographic images. Lateral force imaging on even smaller areas is used to obtain lattice-resolve images as explained in section (3.4.1)

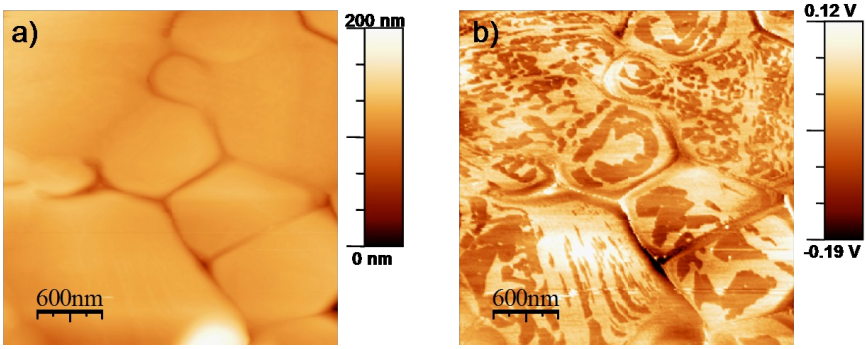

Figure 4.1 Simultaneous SFM (a) topographic and (b) lateral force images of C12 alkanethiol islands on Au(111), acquired at -2nN normal force. On large scanned areas, differences in friction between the organic configurations and the bare gold terraces provide an enhanced contrast in lateral force images rather than in topographic ones.

4.1 ALKANETHIOL ISLANDS.

Samples are routinely measured just after immersion of the gold substrate on the corresponding molecular solution. To minimize any possible damage of the molecular layer and also preserve the tip, the images are generally acquired at a negative load close to the pull-off force value.

4.1.1 Coexistence Of Different Configurations.

Lateral force images show in most cases three different regions, highlighted in figure 4.2: dark areas forming islands of diameters ranging from 30 to 150 nm (A), regions of intermediate friction surrounding the aforementioned islands (B) and brighter areas (C). As commented above, the brighter areas correspond to the bare gold regions. The darker areas, A and B, correspond to molecule-covered regions, described throughout this chapter.

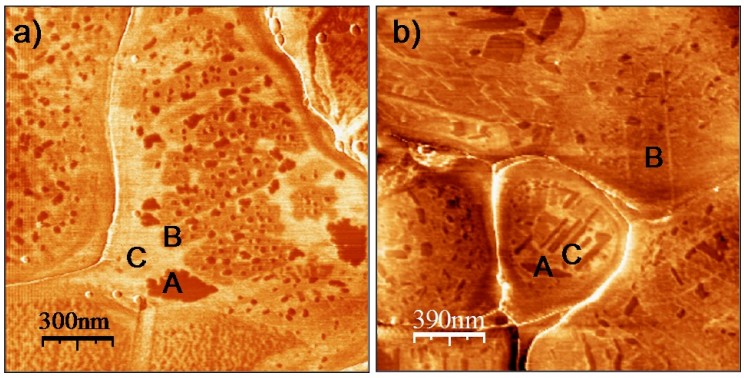

Figure 4.2 Lateral force images of freshly prepared (a) C10 and (b) C16 samples. A and B indicate areas covered by molecules, and C the bare gold regions.

When we decrease the scan size, the thiol-covered areas are also distingushied in topographic images as shown in figure 4.3 for a fresh C18 sample. The presence of bare gold areas allows to in situ measure the height of the different regions. It is important to keep the applied force as

close as possible to the pull-off force, to avoid film's compression and obtain accurate height values. In the case of figure 4.3, the applied load is -3nN and the adhesion force is -7nN (i.e. the total load is ~4nN)

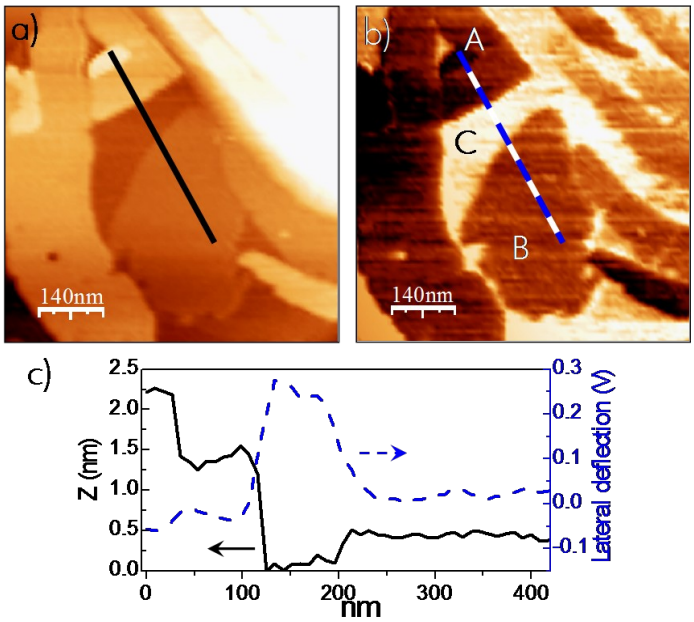

Figure 4.3 (a) Topography and (b) lateral force images of a C18 sample. (c) Line profiles crossing the different regions in both images. Total z-scale: (a) 0-6nm

The line profiles in (c) show that the regions with lowest friction signal, A, correspond in fact to islands of two different heights: 2.2±0.1nm and 1.5±0.3nm. The dashed profile shows that there is a noticeable difference in lateral force contrast between both islands, enough to be resolved in these small scan areas (the number of pixels is the same as in figure 4.2 but the area scanned is considerably smaller, leading to an enhanced resolution). This spontaneous formation of islands of two different heights was already reported for this molecule and ascribed to islands formed by standing up molecules with different tilt angles and different molecular structure (see section 2.2.3.b).

The area with intermediate friction signal, B, is 0.46±0.04nm thick, completely in agreement with the alkanethiol diameter (4.3 Å), thus indicating that we are dealing with molecules lying flat on the surface.

As pointed out in section 2.3.1, the differences in friction signal observed between the molecule-covered regions are related with structural or mechanical differences of the molecular packing, since the chemical nature of the molecules is the same within each region. The higher cohesive energy of the standing up configurations in fact yields mechanically more robust layers in which compression and creation of defects is hindered, and friction is reduced. Besides this, in the lying down configuration an additional contribution to friction exists, due to the CH_2 groups exposed at the layer surface. Lets assume the molecular backbone plane parallel to the substrate surface and both CH_2 and CH_3 contributions to friction to be similar. Because the distance between CH_2 groups

along the chain is substantially shorter than the distance spanned by the CH_3 groups in the standing up configurations (1.52 Å versus 4.99 Å for the hexagonal case), a larger number of end groups might interact with the SFM tip during sweeping on the lying configuration and, subsequently, higher friction is expected.

These arguments are indeed suitable to explain differences in friction among standing up configurations with different tilt angle: the larger the tilt angle is, the lower the cohesive energy and the greater the number of CH_2 groups exposed at the interface. In fact, the lying down configuration can be regarded as the limiting case of a tilted configuration.

This coexistence of configurations has been regularly obtained for all the molecules studied and remains stable upon air exposure during the first 24 hours after sample preparation (see section 4.1.4).

4.1.2 The Lying Down Configuration.

Figure 4.4(a) shows the topography of a C10 sample acquired at -4.8 nN. We again measure a height of ~4.5 Å for the thinner layer, indicating that the thickness of this configuration does not depend on the molecular length (consistent with the picture of lying down molecules). Interestingly, in the corresponding lateral force image it is possible to resolve a striped structure within this thin layer, with a periodicity of ~31.5 Å. By comparing with the lattice-resolved images measured on the same gold terrace (not shown), we find that these stripes run parallel to the next-nearest neighbour (NNN) direction of the underlying substrate.

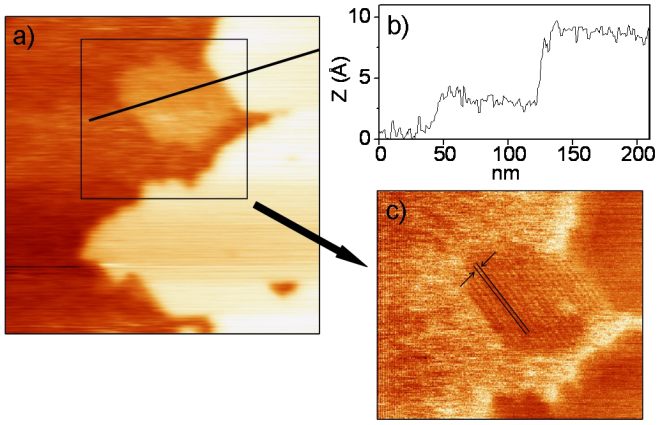

Figure 4.4 (a) Topographic image (250×250 nm^2) of C10 molecules in the standing up (brighter region) and lying flat (intermediate contrast) configurations. (b) Line profile crossing both molecular phases and (c) lateral force image corresponding to the area marked in (a), revealing the striped structure of the thin layer. The stripe periodicity is ~31.5 Å, twice the C10 length. Total z-scale: (a) 0-1.6nm.

From the description of the striped structures in section 2.2.3.a, we see that the measured periodicity of ~31.5 Å extraordinarily fits the (11×√3) striped configuration already reported for C10, which consists of flat lying molecules fully stretched perpendicular to the stripes in a head-to-head

arrangement (see figure 2.7) [Camillone94][Schreiber98][Yamada98][Toerker00][Poirier01] [Qian03]. This striped structure is often observed in STM measurements, yet this is the first time it has been resolved in scanning force microscope imaging.

However, this configuration with a periodicity equal to twice the molecular length was rarely observed under our experimental conditions. Conversely, in most of C10 and every C12, C16 and C18 samples where the striped pattern has been resolved, the measured periodicity differs from 2L. The goal of this section is the determination of the molecular configuration of this particular striped phase.

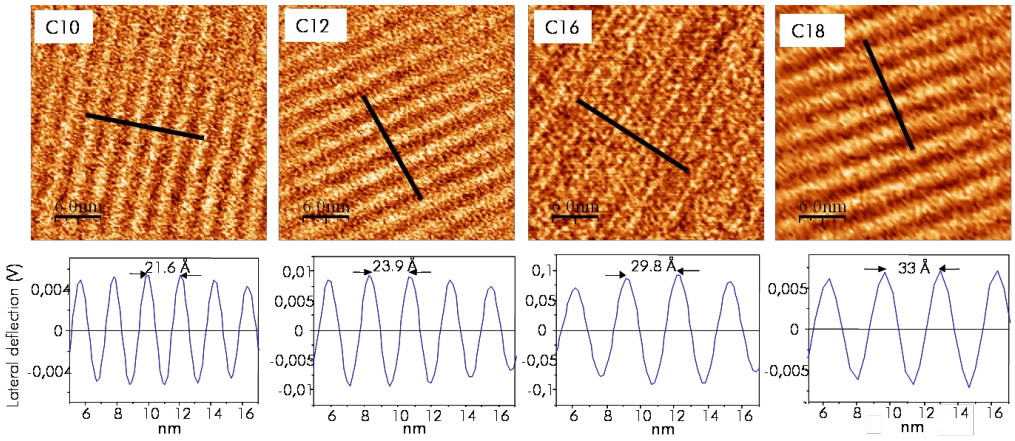

Figure 4.5 Top: small area lateral force images on the lying down molecules exhibiting the striped pattern for the different molecular lenghts. Bottom: lateral force line profiles, averaged over a minimum of 40 profiles, to measure the stripe periodicity.

Figure 4.5 shows a set of high magnification lateral force images (top) taken on top of the lying down configuration for different molecular lengths. Line profiles measured perpendicular to the stripes (bottom) give distances, d, of 21.6, 23.9, 29.8 and 33 Å for C10, C12, C16 and C18 respectively. Using the (p×√3) notation, they correspond to values of p= 7.5, 8.5, 10.5 and 11.5. In all cases the periodicity measured is lower than twice the corresponding molecular length, as shown in table 4.1, where different magnitudes of interest for the discussion below have been collected.

Table 4.1 Magnitudes listed for the molecules at the left column: twice the molecular length (2L), measured stripe periodicity (d), ratio between the measured periodicity and 2L (d/2L), reduced length (**ℓ**) and reduced periodicity (p) in terms of the lattice substrate parameter.

	2L (Å)	d (Å)	d/2L	ℓ (L/2.88 Å)	p (d/2.88 Å)
C10	31.5	21.6	0.68	5.5	7.5
C12	36.5	23.9	0.65	6.3	8.5
C14	–	–	–	–	9.5
C16	46.5	29.8	0.64	8	10.5
C18	51.5	33	0.64	9	11.5

4.1.2.a Comparison with reported striped models

As summarized in chapter 2, intermediate configurations with different striped periodicities have been reported for the Cn/Au(111) system. A comparison of our results with those found in the

literature is presented in figure 4.6, where the periodicity of the striped phases is plotted as a function of twice the corresponding molecular length. The upper line fits most of the existing data and corresponds to the lowest-density ordered phase reported up to now, in which the periodicity is equal to twice the chain length (d=2L).

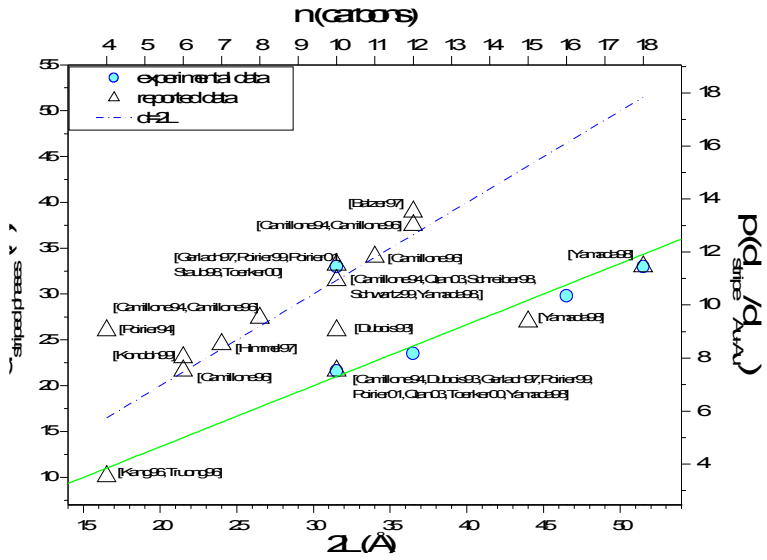

Figure 4.6 Stripe periodicity versus 2L for a series of different molecular lengths. Filled circles correspond to data reported in this work. Data taken from the literature is also shown (triangles) with the corresponding reference. The upper dashed line is the d=2L behaviour. The solid line at the bottom is the best fit to our data.

The data reported in this work for C10, C12, C16 and C18 also point to a linear relationship between the periodicity and 2L. The bottom line of figure 4.6 is the best fit (forced through the origin) to our experimental data which corresponds to d=0.649·(2L). A slope lower than 1 indicates that we are dealing with a configuration different from the fully stretched phase.

Interestingly, this line also fits other author's data (see references in the graph). Therefore, our fist attempt to determine the molecular arrangement within the stripe configuration of figure 4.5 has been the direct comparison between our experimental data and the already reported models.

These models are generally classified into two categories: those where the molecules lie in a prone position and those where the molecules are in a standing up configuration (figure 2.9 shows an example of each category).

The possibility of in situ measuring the thickness of the striped phase is a great advantage of our preparation procedure. The measured value, almost coincident with the van der Waals diameter of the alkanethiol molecule, rules out the picture of a configuration formed by upright molecules, like the one depicted in figure 2.9(c) for the striped configuration we observe. Within the first category, the out-of-plane interdigitation model of figure 2.9(b), though highly criticised, is the most widely cited to account for a measured periodicity lower than 2L. In this model, interdigitation is interpreted as a

consequence of saturation of the fully stretched phase due to increasing coverage. This saturation would make the lateral pressure exceed a threshold and induce the methyl termini of the molecules to slide between counter oriented chains out of the surface plane [Poirier01]. Consequently, the interdigitation model is intimately related with the reduction of available space to place the molecules fully stretched. This poses a severe inconvenience regarding the suitability of this model to describe the lying down configuration of figures 4.3, 4.4 and 4.5: with the low coverages achieved with our preparation procedure, neither saturation nor lateral pressure to induce the uprising of the molecules is expected. Moreover, this interdigitation model yields a layer thickness of ~8.6 Å if the overlapping molecule lies atop the molecule underneath or slightly thinner (~7.8 Å) if the overlapping molecule lies bridging two molecules underneath. In both cases, considerably higher than the height we measure.

Because the spontaneous assembly of alkanethiols substantially differs depending on substrate preparation or molecular film preparation procedure, other possibilities should be taken into account: is it plausible then, that a different striped phase might form under our particular experimental conditions?

4.1.2.b The herringbone model

We explore and suggest here that the short-striped phase reported in this work corresponds to a different out-of-equilibrium configuration, which does not necessarily stand in contradiction to other striped phases and reported models used to explain the alkanethiol phase diagram.

In this section we propose a new model that, besides satisfying the experimental findings (the measured periodicity as a function of the molecular length and the thickness of the layer) additionally leads to favourable van der Waals intermolecular distance, avoids steric effects and is compatible with the substrate symmetry.

Figure 4.7 depicts such a model for the four molecules studied (C10, C12, C16 and C18). In this model, the molecules are arranged in rows following a herringbone structure. To achieve the experimental periodicity while keeping the molecules lying flat parallel to the substrate plane, adjacent molecular axes are oriented at ±30° with respect to the direction of the stripes, thus forming the herringbone structure. The thiol chains lie parallel to a high-symmetry NN direction of the Au(111) substrate and, because of the lamellar angle, the distance between alkane chains remains close to the optimal thiol van der Waals distance (~4.3 Å). Each stripe comprises only one row of sulphur atoms, instead of the double row proposed in the interdigitation model, and following the notation for the striped phases the unit cell size is (p×2√3). This herringbone lamellar model is very similar to that proposed for weakly bounded systems as in the case of alkane-based molecules on graphite [Claypool97] and on Au(111) [Schwartz03].

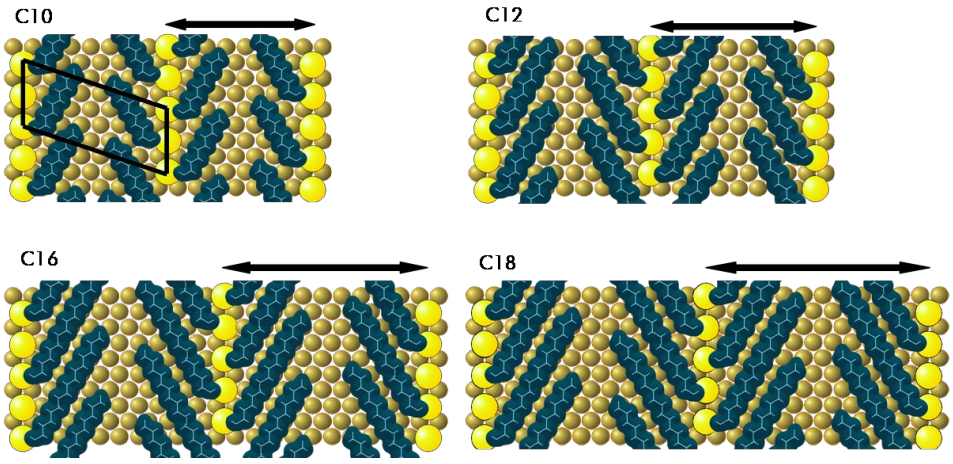

Figure 4.7 Schematic models to show the periodicity as a function of the chain length in the herringbone model described in the text. The chains are oriented at ±30° with respect to the direction of the stripes, running along a high-symmetry NN direction of the Au (111) substrate (small circles), to match the measured periodicity. Each stripe comprises one sulphur row (large circles) and the unit cell is (p×2√3).

Table 4.2 summarizes the packing areas corresponding to the 2L, interdigitation and herringbone models. The packing area of the model proposed in this section is even larger than that of the 2L model, which was the lowest-density ordered phase reported up to now.

Table 4.2 Packing areas (Å^2/molecule) for the different striped models discussed in the text.

	C10	C12	C16	C18
Herringbone	108	122	155	165
2L	83	97	126	140
~~Interdigitation~~	54	61	75	83

In section 4.1.4 we show that this lying down configuration spontaneously evolves with time, in air and without increasing coverage to the more stable upright phases, indicating that this stripe configuration is the result of molecular assembling in clearly out-of-equilibrium conditions. Undoubtedly, the bare substrate available in our samples facilitates the formation of this structure.

4.1.3 The Standing Up Configurations

As already shown in figure 4.3 for C18, islands of two different heights are found to coexist for all the alkanethiol molecules studied. Since islands of equal thickness situated on different adjacent terraces could give the misleading impression of having different heights, it is important to select the adequate substrate reference for each height measurement, otherwise the true island height will be enhanced or reduced by the additional contribution of the A(111) step height (2.35 Å). However, since islands tend to situate along the terrace edges, the choice of the correct substrate reference is not always a simple task. In order to obtain accurate height values sometimes we had to resort to sweeping the islands away with the SFM tip by imaging at high loads (> 20nN), leaving visible the

bare gold underneath. Afterwards we can easily identify the reference terrace for each island and obtain the true island's height.

Table 4.3 summarizes the height values found for the so-called tall and low islands, as a function of the chain length. We note that this is the first time that low islands have been observed for some molecules, namely C12 and C16.

Table 4.3 Islands' height (Å) as a function of the molecular length.

	C10	C12	C16	C18	C22
Tall island	13±1	16.2±0.5	20.1±0.8	22±1	26±1
Low island	10±1	12.1±0.4	14.5±0.7	16.5±0.9	20±1

Assuming that the molecules are in the all-trans configuration, we can calculate the molecular tilt angle within a particular island from the island's height and the corresponding molecular length. Independently of the length, the heights of the taller islands can all be fit with a tilt of ~30° and all the low islands' height corresponds to a ~50° tilt angle. As already reported for C18 molecules, the tall and low islands correspond to regions presenting the hexagonal and rectangular configurations respectively, described in chapter 2. To ascertain this, high resolution images were measured on top of each type of island.

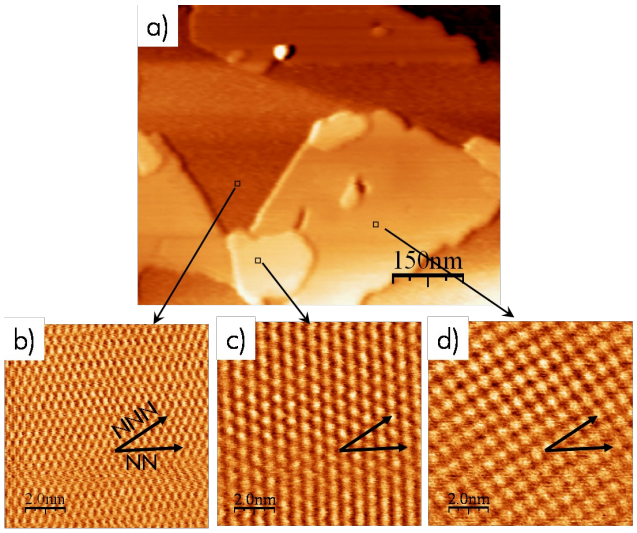

Figure 4.8 Top: SFM topographic image of a C16 partial monolayer, acquired at -5nN, showing the coexistence of islands of two different heights and the bare gold terrace. Bottom: high resolution images (10×10 nm^2) measured in each region showing (b) the hexagonal symmetry of the Au(111) substrate and the commensurate (c) (√3×√3)R30° structure on the tall island and (d) (2×√3) rectangular lattice on the low island. The NN and NNN directions of the gold substrate are indicated. Total z-scale in (a) 0-10nm.

Figure 4.8 presents the results obtained in a C16 sample. High-resolution images on the islands are acquired at relatively low loads (< 2nN) to avoid damage, whereas lattice-resolved images of the Au(111) surface are obtained after increasing the applied load to clean the surface from

possible ambient contaminants or weakly adsorbed molecules. Generally, forces beyond 10nN are used.

The results confirm that the tall island presents the hexagonal symmetry with a lattice parameter of 4.99 Å and rotated 30° with respect to the gold lattice and the low island show the rectangular symmetry with lattice parameters 4.99 Å and 5.8 Å along the NNN and NN directions of the gold substrate. We are dealing thus, with the (√3×√3)R30° and the (2×√3)rect structures, both commensurate with the underlying substrate.

Though less frequently than the rectangular structure shown in the previous figure, low islands of short molecules (C10 and C12) also present the rectangular structure displayed in figure 4.9. As for the (2×√3)rect lattice, the unit cell runs parallel to the NN and NNN directions of the Au(111), but it consists of pairs of rows along the NN direction, clearly visible in the 2D-Fourier transformed image. The distance between double rows is 11.4 Å while along the row we measure a periodicity of 4.99 Å, that is, √3 times the lattice parameter of the Au(111). It corresponds to a (4×√3)rect structure.

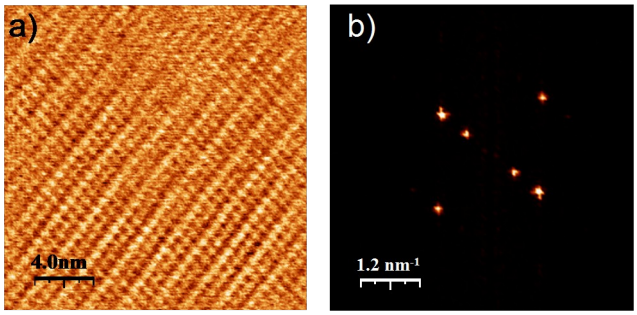

Figure 4.9 (a) Lattice-resolved image on a C12 island showing the (4×√3) rectangular periodicity. The pairs of rows are more clearly visible in the lower part of the image. (b) 2D-Fourier transformed image showing the double periodicity along one of the unit cell directions.

Figure 4.10 summarizes the standing up configurations that spontaneously form under our working conditions for chains containing 10, 12, 16, 18 and 22 carbon atoms. From the experimental data we have determined the molecular tilt, periodicity and relative orientation of the molecular structure with respect to the underlying gold, yet as in complete monolayers, the exact binding site of the sulphur atoms can not be inferred from the SFM images.

The hexagonal and (2×√3)rect configurations contain one molecule per unit cell. In the (4×√3)rect structure there are two molecules (1 and 2 in figure 4.10) per unit cell. The non-equivalence between molecules 1 and 2 is attributed to the existence of two different binding sites in this structure. This has been recently supported by STM high resolution imaging [Vericat05]. From the unit cell dimensions we obtain that the molecular packing area in both rectangular structures is the same, 28.7 $Å^2$/molecule, larger than in the close-packed hexagonal arrangement, 21.6 $Å^2$/molecule. The molecular coverage in the rectangular structures is therefore about 75% of the densest (√3×√3)R30° configuration.

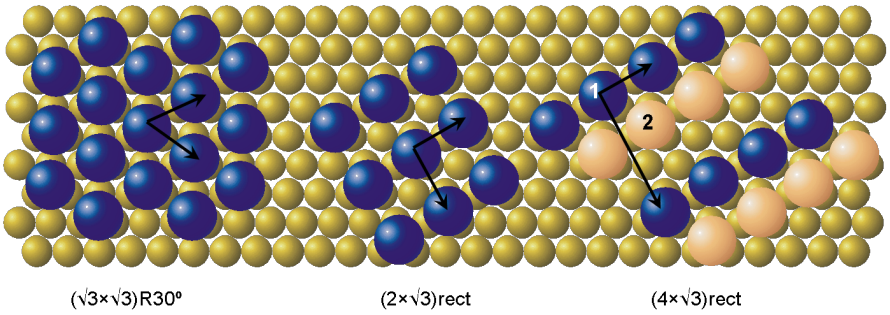

Figure 4.10 Schematic model showing the relative orientation and lattice structure of the standing up configurations observed. Gold atoms are represented by small circles and thiol molecules by large circles. In the (4×√3)rect model the different colours stand for non equivalent molecules (see text).

In Chapter 2 we describe the 3D geometrical model used in previous works to calculate the possible tilt configurations that spontaneously formed in C18 samples. In this model, optimal packing of the chains of adjacent molecules is sought, which imposes discrete values for the tilt angle dictated purely by the geometry of the molecule. As inferred from the description of the model (section 2.2.3.b), the results do not depend on the length of the molecule and so we can extrapolate what was obtained for C18 to the rest of the molecules used. Therefore, the (√3×√3)R30° structure observed is obtained for n=0 and m/2=1, which gives a total tilt angle of θ=35° along the molecular NNN direction. The (2×√3)rect structure is ascribed to a configuration with θ_X=41° and θ_Y=30° (n=1,m/2=1.5) which leads to the total tilt angle of 50° experimentally obtained. Moreover, the (4×√3)rect structure found for short chains is also described with this model, corresponding to the same (n,m/2) values as the (2×√3)rect configuration.

Due to the 2D hexagonal symmetry of both the substrate and the (√3×√3)R30° structure, in SFM images all the possible existing molecular domains are indistinguishable.[8] However, the different symmetry with respect to the substrate does allow distinguishing three possible rectangular domains of the six that can be formed depending on the tilt angle direction. In fact, islands presenting different rectangular domains have been observed coexisting in the same terrace. Yet, what is really interesting is that most of the islands formed following our preparation procedure are single domain islands.[9] From the SFM images shown in this work (which are representative of the numerous samples analyzed) it is thus evident that our procedure yields ordered domains larger in size (up to 800 nm) than those obtained in complete monolayers, even after annealing (~100 nm) [Fenter93][Camillone93].

This is a result of the kinetics of the self-assembly process: due to the low concentrations used in this work (μM), the number of nucleation sites is reduced and their average separation increased which, added to the molecular mobility, results in the formation of larger domains around these

[8] There are twelve domains of the hexagonal structure when the tilt angle direction is taken into account. But the SFM is "blind" to this direction.

[9] This has been confirmed by grazing incidence X-ray diffraction (GIXRD) measurements [BarrenaThesis].

nucleation sites, with all the molecules arranged within the same orientation. Moreover, the finite size of the islands facilitates the healing of defects such as vacancies, at the island's periphery. Consequently, large defect-free single domains are formed. Conversely, the high concentrations generally used to obtain complete monolayers (in the mM range), produce a higher density of nucleation sites followed by a faster growth. If neighbouring growing domains present different orientation, their juxtaposition results in smaller domain sizes.

Figure 4.11 clearly illustrates the difference in quality between one complete monolayer, grown after immersion in a 1mM C12 solution for 24 hours, and one island grown following our preparation procedure (immersion in a 1µM C12 solution for 30 seconds). The presence of defects such as domain boundaries and missing molecules is considerably greater in the complete monolayer, whereas the island forms an almost defect-free domain of 1.7μm of diameter.

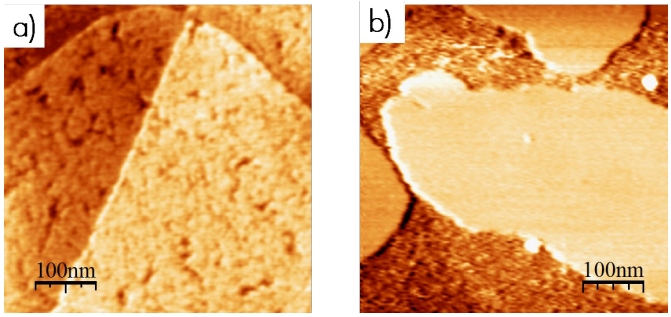

Figure 4.11 SFM topographic images (500×500 nm^2) of a C12 (a) monolayer and (b) island, acquired at 0.5 nN load. The monolayer presents a higher density of defects whereas the island is a defect-free single domain. Total z-scale: 0-1.5nm.

One of the few examples of multi-domain rectangular island we have observed is shown in figure 4.12(a), where we mark with a white arrow the boundary between the domains. When high resolution images are taken on this boundary region, two (2×√3)rect equivalent domains, rotated 30°, are resolved, (b). The schematic in (c) represents the most likely molecular order within both domains.

Though the overall sample coverage is below monolayer completion, in practice, the local coverage in grains like that shown in figure 4.12(a) is close to that of a complete monolayer, which increases the probability of island's coalescence with respect to less populated grains.

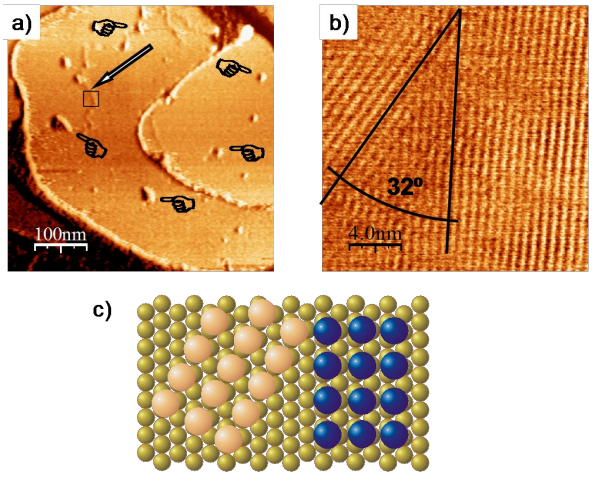

Figure 4.12 (a) Topographic image, at -2nN, of a C18 sample. The white arrow indicates the boundary between two rectangular domains. Pointing fingers have been drawn to highlight some defects within the island. (b) Lattice-resolved image in the area marked in (a) showing the coexistence of two (2×√3)rect domains, 30° rotated. (c) Schematic model showing the relative orientation of the rectangular domains in (b). Total z-scale: (a) 0-2.5nm.

Moreover, in these islands that completely cover the underlying terrace, the presence of defects (pointing fingers in the figure) can be considerably higher due to larger area-to-perimeter ratio and lack of bare substrate that hinder vacancy movement towards the island's periphery. Therefore, our preparation procedure has proved to be conducive to obtain SAMs of a high crystalline quality with large domain sizes. Large gold terraces, to ensure free space for island growth and molecular mobility, and low solution concentration are the key requisites.

From what has been shown in this section, at coverages under a full monolayer, alkanethiols spontaneously self-assemble into two types of upright but tilted configurations: the hexagonal (√3×√3)R30° structure characteristic of the complete monolayer, with the alkyl chains tilted ~30° from the vertical to the surface, and a rectangular (2×√3)rect structure with a molecular tilt of 50°. Additionally, for short molecules (C10 and C12), a (4×√3)rect structure is formed with similar tilt angle and molecular density than the (2×√3)rect configuration. In most cases, the whole island is a single domain, larger in size than those found in complete monolayers.

4.1.4 Time evolution: transition between configurations.

The results presented in the previous sections were mainly collected in fresh samples, measured within the first 24 hours after substrate immersion in solution. However, as stated several times, these systems are highly dynamic and molecular rearrangement plays an important role in determining the final film morphology and properties of the interface. In this section we address the study of the evolution with time of the configurations already described. To tackle this study, we

acquire images of the same area after substrate immersion and at time intervals of ~12 or ~24 hours.[10] In between, the tip is retracted to avoid tip or sample damage.

Figure 4.13 shows two examples measured for C16, just after sample immersion, (a) and (b), and 24 hours later, (a') and (b'). The applied loads are 1nN, -1nN, 0nN and 0nN respectively and the adhesion force is ~5nN. In both regions the area covered by the standing up islands has increased during these first 24 hours.

It is worth noting that, once the substrate is removed from the solution, the total coverage is fixed. Therefore this island growth can only be due to the aggregation of molecules already present on the gold surface. As will be shown in more detail, this is in fact what happens: the flat lying molecules in the striped configuration spontaneously evolve to the standing up phases. Besides this molecular aggregation, in some terraces the coalescence of islands is also observed.

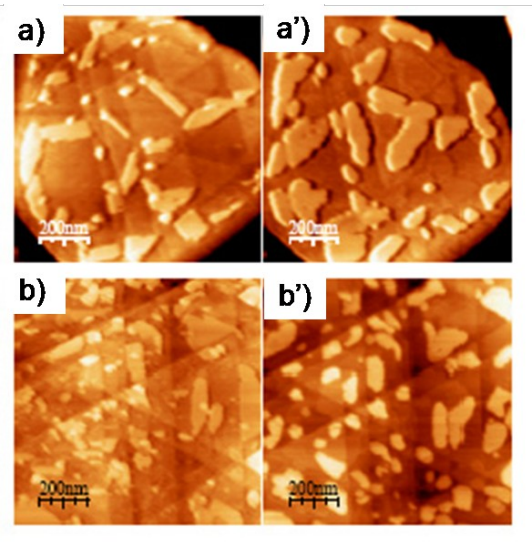

Figure 4.13 SFM topographic images (1×1 μm^2) of freshly prepared C16 samples, (a) and (b), and the same areas 24h after, (a') and (b'). The final size of the islands strongly depends on the width of the (111) gold terraces, separated by monoatomic steps, which present the typical triangular shape. Total z-scale: (a)-(a') 0-9nm; (b)-(b') 0-6nm.

Figure 4.13 also reveals that the final lateral size of the islands is limited by the width of the existing gold surface terraces. Interestingly, there is no mass transfer between terraces. As a result of the steps Erhlich-Shwoebel barrier, the molecules do not cross the substrate steps but remain at the same level. The diffusion and rearrangement process are therefore confined to the same terrace. This results in a non isotropic growth, with the islands mainly located at the upper substrate steps edge.

[10] The stability of our system allows measuring the same area for time periods up to several weeks with minimum drift corrections.

To better see the influence of the substrate morphology, graphs in figure 4.14 show the distributions and mean values of the islands' perimeter and area for the images of figure 4.13.[11] Just after substrate withdrawal from the solution, the distributions are quite similar and in fact, the mean diameter is almost equal in both regions, ~300nm. After 24 hours, we observe a different evolution of the parameters due to the difference in terrace sizes of each grain. In fact, the final mean diameter and area are only slightly larger than the initial ones in the grain with smaller terraces, (b), whereas in the grain with larger terraces the average island area has increased by an order of magnitude (a). This is because, in larger terraces, the total lying down population contributing to island's enlargement is higher.

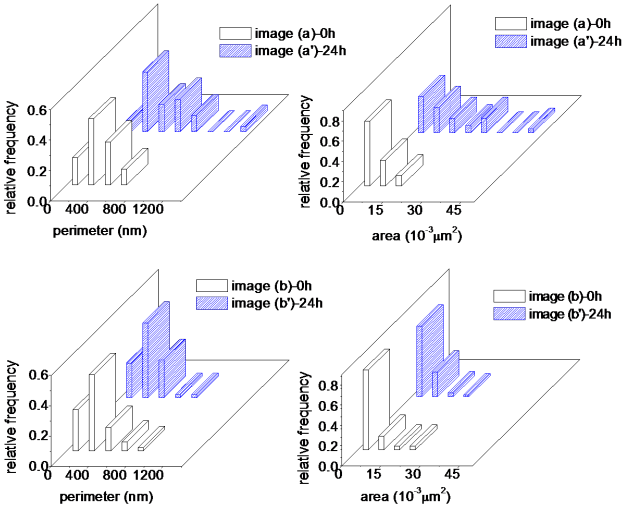

	image(a)-0h	Image(a')-24h	image(b)-0h	image(b')-24h
Mean perimeter (nm)	300±20	450±50	280±20	290±10
Mean area (nm^2)	(5.3±0.7)·10^3	(12±2) ·10^3	(4.6±0.3) ·10^3	(4.8±0.5) ·10^3

Figure 4.14 Top: Island's diameter and area distributions for the images of figure 4.13. Bottom: mean values of the above distributions.

From these distributions we have also calculated the increase in the total area covered by the islands within the first 24 hours: ~12% for the grain with larger terraces and ~2.5% for the grain with the smaller ones.

These calculations have been performed for numerous samples and in different grains within the same sample and, though the substrate morphology clearly influences the growth of the islands, a good estimation of the increase in the area covered by standing up molecules during the first 24 hours

[11] The calculation has been performed using two bitmap images converted from the original SFM topographic images. White (black) pixels indicate the points of the image above (below) a height threshold. To obtain the area covered by the islands, the height threshold is chosen slightly below the islands' height. Besides the total area covered by the white pixels, the WSxM software allows to calculate the area and diameter of each individual island.

is ~15%, which confirms the dynamic character of these systems also at ambient conditions and without increasing total coverage.

For times larger than 24 hours little changes are observed in the islands' size. However, the self-assembly process is not yet concluded. As already mentioned, the evolution with time, apart from the enlargement of the islands, resulted in molecular densification and improved order within the SAMs due to the healing of possible defects such as missing molecules, gauche defects….This ripening process might last up to several days and, though less eye-catching than the changes in island's size, influences the mechanical properties of the film and is responsible for their final high crystalline quality [Barrena99].

From images acquired in randomly chosen areas, we can ensure that this long-term reorganization process is not influenced by the sweeping action of the SFM tip, but is due to spontaneous molecular aggregation driven by van der Waals intermolecular interactions.

4.1.4.a Real time visualization.

To gain a deeper understanding on the time evolution of these systems, we have performed real time visualization of the reorganization process to in-situ follow the transition already mentioned, from the lying down to the standing up phase, responsible for the island's enlargement. Though phase transitions have been observed as a function of molecular coverage, i.e. versus immersion time [Yamada97][Xu98][Noh01], gas phase deposition time [Schreiber98][Schwartz99][Poirier99] [Poirier01] or thermal desorption by annealing [Nuzzo90][Toerker00][Qian03], methods as the present one thought to visualize phase transitions at fixed coverage might help in understanding the dynamics of the system in terms of the mobility of adsorbed molecules on the surface, the solvent effect and the conformational energies. Our method also constitutes a more convenient experiment to independently address the question of the time constant of the transition than experiments at variable coverage, where the interaction with molecules in the gas phase or solution, or the existence of different phase boundaries might complicate the study.

To attain our objectives we select an area in which, immediately after substrate withdrawal, the lying down and standing up configurations coexist, as shown in figure 4.15(a). The extremely flat surface of the grain allows distinguishing not only the islands but also the layer of flat molecules in the topographic image. However, to better follow the time evolution of the different configurations, lateral force imaging, rather than topographic imaging, is used due to the enhanced resolution afforded. Each image of figure 4.15(b) corresponds to a sequence of a SFM movie for C18 obtained by computer-aided monitoring the same area, at constant time intervals. In this particular case, the movie consisted of 477 frames, its total duration was 7h and 15min and the applied load was kept constant at 0nN to minimize the influence of the tip during the scans. Labels at the left top of the images indicate the time interval referred to the first image of the movie which is taken as t=0. The top and

bottom left images are considered as the initial and final states respectively, and the time evolution proceeds as indicated by the solid arrows.

It can be seen that regions initially covered by the striped structure, which present the intermediate friction contrast, decrease in lateral size whereas the islands formed by upright molecules and exhibiting lower friction, increase in lateral size. Brighter areas, once more, correspond to bare gold substrate. After 6h few changes can be detected in lateral force images, i.e. the process can be considered as nearly concluded.

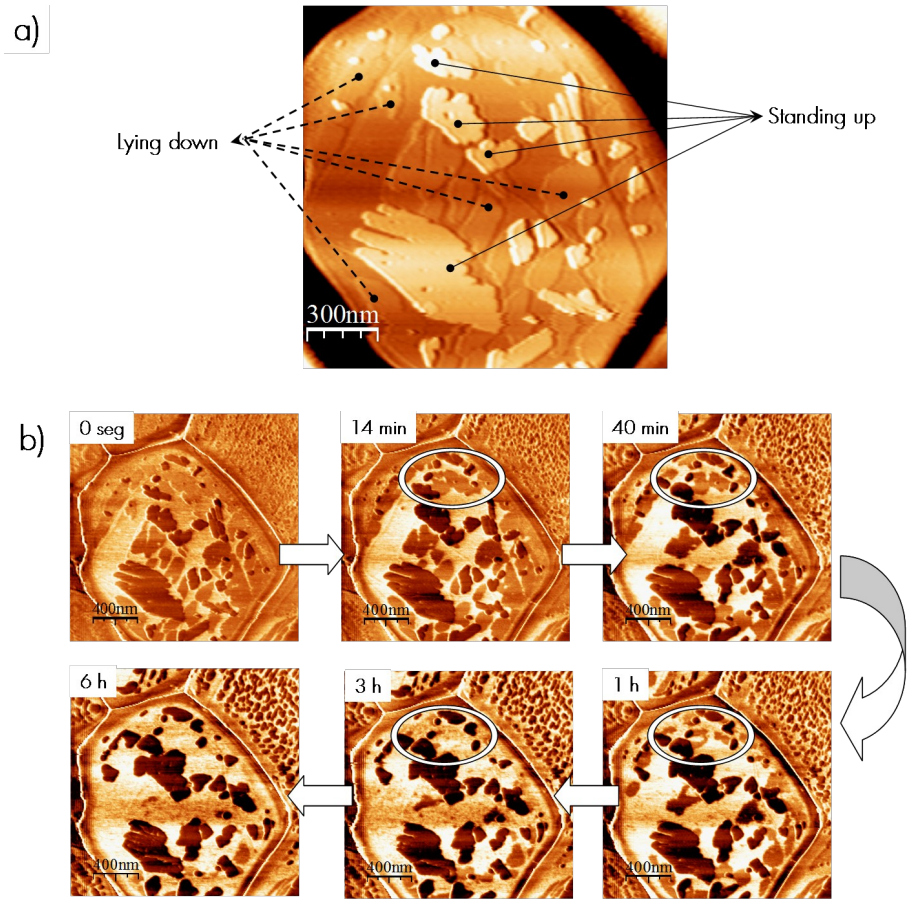

Figure 4.15 (a) Topographic image of a freshly prepared C18 sample showing the coexistence of standing up and lying down molecules. (b) Sequence of lateral force images (2×2 μm^2) of the grain in (a), extracted from a SFM movie. Labels indicate the time passed with respect to the first frame and time evolution is indicated by the large solid arrows. Specific locations on the sample have been marked to highlight the transition between the lying flat and standing upright phases.

Lateral force images at higher magnification are shown in figure 4.16, where we can clearly distinguish the three different regions (standing up and lying down molecules and bare gold). By comparing the top and bottom frames we clearly see that the central island enlarges at the expenses of the lying down phase surrounding it. But additionally, this sequence shows that during this conversion, the region initially covered by lying down molecules appears in the middle frame even brighter than the bare gold terraces, i.e. before adopting the upright configuration the molecules go through a transient state where a significant contribution to friction or energy dissipation exists. From the line

profiles we can compare the lateral deflection signals measured on the gold (≈ +150mV), the striped phase (≈ -50mV), the transient configuration (≈ +200mV) and the standing up phase (≈ -250mV). The corresponding topographic images (not shown) reveal that these transient regions have an intermediate film thickness between the lying down and the standing up configurations

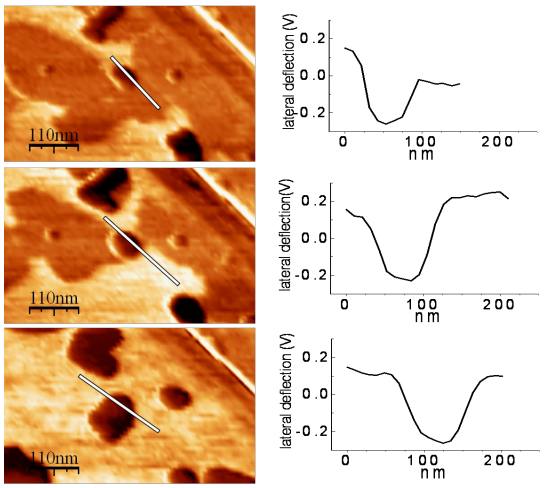

Figure 4.16 Sequence of lateral force images (time runs from top to bottom) for C18. The corresponding line profiles give the friction values for the gold substrate (150 mV), the standing up phase (-250 mV), the striped phase (-50 mV), and the transient configuration (220 mV). The latter is an intermediate molecular arrangement between striped and standing up configurations exhibiting the largest friction.

The process is further illustrated in figure 4.17 together with lattice-resolved images measured on the different regions. These latter images confirm the arrangement in the striped structure of the intermediate-contrast friction region and the final rectangular structure of the island. On areas where the transition is taking place no high resolution images can be obtained. They can only be discerned by a sudden increase in lateral force signal accompanied by intermediate film thickness.

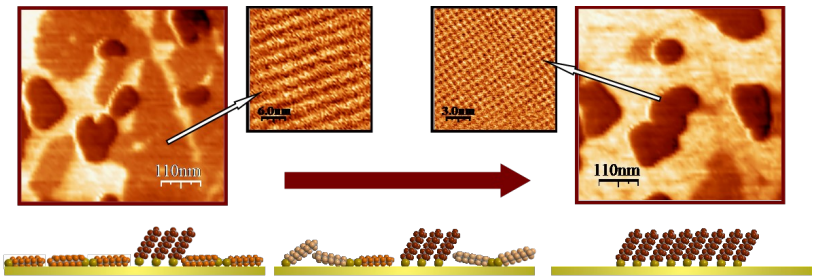

Figure 4.17 SFM images of the fresh (top left) and the few hours aged (top right) C18 sample with the corresponding high resolution lateral force images showing the molecular order within each region (top middle). The scheme (bottom) illustrates the phase transition between the (11.5×√3) and the (2×√3)rect configuration.

The nature of the molecular arrangement on these regions with friction larger than that of both ordered phases is thus understood as an intermediate disordered state in which the molecules are rising up to join the standing up molecules. This process yields a defective packing which facilitates the creation of gauche defects, vibrational modes, rotation of the molecular backbone…in summary, new

mechanisms for energy dissipation contributing to friction signal. This reorganization process is schematically shown in the lower part of figure 4.17: the ordered striped phase starts disordering because lying down molecules adopt a non planar configuration; finally they arrange and closely pack in a more stable standing up phase. This spontaneous transition indicates that, under our experimental conditions, the striped configuration is less stable than the dense close-packed configurations formed by upright molecules.

We have estimated to what extent the number of molecules is conserved as the lying down molecules aggregate to the standing up phase, by evaluating the change in area covered by both configurations.[12] Over a region of $0.3\mu m^2$ in the central part of the grain in figure 4.15 we obtain that the area covered by the islands has increased by ~15% from t=0 to t=6h. Given that the final packing area is 28.7 $Å^2$/molecule, the total number of C18 molecules aggregated to this phase is $(1.4\pm0.2)\cdot10^5$. Within the same area, and provided that from high resolution images we know that the molecules were initially arranged in the (11.5×√3) striped phase, with 165 $Å^2$/molecule, we estimate the decrease in the number of lying down molecules to be approximately $(1.0\pm0.2)\cdot10^5$. This otherwise simple calculation indicates that, within the experimental error, the number of molecules is conserved, confirming that the lying down molecules have joined the standing up phase.

Motivated by these results we put forward the following question: can we obtain from these real-time measurements the time constant of the lying down to standing up transition? And if so, how would it compare with the reported studies at variable coverage?

To answer the above question we have followed the time evolution of individual islands. Four different islands, marked in figure 4.18, with initial perimeters ranging from 170nm to 580nm have been chosen. Since island's growth occurs via molecular aggregation at the border sites, islands of regular shape have been selected to avoid any perimeter irregularities dependence. For time intervals of 1 minute (i.e. every frame of the movie) we have calculated their respective area. The graph shows the evolution of these areas normalized to the respective initial area, a_0.

[12] To calculate the area covered by the standing up molecules the procedure described in footnote (4) has been applied to the lateral force images. Instead of a height threshold we use a friction threshold, below (above) which all the pixels are white (black). By choosing the threshold value similar to the lateral signal of the islands, the area occupied by the white pixels corresponds to the area occupied by the standing up islands. To calculate the area covered by the lying down molecules we chose an upper and lower friction threshold, below and above the friction signal measured on the bare gold and the standing up configuration, respectively. The pixels within the defined interval correspond to the area covered by lying down molecules.

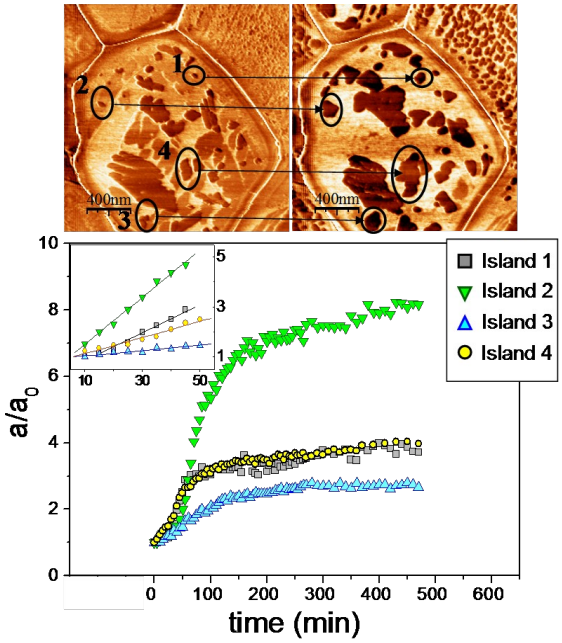

Figure 4.18 Top: First and last frame of the movie of figure 4.15 where we have highlighted the islands under study. Bottom: evolution with time of the islands' area normalized to the initial area. The slope at initial times (inset) gives conversion constant values of $5{\cdot}10^{-4}$, $10{\cdot}10^{-4}$, $1{\cdot}10^{-4}$, and $3{\cdot}10^{-4}$ s^{-1} for initial perimeters of 170 nm (■), 230 nm (▼), 460 nm (▲), and 580 nm (●), respectively.

All curves present a very similar shape, with a steep increase in the island's size during the first 90 minutes. Afterwards, the increase is much slower and an almost steady state is reached. Nonetheless, when comparing the initial and final areas one realizes that islands of similar initial perimeter (■,▼) can grow very differently, whereas islands of very different initial size (■,●) can exhibit a similar growth behaviour. The corresponding conversion constant for the lying down to standing up transition, obtained from the slope at initial times (see inset), shows that this rate indeed depends on the selected island. For the ones selected in figure 4.18 it varies between 10^{-3} and 10^{-4} s^{-1}.

Therefore, no straight relationship between the initial size and the island's growth rate can be inferred from the analysis of individual islands. Moreover, the question of a unique time constant for the transition is still unresolved.

In fact, these results were foreseeable from the images in figure 4.13. Although islands with larger perimeters have more disposable sites for molecular aggregation, the final size strongly depends on the substrate terrace where the particular island is located or, more precisely, on the presence of lying down population within the terrace.

How can we thus address the study of the kinetics of the transition? The solution is based on performing a global analysis, including all the islands present in a grain as a whole, instead of tracking individual islands. This will yield the average time constant of the process.

In order to do so, we have estimated the total number of molecules in the standing up configuration as a function of time, for time intervals of 1min, by calculating the area covered by the

standing up configuration (from two bitmaps converted images) and knowing the island packing density. To ensure accuracy, the calculation has been performed over a total surface area of 2.4 μm^2 avoiding the gold grain boundary regions. The result is plotted in figure 4.19.

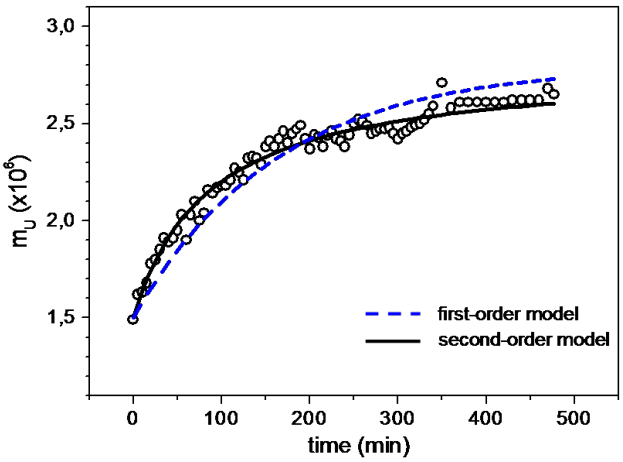

Figure 4.19 Total number of molecules in the upright configuration (m_U) as a function of time. Open symbols are the experimental data whereas the dotted and solid lines are the fits corresponding to the first and second order transitions described in the text.

To obtain the time constant of the transition, the data have been compared with reported kinetic models. The first model considered is the simple Langmuir kinetic model proposed in the early studies on the kinetics of SAMs growth. However, the true growth dynamic is now known to be more complicated, since some of the assumptions of the Langmuir growth, as no lateral interaction during molecular uptake, are not suitable to the self-assembling of alkanethiols. In order to consider such molecular interactions, a second-order Langmuir model has also been taken into account. For each model, the lying down to standing up transition can be sketched as follows:

$$Cn(\text{lying flat}) \rightarrow Cn(\text{transient}) \rightarrow Cn(\text{upright}) \quad \text{(i)}$$

$$2Cn(\text{lying flat}) \rightarrow 2Cn(\text{transient}) \rightarrow 2Cn(\text{upright}) \quad \text{(ii)}$$

Given that the surface coverage is kept constant, the total number of molecules, M, is

$$M = m_L(t) + m_U(t) + m_T(t) \quad (4.4)$$

that is, the population of the upright configuration (m_U) depends on the lying flat (m_L) and transient populations (m_T) at each time ($m_U(t) = M - [m_L(t) + m_T(t)]$), and the conversion rate will obey the following equations:

$$\frac{dm_U}{dt} = k_1[m_L(t) + m_T(t)] \quad \text{for case (i)} \tag{4.5}$$

$$\frac{dm_U}{dt} = k_2[m_L(t) + m_T(t)]^2 \quad \text{for case (ii)} \tag{4.6}$$

The respective solutions are:

$$m_U = M - \exp[-(k_1 t + D)] \quad \text{with } D = -\ln(M - m_{U0}) \tag{4.7}$$

and

$$m_U = M - \frac{1}{k_2 t + D} \quad \text{with } D = \frac{1}{M - m_{U0}} \tag{4.8}$$

where $m_U(t_0) = m_{U0}$ is the initial number of standing up molecules which is obtained from the first frame of the movie.

Both solutions have been used to fit the data in figure 4.19 and, as expected for a system in which the van der Waals interaction between chains plays a crucial role, the best fit is obtained with the second order model. This fit yields a time constant for the lying down to the standing up transition, $k_2 = 1.6 \cdot 10^{-4}\ s^{-1}$.

This result is indeed in good agreement with what was obtained from a combined He beam reflectivity and temperature programme desorption study that explores the energetics and kinetics of adsorption of a variety of alkanethiols onto Au(111) [Lavrich98]. That work addressed the chemisorption conversion from a steady-state physisorbed population to obtain the rate of conversion of the process (k between $3 \cdot 10^{-5}\ s^{-1}$ and $4 \cdot 10^{-4}\ s^{-1}$). The similarity between this value and ours makes us wonder about the nature of the molecule-substrate interaction within the striped configurations reported in this thesis. Based on this similarity and the high mobility exhibited by the lying down molecules, a physisorbed state which transforms to chemisorption during the uprising process is likely.

In short, by following the sample surface evolution with time, we observe an aggregation of the lying down molecules forming the striped phase to the standing up phases. This spontaneous transition, which takes place without coverage increase and under ambient conditions, indicates that this striped configuration is less stable than the dense close-packed configurations formed by upright

molecules and support the assertion that it belongs to configurations not present in the phase diagram of the alkanethiol/Au(111) system. Moreover, by combining lateral force measurements and real time scanning we present the first SFM study evidencing the order-disorder-order nature of the lying down to standing up transition, in which intermolecular interaction plays an essential role.

4.2 DIALKYL DISULPHIDE ISLANDS.

In this section we present the results obtained for samples prepared from two symmetrical (C12C12 and C16C16) and one asymmetrical (C12C16) dialkyl disulphide molecules, employing the preparation protocol of section 3.5. Though these molecules are in principle quite similar to the alkanethiol molecules, it has been reported that dialkyl disulphide monolayers exhibit subtle differences when compared with alkanethiol monolayers in terms of molecular order and packing efficiency. We are particularly interested in studying if similar structural differences are observed when working at submonolayer coverages. Furthermore, motivated by the work of Azehara and coworkers in which phase segregation was reported when the concentration of the disulphide solution was low (<10μM) [Azehara99], we have investigated the possibility of phase segregation for the case of the asymmetrical disulphides at low surface coverages.

4.2.1 The Lying Down Configuration.

Figure 4.20 shows the aspect of fresh C12C12 (a) and C12C16 (b) samples. Akin to what was obtained in alkanethiol samples, we observe standing up islands surrounded by a thinner molecular layer. In the corresponding lateral force images we only distinguish the edges of the gold terraces and some defects within the layer, i.e. the molecules cover most of the substrate and make it difficult to accurately determine the layer's thickness.

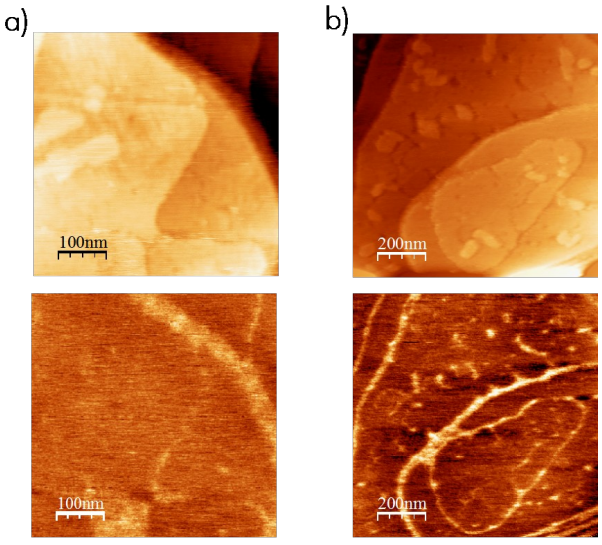

Figure 4.20 Simultaneous topographic (top) and lateral force (bottom) images of a fresh C12C12 (a) and C12C16 b) sample, acquired at -3nN and –1nN, respectively. Total z-scale: (a) 0-2nm; (b) 0-5nm.

Conversely to the alkanethiol samples, we have never resolved any ordered structure within this layer. Therefore, we can not ensure that the molecules surrounding the islands are lying flat on the surface. In fact, the high CSSC angle of the disulphide molecule (see chapter 2) is a sever impediment to placing the molecules in such a flat configuration. Moreover, the formation of the stripe phase requires molecular diffusion on the surface. Since the disulphide molecules are known to be less labile than their alkanethiol counterparts (see chapter 2), their diffusion rate might be considerable lower and consequently, the formation of the striped configuration more difficult.

As occurs in alkanethiol samples, with time and under ambient conditions, the molecules within the layer aggregate into the standing up islands within the next 48 hours after sample preparation.

4.2.2 The Standing Up Configurations.

Differences in the structural characteristics of the standing up configurations have been found for symmetrical and assymetrical disulphides.

4.2.2.a Symmetrical disulphides.

As shown in figure 4.21 for C12C12, islands of two different heights are also found in samples grown from symmetrical disulphides. Topographic profiles and lattice-resolved images confirm that they correspond to the hexagonal (√3×√3)R30° configuration with a 30° tilt and the 50°-tilted (2×√3)rect configuration. This similarity between the growth of alkanethiol and symmetrical disulphides is consistent with a picture in which the disulphide molecule eventually dissociates into two alkyl chains which behave independently on the Au(111) surface.

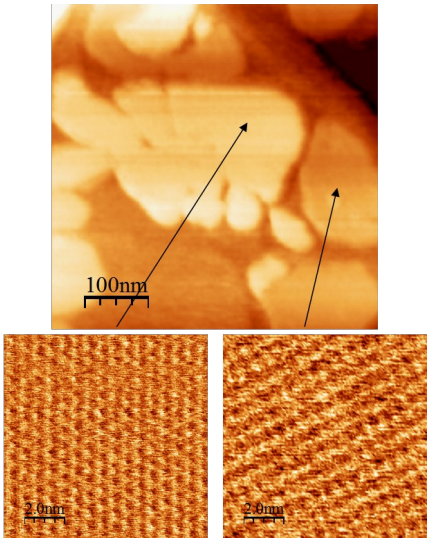

Figure 4.21 Top: topographic SFM image acquired at -6.5nN of a C12C12 sample. Islands of two different heights are observed. Bottom: lattice-resolved images (10×10 nm^2) showing the (√3×√3)R30° structure on the tall island and the (2×√3)rect configuration on the low island.

The structural analysis of the standing up configurations therefore shows that no significant differences are observed between symmetrical disulphide and its alkanethiol counterpart. At submonolayer coverages, both molecules arrange in the 30°- and 50°-tilted configurations.

4.2.2.b Asymmetrical disulphides.

Islands of standing up molecules are also observed in asymmetrical disulphide samples and attempts to obtain high resolution images succeeded in imaging the hexagonal (√3×√3)R30° lattice on every island analysed (figure 4.22). Therefore, though the formation of the rectangular structure can not be totally excluded, in these samples the hexagonal configuration is clearly favoured.

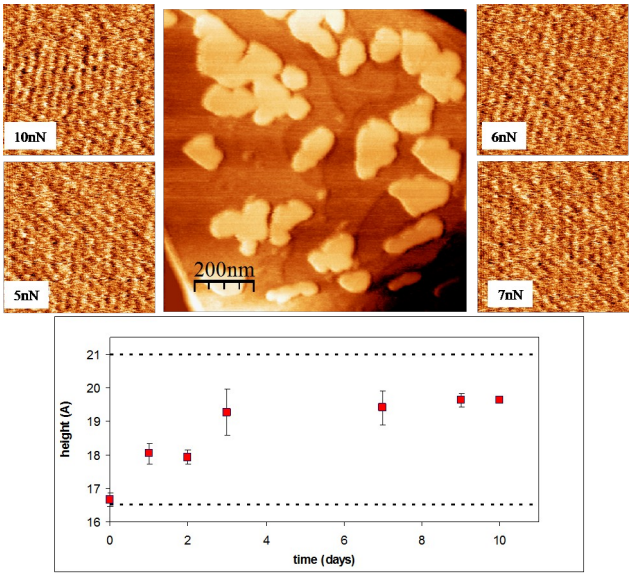

Figure 4.22 Top: SFM topographic image (middle) of a C12C16 sample acquired at -3.5nN. Total z-scale: 0-4nm. High-resolution images (sides) exhibit the hexagonal (√3×√3)R30° structure (10×10 nm^2). The labels indicate the load applied to obtain each image. Bottom: evolution with time of the measured height for the C12C16 islands. The lower and upper dashed lines represent the height of the C12 and C16 hexagonal island, respectively.

However, loads up to 10 nN were frequently necessary to obtain lattice-resolved images like those of figure 4.22 and when comparing with figure 4.8 or 4.9, it is clear that the contrast is considerably worse in these disulphide islands. Both effects (the requirement of higher loads to resolve the molecular structure and the contrast worsening) are probably caused by the existence of gauche defects at the end of the longer disulphide chain. As commented in chapter 2, these gauche defects at the end of the molecule are not energetically costly, but in asymmetrical disulphide samples are even easier to produce in the protruding part of the longer chains since the cohesion energy of these CH_2 groups is considerably lower due to the reduced number of neighbours. This is schematically shown in figure 4.23: due to the chain length difference, the easy distortion of the protruding part of the longer molecules yields a disordered outer SAM region which hinders the observation of molecular order at low loads. At higher applied loads, the SFM tip reaches the inner region where the crystalline packing

is preserved. This lack of order quality in the outer region is responsible for the general worsening of the image contrast in the lattice-resolve images of figure 4.22 (see section 3.4.1)

This result is indicative of the absence of length-chain phase separation in SAMs of asymmetrical disulphides when adsorbed on gold [Chen01][Nelles98] and therefore, mixed C12/C16 islands are formed under our working conditions.

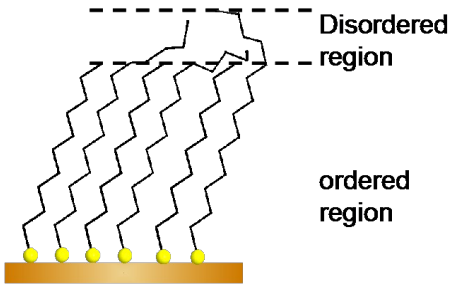

Figure 4.23 Schematic representation of the molecular conformation for a disulphide molecule with a chain length difference, n=4.

Heights measurements support this statement. We did not find islands of different heights, but we did find a remarkable variation of the height measured as a function of the time elapsed since sample preparation. The bottom graph in figure 4.22 shows the evolution of the experimental height, together with the height corresponding to C12 and C16 in the 30°-tilted configurations.

The variation of the measured height is related to the rearrangement process taking place within the islands. Though the applied force is always kept as close as possible to the pull off force when recording images for height measurements, in fresh samples the molecules might have not adopted the all-trans configuration and are more easily compressed, giving rise to lower heights values. Additionally, in mixed islands formed from chains of different lengths, the coadsorbed short chains separate the upper chain segments beyond their equilibrium van der Waals spacing and facilitates the bending and formation of gauche defects at these protruding parts (see figure 4.23). In these fresh islands the height measured is similar to that of a C12 island. After several days, the rearrangement and healing process is nearly concluded, increasing the islands' compactness and the measured height reaches a saturation value, close to that of a C16 island in the hexagonal configuration (this normally occurs ~3 days after sample preparation).

In these mixed monolayers it is often suggested that the free end of the longer molecule is lying down upon the surrounding short molecules, which is plausible in terms of van der Waals interaction (i.e. this configuration increases the cohesive energy of the protruding CH_2 groups, since they are closer to the CH_3-endgrups of the shorter chains). For C12C16, where the length difference is $\Delta n=4$ carbon atoms, in such a configuration only the CH_3 endgroup of the C16 molecules would lie atop the surrounding C12 molecules,[13] and though the outer part of the SAM still is poorly packed, at

[13] It can be assumed that the distance between the lying part of the longer molecule and the CH_3 engroup of the shorter ones is equal to the minimum van der Waals distance, d=4.3Å. Given that the distance between carbon atoms is 1.25 Å, at least the first three protruding CH_2 groups in the longer molecule are vertically oriented.

sufficiently low loads the final island's height (after the reorganization process is complete) approximates to that of a C16 island in the hexagonal configuration, as observed in the graph.

From the SFM data we have excluded phase segregation, i.e. the separate growth of C12 and C16 islands upon adsorption of the C12C16 molecules. Can we however rule out the existence of molecular aggregates of long molecules within the islands?

In these aggregates, the cohesive energy of the long molecule would locally increase when compared to the cohesive energy of the same molecule within a homogeneously mixed monolayer. To have an estimation of the profits in energy, we have calculated the cohesive energy for different configurations. We have extended the calculations to any Cn/C12 system, with $16 \leq n \leq 25$, to include the influence of the chain length difference. The three configurations considered are sketch out in figure 4.24: (i) the homogeneously mixed film in which, at a given distance, the selected long molecule (in black) is surrounded by an equal number of Cn (grey) and C12 (white) molecules; (ii) the formation of a 6-molecules aggregate, i.e. the nearest neighbours of the selected molecule are Cn molecules; (iii) the formation of a 12-molecule aggregates in which the nearest and next-nearest neighbours of the selected molecule are Cn molecules.

To calculate the cohesive energy of the black molecule for the three cases, we use pure van der Waals forces. Assuming additivity, the cohesive energy per molecule can be calculated by summing A/r^6 pair potentials between units of the chain and units in the rest of the film (section 2.2.5). The constant, A, is adjusted so that the computed total energy for a C18 chain in a perpendicular compact hexagonal packing equals the heat of sublimation for the corresponding saturated alkane molecule, which is 1.3 eV/molecule [Israelachvili92]. A value of 26 eVÅ^6 is obtained.

The sum has been performed in the following way. We consider the CH_2 group at position i along the selected chain and sum the A/r_{ik}^6 terms corresponding to all of the CH_2 units situated in a plane located k methylene units away from i (the sum converges for the first 100 neighbours within each plane). The contribution from all planes is then added to obtain E_i. Finally, the cohesive energy of the molecule is calculated by summing over the n CH_2 groups of the chain [Salmeron01]:

$$E_{chains}(n) = \sum_{i=0}^{n-1} E_i \qquad (5.9)$$

In the three configurations considered in figure 4.24, the contribution of the inner 12 planes is the same, corresponding to that of a plane with a close-packed hexagonal arrangement of CH_2 units. However, the contribution of the (n-12) outer planes is slightly different depending on the configuration, since only the CH_2 groups of the long molecules belong to these planes, i.e. those depicted in grey in figure 4.24. This means that, in case (i), the contribution from one of these planes is considered as half

the contribution of a plane with a hexagonal CH_2 close-packing arrangement. In case (ii) and (iii), where the molecule is surrounded by six or twelve Cn molecules, the cohesive energy from the outer planes is calculated from the sum of only the nearest six or twelve CH_2 groups, respectively (note that the contribution of a plane with a hexagonal compact packing of CH_2 groups reaches its saturation value only after summing over ~100 groups; therefore, the contribution of the (n-12) planes in the case (ii) and (iii) is considerably lower than expected in a complete monolayer of Cn molecules).

The bottom graph in figure 4.24 shows the results. Logically, the molecular cohesive energy in all cases is lower than in a close hexagonal packing of Cn molecules. But comparing the different configurations we find that the formation of aggregates is always favoured with respect to the intermixed scenario and that the energy difference increases as the length difference does. For the case we are studying, where Δn=4, the calculation indicates that the three possibilities are energetically similar, being 90% of the maximum cohesive energy for the randomly mixed island and 96%, when aggregates of only six molecules are formed.

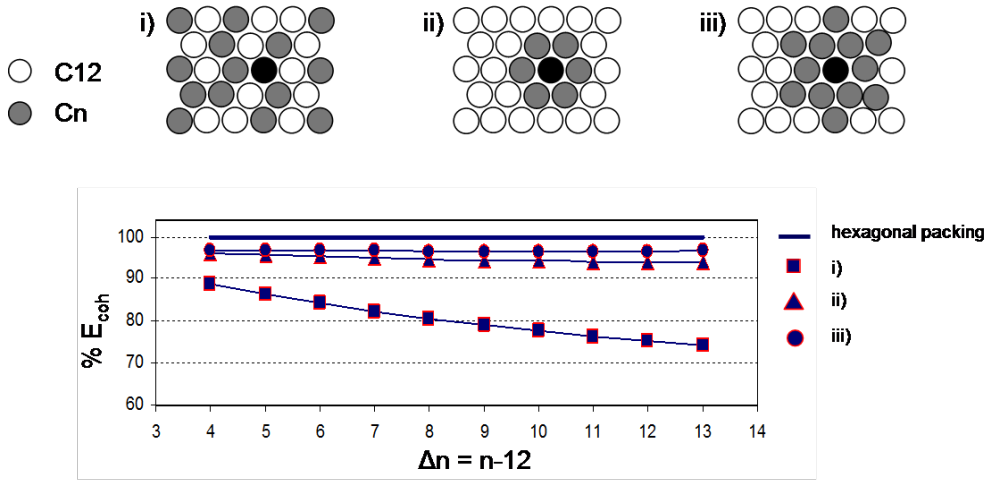

Figure 4.24 Top: models of the different Cn/C12 configurations studied. The black position highlights the selected molecule to perform the calculations (see text). Bottom: Relative cohesive energy per Cn molecule (with respect to the close hexagonal packing) as a function of the difference in the chain length, Δn, calculated for each configuration above depicted.

However, though we can not exclude the formation of small aggregates, not visible with the SFM, the growth of well mixed C12/C16 islands is not only a plausible alternative, given the above calculations, but also the most likely situation expected from a molecular dissociation during adsorption.

The reduction of the cohesive energy due to the difference in molecular length might explain the absence of the rectangular configuration within these islands. While in a film of 50°-tilted Cn thiol molecules the cohesive energy is still enough to provide phase stability, a similar tilt in mixed films would produce configurations highly unstable due to the additional reduction in cohesive energy caused by the difference in molecular length.

4.3 CONCLUSIONS.

Throughout this chapter we have shown the coexistence, for different chain lengths, C10, C12, C16, C18 and C22, of two type of upright configurations (30°- and 50°-tilted) and a striped phase of flat lying alkanethiol molecules. Our sample preparation method combined with both, topographic and lateral force SFM measurements, provides an advantageous choice for the study of these molecular structures. Their symmetry and relative orientation with respect to the gold substrate have been resolved by high resolution imaging and a real-space model for each structure has been proposed, based on the experimental data.

By following the surface evolution with time, we observe the aggregation of the lying down molecules to the standing-up phases. This spontaneous transition indicates that the striped configurations is less stable than the dense close-packed configurations formed by upright molecules and that consequently might not be present in the phase diagram of the alkanethiol/Au(111) system. Moreover, based on real time measurements, we can conclude that the observed transition consists of a molecular rearrangement process, which proceeds via an order-disorder-order transition in which intermolecular interaction plays an essential role.

The study of symmetrical disulphide samples yields results very similar to what is obtained in their respective single-component samples. The most significant difference is the absence of order in the molecular layer surrounding the islands that forms at the early stage of the growth, probably due to the greater steric constraints imposed by the S-S bond and a reduced molecular mobility.

In asymmetrical disulphides the most outstanding result is the absence of phase segregation. We can not exclude the formation of molecular aggregates small enough to be resolved with the SFM but, based on energetic calculations, it is plausible that homogeneously mixed C12/C16 islands are formed. The decrease in cohesive energy due to the presence of short and long molecules within the film hinders the formation of configurations with large tilt angles, which would reduce even more the intermolecular interaction. Only the hexagonal configuration is obtained.

4.4 REFERENCES.

[Azehara99] H. Azehara, S. Yoshimoto, H. Hokari, U. Akiba, I. Taniguchi, M. Fujihira. "Investigation of the structure of self-assembled monolayers of asymmetrical disulfides on Au(111) electrodes by electrochemical desorption" 1999 J. Electroanal. Chem. 473; 68.

[Barrena99] E. Barrena, C. Ocal, M. Salmeron "Evolution of the structure and mechanical stability of self-assembled alkanethiol islands on Au(111) due to diffusion and ripening" 1999 J. Chem. Phys. 111; 9797

[Barrena01] E. Barrena, C. Ocal, M. Salmeron "Structure and stability of tilted-chain phases of alkanethiols on Au(111)" 2001 J. Chem. Phys. 114; 4210.

[BarrenaThesis] E. Barrena ""Fricción y estructura molecular de películas de alcanosilanos y alcanotioles por debajo de la monocapa" 2001 Ph.D. Thesis.

[Balzer97] F. Balzer, R. Gerlach, G. Polanski, H.-G. Rubahn "Chain length dependence of the structure of alkane thiol films on Au(111)" 1997 Chem. Phys. Lett. 274; 1451.

[Biebuyck94] H. A. Biebuyck, C. D. Bain, G. M. Whitesides "Comparison of Organic Monolayers on Polycrystalline Gold Spontaneously Assembled from Solutions Containing Dialkyl Disulfides or Alkanethiols" 1994 Langmuir 10; 1825.

[Camillone93] N. Camillone, C.E.D. Chidsey, G.-Y. Liu, G. Scoles, "Superlattice structure at the surface of a monolayer of octadecanethiol self-assembled on Au(111)" 1993 J. Chem. Phys. 98; 3503.

[Camillone94] N. III Camillone, P. Eisenberger, T. Y. B. Leung, P. Schwartz, G. Scoles, G. E. Poirier, M. J. Tarlov " New monolayer phases of n-alkane thiols self-assembled on Au(ll1): Preparation, surface characterization, and imaging " 1994 J. Chem. Phys. 101;11031

[Camillone96] N. Camillone III, T. Y. B. Leung, P. Schwartz, P. Eisenberger, G. Scoles "Chain Length Dependence of the Striped Phases of Alkanethiol Monolayers Self-Assembled on Au(111): An Atomic Beam Diffraction Study" 1996 Langmuir 12; 2737.

[Claypool97] C. L. Claypool, F. Faglioni, W. A. Goddard III, H. B. Gray, N. S. Lewis, R. A. Marcus "Source of Image Contrast in STM Images of Functionalized Alkanes on Graphite: A Systematic Functional Group Approach" 1997 J. Phys. Chem. B 101; 5978.

[Dubois93] L. H. Dubois, B. R. Zegarski, R. G. Nuzzo "Molecular ordering of organosulfur compounds on Au(111) and Au(100): Adsorption from solution and in ultrahigh vacuum" 1993 J. Chem. Phys. 98; 678.

[Fenter93] P. Fenter, P. Eisenberger, K.S. Liang "Chain-Length Dependence of the Structures and Phases of $CH_3(CH_2)_{n-1}SH$ Self-assembled on Au(111)" 1993 Phys. Rev. Lett. 70; 2447.

[Gerlach97] R. Gerlach, G. Polanski, H.-G. Rubahn "Structural manipulation of ultrathin organic films on metal surfaces: the case of decanethiol/Au (111)" 1997 Appl. Phys. A 65; 375.

[Haehner93] G. Haehner, C. Woell, M. Buck, M. Grunze "Investigation of intermediate steps in the self-assembly of n-alkanethiols on gold surfaces by soft x-ray spectroscopy" 1993 Langmuir 9;1955.

[Heister99] K. Heister, D. L. Allara, K. Bahnck, S. Frey, M. Zharnikov, M. Grunze "Deviations from 1:1 Compositions in Self-Assembled Monolayers Formed from Adsorption of Asymmetric Dialkyl Disulfides on Gold" 1999 Langmuir 15; 5440.

[Himmel97] H.-J. Himmel, Ch. Wöll, R. Gerlach, G. Polanski, H. G. Rubahn "Structure of Heptanethiolate Monolayers on Au(111): Adsorption from Solution vs Vapor Deposition" 1997 Langmuir13; 602.

[Israelachvili92] J. Israelachvili "Intermolecular and surface forces" 1992, Academic Press, London, England.

[Kang96] J. Kang, P. A. Rowntree "Molecularly Resolved Surface Superstructures of Self-Assembled Butanethiol Monolayers on Gold" 1996 Langmuir 12; 2813.

[Kondoh99] H. Kondoh, C. Kodama, H. Sumida, H. Nozoye "Molecular processes of adsorption and desorption of alkanethiol monolayers on Au(111)" 1999 J. Chem. Phys.111;1175.

[Lavrich98] D. J. Lavrich, S. M. Wetterer, S. L. Bernasek, G. Scoles "Physisorption and Chemisorption of Alkanethiols and Alkyl Sulfides on Au(111)" 1998 J. Phys. Chem. B. 102; 3456.

[Nelles98] G. Nelles, H. Schönherr, G. J. Vancso, H.-J. Butt "Monolayers of asymmetrical diethylalkanoat disulfides on gold(111): the influence of chain length difference on atomic force microscope images" 1998 Appl. Phys. A 66; S1261.

[Noh00] J. Noh, M. Hara "Nanoscopic Evidence for Dissociative Adsorption of Asymmetric Disulfide Self-Assembled Monolayers on Au(111)" 2000 Langmuir. 16; 2045.

[Noh01] J. Noh, M. Hara "Molecular-scale growth processes of alkanethiol self-assembled monolayers on Au(111)" 2001 RIKEN review 38; 49.

[Nuzzo90] R.G. Nuzzo, E. M. Korenic, L.H. Dubois "Studies of the temperature-dependent phase behavior of long chain n-alkyl thiol monolayers on gold" 1990 J. Chem. Phys. 93; 767.

[Poirier94] G. E. Poirier, M. J. Tarlov "The c(4X2) Superlattice of n-Alkanethiol Monolayers Self-Assembled on Au(111)" 1994 Langmuir 10; 2853.

[Poirier99] G. E. Poirier "Coverage-Dependent Phases and Phase Stability of Decanethiol on Au(111)" 1999 Langmuir 15, 1167.

[Poirier01] G. E. Poirier, W. P. Fitts, J. M. White "Two-Dimensional Phase Diagram of Decanethiol on Au(111)" 2001 Langmuir 17; 1176.

[Qian03] Y. Qian, G. Yang, J. Yu, T. A. Jung, G-Y. Liu "Structures of Annealed Decanethiol Self-Assembled Monolayers on Au(111): an Ultrahigh Vacuum Scanning Tunneling Microscopy Study" 2003 Langmuir 19; 6056.

[Salmeron01] M. Salmeron "Generation of defects in model lubricant monolayers and their contribution to energy dissipation in friction" 2001 Trib. Lett. 10; 69.

[Schreiber98] F. Schreiber, A. Eberhardt, P. Schwartz, S. M. Wetterer, D. J. Lavrich, L. Berman, P. Fenter, P. Eisenberger, G. Scoles "Adsorption mechanisms, structures, and growth regimes of an archetypal self-assembling system: Decanethiol on Au(111)" 1998 Phys.Rev. B. 57; 12476.

[Schwartz99] P. Schwartz, F. Schreiber, P. Eisenberger, G. Scoles "Growth kinetics of decanethiol monolayers self-assembled on Au(111) by molecular beam deposition: An atomic beam difraction study" 1999 Surf. Sci. 423; 208

[Schwartz03] P. V. Schwartz, D. J. Lavrich, G. Scoles " Overlayers of Long-Chain Organic Molecules Physisorbed on the Surface of Self-Assembled Monolayers of Alkylthiols on Au(111)" 2003 Langmuir 19; 4969.

[Staub98] R. Staub, M. Toerker, T. Fritz, T. Schmitz-Hübsch, F. Sellam, and K. Leo "Flat Lying Pin-Stripe Phase of Decanethiol Self-Assembled Monolayers on Au(111)" 1998 Langmuir 14; 6693.

[Toerker00] M. Toerker, R. Staub, T. Fritz, T. Schmitz-Hübsch, F. Sellam, K. Leo "Annealed decanethiol monolayers on Au(111) – intermediate phases between structures with high and low molecular surface density" 2000 Surf. Sci. 445; 100.

[Truong96] K. D. Truong, P. A. Rowntree "Formation of Self-Assembled Butanethiol Monolayers on Au Substrates: Spectroscopic Evidence for Highly Ordered Island Formation in Sub-Monolayer Films" 1996 J. Phys. Chem.100; 19917.

[Vericat05] C. Vericat, M. E. Vela, R. C. Salvarezza "Self-assembled monolayers of alkanethiols on Au(111): surface structures, defects and dynamics" 2005 Phys.Chem.Chem.Phys. 7; 3258.

[Xu98] S. Xu, S. J. N. Cruchon-Dupeyrat, J. C. Garno, G.-Y. Liu, G. K. Jennings, T.-H. Yong, P. E. Laibinis 1998 J. Chem. Phys. 108; 5002.

[Yamada97] R. Yamada, K. Uosaki "In Situ, Real Time Monitoring of the Self-Assembly Process of Decanethiol on Au(111) in Liquid Phase. A Scanning Tunneling Microscopy Investigation" 1997 Langmuir 13; 5218.

[Yamada98] R. Yamada, K. Uosaki "In Situ Scanning Tunneling Microscopy Observation of the Self-Assembly Process of Alkanethiols on Gold(111) in Solution" 1998 Langmuir 14; 855.

CHAPTER 5.- MECHANICAL STABILITY AND FRICTIONAL RESPONSE UNDER APPLIED PRESSURE.

SAMs are ideal systems in fundamental tribology research to gain additional insights into the molecular level details of interfacial contacts. Therefore, in this chapter we have used the SFM to evaluate the relationships between the mechanical and frictional properties of the SAMs islands and their local conformation and packing arrangement. Both, mechanical and frictional studies are performed as a function of the applied load and the structural characterization of the previous chapter is essential for the discussion of the results.

Firstly, we have tackled the study of the mechanical stability of the rectangular configuration which is aimed at understanding the role of the different interactions in the stability of this configuration, only observed at partial coverages. Interesting results have been found regarding the chain length influence.

In a second set of experiments we have addressed the study of the frictional characteristics. As reviewed in section 2.3.1, different works on friction in SAMs have been reported, but the vast majority has been performed in complete monolayers. The study at submonolayer coverages is indeed an interesting alternative: our preparation procedure, leading to the spontaneous formation of different configurations, is a suitable approach to study the relation between molecular arrangement and tribological properties. Moreover, the coexistence of the different configurations within the same sample offers an ideal scenario for in situ comparisons to be made. Based on this, we have undertaken the comparative frictional study of the rectangular and hexagonal configurations. The results are discussed in terms of the local packing environment of the film components and the pathways for energy dissipation encountered.

However, prior to these comparative studies, it is convenient to address separately the friction properties of each configuration. As already commented, for the hexagonal configuration there is an extensive reported characterization [Lio97][Lio97b][Li99][Qian03][Brewer04][Zuo05], including the studies performed in our group at submonolayer coverages [Barrena00]. However, the rectangular structure is devoid of such characterization, which has been carried out during this thesis and is presented in section 5.3.

We have also undertaken the frictional study of disulphide islands. The structural characterization presented in chapter 4 did not show significant differences in the assembly, at submonolayer coverages, of symmetrical disulphides and their alkanethiol conuterparts. However there are several works reporting a worsening in the crystalline order in disulphide monolayers [Bain89b] [Biebuyck94]. These differences between alkanethiol and disulphide monolayers might arise from a different relative orientation of the C-C-C plane of adjacent chains, a different sulphur binding site…in summary, features that can not be discerned in the SFM structural characterization of the previous chapter. However, these structural differences might influence the tribological properties of SAMs and this, in fact is the motivation for undertaking the comparative study of the frictional characteristics of

alkanethiol and disulphide samples. We have verified that friction measurements are indeed sensible to the packing differences in SAMs of alkanethiol and disulphide molecules.

Furthermore, asymmetrical dialkyl disulphide samples have been used to study the tribological properties in mixed SAMs. In friction studies on these type of SAMs, the attention has been basically focused on systems with similar molecular structure but different terminating groups [Kim99][Schönherr99][Brewer04b][Li05]. The differences found with respect to single-component monolayers were consequently ascribed to a mixture of chemical as well as structural variations. In this work we have isolated the structural contribution, eliminating the chemical effect by using mixed monolayers with the same endgroup facing the contact and different molecular lengths. These systems have seldom been investigated and, in all cases the approach used was based on the growth from a solution containing a mixture of the two different molecules [Barrena01][Zhang05][Zuo05]. Our approach (the use of asymmetrical disulphide) provides a more accurate control over surface composition (both molecules are incorporated with the same probability) and, as demonstrated in the previous chapter, avoids phase segregation yielding true homogeneously mixed SAMs down to the nanoscale.

In addition to the influence of the molecular structure on the frictional properties, the surrounding environment, that plays a critical role in the SAMs growth (see previous chapter), can also influence the tribological response of these systems. This is shown in the last part of the chapter, where we collect the results of the studies performed at low relative humidity. Though similar studies reported on complete monolayers show a negligible influence of the relative humidity on frictional characteristics of alkanethiol SAMs (due to the hydrophobic CH_3 endgroups) [Tian99][Li03][Qian03], submonolayer coverages have been found to offer some new and interesting features.

5.1 BASIC CONCEPTS ON THE STUDY OF FRICTION WITH SFM.

Before presenting the results we will concisely introduce the tribology science and the possible approaches to tackle these studies with SFM.

Tough it is not a common term, tribology is part of our daily life and deserves a few words in this chapter to introduce our and other's interest on it. Etymologically, it is derived from the Greek word *tribo* meaning "I rub" and conventionally, it is defined as the science and technology devoted to the study and, if possible, the understanding of the phenomena involved in the contact between two sliding materials, i.e. the phenomena involved in friction, lubrication and wear.

In particular, friction is the most familiar because it is essential in multiple daily tasks ranging from simple walking to the performance of complex modern machinery, and is also responsible for the lost of approximately 70% of the world energy. Fundamental understanding of tribological phenomena

is essential to reduce energy costs. However, this is not a simple task. For example, the frictional force is a combined effect arising from various physical phenomena: elasticity, adhesion, capillary forces, surface chemistry, phononic and electrostatic interactions, etc…leading to the conversion of kinetic energy into thermal heating and, depending on the experimental conditions, any of the above mechanisms can dominate. This remarks the importance of designing controlled experiments where only one of the contributions can be singled out and studied.

Going down in the scale, modern tribology can be divided into macrotribology, microtribology and nanotribology. The first one deals with large objects and do not take into consideration the structure of matter whereas nanotribology deals with friction at the level of individual atomic interactions.

The macrotribology basic law is the Amontons-Coulomb law stating that the friction force is proportional to the loading (normal) force:

$$F_F = \mu F_n \qquad (5.1)$$

where μ (the dimensionless friction coefficient) is independent of the "apparent" or macroscopic contact area (A) and the sliding velocity (v). This, otherwise surprising, lack of dependence upon the contact area is based on the fact that the roughness of surfaces at the micrometer scale and below causes the true contact area to be much smaller than the apparent one. As shown in figure 5.1, the true contact between the surfaces consists of a number of contacting asperities or protrusions. The mechanical properties of these small asperities can differ substantially from bulk properties.

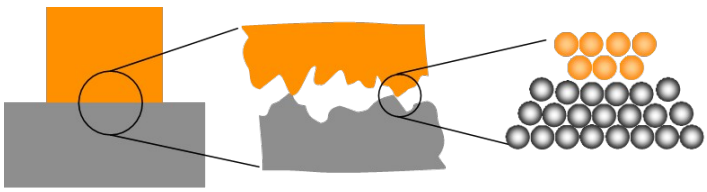

Figure 5.1 Schematic representation of the contact between two surfaces from a macroscopic (left), microscopic (middle) and nanoscopic (right) point of view.

At the microscale, the analogous to the Amontons-Coulomb law is the Bowden-Tabor relation written as:

$$F_F = \tau A_{true} \qquad (5.2)$$

where τ is the shear force and A_{true} is the contact area of a single asperity. It has been demonstrated that equation 5.1 can be reached from equation 5.2, when all the asperities that form the apparent contact area are considered [Greenwood66][Gnecco01]. Therefore, to understand tribological properties on the macroscopic scale it is helpful and even necessary to look into the microscale world.

Though equation 5.2 was introduced in the 1950s, it was not until the end of the 20th century that the tribology science approached the microscopic or even the atomic level in the study of the contacts themselves, thanks to the development of the quartz-crystal microbalance (QCM), the surface force apparatus (SFA) and the scanning force microscopy (SFM) techniques. In fact, the two latter can indeed mimic the behaviour of a single asperity contact, though large differences in the contact areas and pressures are found between both techniques. The radius of curvature of the non deformed surfaces in an SFA experiment is typically R=0.2-2cm, whereas SFM tips have radii of R=10-300nm. Within the load range that can be conveniently reached in the SFA, the maximum pressure in the contact area is usually less than 0.1GPa, whereas typical contact pressures in SFM experiments, even at low loads, are already several GPa. Therefore SFM allows exploring the mechanical response for a wider range of pressures, where not only elastic but plastic deformation can take place. The progress in tribological studies at the micro- and nanoscale has indeed shown a spectacular increase since the advent of this technique. Some of the most relevant results reported on this subject can be found in [Carpick97][Gnecco01][Leggett05].

5.1.1. Modelling A Single Asperity.

In scanning force microscopy, the tip acts as an isolated asperity where subnanonewton friction forces can be easily detected (see chapter 2), which renders it an ideal tool for the study of tribology at the micro/nanoscale. The main drawback stems from the determination of the contact area of the tip-sample system, A_{true} in equation 5.2. In general, the mechanics of the tip-sample contact in SFM are treated using continuum models, but there is no a universal processing approach. Figure 5.2(a) represents the area-load relation for the three most common approaches used.

The simplest one is to model the tip-sample contact as a sphere-plane contact and apply the Hertz model [Johnson85], in which the relation between the contact area and the applied load is given by:

$$A(F_n) = \pi\left(\frac{R \cdot F_n}{E^*}\right)^{\frac{2}{3}} \tag{5.3}$$

where R is the sphere radius and E* is an effective modulus related to the Young´s moduli (E) and the Poisson ratio (ν) of both sphere and plane materials by:

$$\frac{1}{E^*} = \frac{3}{4}\left(\frac{1-\nu_1^2}{E_1} + \frac{1-\nu_2^2}{E_2}\right) \tag{5.4}$$

The major restriction when using the Hertz model comes from the fact that it neglects any adhesion between contacting surfaces and assumes that there are no attractive forces acting between them: at zero external loads, the contact area, and hence the frictional force, reduces to zero (top panels of figure 5.2(b)).

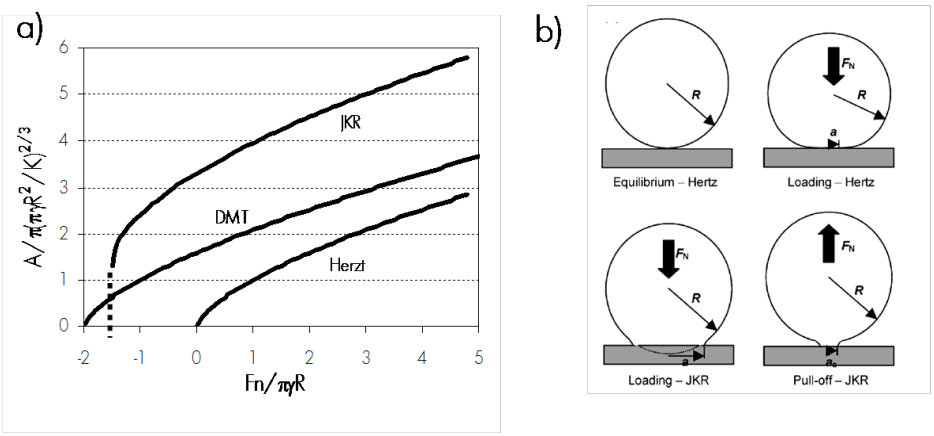

Figure 5.2 (a) Dimensionless area-load curves for the DMT and JKR model. Both curves approach the Hertz model when adhesion is not considered. (b) Schematic diagrams showing: a sphere on a flat surface at zero applied load, under Hertzian conditions (top left); deformation of a sphere under loading according to the Hertz model (top right); deformation of a sphere under loading according to JKR model (bottom left); the existence of a finite contact area immediately prior to separation of the sphere from the surface in the JKR model(bottom right) . From [Leggett05].

However, as explained in chapter 2, adhesion plays an important role especially when SFM measurements are not made under vacuum conditions. Adhesive interactions are incorporated in two other contact mechanics models: i) the Johnson, Kendall and Roberts (JKR) model [Johnson71] for the case of short-range adhesion between relatively soft materials and ii) the Derjaguin, Muller and Toporov (DMT) model [Derjaguin75] applicable to long-range interactions between materials of high modulus.

The contact area predicted by the JKR model is expressed as:

$$A = \pi\left(\frac{R}{E^*}\right)^{2/3}\left[F_n + 3\pi\gamma R + \sqrt{6\pi\gamma R F_n + (3\pi\gamma R)^2}\right]^{2/3} \qquad (5.5)$$

where $\gamma = \gamma_1 + \gamma_2 - \gamma_{12}$, being γ_1 and γ_2 the surface energies of tip and sample and γ_{12} the interfacial energy. This model predicts that a finite negative load is required to separate the surfaces, which is often referred as the critical load, F_c:

$$F_c = -\frac{3}{2}\pi\gamma R \qquad (5.6)$$

The pull-off force measured in force versus distance curves (section 3.3.1) is generally identified with this critical load. As shown in the lower panels of figure 5.2(b), at this load a finite contact area exists.

In the DMT model, the expression for the contact area is similar to the Hertz model except for an offset due to adhesion forces:

$$A = \pi\left(\frac{R}{E^*}\right)^{2/3}(F_n + F_{adh})^{2/3} \tag{5.7}$$

In this case, the critical force to separate both surfaces is higher than in the JKR model:

$$F_c = -2\pi\gamma R \tag{5.8}$$

These two models are, of course, limiting cases, and descriptions of intermediate situations between them are provided by Müller et al. [Müller80], Maugis [Maugis92] and Johnson and Greenwood [Johnson97]. Different works have proved the suitability of each of these models to reproduce the experimental data [Leggett05].

However, the uncertainty in the tip-sample contact area (not only due to the model used, but also to the uncertainties about tip radius or elastic constant of the materials involved) might introduce considerable errors when trying to compare absolute values of friction obtained with different SFM setups. To overcome this problem, we have taken advantages of our preparation procedure and relative rather than absolute frictional behaviour has been studied. The presence of the bare gold areas serves as an in situ reference for all the samples and, to be able to establish accurate comparisons, the same cantilever has been used for the whole data set presented in a given figure. Tip conditions have been checked prior and after each experiment by measuring the adhesion force.

5.2 MECHANICAL PROPERTIES.

Since friction studies involve investigations under applied load, knowing about the mechanical stability of our films under pressure is of crucial interest. Furthermore, this will allow us to situate and establish the working experimental conditions.

5.2.1 Mechanical stability of the rectangular configuration.

We have shown that two differently tilted structures (30° and 50°) are formed spontaneously by nucleation during growth for all the molecules studied. For C18, this structure is metastable and, when perturbed with the SFM tip, it converts irreversibly to the (√3×√3)R30° structure, i.e. when scanning at an applied load above a certain value (threshold value), the energy provided by the tip is

sufficient to disturb the molecular packing of the islands (via creation of vacancies, removal of molecules, etc...) and, after load release, the molecules rearrange in the lowest energy hexagonal phase [BarrenaThesis][Barrena01b].

As shown in figure 5.3, this tip-induced transition has been used to produce intentional marks on the islands by scanning an area (150×150 nm^2) at the threshold load (in this particular case, ~5nN). After decreasing the load (-1nN), the scanned area appears brighter, being the height difference ~6 Å, which corresponds to the difference between the tall and low C18 islands (see table 4.3). Once the transition has been induced, the initial rectangular structure is not recovered either with time or by further manipulation, the transition is not reversible. Since the (√3×√3)R30° is denser than the (2×√3)rect (21$Å^2$/molecule versus 28$Å^2$/molecule) after the transformation, vacancies are formed mainly at the periphery, but also inside the perturbed area. In addition, local deficiencies of ordering and probably a certain amount of molecules with conformational gauche defects within this area contribute to the worsening of the lattice resolved image measured on the mark. As explained in chapter 2, the SFM is not totally blind to these vacancies and whereas the rectangular periodicity in figure 5.3 is extraordinary well-defined, the hexagonal lattice appears slightly blurred with the stick-slip signal poorly defined.

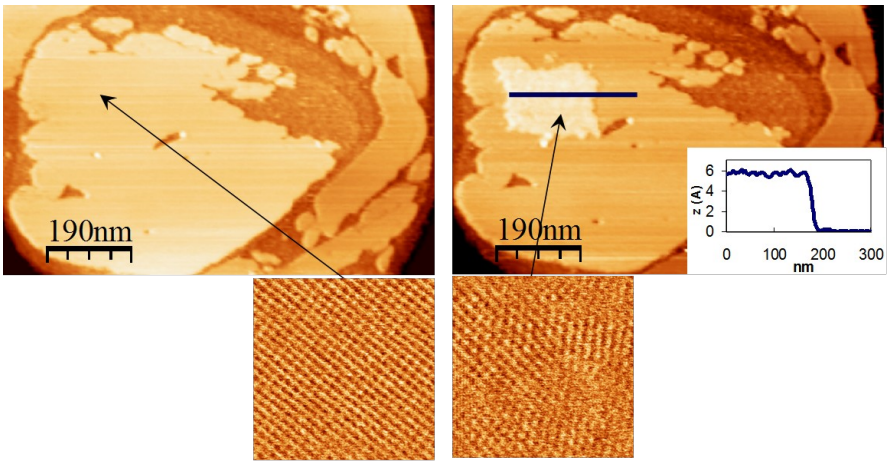

Figure 5.3 Top: topographic image of a C18 island before (left) and after (right) scanning at 5nN a 150×150 nm^2 region on the island. The inset corresponds to the profile in the right image Bottom: lattice-resolved images (15×15 nm^2) showing the rectangular (left) and hexagonal (right) configurations on the marked area. Total z-scale: 0-3.5nm.

The stability of any configuration adopted by these molecules depends on the balance between several interactions which includes the intermolecular interaction, but also the S-Au and molecule-substrate interactions. It is indisputable that a large tilt angle reduces the former. But it is also true that a large tilt angle increases the interaction of the molecules with the substrate.

Therefore, the lower stability of the (2×√3)rect configuration found in C18 islands is explained based on the decrease of the van der Waals contribution to the cohesive energy of the film since, because of a larger molecular tilt (50°), part of the molecule is no longer in contact with the

neighbouring CH_2 groups. However, for shorter chains, this lost of cohesive energy may be compensated with the gain in molecule-substrate interaction. How would this affect the stability of the rectangular configuration for these molecules?

To further investigate the differences in the relative stability of the rectangular structure as a function of the molecular chain length, we have studied two limiting cases: molecules longer than C18, where intermolecular interaction is expected to dominate the assembly, and molecules much shorter than C18, in which the substrate interaction competes with the interchain van der Waals stabilization, namely C22 and C10, respectively.

The mechanical stability of the rectangular configuration is tested following the same experimental protocol: (i) an area containing the rectangular configuration (50° tilted) is initially imaged at low load; (ii) the same area is scanned at a higher load; (iii) the possible induced changes are monitored by restoring the load to its initial low value. The procedure is repeated changing the load at step (ii) by small increments.

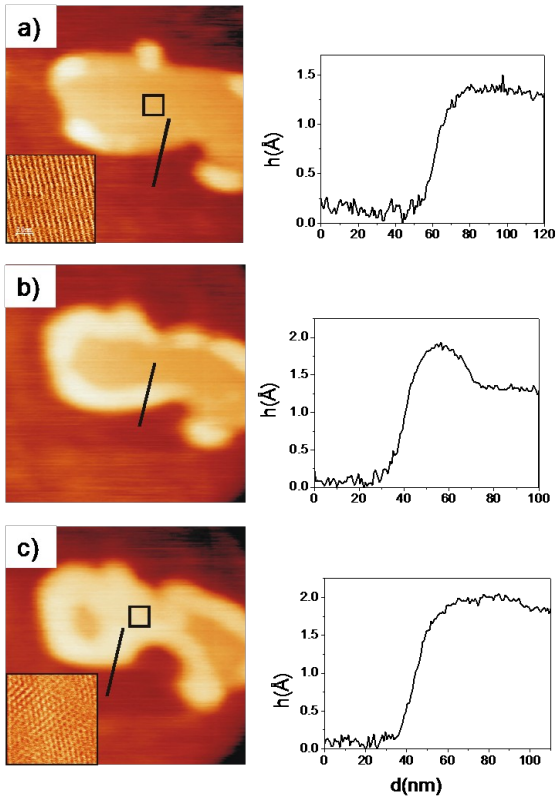

Figure 5.4 Left column: SFM topographic images (290×290 nm^2) of a C22 island (a) prior to increasing the load, (b) ater scanning slightly above the critical load (F=20nN) and (c) after scanning at higher load (F=30nN). All three images were acquired at F=0nN. Insets: high-resolution images (12×12 nm^2). Right column: line profiles showing the height changes.

Figure 5.4 depicts such experiments for C22. In this case, the low load at step (i) is 0nN and the load increment applied in step (ii) is 1nN. Only images obtained in step (iii), i.e. after load release, are shown to illustrate the induced changes. The image of figure 5.4(a) is the first image of the experiment (prior to any load increase) and shows a large island with the central part consisting of

molecules in the 50° tilted configuration. Note that at the edges, molecules in the 30° tilted configuration can be already seen (brighter in the images).

Up to 15nN, no appreciable changes were observed. However, after scanning at 20nN, regions near the rim acquire a height equal to that of the tall regions (part b). After the force is further increased in step (ii) to 30nN, most of the island exhibits a uniform height of ~21 Å (part c). High resolution images reveal that the molecules initially in the low regions, with a (2×√3)rect structure, are now ordered in the (√3×√3)R30° structure. The height changes are illustrated by the profiles in the topographic images.

This behaviour is similar to that found for C18 molecules. The transition requires the presence of free space for the molecules to rearrange, and thus it starts at the island periphery. The threshold pressure necessary to induce the transition is similar for both molecular lengths, but obviously varies depending on the degree of compactness of the islands. From our tip radius of 20nm (estimated by imaging a high aspect ratio conical feature of a calibration sample) and using equation 5.7 to calculate the contact area,[14] we estimate a threshold pressure of about 1GPa. After several days from sample preparation, the ripening process increases the film compactness due to the healing of defects inside the island. In those islands, the threshold pressure required to induce the transition is 1.5-2 times higher.

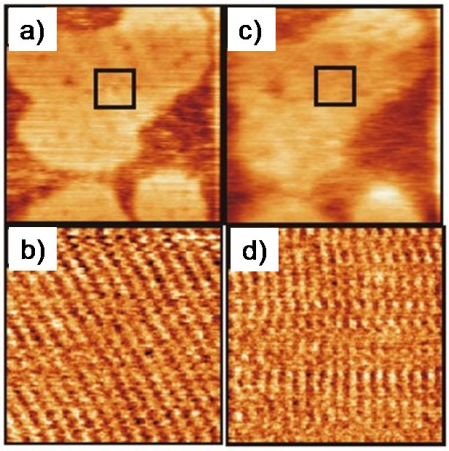

Figure 5.5 (a) SFM topographic image (225×225 nm^2) of a C10 island acquired at low load after scanning at (a) 8nN and (c) 16 nN. (b) and (d) are the respective high resolution images 9.5×9.5 nm^2.

The same experiment is performed with islands of C10 molecules in the 50° tilted configuration. The results differ completely from those described above for long molecules: no transition to the hexagonal structure is observed. Figure 5.5 presents a typical example, with images (a) and (b)

[14] The applied pressure is obtained dividing the total load (F_n + F_{adh}) by the contact area (A). To calculate A for our tip–SAM system, the respective Young'smoduli (E) and Poisson ratios (ν) are: E_{Si3N4} = 140 GPa and ν_{Si3N4} = 0.2, and E_{SAM}=10 GPa and ν_{SAM} = 0.33.

corresponding to the step (iii) after scanning, in this case, at a load of ~8nN and showing the (4×√3)rect periodicity. After increasing the load up to ~16nN, followed by load release, we obtain images (c) and (d). The island retains its original height and shape. However, close inspection by high resolution imaging reveals that structural changes have occurred. While the (4×√3)rect periodicity is maintained, the molecules have rearranged into an equivalent but different domain (60° rotated) of the same rectangular structure.

As for C18, the behaviour found for C10 and C22 molecules is understood as disturbing the cohesive packing when scanning at the threshold pressure. When the load is released, fast rearranging and reordering processes driven by the van der Waals interaction between molecules lead to molecular reassembling in a time-scale lower than the scanning time (seconds). But, as we have seen, while the long molecules (C18 and C22) reassemble in the hexagonal configuration, the short molecules (C10) reassemble once more in the rectangular configuration. Throughout this section we will see that this different behaviour is justified by the difference in energetic balance for each configuration as a function of the chain length.

Although the threshold pressure may vary from sample to sample, the energy dissipated during the process can be estimated (provided that both, the load and molecular density are known) by evaluating the work done by the tip and the number of molecules under the tip at the threshold load [BarrenaThesis]. The value obtained, ~0.4 eV per molecule, is of the order of magnitude of the chain packing cohesive energy and therefore sufficient to separate the close-packed molecules necessary to permit molecular rearrangement. In fact, it is also sufficient to induce changes in the adsorption site of the sulphur atoms at the interface (the corrugation energy of the Au(111) surface is 0.26eV [Yourdshahyan01]).

Before discussing this different behaviour found between short and long molecules, we present the results of the same study for symmetrical dialkyl disulphide molecules, which also arranged in the rectangular configuration at submonolayer coverages. Figure 5.6 correspond to a C16C16 sample. Though the surface coverage of this sample is unusually high, which could hinder accurate height measurements, high resolution images (not shown) prove that the molecules are in the rectangular 50°-tilted configuration. The image in (a) is acquired after scanning at low load, 0nN. After increasing the load up to 5nN and releasing it back to 0nN, regions near the edge of the upper terrace acquire a brighter contrast, image (b). High resolution images exhibit now the hexagonal arrangement of the 30°-tilted configuration on these brighter regions. The measured height difference, 5.6±0.1 Å, confirms the transition from the rectangular to the hexagonal structure at the terrace edges. If the load is further increased up to 10nN, all the molecules in the upper terrace reach a uniform height and the transition is complete, image (e).

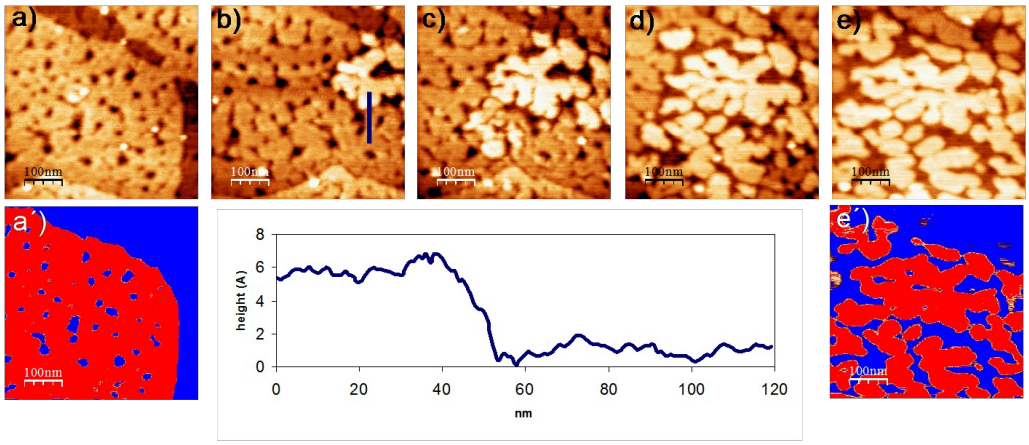

Figure 5.6 Top: SFM topography images (500×500 nm^2) of a C16C16 sample, at 0nN. (a) Image taken prior to the loading experiment. (b, c, d, e) Images acquired after scanning the same area at 5nN, 7nN, 9nN and 10nN, respectively. Bottom: (a´) and (e´) two bitmap images used to calculate the molecular coverage in (a) and (e) respectively. Middle graph: profile along the line marked in (b). Total z-scale: (a) 0-1.1nm; (b) 0-1.2nm; (c) 0-1.5nm; (d) 0-1.8nm; (e) 0-2.9nm

As expected from the different packing density of the configurations (~75%), when comparing the first and last images of figure 5.6 it can be seen that the area covered by molecules in the upper terrace has decreased, leaving more gold substrate visible in image (e). We have estimated both areas from their respective two-bitmap images and the results, 0.17±0.02 μm^2 in (a') and 0.13±0.01 μm^2 in (e'), definitively confirms the transition from the hexagonal to the rectangular configuration.

Though the overall behaviour is the same as in alkanethiol samples, the threshold load to induce the transition is always considerably lower in disulphide islands, being usually half of those found in alkanethiol islands. This can be attributed to the presence of a greater number of defects within the disulphide SAM that facilitates the rupture of the cohesive packing at lower pressures. A poorer packing was indeed reported for complete monolayers of symmetrical disulphides [Haehner93][Biebuyck94] and, from the above result, it is also found for submonolayer coverage. Well-packed islands might be more difficult to obtain, probably due to intermolecular steric interactions caused by the bulky disulphides.

We now resume the investigation of the different behaviour found for long and short molecules.

5.2.2. Van der Waals modelling

To understand the relative stability of the tilted configuration as the molecular length varies, we have performed energetic calculations based on a simple model. In this model, the alkane chains are represented by a linear array of spherical methylene units that lying in planes parallel to the gold substrate, as shown in figure 5.7(a). In the hexagonal configuration, we impose a tilt angle of 30° but neglect any possible variation that might exist as a function of the chain length. Within each plane, the 2D symmetry of the (√3×√3)R30° is imposed, with the CH_2 groups ordered in a hexagonal structure

with a lattice parameter of 4.99 Å. Since the distance between methylene units along the chain is 1.25 Å (projection of the C-C bond along the chain axis), the planes are separated by 1.25·cos30°=1.08 Å. Similarly, the 50° tilted rectangular configurations are described in terms of planes separated 0.88 Å with the CH_2 groups ordered in a 5.8 Å × 4.9 Å lattice (the 2D rectangular dimensions) within each plane. Since both configurations have the same tilt angle and molecular packing area, we have made no distinction between the (2×√3)rect and the (4×√3)rect structures.

The interactions to be considered are: (i) between chains, (ii) between chains and gold substrate and (iii) between sulphur and the Au(111) surface. Although of crucial importance for the assembling process, we can assume that the third term (covalent S-Au interaction) does not depend on the chain length and that few differences exist depending on possible deviations in the adsorption site. Therefore, we will not consider this term in the calculation, where only differences in energy are relevant.

As already done in section 4.2.2.b, to calculate the intermolecular interaction we use pure van der Waals forces, assuming additivity. In this case, the contribution of the n planes to the cohesive energy is the same, since all the molecules within an island have the same length. The difference between the hexagonal and rectangular configurations stems from the arrangement of the CH_2 units within each plane and from the distance between planes, which eventually leads to different contributions.

The energy is considered positive for attractive potentials, that is, the higher the energy is, the more stable the structure is.

The total van der Waals energy per molecule obtained in both configurations, hexagonal and rectangular, is represented in the top graph of figure 5.7(b). It shows that a tilt of the molecular axis considerably reduces the cohesive energy with respect to the perpendicular packing (e.g. for C18 we obtain 1.3 eV, 0.6 eV and 0.4 eV for the perpendicular, the 30°-tiled and the 50°-tilted configurations, respectively) and consequently, the cohesive energy due to the packing is always smaller for the 50° tilted (rectangular) than for the 30°-tilted (hexagonal) configuration. This was expected from the experiments above shown and can be intuitively understood on the basis of pure geometric arguments: although the chain to chain distance is the same in both configurations, the methylene groups located near the end of the chains have fewer nearest neighbours for the more tilted chains thus reducing the overall cohesive energy per molecule.

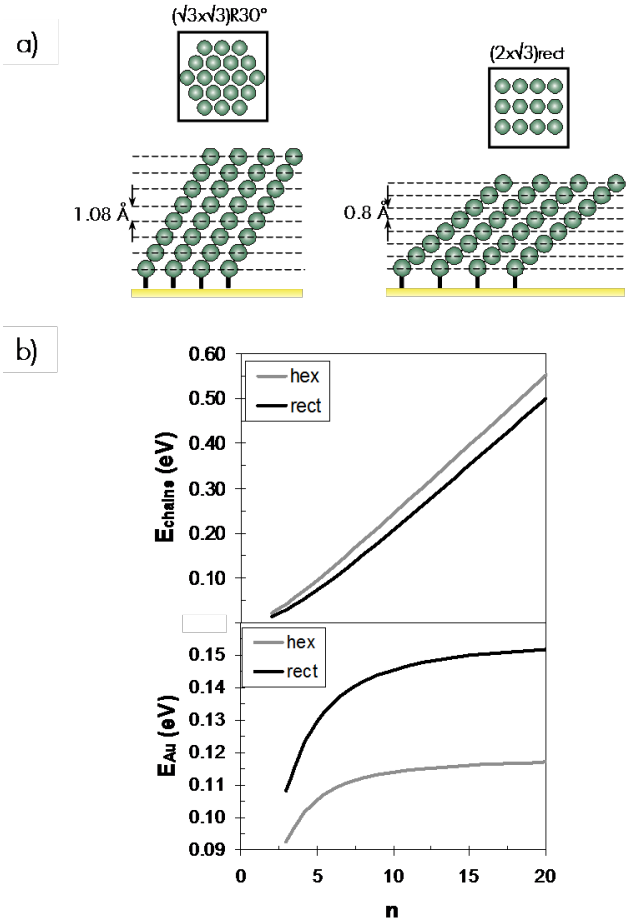

Figure 5.7 (a) Model used to calculate van der Waals energies. (b) Top graph: cohesive energy per molecule. Bottom graph: energy per molecule due to the interaction with the substrate (see text).

To estimate the second contribution considered, we focus the attention now on the interaction of each CH_2 group with the Au(111), which is also of van der Waals type. The value of the Hamaker constant should now be higher because one of the interacting bodies is a metal (high polarizability). The force will be stronger the closer the methylene unit is to the gold surface, that is, the larger the tilt angle is. This interaction between CH_2 groups and the gold can be described by the Lennard-Jones potential as proposed by Hautman and Klein [Hautman89], where the attractive term has been integrated over the substrate (a half-space). The resulting interaction of one CH_2 group with the Au(111) surface is:

$$U(z)_{Au} = \frac{-2413}{(z-0.86)^{12}} + \frac{1.47}{(z-0.86)^{3}} \qquad (5.9)$$

where z is the distance between the CH2 group and the substrate in Å. We maintain the convention of attractive forces giving positive energies and assume that the distance between the carbon closest to the S and the gold surface is the same for both configurations. The Au-S-C and the C-C-C angles are taken as 110°, and the bond lengths are taken as Au-S=2.21Å, S-C=1.81Å and C-Au=3.28Å. The

energy per molecule (E_{Au}) has been calculated for both configurations by summing over the n methylene groups of the chain to obtain:

$$E_{Au}(n) = \sum_{i=0}^{n-1}\left[\frac{-2413}{(i*1.25\cdot\cos\theta+3.28-0.86)^{12}}+\frac{1.47}{(i*1.25\cdot\cos\theta+3.28-0.86)^{3}}\right] \qquad (5.10)$$

where θ is the tilt angle (30° or 50°). The results are presented in figure 5.7, bottom graph. The energy increases with the chain length, but saturates at approximately n=9 for the hexagonal and n=12 for the rectangular structures. Not surprisingly, the more tilted configurations are energetically favoured.

The total energy can then be calculated for each structure by adding both terms, interchain and chain-substrate contribution. The difference of total energy between the hexagonal and the rectangular configurations is represented in figure 5.8, as a function of the number of carbons in the chain:

$$\Delta E(n) = E_{hex}(n) - E_{rect}(n) \qquad (5.11)$$

For films of molecules with more than 9 carbons, the difference in energy is positive, indicating that the hexagonal configuration is energetically more favourable. Interestingly, for the shorter lengths, the attractive interaction with the substrate turns out to be more important than the intermolecular interaction between chains. The energy difference between both structures decreases and finally becomes negative for molecules with less than nine carbons: the rectangular structure becomes more stable for shorter chains.

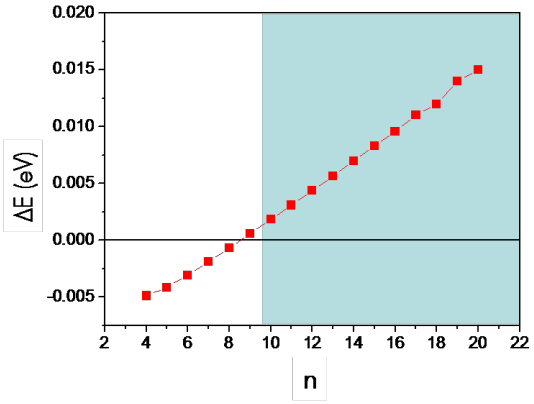

Figure 5.8 Calculated energy difference between the hexagonal and rectangular configurations as a function of the chain length, ΔE(n). For chains with less than nine methylene units, the rectangular configuration is energetically favoured.

Despite its simplicity, this calculation allows us to understand the experimental results and clearly illustrates the role played by the different interactions in the energetic balance determining the island structure.

For long molecules (C18, C22 and C16C16) the van der Waals interaction between chains plays the dominant role, and the hexagonal structure is the most stable configuration even at partial coverage. The metastable 50°-tilted configuration corresponds to a local minimum in the energy diagram (left part in figure 5.9) and forms most likely as a result of favourable kinetics pathways. Once formed, an activation barrier has to be overcome to reach the most stable configuration. When energies higher than the barrier are brought to the system, like perturbation by the SFM tip, the molecules reorganize into the more stable hexagonal configuration.

For short molecules, the interaction with the substrate turns out to be at least an equally important contribution, that increases the stability of the 50° tilted phase (central and right diagram in figure 5.9). This explains why, after perturbation, the C10 molecules rearranged again in the rectangular configuration.

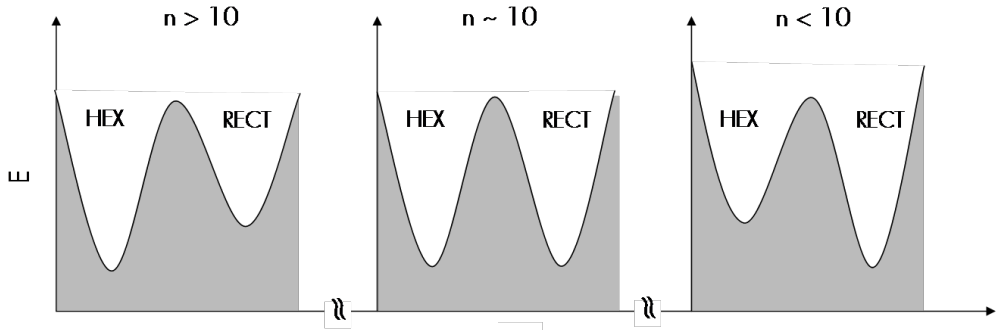

Figure 5.9 Schematic drawing of the energy diagram for the hexagonal and rectangular configurations based in the results obtained. Their relative stability depends on the length of the molecule (see text).

5.3 FRICTIONAL PROPERTIES OF THE RECTANGULAR CONFIGURATION.

After the study of the mechanical stability, we address in this section the study of the frictional properties of the rectangular configuration. To obtain reproducible and reliable frictional data, the results collected in this section have been measured in aged samples (at least, 12h after preparation) since fresher islands often resulted irreversibly damaged under low applied loads and showed higher dispersion in the friction plots. All the experiments have been performed under ambient conditions (T~20-25°C; RH~30%-35%).

The investigation is based in the acquisition of friction versus applied load plots by means of two different approaches. Both are costly and time consuming but their reproducibility make them accurate and worthwhile. Briefly, the first one follows a similar protocol as the one used to test the mechanical stability (previous section). In this case, the selected area is scanned at a given load and topographic

and lateral force (forward and backward) images are simultaneously recorded. The same area is successively scanned increasing the applied load by small increments, after completing each image. Unlike in the mechanical experiments, no load release is performed in these experiments. Since the scanned area generally include regions of different frictional properties (gold surface and different molecular configurations) their corresponding friction value, at any load, is calculated following the protocol of section 3.4.1: firstly the zoom of the lateral force images selecting only one of the regions, secondly the calculation of the friction force at each line and eventually averaging over the total number of lines in the zoomed image. This process is repeated for each region and for the different applied loads to obtain the corresponding friction versus loads plots. The second approach is based on the 3D modes and is explained in section 3.4.2. In this case $F_n(xy,z)$ and $F_l(xy,z)$ images provide the applied load (Fn is obtained from $F_n(xy,z)$ images) and friction value (calculated from the corresponding back and forth profiles in the $F_l(xy,z)$ images) for every z value (see figure 3.11). Since both images are acquired simultaneously, we can obtain a friction versus load plot. The main differences between the approaches reside in both, the acquisition time and the posterior image analysis. Roughly speaking, whereas a 3D measurement takes ~1minute and the corresponding friction versus load plot is obtained from the analysis of three images, the first approach takes ~1 hour of measurement and the friction versus load plot requires the analysis of about 200 images. The difference is considerable.

Figure 5.10 shows the friction versus load plots obtained for the island shown in the inset, using both approaches. It can be checked that the friction response does not depend on the approach used. The similar pull-off force measured before and after each experiment (see inset) ensures minimum tip changes during the measurement.

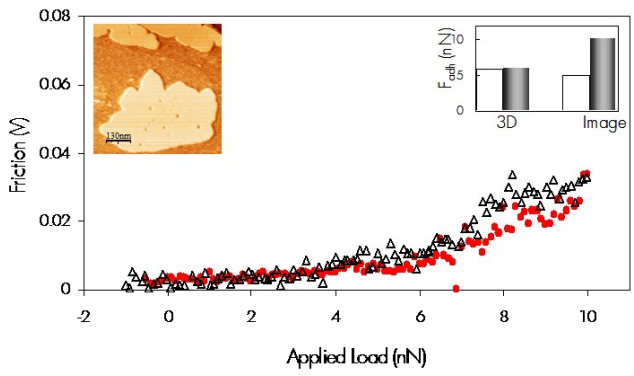

Figure 5.10 Friction versus load plot for a C16 island, acquired by scanning successively the area shown in the inset (solid symbol) and applying the 3D modes (open symbol). Top right: Adhesion force measured before (white) and after (grey) each experiment.

Although statistically speaking, the former approach is more accurate than the latter (values are obtained averaging over a scanned area instead of a single line), the short acquisition time of the

3D measurements considerably reduces the possibility of tip and sample damage and minimizes drift variations during the measurement.

We have mainly used this second approach to obtain the plots presented in this chapter, whereas the first one has been employed to monitor the possible topographic changes induced by the applied load and correlate them with the friction response.

Figure 5.11 shows the variation of the friction response as a function of the applied load for islands of C10, C12, C16 and C18. The data for the bare gold terrace is also shown as a reference. The lubricant character of the organic material immediately becomes manifested: all curves lie well below the curve measured on the gold.

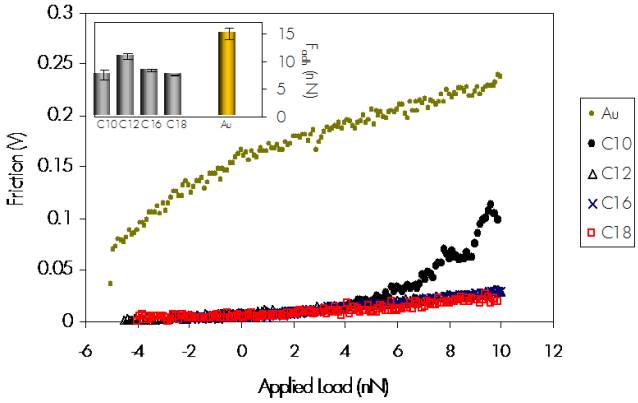

Figure 5.11 Comparison of the friction versus load plots for Au and islands of different alkanethiol molecules. Inset: adhesion force measured after each experiment to test tip conditions.

In the whole force range, the friction seems to exhibit little or none dependence on the chain length. Only the data for C10 deviate, at 5nN, towards higher friction values. This increase in friction marks the onset of the wear regime, in which the molecules are being displaced from the tip contact area. As expected, if higher loads are applied, the friction eventually reaches the values measured on the gold substrate, which at that point is, in fact, contacted by the tip. Further details of this regime are given in section 5.3.1.

The pull-off forces for all the chain lengths as well as for the bare substrate are shown in the inset. The homogeneity in pull-off forces measured on the different islands indicates a similar surface energy, as expected from their common chemical nature. On the gold terrace, the values obtained are always larger. This is attributed to the contribution of the water meniscus formed between the tip and the bare gold, due to its more hydrophilic character. Conversely, the hydrophobic CH_3 endgroups of the molecules prevent the formation of the water layer on top of the islands, minimizing the capillary force. The adhesion measured on top of the layer is mainly due to van der Waals interaction.

5.3.1. The Onset Of The Wear Regime.

The damage caused on the islands when the wear regime is reached can be observed when imaging the area after the friction experiments, as shown in figure 5.12. The black circles highlight the location of the measurement. By comparing the island morphology prior (a) and after (b) the experiment, we see that a hole has been created and material debris piles up at its edges. These unbounded molecules can be removed in subsequent scans, but the hole is left as a permanent mark: the island is irreversibly damaged. This wear occurs when the applied load is enough to penetrate through the molecular film and therefore, the value of the critical load is directly related with the packing density of the film: loosely packed islands with numerous defects indeed facilitate tip penetration.

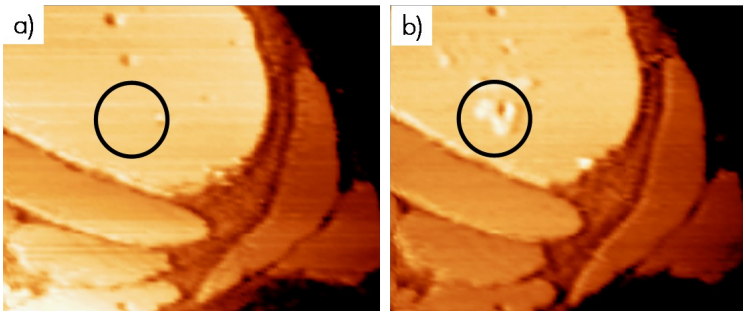

Figure 5.12 SFM topographic images (430×350 nm^2) of a C12 island (a) before and (b) after the 3D friction experiment was done at the circled location. Total z-scale: (a) 0-4.5nm; (b) 0-5nm.

We have studied the variation of this threshold pressure for different molecular lengths (C10, C12 and C16) and as a function of the time elapsed since sample preparation. Though among different islands, made of the same type of molecules, this pressure is found to vary (due to local differences in packing density) the average values plotted in figure 5.13 does not show any evident correlation with chain length. Conversely, a similar trend as a function of time is observed for all the molecules: the pressure increases with time, and saturates after 7-10 days. After that time, the threshold pressure is ~1.3 times higher than for fresh islands. In the plot we have also included the values reported from a similar experiment performed on C16 islands in the hexagonal configuration (filled symbols) [Barrena99]. The evolution with time is similar regarding the molecule and the configuration. However, higher values are always found in islands arranged in the (√3×√3)R30° structure. Even for 10-days aged islands, the pressure for 50°-tilted configuration is ~75% of that found in the 30°-tilted ones (in fact, matching the difference in packing density).

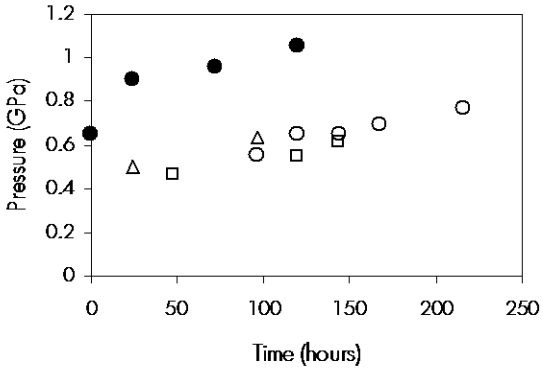

Figure 5.13 Threshold pressure for tip penetration through molecular island versus ripening time, for C10 (□), C12 (△) and C16 (○) molecules arranged in the rectangular configuration. The reported values for the C16 molecules arranged in the hexagonal configuration (●) have also been included for comparison [Barrena99].

The increase of the threshold pressure with time reflects the effect of the reorganization process described in chapter 4 which increases the density of the packing and reduces the number of defects within the islands, consequently hindering tip penetration through the film. The difference found between both, hexagonal and rectangular configurations, can be directly related with the results of figure 5.7: the larger the tilt angle, the lower the cohesive molecular energy. Therefore, for islands in the rectangular configuration, lower pressures are needed to disrupt the molecular packing and reach the underlying substrate.

5.3.2. Friction Versus Applied Load.

Going back to frictional characterization, when carefully looking into the friction data we have found differences in the properties of long (C16 and C18) and short (C10 and C12) molecules. Figure 5.14 is representative of the results obtained for short-chain islands. The graph shows the friction versus load plots obtained for the same island,12 hours (circles) and 24 hours (triangles) after preparation. The almost identical adhesion force obtained ensures similar tip conditions in both cases.

As expected from the trend observed in the threshold pressure in figure 5.13, wear is not observed one day after preparation for loads up to 10nN, whereas twelve hours before, at ~7nN, the tip penetrates through the film. For forces below 7nN, friction shows a monotonous increase in both plots, but lower values are measured on the ripe island. In fact, within an interval of twelve hours, the friction is roughly half of the initial value. This monotonous increase of the friction signal with the applied load has already been reported for alkanethiol monolayers [Lio97][Schönherr99][Brewer04] and is mainly due to the increase in contact area caused by the elastic deformation of the layer. The larger the contact area, the greater the number of molecules that contribute to the friction signal. The mechanisms of energy dissipation in these cases comprise mainly local deformations within the films: C-C bond rotations and the trans-gauche conformational changes. The reported activation energy of

such deformations is ~0.14 eV for gauche defects at the free end of the molecule (see chapter 2). The higher friction values measured on the fresh island might be due to the additional contribution of internal gauche defects, easier produced in loosely packed films. It has also been proposed in [Lee00] that films with lower packing density would present a lower elastic modulus (E_{SAM}), which in turn gives rise to an increased contact area at any given load (see equation 5.7). Since friction force is proportional to the contact area (equation 5.2), lower elastic modulus will yield greater frictional response on the loosely packed film.

After the reorganization process is complete friction versus load plot shows no significant differences with time.

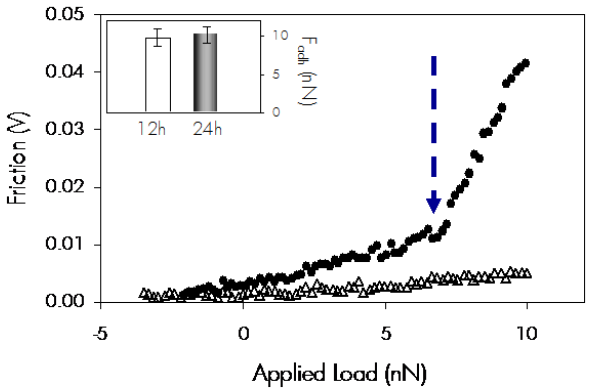

Figure 5.14 Friction versus load plot for a C12 sample 12h (circles) and 24h (triangles) after preparation. The dashed arrow marks the onset of the wear regime. Inset: adhesion values measured on top of the island after each experiment.

Figure 5.15 collects the results for C16 and C18 samples. For long molecules, the reorganization process has been found to last longer, therefore measurements were performed in the same island two and six days after preparation for C16 and two, six and eleven, days for C18. Instead of a monotonous increase of the friction signal with the applied load, a clear stepwise behaviour is obtained, with discrete changes in the friction response. Because both molecules have been found to behave similarly, only numerical data for C16 are given in the following description.

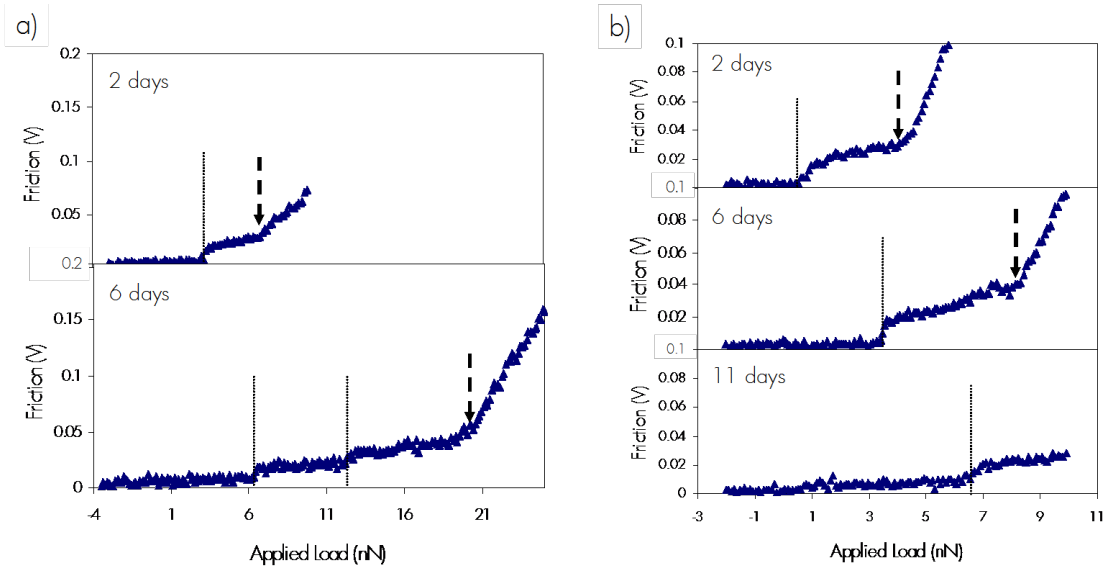

Figure 5.15 Force versus load plot measured on (a) C16 and (b) C18 islands. The labels indicate the time elapsed since sample preparation. Dotted lines mark the jumps in friction signal and dashed arrows, the onset of the wear regime.

Starting with the 2-days aged island, top graph of figure 5.15(a), two plateaus of almost constant friction response, are distinguishable. The first one extends up to a force of ~3nN (to compute the total load the adhesion force, F_{adh}= 7nN, must be added). At this load, there is a jump in friction response and a second plateau is observed, which extends up to ~7nN. Further increase in the applied force results in tip penetration through the molecular film with a steep increase of the friction signal.

When the same experiment is performed four days after, besides increasing the critical load at which molecular wear is observed (from ~7nN to ~20nN for the C16 island), the reorganization process also influences the width and, in this case, the number of plateaus. The first plateau now extends up to ~6.5nN of applied force (F_{adh}=7.5nN), the second one, up to ~12.5nN, and there is a third plateau that was not observed in the 2-days upper graph. The friction value of the first and second plateaus is similar regardless the time elapsed since preparation. The pressure at which the jump from one plateau to the next occurs is, on average, 1.2 times higher for the one-week aged island, as expected for a more compact packing.

This discrete behaviour of the friction response under pressure reminds of that observed for C16 in the hexagonal configuration [Barrena00] and for alkylsilanes on mica [Barrena99], and is caused by the collective tilts of the molecules under applied pressure. As explained in chapter 2, to tilt the molecules one must first introduce a small separation between chains to allow chain disengagement. This makes necessary the presence of defects, to facilitate this molecular separation. Once separated, the chains are able to slide and arrange with a different tilt angle. The energy cost of this change in the tilt angle is reflected in the friction signal. The stepwise behaviour resides in the fact

that only a discrete number of angles, dictated by the interlocking of the molecular backbone (chapter 2), are possible. Thus, each time the molecules pass from one angle to the next one, the barrier for molecular separation has to be overcome. These tilt configurations, conversely to the 50°-tilted rectangular that is spontaneously formed, can only be observed under applied pressure, i.e. once the pressure is released the molecules recover their original configuration.

We verify that collective tilts are also responsible for the stepwise behaviour observed in figure 5.15 by acquiring simultaneous topographic and friction images of a selected area, following the protocol already described. After each image, the applied load is increased by 0.1nN. In this way, simultaneous friction and height versus load plots are obtained, as shown in figure 5.16. It can be seen that every step increase in friction (bottom graph) is accompanied by a simultaneous decrease in height (top graph).

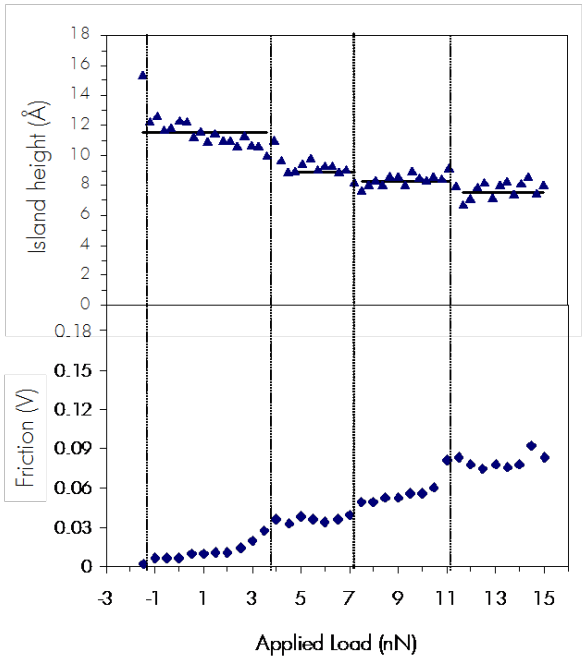

Figure 5.16 Height (top) and friction (bottom) versus applied load plots for a C18 island arranged in the rectangular configuration. Solid lines in the upper plot correspond to the heights predicted by the interlocking model (see text)

At the lowest practical load, the height measured is smaller than the corresponding to a 50°-tilted C18 molecule (see table 4.3), due to the presence of weakly bounded molecules on the gold terrace that reduces by about one molecular diameter the true standing up heights. These molecules are swept when the load is further increased. Different experiments have been performed to ensure that the heights measured are reproducible; several of the same plateaus are obtained in different islands.

The discrete changes of height versus applied load confirm the existence of particularly favourable molecular configurations, dictated by the interlocking of the molecular backbone. The tilt angles of such configurations can be therefore obtained from the 3D model described in chapter 2.

Our starting configuration is, in this case, the rectangular 50°-tilted structure which correspond to θ_X=30° (n=1) and θ_Y=41° (m/2=1.5), and intermolecular distances d_X=4.3 Å and $d_Y/2$=4.4Å. [15] The new configurations that might appear under tip compression are obtained varying the (n,m/2) values in equations (2.2) and (2.3).

Table 5.1 collects the possible configurations, the total tilt angle and the corresponding height calculated for a C18 molecule. We have also included the experimental heights observed in figure 5.16. It can be seen that the 3D model accurately predicts these experimental values.

The fact that not all the predicted heights are always observed, is related to the relative stability of the configurations. Similar to what has been shown for the 50°-tilted configuration, the interplay between intermolecular and molecule-substrate interactions might energetically favour the formation of some configurations, not enough to promote their spontaneous formation but sufficiently to increase their frequency under applied pressure. Thus, as commented commensurate structures will give favoured and more stable configurations. Besides, different (n,m/2) values yield the same total tilt angle, which also increases the probability to observe the corresponding height.

Though the tilting direction will depend to a great extent on the relative orientation between the molecular structure and the scan direction, for all the experiments performed in this work the heights are well reproduced considering only a change in the tilt along the NNN molecular direction. Since on the other hand, it is plausible that tilting along that direction, in which the molecules are already tilted by 41°, is favoured we keep constant the n value in table 5.1.

Table 5.1 Different configurations predicted by the 2D interlocking model considering tilts only along the Y direction. The corresponding height has been calculated for a C18 molecule (h_{cal}). The last column corresponds to the experimental heights observed in figure 5.16.

n	m/2	θ_X	θ_Y	θ	h_{cal} (Å)	h_{exp} (Å)
1	2	30°	49°	55°	15.1	---
1	2.5	30°	55°	60.3°	13.1	---
1	3	30°	60°	64.2°	11.5	11.3±0.6
1	3.5	30°	63.4°	67.2°	10.2	---
1	4	30°	66.4°	70°	9.17	9.3±0.3
1	4.5	30°	69°	72°	8.29	8.3±0.3
1	5	30°	71	73.4°	7.6	7.7±0.5

From the frictional characterization under applied load of the rectangular configuration we have found different behaviours for short (C10 and C12) and long (C16 and C18) molecules. In the former, a monotonous increase of friction is observed and related to the increase in contact area with applied load: the larger the contact area, the greater the number of molecules under the tip that contribute to friction signal. The mechanism for energy dissipation is distortion of the chains (gauche defects, bending…). In the latter, a stepwise behaviour is obtained indicating that the mechanism for energy dissipation is mainly due to collective tilts of the molecules under the tip.

[15] The definition of d_Y in chapter 2 was twice the separation between molecular planes in the Y direction. Therefore, the molecular separation along that direction in the rectangular configuration is $d_Y/2$.

The origin of this difference between long and short molecules might be at the difference in relative stability of the rectangular configuration shown in section 5.2. To induce collective tilts, the original configuration should be destabilised and the molecules separated. Though it might seem easier to disrupt the packing of short molecules, which have lower cohesive energy, we have proved that when considering the molecule-substrate interaction, the rectangular configuration becomes energetically favoured for these molecules. Therefore, it will be more difficult to destabilise this configuration for short molecules, hindering the observation of collective tilts.

As commented several times throughout this work, the loads or pressures at which a specific event takes place (onset of the wear regime, collective tilts….) are not absolute values because depend on island specific characteristics, as for instance the density or packing quality, depend on the island under study. Nonetheless, there is a clear trend as a function of time intimately related with the reorganization process: larger loads are required for ripe islands. This has an important consequence: for ripe islands (more than one week aged) it is difficult (high loads would be necessary) to observe the steps in friction due to the dense packing achieved. Conversely, the stepwise behaviour is easier observed in small islands (diameters of ~ 0.6-0.8 μm) or at the edges of the larger ones, because these edges consist of low coordinated molecules, which can more easily move to provide free space for molecular separation under tip pressure. From the experience acquired during this work, the optimum conditions to observe collective tilts are islands of average diameter lower than 1μm and within the first week after preparation (relatively fresh samples, 24h after preparation, are still too loosely packed and wear is often produced before collective tilts).

5.4 COMPARISON OF THE FRICTIONAL PROPERTIES.

Once the frictional characteristics of the rectangular configuration have been studied, we resume the experiments proposed at the beginning of this chapter based in the direct comparison of different systems to gain further insight into fundamental aspects of the friction response in SAMs. Firstly we compare the frictional characteristics of the same molecules arranged in different configurations, the hexagonal and the rectangular ones. Secondly, we present a similar study comparing alkanethiol and dialkyl disulphide islands.

5.4.1. The Hexagonal Versus The Rectangular Configuration.

To study solely the influence of the different molecular arrangement we must eliminate (or at least, minimize) any difference between the experiment performed in the hexagonal and that performed in the rectangular configuration. These differences include tip, ambient conditions, time elapsed since sample preparation… which are known to influence the friction response. Our approach to isolate differences due only to the molecular arrangement has been the simultaneous measurement on both configurations. This requires the complex task of obtaining both configurations coexisting in areas with

adequate sizes, but once the area is located, this approach allows a more controlled comparison, since any change in tip or ambient condition will affect equally both frictional responses. Moreover, the time passed since preparation is the same for both islands. This does not ensure the same packing quality, but minimizes the differences due to the ripening process.

The topographic image of figure 5.17(a) shows one of these areas, with tall and low C18 islands coexisting in the same gold grain. Note that because of the partial coverage, the presence of substrate steps (2.35 Å) does not impede but helps obtaining accurate heights determination. The graphs in part (b) depict the simultaneous height and friction changes as a function of the applied load, for the marked islands.

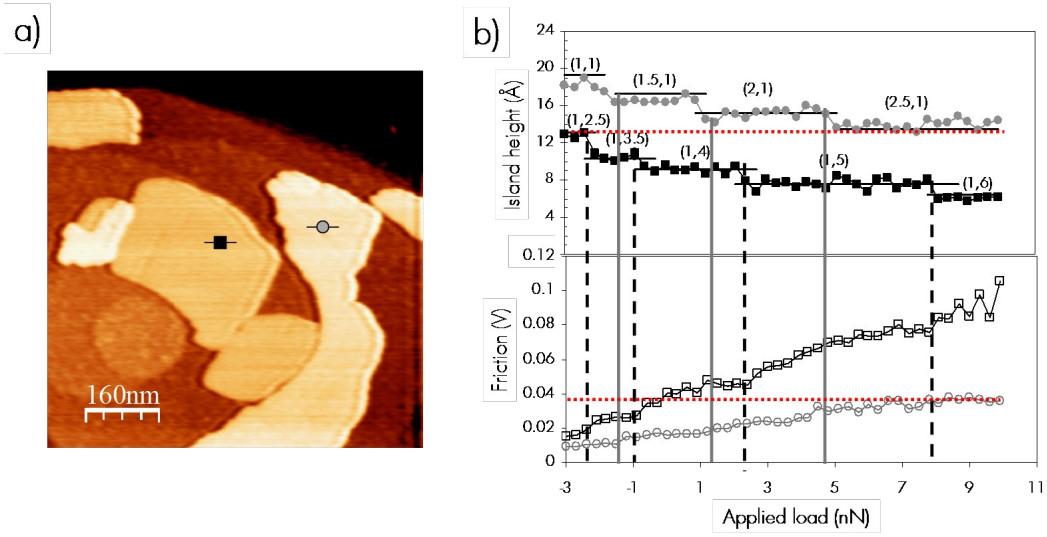

Figure 5.17 (a) SFM topographic image of a C18 sample. (b) Simultaneous height (top) and friction (bottom) versus applied load plots corresponding to the tall (circle) and low (squares) islands marked in (a). The solid horizontal lines in the height plot correspond to calculated heights based in the 2D model. The corresponding (n,m/2) values are indicated. The solid and dashed vertical lines highlight the steps in the hexagonal and rectangular configuration, respectively. The dotted red horizontal line marks the presence of the same configuration for both islands which exhibits the same height (upper graph) but different friction response (lower graph) .

The stepwise behaviour is observed for both configurations and the experimental heights can all be described with the interlocking model. The (n,m/2) values and total tilt angles for the plateaus observed in figure 5.17 have been collected in table 5.2.

When comparing the friction signal, we observe that the friction, at any given load, is always higher when measured in the low island. From the data in table 5.2, we can see that, the plateaus observed in the low islands correspond to larger tilt angles than those in the tall island (except for the one with a tilt angle of 60°, observed in both islands). We note that larger tilt angles increase the atomic contacts between tip and the chain backbones, since more CH_2 groups are exposed to the film outermost surface. The additional interaction between the SFM tip and these groups can explain the

observed higher friction values on the (initially) 50°-tilt island. If this were the only contribution to friction, configurations with similar tilt angles should yield similar friction signal. However, this is not fulfilled in figure 5.17, where the last plateau of the tall island and the first one of the low island correspond to the same tilt angle and present different frictional characteristics: the friction is higher for the island initially arranged in the hexagonal configuration (see the red dotted line in figure 5.17).

Table 5.2 Configurations predicted by the 2D interlocking model (n,m/2 and θ values) that reproduce the experimental heights observed in figure 5.17. The estimated packing area (Å²/molecule) of each configuration is shown (see text).

HEXAGONAL				RECTANGULAR			
n	m/2	θ	Å²/molelcule	n	m	θ	Å²/molecule
1	1	43°	24.1	1	2.5	60°	35
1.5	1	49°	28	1	3.5	67°	48.8
2	1	55°	30.5	1	4	70°	54.4
2.5	1	60°	35	1	5	73°	66
				1	6	76°	78

In addition to changing the tilt angle of the molecules, we have to take into account that the load changes the contact area which in turns affects the friction force. Moreover, changes in tilt angle also affect the packing area and the number of molecules at the contact that are those contributing to the frictional response. For a proper comparison between islands, we have normalized both friction plots of figure 5.17(b) to the friction per molecule, by computing the variation of contact area as well as the molecular packing area at each load. The former has been performed using the DMT approach as done several times throughout this chapter. To estimate the area per molecule corresponding to each (n,m) configuration, we have calculated L_X and L_Y, the projection of the lattice parameter along the NN and NNN molecular directions, using equations:

$$L_X = \frac{d_X}{\cos\theta_X} \tag{5.12}$$

$$L_Y = \frac{d_Y/2}{\cos\theta_Y} \tag{5.13}$$

where dx and dy have been defined in chapter 2 and correspond to intermolecular distance along the X direction and twice the separation between molecular planes along the Y direction. Therefore, the packing area is obtained from:

$$p = \frac{L_X \cdot L_Y}{2} \tag{5.14}$$

Again, due to the definition of d_Y, dividing by two is necessary to obtain the area occupied by a molecule.

The packing areas obtained, by multiplying both projections, have been also summarized in table 5.2. The normalized plot is shown in figure 5.18. Instead of the applied load, we have plot the friction versus the tilt angle of each configuration. It can be seen that both plots perfectly match at the 60°-tilt plateau.

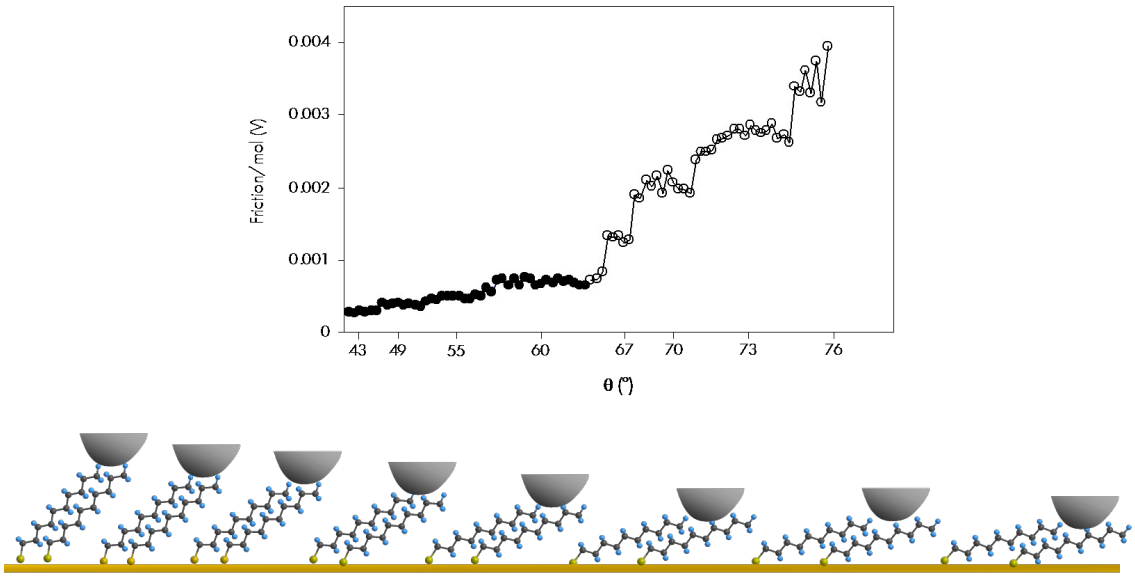

Figure 5.18 Top: friction, normalized to the number of molecules, versus the tilt angle of each configuration for the tall (filled symbol) and low (open symbol) islands of figure 5.17. Bottom: schematic representation of the molecular configuration for each of the plateaus observed in the top graph.

This illustrative experiment proves the intimate relationship between friction response and molecular arrangement in these organic layers. The stepwise behaviour is a consequence of the existence of energetically favoured configurations at specific tilt angles. The friction measured at each plateau is a sum of the energy employed to separate the molecules, prior to tilting, and the contribution of gauche defects, bending and other distortions created along the molecule. The former can be regarded as invariant for each tilt,[16] the latter increases with the tilt angle, since more part of the molecular backbone is in contact with the tip and, consequently, the contribution to energy dissipation is higher. This has been schematically drawn in figure 5.18.

5.4.2. Alkanethiol Versus Dialkyl Disulphide Islands.

Conversely to the results of the structural characterization, that showed negligible differences among disulphide and alkanethiol samples, we have observed differences in the mechanical stability

[16] Note that the tilting only occurs for the molecules under the tip and once the tip has passed, the molecules recover the initial configuration. Therefore, in the subsequent scan, the same energy is again dissipated due to molecular separation.

of the rectangular configuration for symmetrical disulphides that point to a worse packing within these islands. In this section we have investigated if this is also reflected in the frictional characteristics of disulphide islands. Additionally, we have also undertaken the study of the friction response in mixed islands grown from asymmetrical disulphides.

5.4.2.a Symmetrical disulphides.

The results of the friction study versus applied load are shown in figure 5.19. For short molecules (C12C12 and C12) we have plotted the average of several measurements performed on different islands, to ensure that the observed differences are beyond the dispersion found within islands of the same molecule. Though this has been also verified for long molecules (C16C16 and C16), to better visualize the stepwise friction, only a representative measurement for each type of molecules is shown in graph (b).

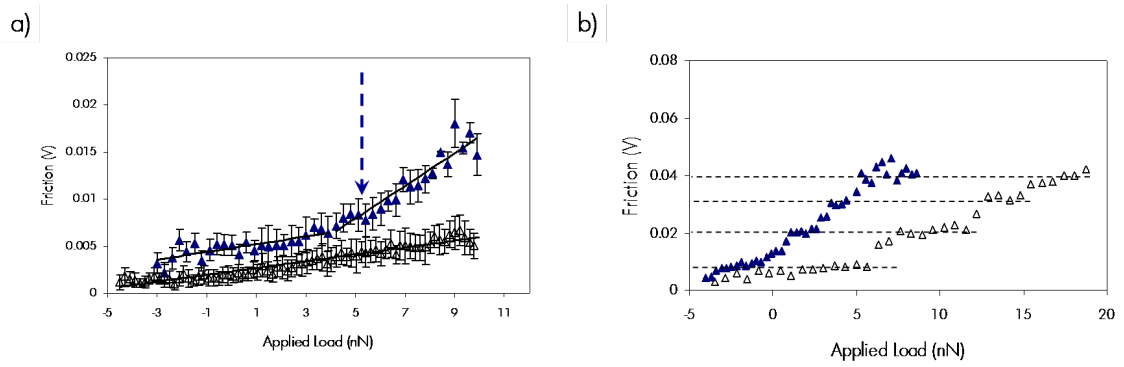

Figure 5.19 (a) Friction versus load plots, averaged over five measurements, for C12 (△) and C12C12 (▲) samples. The vertical arrow marks the onset of the deviation of the disulphide behaviour. (b) Friction versus load plots for C16 (△) and C16C16 (▲) samples. Dashed horizontal lines mark the values of the plateaus.

In graph (a) we can identify two different regimes in the disulphide plot: below 4nN in which both plots show a similar slope, with slightly higher friction values measured on the C12C12 islands, and above 4nN, in which the slope of the disulphide plot is ~4 times higher than that measured for C12 (solid lines have been drawn as a guide). By imaging the island at low loads we have checked that this increase observed for C12C12 samples is not due to wear of the island.

In graph (b) it can be seen that both, C16C16 and C16 islands, exhibit the stepwise behaviour in friction response. Though the friction measured at each plateau is quite similar for both samples, clear differences are found regarding the load at which each one appears and its width: for disulphide islands these widths are roughly half of that measured in alkanethiol islands.

As commented at the beginning of the chapter, some works have reported a worsening of the crystalline quality on disulphide monolayers with respect to alkanethiol monolayers. The results of figure 5.19 can be accounted for if this is also true at submonolayer coverages. In short-chain islands, the

deformation of the alkyl chains, mainly due to the formation of gauche defects, bending and torsion of the chains is believed to be the principal mechanism for energy dissipation. At low loads, these defects are mainly created at the external part of the layer, which always presents a lower cohesive energy, and the lower packing quality of the disulphide is not noticed in the friction plot. This explains the similar slope found in this region for both, the C12 and C12C12 islands. At higher loads, the tip can access to the internal part of the disulphide layer, increasing the possibility of creating internal defects and the differences in packing quality become noticeable. This is reflected in the increase of the slope found in figure 5.19(a).

In C16C16 islands, the worsening of the crystalline quality facilitates the necessary separation of the molecules prior to each collective tilt, which is reflected in the shortening of the length of each plateau.

Therefore, even at submonolayer coverages, where molecular mobility and healing of defects are favoured due to the free space available, disulphide molecules are less labile than their alkanethiol counterparts, yielding islands of worse crystalline quality. Friction force analysis is sensible to these differences.

5.4.2.b Asymmetrical disulphides.

Before presenting the results of the frictional measurements in asymmetrical disulphide islands, we would like to comment that, in these samples, we have never observed the stepwise behaviour reported for alkanethiol islands. Therefore, to compare the friction of asymmetrical disulphide and alkanethiol molecules, the measurements have been performed on ripe islands of C12C16, C12 and C16, all of them showing a linear response. Moreover, as the behaviour of the ripe C12 and C16 islands is almost indistinguishable, we will only present the comparison with C16 samples.

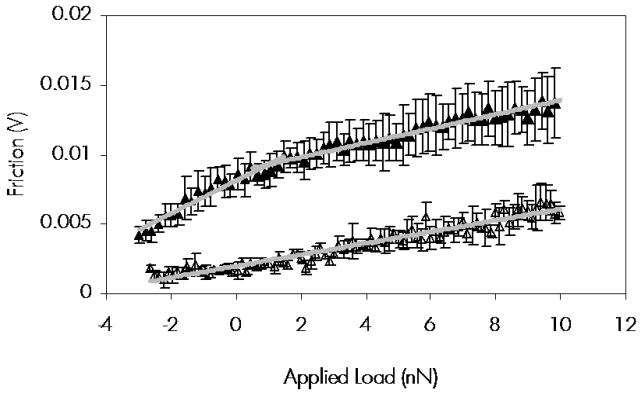

Figure 5.20 Friction versus load plots for C16 (△) and C12C16 (▲) samples. Each point is the average over five measurements.

Figure 5.20 shows the friction as a function of the applied load for C12C16 and C16 islands. We can also distinguish two different regimes in the disulphide plot, as in the case of

C12C12 islands, but in this case the former, which extends up to a force of 1.5nN, is the one with the higher slope whereas the latter present a slope similar to the C16 plot.

This behaviour in asymmetrical disulphide islands is likely associated with the formation of defects under applied load at the ends of the longer chains. As described in section 4.2.2, these protruding part of the chains have a reduced number of direct neighbours and are not so tight-packed, implying that they can be easily distorted even at low applied loads. Therefore, the number of gauche defects which can be created at a given load is larger in C12C16 islands, consequently a higher value of the friction is obtained. Furthermore, this interpretation explains the change observed in the slope ~2.5 times higher, in the low load regime with respect to the alkanethiol plot. At higher loads, the gauche defects density in the protruding ends of the C16 molecules under the tip should saturate and does not increase further with applied load. This explains the similar slope observed between alkanethiols and disulphides, due mainly to the change in contact area.

The absence of collective tilts in asymmetrical disulphide islands might be also due to the easy formation of gauche defects in the C16 molecules. These chain distortions would hinder the separation and subsequent sliding of adjacent molecules, necessary to observe the steps in friction force.

The ensemble of results presented here also support the formation of homogeneously mixed C12C16 islands, anticipated in chapter 4. If phase segregation would happened over the detection limit of the SPM, we would have obtained the same frictional properties for ripe C12C16, C12 and C16 islands.

In short, different frictional characteristics have been obtained for disulphide and alkanethiol samples. For symmetrical disulphides, differences can be attributed to a worsening of the crystalline quality of the packing whereas the even larger differences in asymmetrical disulphides arise from the contribution of the free ends of the longer chains. This is reflected in the shape of the friction versus load plots. Interestingly, though when comparing the results of C12C12 and C12C16 samples, both present a two-regime response, the symmetric disulfide presents a behaviour similar to the single component case at low loads, while asymmetrical disulfides behave as single component films for high loads. This makes sense if we consider the mechanisms involved: internal distortion for symmetrical disulphides and external gauche defects, at the protruding parts of the longer molecules, for asymmetrical disulphides. Obviously, the latter are energetically less costly than the former and are created at lower loads. The same behaviour obtained in disulphide samples was found for mixed films obtained from immersion in a mixed C12-C16 solution, in which neither phase segregation was detected [Barrena01]. Looking at the shape of the plots we can indeed identify the different mechanisms giving rise to the friction response.

5.5 EFFECT OF RELATIVE HUMIDITY ON FRICTIONAL PROPERTIES.

In this section we address the study of the relation between environmental conditions and frictional characteristics of SAMs. In particular, we have focused on the humidity effect by comparing experiments under ambient conditions and at low relative humidity (RH). As commented in chapter 3, we can control the RH in the working chamber by means of a N_2 flux. For a proper comparison, the measurements have been performed on the same islands prior and after switching on the N_2 flux. The results of these experiments are shown in figure 5.21, for a C18 sample.

The top graph shows the friction versus load plot obtained at ambient conditions (filled symbols) and at low RH (open symbols). At a first sight, the effect of the RH on the friction force seems to be a "shifting" of the data towards lower applied loads as the RH is reduced. In both plots we observe the same number of plateaus with similar width, and the friction measured within each plateau is almost coincident. From the force versus distance curves we can confirm that the change in RH does not affect the value of the adhesion force (F_{adh}=8nN). However, the loads at which the steps and the onset of the wear regime appear considerably decrease with decreasing RH.

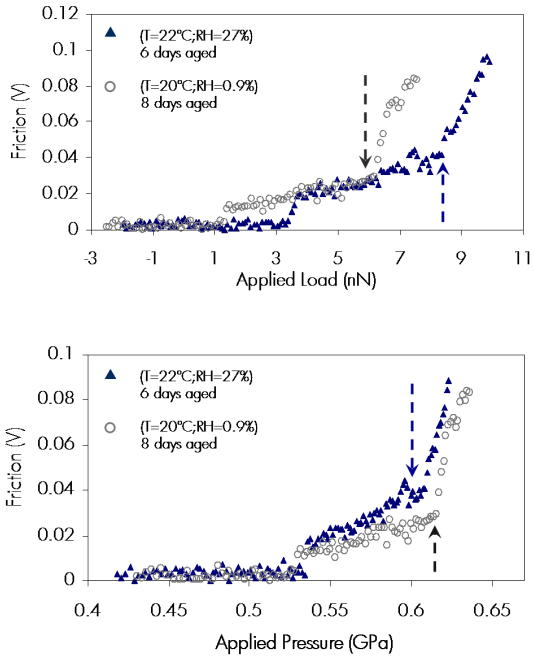

Figure 5.21 Top: friction versus load plots for a C18 island measured under ambient conditions (filled circles) and at low relative humidity (open symbol). Bottom: the friction data of the top graph represented as a function of the applied pressure (see text). Labels indicate the experimental conditions and dashed arrows mark the onset of the wear regime.

As already commented, several works reported an almost humidity-independent friction response on CH_3-terminated alkanethiol SAMs [Li03][Qian03]. This is based on the hydrophobic character of these layers that prevent water adsorption, even at high relative humidity. In fact, it has also been demonstrated that no water meniscus can be formed between an SFM tip and a CH_3-

terminated SAM over the entire humidity range, leading to an also humidity-independent adhesion force, mainly due to van der Waals forces [Xiao00]. This explains the similar plot shape and measured adhesion we obtain under ambient conditions and at low RH, but fails to predict the "shift" of the data shown in figure 5.21.

A possible explanation of the results found can be as follows: in ambient conditions no water layer is formed on the alkanethiol islands, but a water layer indeed covers the hydrophilic tip surface which increases the nominal tip radius and consequently the contact area at a given force. Under the N_2 atmosphere, no changes are expected on the island surface but the water layer adsorbed on the tip is reduced. Therefore, at the same load, the applied pressure is higher at low RH.

We have estimated the threshold pressures for the steps and wear onset observed in the two plots of the top graph in figure 5.21, following the DMT approach, and we have found that at low RH the values are 0.9 times lower the values found at ambient conditions. After statistical analysis of measurements performed on different islands, this value has been found to vary between 0.8-0.95. To account for a change of a factor of 0.9 in the pressure, the variation in the tip radius should be about 2-3nm, considering equation 5.7. This value agrees with the increase expected by the thickness, in this range, of the water layer formed at ambient conditions on hydrophilic surfaces.

To better see the influence of such a change in the tip radius, we have represented the friction values versus the applied pressure. For the data acquired at ambient conditions, the pressure has been calculated using a tip radius of ~25nm (the average value measured for the tips used), whereas for the data at low RH, a ~22nm tip radius has been employed. The result is shown in the bottom graph of figure 5.21, in which both plots almost overlap. This change in tip radius does not affect the measured adhesion because neither at ambient conditions nor under N_2 atmosphere the water meniscus is formed between the tip and the island.

A change in tip radius of 2-3 nm is likely to occur due to tip damage and not to the presence/absence of a water layer. In order to support our above argument, a third set of measurements has been performed on the same island, with the same tip after switching off the N_2 flux, i.e. again under ambient conditions. The behaviour of the former measurement was recovered (not shown).

In order to corroborate these experiments it would be interesting to perform this kind of measurements with hydrophobic tips, where the presence of a water layer is also inhibited even at high relative humidity. In that case, both plots (at ambient conditions and low RH) should overlap. We note at this point, that these results do not contradict what has been reported for complete monolayers, where steps in friction are not observed and the measurements are restricted to the wearless regime. In those cases, no difference would be appreciated as a function of the RH.

5.6. CONCLUSIONS

This chapter collects the results of the mechanical and frictional studies performed on the 50°-tilted configuration, which are mainly aimed at understanding the spontaneous formation of this configuration at submonolayer coverages.

The mechanical stability of the 50° tilted configuration has been found to vary as a function of the chain length. Long molecules (C18, C22) initially in the rectangular 50° tilted configuration transform into the (√3×√3)R30° structure (30°-tilted) after mechanical perturbation by the SFM tip that can deliver energy, substantially above thermal energy fluctuations at room temperature, to promote the rupture of molecular cohesion. In contrast, short molecules reassemble again in the rectangular 50°-tilted structure after the same manipulation which evidences a higher stability of the rectangular structure for the shorter chain lengths. We have estimated the difference in energy between the 30° and 50° tilted configurations by considering the competition between intermolecular and molecule-substrate interactions. The calculation indicates that, whereas the cohesive energy of the chain packing diminishes for large tilt angles, the energy due to the interaction with the substrate increases, with the balance between the two contributions depending on chain length. The intermolecular van der Waals interaction dominates for long molecules, and the close-packed (√3×√3)R30° structure is the most stable. For short molecules (around 10 carbons long), the interaction with the substrate turns out to be an equally important contribution that favours the stability of the 50° tilted phase.

This different energy balance for short and long molecules also affect the friction response of the rectangular configuration: friction shows a monotonous increase with applied load for short molecules whereas a stepwise behaviour is observed in long molecules. The former is caused by the increase in contact area with increasing loads and the latter, by the collective tilting of the molecules under applied pressure. These tilts occur at specific angles, dictated by the interlocking model, and tip pressure is necessary to separate the molecules prior to the change in tilt angle. The larger relative stability of the rectangular configuration found in short chains can hinder this separation and consequently, the observation of the collective tilts.

We have performed the first simultaneous frictional study on islands presenting different molecular configurations. The results show that friction is sensible to the molecular tilt angle, because the number of contacts along the molecular backbone increases with increasing tilt angle.

The experiments on symmetrical disulphide islands point to a worsening in crystalline quality with respect to their alkanethiol counterpart, which is reflected in both, the mechanical stability and the friction response under applied pressure. Asymmetrical dialkyl disulphides have been used to study the friction properties of homogeneously mixed islands, formed by molecules of different chain length. The main contribution to energy dissipation in these islands is the creation of gauche defects at the protruding ends of the longer molecules, due to the larger space available.

Finally, the reduction of the relative humidity has been found to affect to a larger extent the tip conditions rather than the SAMs properties.

5.7 REFERENCES.

[Bain89b] C. D. Bain, H. A. Biebuyck, G. M. Whitesides "Comparison of Self -Assembled Monolayers on Gold: Coadsorption of Thiols and Disulfides" 1989 Langmuir. 5; 723.

[Barrena99] E. Barrena, C. Ocal, M. Salmeron "Evolution of the structure and mechanical stability of self-assembled alkanethiol islands on Au(111) due to diffusion and ripening" 1999 J. Chem. Phys. 111; 9797

[Barrena00] E. Barrena, C. Ocal, M. Salmeron "Molecular packing changes of alkanethiols monolayers on Au(111) under applied pressure" 2000 J. Chem. Phys. 113; 2413.

[Barrena01] E. Barrena, C. Ocal, M. Salmeron. "A comparative AFM study of the structural and frictional properties of mixed and single component films of alkanethiols on Au(111)" 2001 Surf. Sci. 482; 1216.

[Barrena01b] E. Barrena, C. Ocal, M. Salmeron "Structure and stability of tilted-chain phases of alkanethiols on Au(111)" 2001 J. Chem. Phys. 114; 4210.

[BarrenaThesis] E. Barrena ""Fricción y estructura molecular de películas de alcanosilanos y alcanotioles por debajo de la monocapa" 2001 Ph.D. Thesis.

[Biebuyck94] H. A. Biebuyck, C. D. Bain, G. M. Whitesides "Comparison of Organic Monolayers on Polycrystalline Gold Spontaneously Assembled from Solutions Containing Dialkyl Disulfides or Alkanethiols" 1994 Langmuir 10; 1825.

[Brewer04] N. J. Brewer, T. T. Foster, G. J. Leggett, M. R. Alexander, E. McAlpine. "Comparative Investigations of the Packing and Ambient Stability of Self-Assembled Monolayers of Alkanethiols on Gold and Silver by Friction Force Microscopy" 2004 J. Phys. Chem. B. 108; 4723.

[Brewer04b] N. J. Brewer, G. J. Leggett. "Chemical Force Microscopy of Mixed Self-Assembled Monolayers of Alkanethiols on Gold: Evidence for Phase Separation" 2004 Langmuir. 20; 4109.

[Carpick97] R. W. Carpick, M. Salmeron. "Scratching the Surface: Fundamental Investigations of Tribology with Atomic Force Microscopy" 1997 Chem. Rev. 97; 1163.

[Derjaguin75] B. V. Derjaguin, V. M. Muller, Y. P. Toporov. "Effect Of Contact Deformations On Adhesion Of Particles" 1975 J. Colloid Interface Sci., 53; 314.

[Gnecco01] E. Gnecco, R. Bennewitz, T. Gyalog, E. Meyer "Friction experiments on the nanometre scale" J. Phys.: Condens. Matter 2001 13;R619.

[Greenwood66] J. A. Greenwood, J. B. P. Williamson. "Contact of nominally flat surfaces" 1966 Proc. R. Soc. A 295; 300.

[Haehner93] G. Haehner, C. Woell, M. Buck, M. Grunze "Investigation of intermediate steps in the self-assembly of n-alkanethiols on gold surfaces by soft x-ray spectroscopy" 1993 Langmuir 9;1955.

[Hautman89] J. Hautman, M. L. Klein "Simulation of a monolayer of alkyl thiol chains" 1989 J. Chem. Phys. 91; 4994.

[Israelachvili92] J. Israelachvili "Intermolecular and surface forces" 1992, Academic Press, London, England.

[Johnson71] K. L. Johnson, K. Kendall, A. D. Roberts.1971 "Surface Energy And Contact Of Elastic Solids" Proc. R. Soc. London A, 324; 301.

[Johnson85] K. L. Johnson. "Contact Mechanics" 1985 (Cambridge: Cambridge University Press).

[Johnson97] K. L. Johnson, J. A. Greenwood. "An adhesion map for the contact of elastic spheres" 1997 J. Colloid Interface Sci. 92; 326.

[Kim99] H. I. Kim, M. Graupe, O. Oloba, T. Koini, S. Imaduddin, T. R. Lee, S. S. Perry. "Molecularly Specific Studies of the Frictional Properties of Monolayer Films: A Systematic Comparison of CF_3-, $(CH_3)_2CH$-, and CH_3-Terminated Films" 1999 Langmuir. 15;3179.

[Lee00] S. Lee, Y. S. Shon, R. Colorado, R. L. Guenard, T. R. Lee, S. S. Perry. "The Influence of Packing Densities and Surface Order on the Frictional Properties of Alkanethiol Self-Assembled Monolayers (SAMs) on Gold: A Comparison of SAMs Derived from Normal and Spiroalkanedithiols" 2000 Langmuir 16; 2220.

[Leggett05] G. J. Leggett, N. J. Brewer, K. S. L. Chong. "Friction force microscopy: towards quantitative analysis of molecular organisation with nanometre spatial resolution" 2005 Phys . Chem. Chem. Phys . 7; 1107.

[Li99] L. Li, K. Yu, S. Jiang. "Quantitative Measurements of Frictional Properties of n-Alkanethiols on Au(111) by Scanning Force Microscopy"1999 J. Phys. Chem. B. 103; 8290.

[Li03] L. Li, S. Chen, S. Jiang. " Nanoscale Frictional Properties of Mixed Alkanethiol Self-Assembled Monolayers on Au(111) by Scanning Force Microscopy: Humidity Effect" 2003 Langmuir 19; 666.

[Li05] S. Li, P.l Cao, R. Colorado, Jr., X. Yan, I. Wenzl, O. E. Shmakova, M. Graupe, T. R. Lee, S. S. Perry. "Local Packing Environment Strongly Influences the Frictional Properties of Mixed CH3- and CF3-Terminated Alkanethiol SAMs on Au(111)" 2005 Langmuir 21;933-

[Lio97] A. Lio, D. H. Charych, M. Salieron. "Comparative atomic force microscopy study of the chain length dependence of frictional properties of alkanethiols on gold and alkylsilanes on mica" 1997 J. Phys. Chem. B. 101; 3800.

[Lio97b] A. Lio, C. Morant, D. F. Ogletree, M. Salmeron. "Atomic Force Microscopy Study of the Pressure-Dependent Structural and Frictional Properties of n-Alkanethiols on Gold" 1997 J. Phys. Chem. B. 101; 4767.

[Maugis92] D. J. Maugis. "Adhesion Of Spheres - The JKR-DMT Transition Using A Dugdale Model" 1992 J. Colloid Interface Sci. 150; 243.

[Müller80] V. M Müller, V. S Yushenko, B. V. J. Derjaguin. "On The Influence Of Molecular Forces On The Deformation Of An Elastic Sphere And Its Sticking To A Rigid Plane" 1980 J. Colloid Interface Sci., 77; 91.

[Qian03] L. Qian, F. Tian, X. Xiao. "Tribological properties of self-assembled monolayers and their substrates under various humid environments" 2003 Trib. Lett. 15; 169.

[Salmeron01] M. Salmeron "Generation of defects in model lubricant monolayers and their contribution to energy dissipation in friction" 2001 Trib. Lett. 10; 69.

[Schönherr99] H. Schonherr, G. J. Vancso. " Tribological properties of self-assembled monolayers of fluorocarbon and hydrocarbon thiols and disulfides on Au (111) studied by scanning force microscopy" 1999 Materials Science and Engineering C 8–9; 243.

[Tian99] F. Tian, X. Xiao, M. M. T. Loy, C. Wang, C. Bai "Humidity and temperature effect on frictional properties of mica and alkylsilane monolayer self-assembled on mica" 1999 Langmuir 15; 244.

[Xiao00

] X. Xiao, L. Qian. "Investigation of Humidity-Dependent Capillary Force" 2000 Langmuir 16; 8153.

[Yourdshahyan01] Y. Yourdshahyan, H. K. Zhang, A. M. Rappe "n-alkyl thiol head-group interactions with the Au(111) surface" 2001 Phys. Rev. B: Condens. Matter. 63; 81405(R).

[Zhang05] Q. Zhang, L. A. Archer. " Interfacial Friction of Surfaces Grafted with One- and Two-Component Self-Assembled Monolayers "2005 Langmuir 21; 5405.

[Zuo05] L. Zuo, Y. Xiong, X. Xie, X. Xiao. "Enhanced Lubricity in Mixed Alkanethiol Monolayers" 2005 J. Phys. Chem. B. 109; 22971.

CHAPTER 6.- TRANSPORT PROPERTIES OF SAMs AT SUBMONOLAYER COVERAGE.

The enormous interest in understanding how electrons flow through organic matter was already mentioned in chapter 2. Its importance in different research areas (rationalizing electron transfer in biological molecules, fabrication of microelectronic devices and sensors, developing molecular electronics, or interpreting STM data) has triggered the development of numerous experimental approaches to measure transport trough organic layers to gain further insight into the transport mechanisms. Unfortunately, the characterization of charge transport at the molecular scale has to date been dependent on the particular device fabrication and sample preparation. The difficulties in making reproducible electrical contacts and understanding the full spectrum of factors influencing the electrical properties of metal-molecule-metal junctions (molecular length, molecular conformation, highest occupied molecular orbital-lowest unoccupied molecular orbital (HOMO-LUMO) gap, molecule-electrode contact, electrode work function….) make these transport measurements experimentally challenging and intriguing and might, to a great extent, explain the wide dispersion of results collected for the particular alkanethiol molecular system [Salomon03][Lee04]. In fact, for these a priori fairly simple molecules (non-conjugated, sigma bonded, localized orbitals) there is still considerable ongoing investigations to elucidate the different transport mechanisms leading to current signal.

We agree with other groups who have addressed the study of the mechanisms of electron transfer through organic matter that a fruitful experimental approach is to correlate rates of electron transfer with molecular structure, and to infer mechanisms from these correlations. Therefore, the structural and mechanical characterization presented in chapters 4 and 5 are essential for the discussion of the results presented in this chapter.

We have taken advantage of the versatility of the SFM technique to study the transport properties of alkanethiol SAMs, since the use of a conductive tip provides a straightforward manner of contacting the organic layer. The additional use of submonolayer coverages has emerged as an interesting alternative to avoid some of the uncertainties above mentioned and perform an accurate transport characterization. The experimental setup is schematically shown in figure 6.1: the conducting tip is placed in direct contact with the sample surface, and the current can be measured as a function of the bias voltage applied between tip and substrate, thus providing the current-voltage (I-V) characteristics of the molecular junction. In our experimental setup, voltages are always applied to the tip and the substrate is grounded. The measurements have been performed in a N_2 environment to diminish the effect of humidity.

The use of SFM for junction investigations does not need of micro- or nanofabrication processes as in, for example, the nanopore methodology [Wang03]. This, in terms of time, means that the study of the junction is limited by the synthesis of the molecules and their assembling on conducting substrates, and not by the measurement methodology itself. Besides, the formation of the junction contact by C-SFM is a "soft" process where high-temperature contact-forming steps, that might damage

the organic layer, are avoided. Other techniques as the scanning tunnelling microscope and the Hg drop junctions [Slowinski97] [Holmlin01][Rampi02] share these characteristics with the C-SFM.

Nonetheless, it is important to note the difference between the C-SFM method and the STM for characterizing molecular junctions. In STM, current, not force, is used to control tip positioning. Because the conducting properties of the molecules under study are generally unknown, the position of the probe with respect to the molecules might be uncertain. If the STM tip is not in contact with the monolayer, the junction transport properties are determined by the molecules and the vacuum (or air) gap between the molecules and the tip. If the tip penetrates the monolayer, it is difficult to know how deep it has penetrated. C-SFM does not have this difficulty because the tip-sample distance is controlled by the feedback in normal force, which allows accurate positioning the probe to be just in contact with the monolayer. At low contact forces, there is no ambiguity in C-SFM about where the tip is with respect to the endgroups of the SAM. Moreover, the ability to control and vary the applied load on the contact (in the nN range) is a unique characteristic of this technique and opens opportunities for exploring the electron transfer as a function of molecular deformation under pressure.

Though SFM has been used in different works to probe the electrical properties of organic layers [Wold01][Sakaguchi01][Cui02][Song06], the contribution of the present work resides in the simultaneous and controlled investigation of the structural, mechanical and electrical properties of organic SAMs. In order to that, we use the so called three-dimensional (3D) modes described in section 3.4.2.

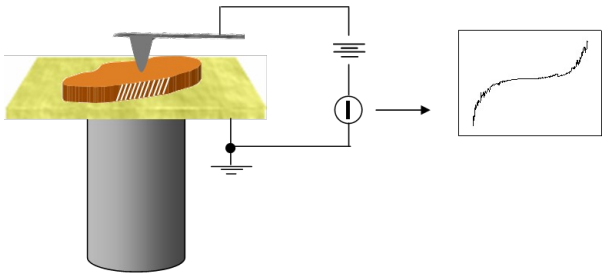

Figure 6.1 Schematics of the experimental setup used. The top and bottom contacts are the SFM probe (coated with a conductive-diamond layer) and the gold substrate. I-V curves are measured varying the voltage applied to the tip. The substrate is grounded.

The inherent chemical and physical properties of the alkanethiol molecules to form controlled local geometries and the excellent contact derived from the strong S-Au covalent bond at the interface, facilitates the junction formation. Reported behaviour for this system (SFM-tip-alkanethiolate-gold) is often consistent with nonresonant tunnelling models which include temperature independence, exponential length dependence and sigmoidally shaped I-V traces (see next section). Nonetheless,

akin to the frictional studies, most of the reported results have been obtained in complete monolayers, which often present a higher density of defects. This, in fact, can affect the measured conductivity due to variations in current along boundaries between metal grains and organic domains. Moreover, the presence of defects such as pinholes, gauche defects and missing molecules, would reduce the efficiency of electronic coupling through chains and consequently influence the transport characteristics. The advantages of using submonolayer coverages have been listed several times in this thesis: larger domains with higher crystalline quality, bare gold as an in-situ reference, coexistence of different configurations for the same molecule… We therefore believe that the use of islands instead of complete monolayers is an innovative and appropriate approach to study the transport properties in alkanethiol layers.

In the first part of section 6.2 we have proved the suitability of the C-SFM and the 3D modes for transport measurements on the alkanethiol islands. Next, we have focused on the confirmation of the tunnelling conduction mechanism for alkanethiol molecules and the identification of the effects of tip induced loading force on the junction properties. These experiments have been performed for different molecular lengths and the results obtained are discussed on the basis of the structural and mechanical characterization presented in the previous chapters.

In the final part of the chapter, we have addressed the question of the existence of different transport mechanisms in these alkanethiol junctions. The spontaneous formation of two differently tilted configurations for the same molecular length offers the opportunity to elucidate the relative importance of the different transport mechanisms that have been proposed in order to account for the tunnelling current in alkanethiol molecules (see next section). Briefly, if the electron pathway is along the chain, negligible differences would be expected in the current response of the 30°- and 50°-tilted configurations, since in both cases the molecular length is the same. Conversely, if other inter-chain pathways are involved, the different tilt angle should yield different current signals. Interesting results are obtained as a function of the chain length.

6.1 BASIC CONCEPTS ON TRANSPORT THROUGH ALKANETHIOL SAMs.

The transport mechanisms in molecular junctions depend mainly on the position of the Fermi levels of the metal electrodes relative to the HOMO and LUMO of the molecular bridge. When the difference in energy between the Fermi level and the molecular orbitals is large, electron transport is dominated by a non-resonant tunnelling mechanism. Moreover, depending on the magnitude of the applied bias (V) as compared with the tunnelling barrier height (Φ_B) [17], this tunnelling can be classified into either direct ($V < \Phi_B/2$) or Fowler-Nordheim ($V > \Phi_B/2$) tunnelling. These two mechanisms can be distinguished due to their distinct current-voltage dependence (see [Wang03]). If the Fermi level

[17] Φ_B is a qualitative measure of the position of the Fermi level within the HOMO-LUMO gap.

approaches the energy of the molecular orbitals, the electron transfer process will take place according to a resonant tunnelling or a hopping mechanism [Wang03].

Phenomenologically, the non-resonant and resonant regimes differ in the dependence of the current on distance and applied voltage. Non-resonant tunnelling predicts an exponential decrease in current with distance [Ratner98]; resonant tunnelling predicts weak distance dependence. For the former, current should be linear with applied voltage in the low-bias regime (generally between ±0.5V) and increase exponentially at higher applied voltages; in the resonant regime, current should increase sharply, approaching an ohmic behaviour [Ratner98] [Wang03][Wang05][Tran06]. Based on this description and the existing results (obtained for applied voltages in the range -3< V < 3V), conduction through the alkanethiol films is consistent with coherent non-resonant electron tunnelling, with the Fermi level of the metallic contacts lying within the large HOMO-LUMO gap of the molecules (~8eV [Fujihira72]).

6.1.1 The Simmons Model.

To further investigate the characteristics of the transport through alkanethiol SAMS, the tunnelling behaviour observed has frequently been roughly approximated as tunnelling through a rectangular barrier. Then current density can thus be modelled with the simple Simmons relation [Simmons63]:

$$J = \left(\frac{e}{4\pi^2\hbar d^2}\right)\cdot\left\{\left(\Phi_B - \frac{eV}{2}\right)\cdot\exp\left[-\frac{2\sqrt{2m}}{\hbar}\cdot\alpha\cdot d\cdot\left(\Phi_B - \frac{eV}{2}\right)^{1/2}\right]\right.$$

$$\left.-\left(\Phi_B + \frac{eV}{2}\right)\cdot\exp\left[-\frac{2\sqrt{2m}}{\hbar}\cdot\alpha\cdot d\cdot\left(\Phi_B + \frac{eV}{2}\right)^{1/2}\right]\right\} \qquad (6.1)$$

where m is electron mass, d is barrier width (generally taken as the molecular length), Φ_B is barrier height, V is applied voltage and ħ is Planck's constant divided by 2π. To obtain more accurate fittings to the experimental data, for alkanethiol junctions the Simmons model has been modified with a parameter α [Holmlin01][Wang03]. This parameter provides either a way of applying the tunnelling model of a rectangular barrier to tunnelling trough a nonrectangular barrier [Holmlin01] or an adjustment to account for the effective mass (m*) of the tunnelling electrons through a rectangular barrier [Cui02][Wang03]. The success of this model in describing the current versus voltage characteristics of alkanethiol SAMs has been proven in different works.

Particularly, in the low bias region, equation (6.1) can be approximated as

$$J \approx \left(\frac{(2m\Phi_B)^{1/2} e^2 \alpha}{h^2 d} \right) \cdot V \cdot \exp\left[-\frac{2\sqrt{2m}}{\hbar} \cdot \alpha \cdot d \cdot (\Phi_B)^{1/2} \right] \quad (6.2)$$

and a tunnelling decay coefficient, β, can be defined from $J \approx (1/d) \cdot \exp(-\beta \cdot d)$ as:

$$\beta = \frac{2\sqrt{2m}}{\hbar} \alpha (\Phi_B)^{1/2} \quad (6.3)$$

Therefore, by fitting individual I-V curves using equation 6.1, α and Φ_B values can be determined and β can be calculated from equation 6.3.

This β parameter is a structure-dependent factor that has emerged as a characteristic parameter of the junction and can be used to classify the ability of molecular structures to provide a medium that facilitates tunnelling from one electrode to the other.

To obtain β-value, instead of fitting individual I-V curves for a specific molecular system, the tunnelling current is measured as a function of the electrode separation, d, which can be done, for instance, by changing the length of the molecules forming the SAM. Though equation 6.2 is not strictly exponential in d, it is generally approximated as such since the exponential factor dominates. Therefore, in the low voltage region where equation 6.2 is valid (±0.5V), the slope of the ln(J) versus d plot yields the value of β. The values reported from different experimental techniques for alkanethiolate SAMs on Au and Hg range from 0.8 to 1.1 $Å^{-1}$[Wang05].

6.1.2 Through-Bond And Through-Space Tunnelling Mechanisms.

When calculating this β parameter in units of $Å^{-1}$, the value of d (junction separation) is usually identified with the molecular length, which do not necessarily correspond to layer thickness (depends on the molecular tilt). This assumption means that the major tunnelling pathway involves tunnelling through the σ-bond path, i.e. electron flows primarily along the alkyl backbone. This pathway is the so-called through-bond (TB) tunnelling and is taken as the dominant mechanism in alkanethiol molecules.

However, through-bong tunnelling may not be the only contribution to the transport mechanisms in alkanethiol molecules. In [Slowinski97] Slowinski and coworkers measured an increased in the current through an alkanethiol SAM on a hanging Hg drop electrode, during drop expansion. The authors claimed that, in response to that expansion, the molecules increased their tilt with respect to the surface normal, thus reducing the film thickness while maintaining the TB channels invariant (i.e. the length of the molecules was not changed). To account for the observed increase in current, an additional pathway for tunnelling through the alkanethiol SAMs had to be considered.

This is schematically shown in figure 6.2: in addition to the through bond (TB) tunnelling in which the electrons flows along the backbone of the alkane chains (solid arrows in figure 6.2), a second pathway exists, the so-called chain-to-chain tunnelling, in which the electrons pass across the

film through states located on neighbouring chains, lying in the shortest direct path for tunnelling. This chain-to-chain pathway involves one (or more) through-space (TS) hops between adjacent alkyl chains (dashed arrow in figure 6.2). The total length of pathways involving a TS hops decreases with respect to the TB path length by $x=d_{cc}tg\theta$, where d_{cc} is the distance between adjacent molecules and θ is the tilt angle. This corresponds to the white segment in figure 6.2. Therefore, the larger the tilt angle, the shorter the chain-to-chain pathway is with respect to the TB one. In reference [Slowinski97] a value for the through-space decay constant of β_{TS} = 1.31 $Å^{-1}$ was reported. Its higher value, with respect to the value reported for TB tunnelling (β_{TB} = 0.9 $Å^{-1}$), was explained based on the weaker through-space coupling across the van der Waals bridges between two adjacent chains, compared to the coupling along the σ-bonded alkane chain. Nonetheless, this chain-to-chain interaction must be taken into account for SAMs with large tilt angles.

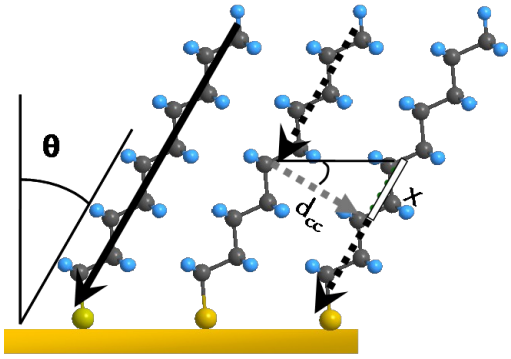

Figure 6.2 Schematics of the two electron tunnelling mechanisms. Black arrows mark the through-bond (TB) tunnelling pathway along the molecular backbone. The chain-to-chain mechanism is marked by the dashed arrows. It involves a sum of through-bond (black dashed arrows) and through-space (grey dashed arrow) pathways. The white segment marked x corresponds to the decrease of the TB pathway length due to chain-to-chain hop.

Being aware of the problems of the Hg technique, used in the above described experiment, when facing the study of long molecules (the corresponding SAMs tend to fracture as the drop expands for (n>14), [Slowinski97]), we have tried to fill this gap undertaking the study of the transport properties for long and short alkanethiol molecules with C-SFM. Particularly, we are interested on getting further insight on the chain-to-chain tunnelling mechanism aforementioned, which has been scarcely investigated since it requires the complex task of changing the SAMs thickness without changing the length of the molecules. The approach presented in this chapter has proved to be a suitable way of attaining such objective.

There have been other groups studying the transport mechanisms of SAMs by means of C-SFM, which indeed endorse the suitability of the technique for electrical measurements [Salmeron93] [Leatherman99][Wold00][Cui02][Ishida02][Selzer02][Wold02][Nakamura03][Engelkes04][Jiang06] .Unfortunately, the study of the different transport mechanisms is not so straightforward with this technique as it is with Hg electrodes, because varying the SAM thickness without changing the

molecular length (to isolate the chain-to-chain contribution) is not a simple task. The most direct approach used up to now is to compress the monolayer by increasing the load applied with the tip. Nonetheless, care has to be taken since increasing the applied load does not only lead to chain tilting but it also produces conformational defects (gauche defects, molecular bending) and even tip penetration through the SAM, affecting the measured current. Another interesting approach to study the TS contribution has been reported in [Yamamoto02], where results for SAMs presenting different tilt angles due to adsorption on different substrates were compared. However, an accurate study of the effect of the tilt angle on the transport properties, implies measurements where any possible contribution to the current coming from external factor (e.g. different electrodes) is minimized.

Our preparation procedure, leading to the spontaneous formation of differently tilted configurations provides an ideal scenario for these studies. Different SAM thicknesses are available for the same chain length, because molecules are arranged with different tilt angles, without SAM compression, within the same substrate and for short and long molecules. Moreover, in order to avoid tip dependent features, the same conducting probe has been used for the data presented within each graph.

6.2 TRANSPORT PROPERTIES OF ALKANETHIOL ISLANDS.

Prior to any current versus voltage measurement the tip conditions have been tested by acquiring, at the lowest practical force, simultaneous topographic and current images of a selected area presenting alkanethiol islands and bare gold terraces. When the conductive layer of the tip is not damaged, images like the one shown in figure 6.3 are routinely obtained. This figure shows three examples acquired on C12, C16 and C18 samples at different applied voltages. We have also included the same measurement performed on a C16 complete monolayer (bottom figures).

Following the colour code for all the images presented in this work, in the current images bright (dark) corresponds to higher (lower) current values. Akin to the lateral force images, the current shows an enhance contrast with respect to the topographic images, due to the different electrical character of the bare gold (metallic) and the alkanethiol molecule (insulator). The islands are easily identified as black patches in the right column of figure 6.3. These images ensure that the conducting tip is in good conditions to perform the current versus voltage analysis. When the conductive layer is damaged or some unbounded molecules or contaminants are adsorbed on the tip, no current is measured within the bare gold areas. In the latter case, the tip can be cleaned by applying a bias pulse (5-10V) to eliminate the possible contaminants. If the conducting behaviour is not recovered, the tip is then replaced by a new one.

It can be seen that the non-conducting character of the complete monolayer is considerably worse than in the alkanethiol islands. This is due to the higher density of defects present in the

monolayer (domain boundaries, missing molecules…) that facilitate electron transport between tip and substrate.

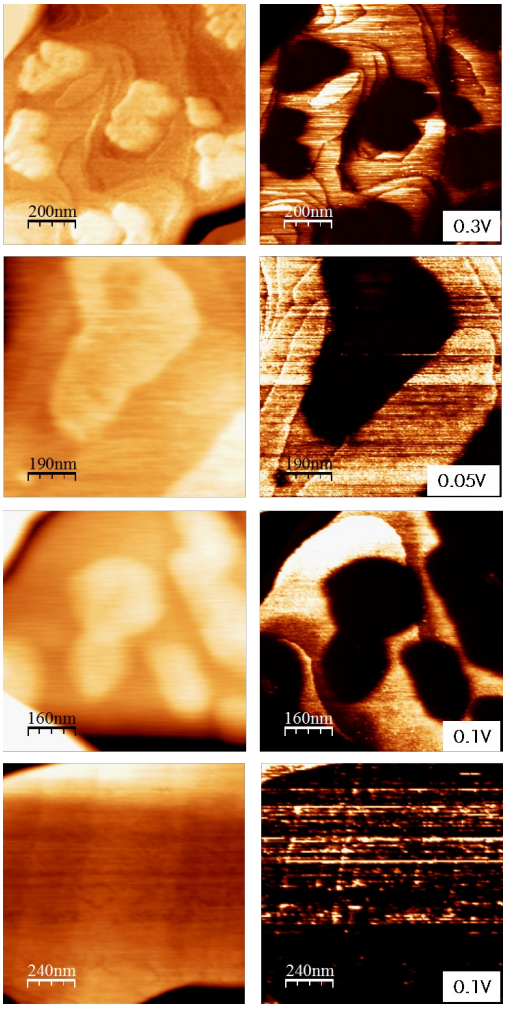

Figure 6.3 Simultaneous SFM topographic (left) and current (right) images acquired on C12, C16 and C18 samples (from top to bottom). The bottom images correspond to a C16 monolayer. Bright (dark) corresponds to high (low) values of the respective images.

The current measured on the bare gold areas may vary among different samples. The presence of a water layer and unbounded molecules on the gold terraces and the tip surface seem to be at the origin of this variation. This is corroborated by the fact that scanning several times the same area generally leads to an increase of the current signal that reaches the saturation value: with the sweeping action of the tip we can clean the electrodes surfaces and the ohmic tip-Au contact is observed.

These simultaneous topographic and current images are not only acquired prior to the I-V analysis but also after the 3D measurements have been performed. Since the 3D modes imply acquiring I-V curves at increasingly applied load over a selected point (see section 3.4.2), it is necessary to check if any damage has occurred to the island (we know from chapter 5 that wear can

occur when increasing the load). This is done by reimaging the islands after the acquisition of the 3D measurements.

This is illustrated in figure 6.4 for a C12 island presenting the hexagonal configuration. Both, topographic (left) and current (right) images correspond to before (top) and after (bottom) several conductivity measurements were performed on top of the island. The non-conducting character of the molecular island, at low voltages (tip bias of +0.1V), and the piercing effect when applied load is enough to penetrates through the film are clearly visible comparing the four images. The aforementioned "cleaning" effect of the sweeping is also observed.

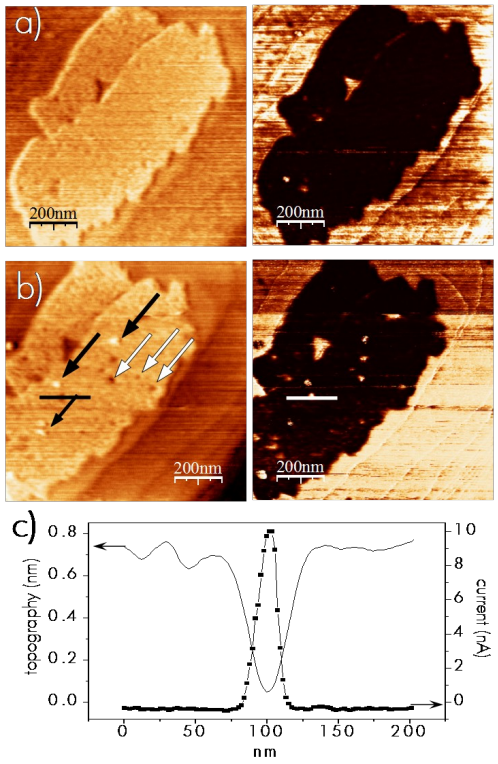

Figure 6.4 Topographic (left) and current (right) SFM images taken at a tip bias voltage of +100 mV, before (a) and after (b) loading experiments were done on top of the alkylthiol island. (c) Line profiles across pinholes in both topographic and current images after tip penetration through the island.

In some of the specific positions where the load increasing experiments have been performed, molecules have been displaced away (holes marked by white arrows) indicating that the tip has penetrated the film. The maximum applied force in this case has been 35nN (when the applied load is kept below this value, no damage is observed).

Whereas the resulting debris of non-bonded material (bright spots marked by black arrows) disappears by subsequent tip sweeping, the pinholes induced by tip penetration remain as permanent marks. At these position, the tip reaches ohmic contact with the gold substrate underneath and, as can

be seen in the current image (right), the produced pinholes behaves as conductive dots within a non-conducting film.

The damage induced when the tip penetrates through the molecular layer serves to in situ estimate the tip radius. Due to smaller convolution effects (figure 6.4(c)), the tip radius is obtained from current profiles rather than from topographic profiles. After statistically averaging measurements taken on different points, a tip radius of ~10±2 nm is obtained in accordance with the technical specifications. Once the tip radius is known, we can calculate the pressure exerted when indentation marks appear using the DMT model (equation 5.7).[18] The value obtained, ~1.1GPa is in good agreement with the previously reported threshold pressure needed for tip penetration through an alkanethiol island which have been reproduced in figure 5.13.

These results emphasize the extreme care that has to be taken when interpreting C-SFM transport measurements, in general, and through organic films and alkanethiol SAMs, in particular. In most of the reported works, imaging of the sample is avoided to preserve the conducting coating of the probe. In this way, any damage like those shown in figure 6.4 is not visualized. Moreover, it is generally assumed that the main effect of tip compression is molecular tilting. However, from the above images it is clear that film distortion and even tip penetration can occur even at low applied load values. All this would influence the transport measurements making it difficult to accurately discriminate between the different transport mechanisms and obtain the corresponding decay parameter. This can also be among the reasons of the difficulties found to conciliate results from different groups and different measuring conditions.

In this context, the 3D modes have emerged as a suitable approach to perform transport measurements while maintaining a precise control over the applied load and tip position. Though in section 3.4.2 we described the main features of these measuring modes, in the next section we have detailed the plentiful information that can be obtained from a single measurement.

6.2.1 Simultaneous Measurement Of I(V,z) And F(V,z) Images.

The simultaneous measurements of the vertical cantilever deflection (F) and the current (I), both as a function of the bias voltage (V) and the vertical piezo displacement (z), are shown in figure 6.5 for a C12 island.[19] The F(V,z) image has been represented as a top view (a) and as a three-dimensional plot (b). Along the fast scan direction the applied voltage is varied between ±2 V and along the slow scan direction the piezo moves 25nm (positive values indicate the piezo moves the sample towards the tip). We also show the common way of presenting the F-z curves (c). It corresponds to the vertical line profile, taken at V= 0V, on the image in (a). The different regions

[18] For the diamond-coated conductive tips used the Young modulus and Poisson ratio are E_{tip}=1000GPa and ν_{tip}=0.15, respectively [Alamarguy04].

[19] The applied load can be obtained straightforward from the vertical cantilever deflection with equation 3.1. For this reason we have already labelled it as (F) and the data shown in figure 6.5 is presented in nN.

described in section 3.3.1 (approaching, snap-in point, repulsive regime...) can be straightforward identified in (c). Clearly, the tip is not initially in contact with the surface.

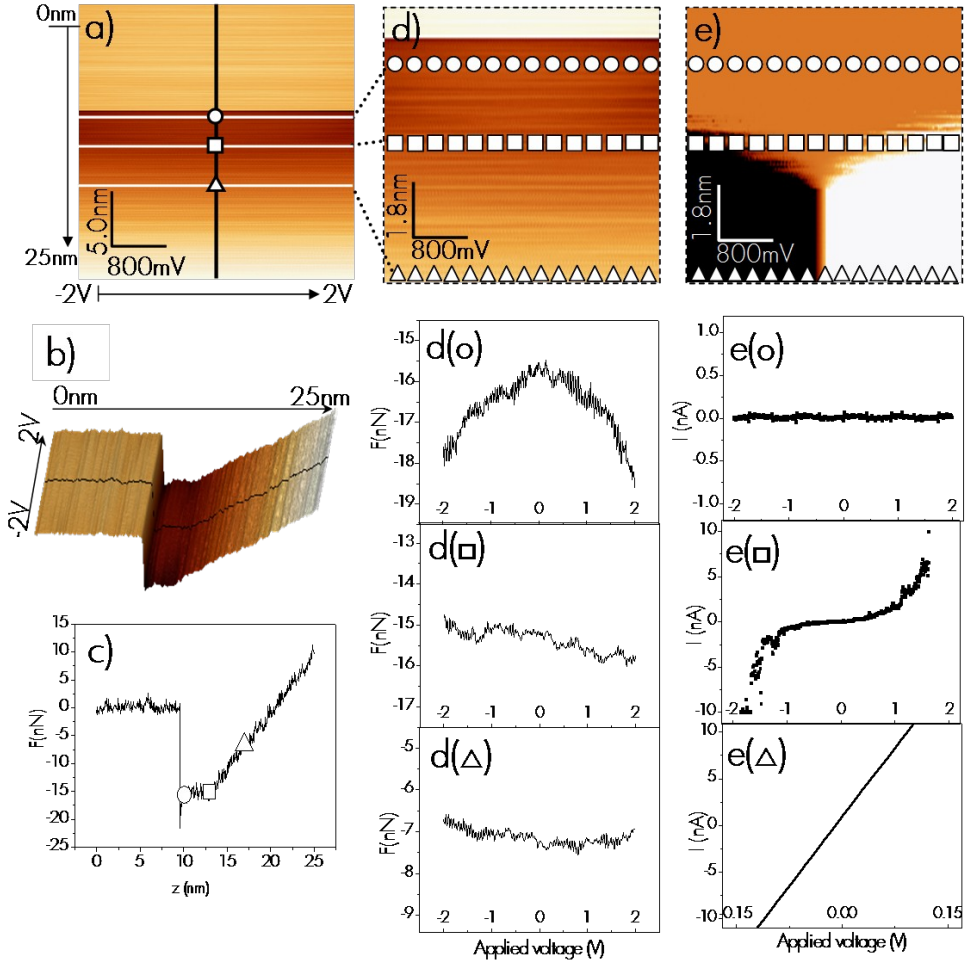

Figure 6.5 Top view (a) and three-dimensional view (b) of the normal force image, *F(V, z)*, for a total piezo-displacement of z = 25 nm. (c) Line profile marked as black lines in (a) and (b) that corresponds to the *F–z* curve at V = 0 V. Magnification (total piezo-motion$z$ = 9 nm) of the simultaneously acquired normal force (d) and current (e) images. The voltage range is ±2 V for all these images. The horizontal line profiles marked on each image are the *F–z* curves, d(○, □, △) and the *I –V* curves e(○, □, △) measured at the z piezo-position indicated by the corresponding symbol in (c). For clarity, the same symbols have also been used to draw the respective lines in (d) and (e).

Figure 6.5(d) shows a magnification (note the new z-scale) of (a) and figure 6.5(e) is the corresponding I(V,z) image. For each tip-sample distance (i.e. for a given point of the F-z curve) horizontal profiles taken on the image (d) and (e) provide the corresponding F-V and I-V curves, at the selected z.

To better describe the junction properties, three representative points have been selected in the F-z curve in (c), marked with three different symbols (○, □, △) which are also used to label the F-V and I-V curves measured at each location. Though the sudden drop of F at point (○) is characteristic of the jump into contact regime, at this point, the data in e(○) indicate that no current flows between tip and

sample. Furthermore, from d(○) it can be seen that the force has a parabolic dependence with the applied voltage, indicating that the interaction between tip and sample at this point is mainly electrostatic, described by equation (3.9). Therefore, both the current and force behaviour suggests that the tip is not yet in contact with the alkanethiol island. Note also that the almost constant cantilever deflection from point (○) to point (□) in the F-z curve indicates that during this part of the piezo motion the applied force is constant while the tip-substrate distance is decreased. A similar behaviour has already been reported and was ascribed to the presence of a layer of non-bonded molecules on the tip [Mate92][Salmeron93]. To contact the alkanethiol island, the tip must penetrate this layer, which requires an extra piezo motion. At point (□), the tip-island-substrate junction is finally formed.

As can be seen in e(□), at this point the corresponding measured I-V curve shows a sigmoidal shape over the ±2 V voltage range, with a linear response in the low bias region (±0.5 V). This is in good agreement with the tunnelling mechanism modelled by the Simmons relation (see section 6.1). A noticeable asymmetry with respect to the voltage sign is observed. In fact, slightly more current is consistently measured when the tip is biased negatively relative to the substrate. This asymmetry in the I-V characteristics of alkanethiol junctions is associated to the difference in coupling at the two metal-molecule interfaces: one end of the molecule is chemisorbed to the bottom contact and the other end is in physical contact to the probe [Engelkes04][Lee04].

The sigmoidal shape of the I-V curves persists during some extra piezo motion of $\Delta z \approx 2.5$ nm, coinciding with a F-z linear response.[20] As the tip-substrate distance decreases, the slope of the linear I-V region (around ±0.5 V) becomes steeper, leading to the triangular shape observed in figure 6.5(e). The substrate is eventually contacted at the triangle vertex, in this particular case at a total load of about 10nN (F_{adh}=20nN). A linear shape of the I-V curve corresponding to the ohmic response of the metallic contact is observed from this point until the bottom end of the image. This behaviour has been depicted in e(△) for the selected location.

When the tip is in contact with the alkanethiol island, the F-V curves in d(□) and d(△) show that the applied load is relatively insensitive to the bias voltage. This is a very interesting result, since few works have tried to estimate the role of the "electrostatic" load on the junction when I-V curves are acquired [Wold01]. Our measurement procedure is a direct probe that at a bias voltage as high as 2 V, the additional load due to electrostatic interaction is lower than 0.5nN.

6.2.2 Determination Of The Decay Parameter (β).

Similar 3D measurements have been performed as a function of the chain length (C12, C16 and C18) and for two molecular configurations (hexagonal and rectangular). The voltage range has

[20] In this region the dimensionless slope of the F-z curve is ≈ 0.7, i.e. due to the presence of the SAM, the cantilever deflection is reduced by this factor with respect to the piezo-displacement. This implies some kind of deformation (elastic deformation, molecular tilting…) within the island as the applied load is reduced since in a hard surface (where deformations can be neglected), the dimensionless slope is 1.

been maintained well below the junction breakdown voltage, which is known to cause irreversible changes in the junction properties. This breakdown voltage has been found to be length dependent (increasing for longer molecules), and for C12 molecules is ~2.5 V. In fact, the breakdown process has been reported to be field, not voltage, dependent with a value for the breakdown field in the range of $1 \cdot 10^8$ V/cm [Haag99][Wold01][Cui02].

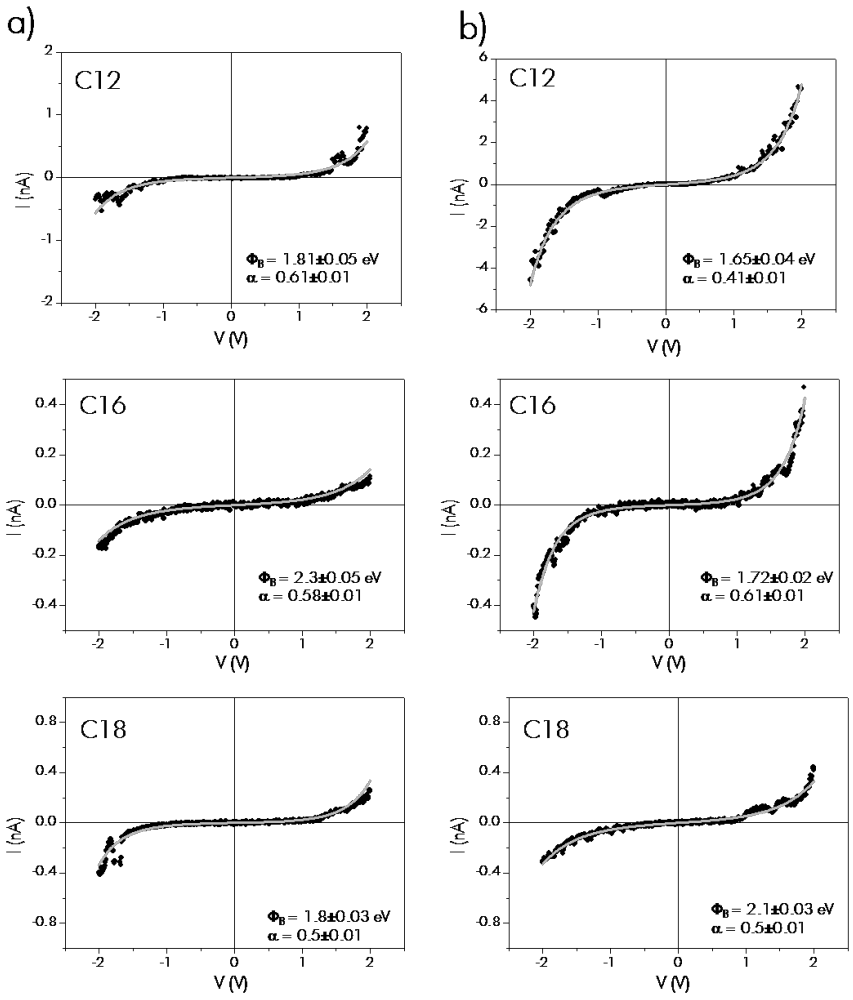

Figure 6.6 Current-voltage (I-V) curves for C12, C16 and C18 islands presenting the hexagonal (left) and rectangular (right) configurations. The solid grey line is a fit to the experimental data using equation 6.1, adjusting the parameters Φ_B and α. Their final values are shown within each graph.

Figure 6.6 shows some representative I-V curves (i.e. horizontal profiles in the I(V,z) images) obtained for C12, C16 and C18 islands presenting the hexagonal (a) and the rectangular (b) configurations. All the curves in this figure have been acquired at minimum applied loads, where SAMs deformation is negligible. The voltage swept has been performed from positive to negative values and vice versa (i.e. two I(V,z) images are always recorded), and no significant differences are appreciated between the corresponding I-V curves.

The characteristic sigmoidal shape is observed in all the curves and, though the current values depend on the corresponding contact area (the larger the area, the larger the number of molecules that contributes to the signal), on overall the current decreases for increasing chain length. Moreover, for a given voltage value, islands presenting the rectangular configuration often yield higher current values than the corresponding hexagonal one. Though both observations could be, in principle, understood based on the exponential decay of the current with electrode separation, predicted by the tunnelling mechanism, we will see that their combination points to the existence of a transport mechanism different from through-bond tunnelling since, for a given molecule, the rectangular and hexagonal configurations present the same number of TB channels (i.e the length of the chains is the same). The detailed analysis of the different mechanism is carried out in section 6.2.4.

In order to compare these curves to what is expected for a simple tunnelling process, we have used the simple Simmons model. From equation (6.1) by adjusting two parameters, Φ_B and α, a non-linear square fitting has been performed to the data of figure 6.6.[21] The results of the fits are shown as the solid lines in each graph. In all cases, the I-V curves are well reproduced by this simple model and the values obtained for Φ_B and α, indicated within each graph, are within the range of experimental and theoretical reported values for alkanethiol based junctions [Lee04].

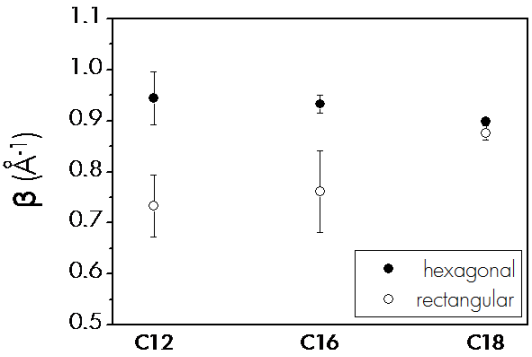

Figure 6.7 Value of the decay parameter (β) obtained from equation 6.3 for the hexagonal (solid symbol) and rectangular (open symbol) configurations.

We can now estimate the value of the decay coefficient β, from equation (6.3) using Φ_B and α obtained from the I-V fitting. In figure 6.7 we have plotted the averaged values for the different chains and for the rectangular and hexagonal configurations. To give an idea of the level of reproducibility and range of accuracy, we have included the error bars corresponding to the statistical deviation of a series of measurements performed in different islands with the same probe and from measurements performed using different probes. The low error bar for C18 does not comes from a

[21] In order to fit current (instead of current density) versus voltage curves, we multiplied equation 6.1 by the corresponding contact area, calculated with the DMT approach. Nonlinear least-square fittings have been performed using Microcal Origin 7.5.

better accuracy but to inherent difficulties in obtaining good and reproducible transport data for these long molecules, which reduces the statistics.

The values obtained for the islands presenting the hexagonal arrangement are in reasonable agreement with previously reported values for complete alkanethiol monolayers (0.8-1.1 $Å^{-1}$). This confirms the suitability of our measurement method to probe the transport characteristics of molecular junctions. More interesting are the results obtained on islands presenting the rectangular configuration. The β values measured are always smaller than those of the hexagonal configuration for C12 and C16. The mean value is 0.75±0.07 $Å^{-1}$. Conversely, for the C18 islands, the difference between both configurations is not significant. In next sections we will try to unravel whether this difference comes from the lack of statistics which hinders an accurate determination of the decay coefficients or to a different transport behaviour operating in these long molecules.

If through-bond tunnelling were the only transport mechanism along these alkanethiol junctions, the values of the decay parameter should be equal, within experimental error, for the 30°- and 50°-tilted configuration. The lower β values measured in the more tilted configuration points to a less attenuation of the current per unit distance in these islands, in other words, that more efficient tunnelling occurs along the 50°-tilted molecules.

It is worth noting that, since these results have been obtained without SAM compression (used to change the layer thickness in the reported works) and at the minimum practical load, the measured differences in current can be attributed to the different tilt angle between configurations and not to the presence of conformational defects or tip penetration that might also alter the current signal.

6.2.3 Load-Dependence Of The Junction Transport Properties.

The use of the 3D modes considerably facilitates the study of the loading effect on the junction properties, since from simultaneous F(V,z) and I(V,z) images akin to those shown in figure 6.5 we can obtain the I-V characteristics (horizontal profiles in the I(V,z) image) at the different applied loads. Generally, for a given voltage, the current through the junction increases as the applied load is increased. This is shown in figure 6.8 for C12 and C18 samples where each curve corresponds to a different applied force (shown in the inset).

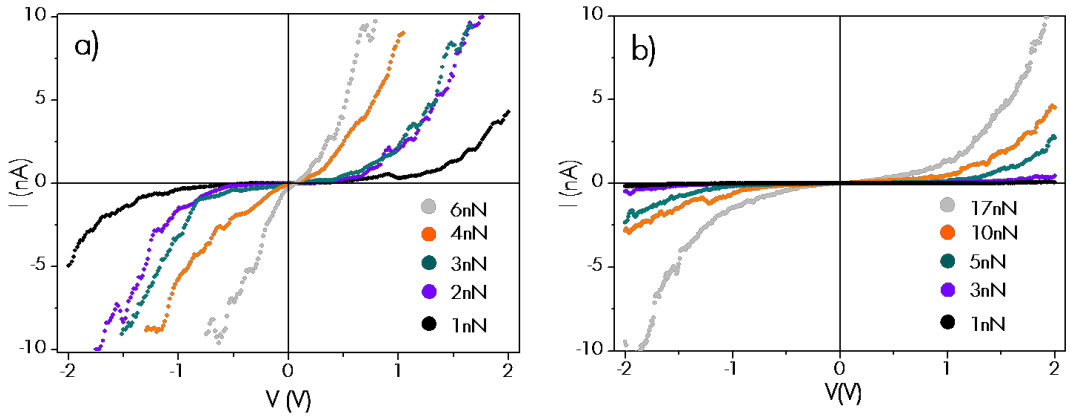

Figure 6.8 Set of I –V curves as a function of the applied load for C12 (a) and C18 (b) islands in the hexagonal configuration.

Comparing both graphs reveals that the effect of the applied load is more dramatic in the short-chain island. At loads above 6nN, the almost linear behaviour of the I-V curve indicates that the tip is penetrating through the island and reaching the underlying substrate. Conversely, at 20nN of applied load, the sigmoidal shape of the I-V curves is still observed in the C18 island. This is in agreement with the results presented in the previous chapter proving a higher resistance to wear in islands of longer chains (section 5.3.1) due to the larger cohesive energy.

Which are the reasons for the current increase as the load is increased? Some plausible effects of the applied load are, for instance: (1) increase in the junction contact area which in turns affect the number of molecules contributing to the current signal; (2) compression of the film either due to molecular tilting or elastic deformation; (3) changes in electronic properties as a result of film deformation. We have tried to discern among the possible effects by analyzing the behaviour of the junction resistance.

At low bias, equation 6.2 can be used to determine the resistance R of the junction, defined as the inverse slope of the linear region (±0.5 V) of the I-V curve. Therefore, for each curve of figure 6.7, we have calculated the corresponding resistance. The results plotted in figure 6.9(a) correspond to the I-V curves of figure 6.8(a). As expected from the I-V characteristics, the junction resistance decreases when increasing the applied load. For C12 monolayers, Frisbie and co-workers gave junction resistances, at applied loads of 2nN, as different as 1.2 GΩ and 45 MΩ, for tip radius of 22 and 50 nm [Wold01]. In extraordinary agreement, we obtain R=5 GΩ for the same load value and a tip radius of 10nm, as estimated from figure 6.4.

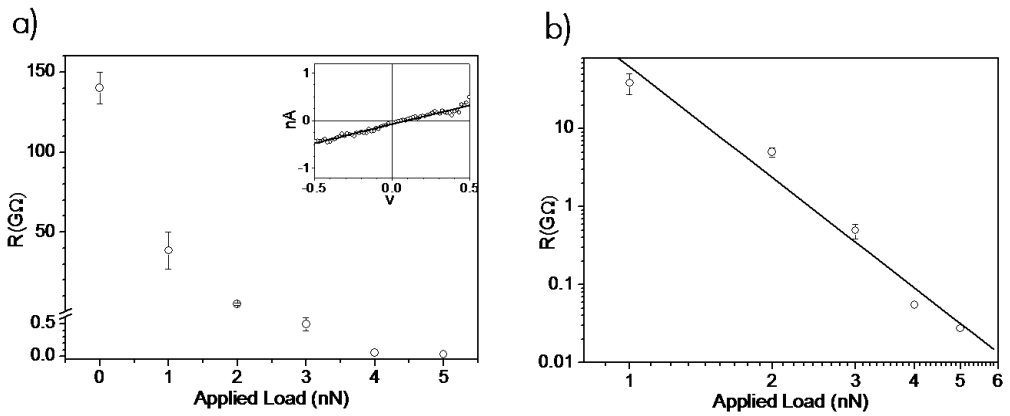

Figure 6.9 (a) Junction resistance as a function of the applied force. The inset shows the I –V data over ±0.5 V and the corresponding linear fit for the case of F = 2 nN. (b) Log-log plot of the junction versus the applied load. The linear fit yields a power law exponent of 4.7 ($R \propto (F)^{-4.7}$)

Figure 6.9(b) corresponds to the log-log plot of the data in Fig. 6.8(a). From the linear fit to the data we obtain the power law exponent, n= 4.7. This means that the junction resistance scales as $R \propto (F)^{-4.7}$. If the reduction in the junction resistance values were mainly due to an increase in the contact area, R would be expected to scale as $(F)^{-0.67}$ (equation 5.7) because the resistance is inversely proportional to the contact area. The clear deviation from this behaviour indicates that the resistance depends not only on contact area, but also on the deformation of the molecular structure and/or tip penetration through the island. The dispersion in the values of the power law exponent after statistical analysis is quite large, varying between 3 and 6.5, which can be due to possible differences in tip conditions and/or island compactness. Nonetheless, values much larger than 0.67 are always obtained, indicating that some structural changes take place.

This result poses some questions on the analysis of the tunnelling mechanisms through alkanethiol SAMs under applied load. Generally, increasing the load is the way used to change the film thickness and study transport mechanism different from through bond. It is assumed that most of the deformation is taken up by the tilting of the molecules, and the decrease in junction resistance (i.e. the increase in current) observed is then attributed to the contribution of the chain-to-chain mechanism [Cui02][Selzer02]. This can be true for SAMs adsorbed in Hg, which present a "liquid like" structure that facilitates the continuous tilting of the molecules when compressed [Slowinski97]. However, this might not be the case for SAMs presenting a well-defined 2D structure, as is the case of alkanethiols on Au(111). Instead, other defects such as gauche conformations might be formed under applied load.[22]

[22] We would like to mention that we have never observed the stepwise behaviour in the measured current, expected akin to that obtained because of molecular tilting under tip pressure in the friction versus load plots of chapter 5. This is due to the two strategies used while increasing the applied load: transport measurements are performed on a single point whereas friction measurements are acquired by scanning a selected line.

The comparison of the transport properties for the differently tilted configurations that spontaneously formed under our preparation conditions emerged as the correct answer to study the influence of the tilt angle on the tunnelling mechanisms avoiding tip perturbation of the films. The results obtained are presented in next section.

6.2.4 Influence Of The Tilt Angle On The Transport Properties.

The transport measurements collected in this section have been performed on islands arranged in the hexagonal and the rectangular configurations for different chain lengths (C12, C16 and C18). Only the I-V curves corresponding to the lower practical load have been analysed since, at these low loads, conformational defects within the island are avoided. Values of the junction resistance have been calculated from the linear region of the curves (±0.5 V), as in the previous section, and have been plotted in figure 6.10 as a function of the number of carbon atoms (a) and the island thickness (b). For a proper comparison between configurations, we have plotted the values after normalizing to the molecules under the contact area, i.e. correcting for the difference in molecular packing density (21.6 $Å^2$/molecule and 28.7 $Å^2$/molecule for the hexagonal and the rectangular configurations, respectively).

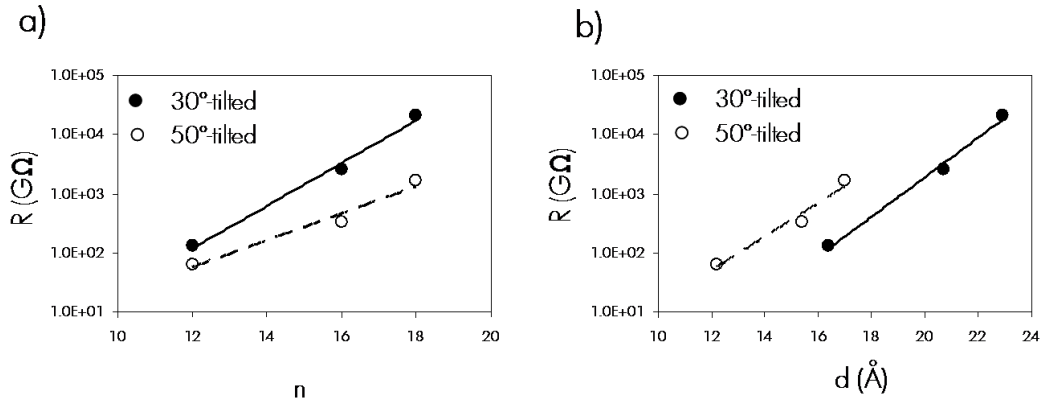

Figure 6.10 Log-plot of the junction resistance as a function of the number of carbon atoms (a) and the island thickness (b) for islands presenting the hexagonal (solid symbol) and rectangular (open symbol) configurations.

From the above graphs the following results can be inferred:

1.- The junction resistance exponentially decreases with decreasing the molecular length, for both configurations. This is expected for a tunnelling mechanism (either through-bond or chain-to-chain) in which the current scales exponentially with the electrodes distance.

2.- The transport mechanism for alkanethiol SAMs can not be totally ascribed to through-bond tunnelling. This is clearly seen in part (a), where islands formed by the same molecule (i.e. equal through-bond contribution) present different values of junction resistance. This has been already reported in [Slowinski97] for SAMs adsorbed on Hg electrodes, but this is the first time it has been

observed with C-SFM, avoiding film compression due to tip loading. Thus, the differences found can be almost exclusively attributed to the different tilt angle. The additional tunnelling pathway proposed in [Slowinski97] is the chain-to-chain tunnelling which involves intermolecular coupling between adjacent hydrocarbon chains. In figure 6.2 it is shown that, in relative terms, the chain-to-chain contribution to the overall current becomes more effective than the through-bond contribution with increasing tilt angle. The results of figure 6.10 are in agreement with that assertion. Moreover, we observe that the influence of the tilt angle is steeper the longer chains is (see graph (a)).

The data in graph (b) yields the β values in $Å^{-1}$ units, corresponding to the slope of the linear fits shown as solid (hexagonal islands) and dashed (rectangular islands) lines. The experimental values obtained are β_{HEX}=0.8±0.1 $Å^{-1}$ and β_{RECT}=0.65±0.09 $Å^{-1}$. This difference in the decay coefficient value was already observed in figure 6.7, where β was calculated from the fitting of individual I-V curves. We again obtain consistently lower β for the molecules tilted 50°, though the absolute values are slightly lower than in figure 6.7. Still, the β value obtained for the hexagonal configuration is within the range of those reported for complete alkanethiol monolayers.

3.- For islands presenting a similar thickness (see, for example, the data corresponding to C12-hexagonal and C18-rectangular in graph (b)), the junction resistance is always higher for the longer molecule. This result is explained considering the relative efficiency of both, through-bond and chain-to-chain mechanisms. Whereas the former implies tunnelling through the σ-bonds of the alkane chain, the latter includes through-space hops across van der Waals bridges which, in relative terms, have been reported to be equivalent to tunnelling across ~5.5 σ-bonds [Slowinski97]. This point is therefore a consequence of the greater efficiency of the through-bond mechanism.

In summary, the results shown in figure 6.10 are in good agreement with the proposed two-pathway model for tunnelling through alkanethiol SAMs: one is the through-bond tunnelling, which is independent of the tilt angle, and the second is the chain-to-chain coupling, involving through-space tunnelling, which is a function of the tilt angle.

To verify that this chain-to-chain contribution is responsible for the different measured current between the 30°- and the 50°-tilted configurations, we have compared our data with the tunnelling current expression proposed in [Slowinski97] that is given by:

$$I_t = I_0 \cdot \exp(-\beta_{TB} \cdot d) + I_0 \cdot n_s \cdot \exp\left[-\beta_{TB} \cdot (d - d_{cc} \tan\theta)\right] \cdot \exp(-\beta_{TS} \cdot d_{cc}) \qquad (6.4)$$

where I_t is the tunnelling current through the SAM, d is the length of the molecule, d_{cc} is the chain-to-chain distance (~4.3 Å), n_s is is an statistical factor accounting for the number of pathways containing a single lateral hop as compared to those containing only through-bond hops (it is assumed to be equal to the number of methylene units in the chain), β_{TB} and β_{TS} are respectively through-bond and

through-space decay constants. For C12, their reported values are β_{TB} = 0.91 Å^{-1} and β_{TS}= 1.31 Å^{-1} [Slowinski97].

The assumption that solely pathways including a single hop contribute to the chain-to-chain mechanism might be correct for small tilt angles, since the reduction of the tunnelling pathway due to TS tunnelling might not be significant for these angles (see figure 6.2) and still the more efficient TB mechanism dominates. However, for large tilt angles or long molecules the profits of the TS tunnelling, in terms of reduction of the electron pathway, might favour the contribution of pathways including several lateral hops. As shown below, this is the case for C18 in the rectangular configuration (50°-tilted)

Solid lines in figure 6.11 correspond to the tunnelling current calculated with equation (6.4). It can be observed that this equation adequately describes the experimental results obtained in C12 and C16 samples. However, it fails to predict the data measured in C18 molecules: the current shows stronger angle dependence than the predicted considering only a single interchain hopping. A similar result has been found for alkanethiols on InP(100), which present a molecular tilt angle of ~55° (very similar to that found in the rectangular configuration) [Yamamoto02]. However, we believe that our experimental approach is more suitable to study the transport properties of SAMs, than comparing data using different substrates. The nature of the contact between molecule and substrate also affect the measured current hindering the solely study of the influence of the tilt angle.

The difference between the experimental data and the predicted behaviour of equation (6.4) for C18 molecules can be overcome by including more than one interchain hop in the chain-to-chain mechanism. If N interchain hops are considered, the effective distance is reduced by $Nd_{cc}\tan(\theta)$ whereas the distance for through-space hopping is given by Nd_{cc}. In addition, the number of possible pathways grows with the number of interchain hops. The expression of the total current is then given by:

$$I_t = I_0 \cdot \exp(-\beta_{TB} \cdot d) + I_0 \cdot \sum_{N=1}^{\frac{d\cos\theta}{dcc}} \frac{n_s!}{(n_s - N)!\cdot N!} \cdot \exp\left[-\beta_{TB} \cdot (d - N \cdot d_{cc} \tan\theta)\right] \cdot \exp(-\beta_{TS} \cdot N \cdot d_{cc}) \qquad (6.5)$$

The upper limit in the sum ($d\cdot\cos\theta/d_{cc}$), ensures that through-space hops do not exceed the film thickness. For C18, this value is 4 for a tilt angle of 50°. Therefore, a chain-to-chain pathway along a C18 molecule in the 50°-tilted configuration can contain up to a maximum of four through-space hops.

The red symbol in the lower graph of figure 6.11 corresponds to the value of the current obtained from equation (6.5) for C18 and $\sum_{N=1}^{2}$. Thus, the experimental data for 50° is excellently reproduced by including the possibility of both, single and double interchain hops between molecules (red triangle).

For shorter chains, the contribution of pathways with multiple hops might not be significant since the maximum number of hops decreases with decreasing the molecular length ($N \leq d \cdot \cos\theta / d_{cc}$). This might explain the reasonable agreement between the experimental data for C12 and C16 and the model considering a single hop.

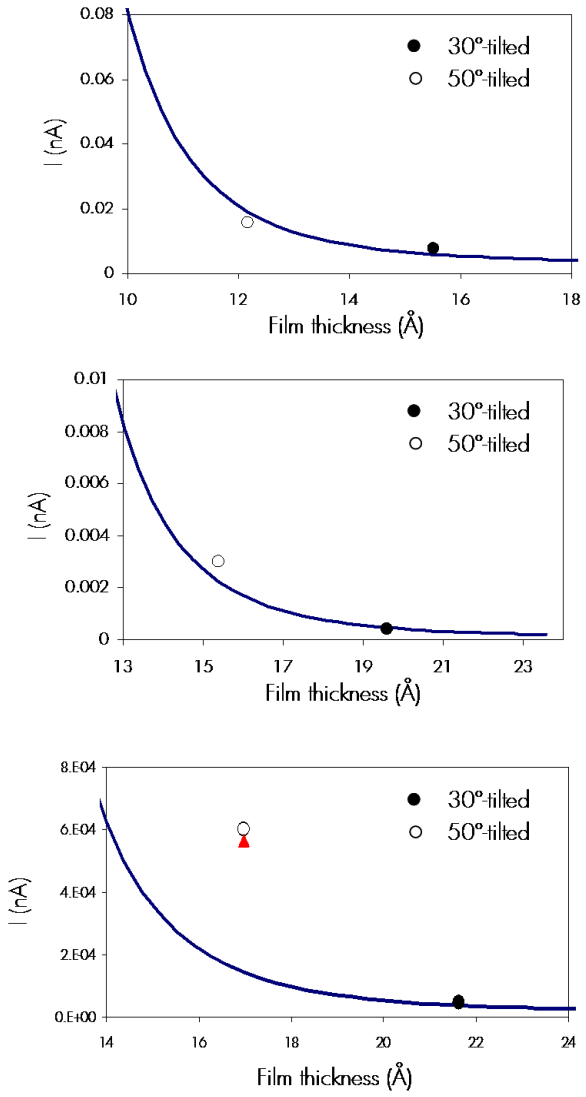

Figure 6.11 Tunnelling current measured on C12 (top), C16 (middle) and C18 (bottom) islands presenting the hexagonal (solid symbol) and rectangular (open symbol) configurations. The solid line correspond to the tunnelling behaviour predicted by equation (6.4). The triangle and square symbols in the bottom graph are the current values calculated from equation (6.5) when more than one single hop is considered (see text).

6.3 CONCLUSIONS.

Transport measurements through metal-SAMs-metal junctions have been conducted using C-SFM. Two innovative approaches are presented for the study of the transport properties The first one is the use of the so-called 3D modes for data acquisition. This method presents the advantages of independent but simultaneous data acquisition, thus minimizing time-dependent changes in sample or probe properties or any position uncertainty. The second one is the use of submonolayer coverages, which provides islands of different thickness, due to the different tilt angle, for the same molecular length. Being aware of the interest of elucidating between possible pathways for electron transport in these monolayers, the spontaneous formation of differently tilted configurations offers a great opportunity for studying the role of this tilt angle in the transport characteristics, without tip-induced distortion of the SAM.

Current-versus voltage curves have been measured for different molecular lengths and different molecular configurations. I-V fitting with Simmons tunnelling model and comparison of the obtained transport parameters with previous reported values, suggest that the main conduction mechanism in this alkanethiol islands is tunnelling. Nonetheless, noticeable differences are found in the decay parameter β between the rectangular and the hexagonal configurations. This result points to an angle-dependent contribution to the tunnelling current.

The junction resistance has been calculated from the linear region of the I-V plots. The tip-loading force has been found to dramatically influence the molecular junction properties, not only due to the increase in contact junction area, but also by a potential structural distortion of the packing. Current images show that, at sufficiently high loads, molecules under the tip are displaced and the tip contacts the underlying substrate.

The comparison of the junction resistance values (measured at the lowest practical load) for the rectangular and the hexagonal configurations, clearly indicates the existence of an additional tunnelling mechanism besides the widely reported through-bond pathway. This mechanism is consistent with the chain-to-chain pathway proposed in [Slowinski97], which takes into account interchain coupling. Tough in relative terms, through-bond tunnelling is still more efficient. Our experimental results are well-reproduced by the two-pathway model reported to describe the transport characteristics of SAMs on Hg. Nonetheless, for longer chains (C18), a slight modification of the chain-to-chain pathway to include the possibility of multiple hops between adjacent chains is likely and results useful to accurately reproduced the experimental data for the 50°-tilted configuration.

6.4 REFERENCES.

[Alamarguy04] D. Alamarguy, O. Schneegans, S. Noël, L. Boyer "Correlation between the electrical and mechanical behaviours of a nanocontact with an alkanethiol monolayer" 2004 App. Surf. Sci. 225; 309.

[Cui02] X. D. Cui, X. Zarate, J. Tomfohr, O. F Sankey, A. Primak, A. L. Moore, T. A . Moore, D. Gust, G. Harris, S. M. Lindsay "Making electrical contacts to molecular monolayers" 2002 Nanotechnology 13; 5.

[Engelkes04] V. B. Engelkes, J. M. Beebe, C. D. Frisbie. "Length-Dependent Transport in Molecular Junctions Based on SAMs of Alkanethiols and Alkanedithiols: Effect of Metal Work Function and Applied Bias on Tunneling Efficiency and Contact Resistance" 2004 J. Am. Chem. Soc. 126; 14287.

[Haag99] R. Haag, M. A. Rampi, R. E. Holmlin, G. M. Whitesides. "Electrical breakdown of aliphatic and aromatic self-assembled monolayers used as nanometer-thick organic dielectrics" 1999 J. Am. Chem. Soc. 121;7895.

[Holmlin01] R. E. Holmlin, R. Haag, M. L. Chabinyc, R. F. Ismagilov, A. E. Cohen, A. Terfort, M. A. Rampi, G. M. Whitesides "Electron transport through thin organic films in metal-insulator-metal junctions based on self-assembled monolayers" 2001 J. Am. Chem. Soc. 123; 5075.

[Ishida02] T. Ishida, W. Mizutani, Y. Aya, H. Ogiso, S. Sasaki, H. Tokumoto "Electrical Conduction of Conjugated Molecular SAMs Studied by Conductive Atomic Force Microscopy" 2002 J. Phys. Chem. B, 106; 5886.

[Jiang06] W. Jiang, E. Garfunkel, N. Zhitenev, D. Abusch-Magder, D. Tennant, Z. Bao "Molecular conductance measurements through printed Au nanodots" 2006 App. Phys. Lett. 89; 113107.

[Leatherman99] G. Leatherman, E. N. Durantini, D. Gust, T. A. Moore, A. L. Moore, S. Stone, Z. Zhou, P. Rez, Y. Z. Liu, S. M. Lindsay "Carotene as a Molecular Wire: Conducting Atomic Force Microscopy" 1999 J. Phys. Chem. B 103; 4006.

[Lee04] T. Lee, W. Wang, J. F. Klemic, J. J. Zhang, J. Su, M. A. Reed "Comparison of Electronic Transport Characterization Methods for Alkanethiol Self-Assembled Monolayers" 2004 J. Phys. Chem. B 108; 8742.

[Nakamura03] M. Nakamura, H. Yanagisawa, S. Kuratani, M. Iizuka, K. Kudo "Characterization of organic nano-transistors using a conductive AFM probe" 2003 Thin Solid Films 438–439 ; 360.

[Ratner98] M. A. Ratner, B, Davis, M. Kemp, V. Mujica, A. Roitberg, S. Yaliraki "Molecular Electronics: Science and Technology" 1998 Ann. N.Y. Acad. Sci. 852; 22

[Sakaguchi01] H. Sakaguchi, A. Hirai, F. Iwata, A. Sasaki, T. Nagamura, E. Kawata, S. Nakabayashi "Determination of performance on tunnel conduction through molecular wire using a conductive atomic force microscope" 2001 Appl. Phys. Lett. 79; 3709.

[Salmeron93] M. Salmeron, G. Neubauer, A. Folch, M. Tomitori, D. F. Ogletree, P. Sautet "Viscoelastic and Electrical Properties of Self-Assembled Monolayers on Au(11 1) Films" 1993 Langmuir 9; 3600.

[Salomon03] A. Salomon, D. Cahen, S. Lindsay, J. Tomfohr, V. B. Engelkes, C. D. Frisbie. "Comparison of electronic transport measurements on organic molecules" 2003 Adv. Mater. 15; 1881.

[Selzer02] Y. Selzer, A. Salomon, D. Cahen "The Importance of Chemical Bonding to the Contact for Tunneling through Alkyl Chains" 2002 J. Phys. Chem. B. 106; 10432

[Slowinski97] K. Slowinski, R. V. Chamberlain, C. J. Millar, M. Majda. "Through-Bond and Chain-to-Chain Coupling. Two Pathways in Electron Tunnelling through Liquid Alkanethiol Monolayers on Mercury Electrodes"1997 J. Am. Chem. Soc. 119; 11910.

[Song06] H. Song, C. Lee, Y. Kang, T. Lee " Electronic transport and tip-loading force effect in self-assembled monolayer studied by conducting atomic force microscopy" 2006 Colloids and Surfaces A: Physicochem. Eng. Aspects 284–285; 583.

[Tran06] E. Tran, M. Duati, V. Ferri, K. Müllen, M. Zharnikov, G. M. Whitesides, M. A. Rampi "Experimental Approaches for Controlling Current Flowing through Metal–Molecules–Metal Junctions" 2006 Adv. Mater. 18; 1323.

[Wang03] W. Wang, T. Lee, M.A. Reed "Electronic transport in self-assembled alkanethiol monolayers" 2003 Physica E 19; 117.

[Wang05] W. Wang, T. Lee, M.A. Reed "Electron tunnelling in self-assembled monolayers" 2005 Rep. Prog. Phys. 68; 523.

[Wold00]] D. J. Wold, C. D. Frisbie "Formation of Metal-Molecule-Metal Tunnel Junctions: Microcontacts to Alkanethiol Monolayers with a Conducting AFM Tip" 2000 J. Am. Chem. Soc.122; 2970.

[Wold01] D. J. Wold, C. D. Frisbie "Fabrication and Characterization of Metal-Molecule-Metal Junctions by Conducting Probe Atomic Force Microscopy" 2001 J. Am. Chem. Soc.123; 5549.

[Wold02] D. J. Wold, R. Haag, M. A. Rampi, C. D. Frisbie " Distance Dependence of Electron Tunneling through Self-Assembled Monolayers Measured by Conducting Probe Atomic Force Microscopy: Unsaturated versus Saturated Molecular Junctions" 2002 J. Phys. Chem. B, 106; 2813.

[Yamamoto02] H. Yamamoto, D. H. Waldeck "Effect of Tilt-Angle on Electron Tunneling through Organic Monolayer Films" 2002 J. Phys. Chem. B, 106; 7469.

SUMMARY

Within each chapter of this thesis we have included a "conclusion" section where we have detailed the main results obtained from the corresponding study. Nonetheless, in this section we give a more general overview of the work reported in this thesis.

This thesis has pursued the understanding of the growth of self-assembled monolayers under ambient conditions. For that purpose, alkanethiol and disulphide molecules (Cn and CnCm) have been chosen because in spite of being one of the most studied systems, there are some controversial points regarding the growth and final structure of these organic layers. Moreover, most of the reported results have been obtained for complete monolayers, whereas this work is focused to the study of partial coverages which, as has been shown throughout this manuscript, yield considerably different results. We have taken advantages of the versatility of the scanning force microscopy technique to address the combined study of the growth, the structure and the frictional and transport properties of alkanethiol and disulphide islands. Different molecular length have been used in all these studies to further address the role played by the molecular chain both, in the tribological and the transport properties.

The studies devoted to the structural characterization have been mainly focused on the determination of the molecular configuration of the different phases found at submonolayer coverages. Conversely to the complete monolayer, at these partial coverages different configurations coexist for all the molecules studied (except for asymmetrical disulphide). From topographic measurements and high resolution images we have determined the molecular structure for each of the observed configurations. The finding reveals the formation of a striped phase in which the molecules are arranged lying flat on the substrate and two standing up phases in which the molecules are oriented perpendicular to the surface plane, but with different tilt angles (50° and 30°). These are the (px2√3), (2x√3)rect and (√3x√3)R30° configurations, all commensurate with the underlying substrate. From real time SFM visualization we have found that the stripe phase, with time and without increasing coverage, transform irreversibly into the two other standing up phase, indicating that this lying phase is a metastable configuration only formed under our experimental conditions. We have also disclosed a length-dependent mechanical stability of the rectangular 50°-tilted configuration which is explained based on the competition between intermolecular and molecule-substrate interactions. A model based in the calculation of the total film energy as a function of the chain length has been found to extraordinarily predict the observed behaviour.

The use of submonolayer coverages for frictional and transport measurements have been proved to be a convenient strategy to address the relation between structural parameters and physical phenomena. We have found that depending on the molecular length, the mechanisms of energy dissipation contributing to friction are different. For short molecules (C10 and C12) friction is mainly due to the formation of gauche defects and the increase in contact area. This implies a monotonous

increase of the friction signal as a function of the applied load. Conversely, long molecules (C16 and C18) shows a stepwise behaviour in the friction signal due to collective tilting of the molecules under the tip. The existence of favoured tilt angles is justified with a 3D model and predicts the experimental results obtained. By comparing the behaviour of the differently tilted configurations, we have also faced the influence of the molecular structure on the frictional properties of these organic layers. Furthermore, the investigation of disulphide samples has allowed deciphering the different contribution between internal and external gauche defects to the total friction measured.

Finally, we have faced the study of the transport mechanism in alkanethiol samples by means of conductive-SFM. The results presented confirms the suitability of the technique to address these type of measurements and the use of differently tilted configurations has emerged as an accurate approach to address the role played by the molecular length and the molecular tilt on the transport properties of SAMs. The experimental data is well explained considering the existence of two tunnelling mechanism for electron transfer: the through-bond tunnelling, which implies tunnelling along the molecular backbone and consequently depends on the molecular length, and a chain-to-chain pathway, which takes into account interchain coupling. This latter mechanism becomes more efficient for longer chains and larger tilt angles as shown by comparing the results of C12, C16 and C18 molecules.